
Electronic Thesis and Dissertation Repository

3-27-2018 10:30 AM


Multiresonant Anisotropic Nanostructures for Plasmon-Mediated Spectroscopies

Gregory Q. Wallace
The University of Western Ontario

Supervisor
Lagugné-Labarthe, François
The University of Western Ontario

Graduate Program in Chemistry
A thesis submitted in partial fulfillment of the requirements for the degree in Doctor of Philosophy
© Gregory Q. Wallace 2018

Follow this and additional works at: <https://ir.lib.uwo.ca/etd>

 Part of the [Analytical Chemistry Commons](#), [Materials Chemistry Commons](#), and the [Physical Chemistry Commons](#)

Recommended Citation

Wallace, Gregory Q., "Multiresonant Anisotropic Nanostructures for Plasmon-Mediated Spectroscopies" (2018). *Electronic Thesis and Dissertation Repository*. 5268.
<https://ir.lib.uwo.ca/etd/5268>

This Dissertation/Thesis is brought to you for free and open access by Scholarship@Western. It has been accepted for inclusion in Electronic Thesis and Dissertation Repository by an authorized administrator of Scholarship@Western. For more information, please contact wlsadmin@uwo.ca.

Abstract

To detect and analyze molecular species of interest, analytical sciences and technologies exploit the variation in the chemical properties associated with the analytes. Techniques involving vibrational spectroscopy rely on the unique response observed when a molecule interacts with light. Although these methods can provide the specificity needed for detection, they are traditionally hindered by the need for large quantities of material, and long acquisition times. To minimize these issues, advancements in plasmon-enhanced techniques, such as surface-enhanced Raman spectroscopy (SERS) and surface-enhanced infrared absorption (SEIRA) are being made. Such techniques make use of the strong interaction between an optical field and a metallic nanostructure to locally enhance the electromagnetic field at the surface of the nanostructure. When a molecule of interest is adsorbed onto or located near the metal surface, it is possible to amplify the vibrational fingerprint needed for chemical differentiation. To achieve the amplification necessary for sensitive and ultra-sensitive analytical measurements, the optical properties of the nanostructures must be highly tuned.

In this thesis, the rational design and fabrication of a variety of anisotropic gold nanostructures capable of probing molecular systems at the monolayer level is described. An emphasis is placed on fabricating nanostructures and platforms capable of supporting multiple plasmonic resonances that span the visible through mid-infrared spectral domains. Relying on advanced nanofabrication techniques, two-dimensional arrays of metallic nanostructures were inscribed onto a variety of substrates. Once prepared, the platforms are then rigorously analyzed both numerically and experimentally to determine their physical and optical properties. An emphasis is placed on developing means of tailoring the properties to specific optical processes. Once tuned, the compatibility of the structures and platforms towards the techniques of linear dichroism, SERS, SEIRA, and correlative SERS/SEIRA measurements are examined and evaluated. This thesis offers new insight into the development of plasmonic nanostructures that exhibit multiple optical resonances, and how to tailor these resonances to specific optical processes.

Keywords

Plasmonics, localized surface plasmon resonance, gold, anisotropic nanostructures, fractal nanostructures, finite-difference time-domain, surface-enhanced Raman spectroscopy, surface-enhanced fluorescence, surface-enhanced infrared absorption, electron-beam lithography, mid-infrared synchrotron beamline, polarization-modulation infrared linear dichroism microscopy

Dedication

To my parents, *Rob and Pam Wallace*,
for their constant love and support.

And to my grandparents, *Joan and Ted Wallace*,
for being with me every step of the way.

Co-Authorship Statement

Prof. François Lagugné-Labarthe was the corresponding author on the papers presented in this thesis, and was responsible for the supervision of Gregory Wallace over the course of his studies. This thesis includes materials from five publications, all of which had contributions from co-authors.

Gregory Wallace was the primary author of the papers presented in Chapters 3, 4, 5, 6, and 7. He was responsible for the acquisition of most of the experimental work in the papers, as well as the writing and revision for all drafts, including the final manuscripts. Throughout this work, data was acquired or jointly acquired and analyzed by co-authors as summarized below:

Chapter 3: Wallace, G.Q.; Coady, M.J.; Foy, H.C.; McRae, D.M.; Lagugné-Labarthe, F. Achieving high hot-spot densities in anisotropic nanostructures compatible with plasmon-enhanced spectroscopies. *Manuscript in preparation.*

Matthew J. Coady was responsible for the fabrication and SEM imaging of the singlet and doublet nanorods, and the Sierpiński hexagonal gasket fractal. He was also involved in the data acquisition for the absorbance and SERS measurements on the nanorod patterns. Hayden C. Foy was responsible for the FDTD calculations involving the multimer arrays of nanoprisms and nanoarrowheads. Danielle M. McRae was also involved in the FDTD calculations both for the multimer, and nanorod arrays.

Chapter 4: Wallace, G.Q.; Tabatabaei, M.; Hou, R.; Coady, M.J.; Norton, P.R.; Rosendahl, S.M.; Merlen, A.; Lagugné-Labarthe, F. Superimposed arrays of nanoprisms for multispectral molecular plasmonics. *ACS Photonics*, **2016**, *3*, 1723-1732.

Dr. Mohammadali Tabatabaei trained Gregory Wallace on the operation of the combined AFM-confocal fluorescence instrument used for the SEF measurements. He was also involved in the analysis of the SEF data, and in the writing of the SEF portions of the manuscript. Dr. Renjie Hou trained Gregory Wallace on performing FDTD calculations and was involved in the analysis of the FDTD results. Matthew J. Coady was responsible for the fabrication and SEM imaging on the superimposed arrays of nanoprisms. Prof. *Emeritus*

Peter R. Norton kindly provided the combined AFM-confocal fluorescence instrument used for the SEF measurements. Dr. Scott M. Rosendahl is the beamline scientist for the mid-infrared beamline at the CLS, where most of the mid-infrared measurements were acquired. He was also responsible for the training of Gregory Wallace on the operation of the mid-infrared instrument at the CLS and was involved in reviewing the mid-infrared portion of the manuscript. Prof. Alexandre Merlen (Université de Toulon, France) accompanied Gregory Wallace and Prof. François Lagugné-Labarthe to the CLS. He performed the initial analysis of the mid-infrared measurements and was involved in the analysis of the FDTD calculations.

Chapter 5: Wallace, G.Q.; Foy, H.C.; Rosendahl, S.M.; Lagugné-Labarthe, F. Dendritic plasmonics for mid-infrared spectroscopy. *J. Phys. Chem. C*, **2017**, *121*, 9497-9507.

Hayden C. Foy performed some of the FDTD calculations. Dr. Scott M. Rosendahl supervised Gregory Wallace during the acquisition of the mid-infrared measurements at the CLS.

Chapter 6: Wallace, G.Q.; Read, S.T.; McRae, D.M.; Rosendahl, S.M.; Lagugné-Labarthe, F. Exploiting anisotropy of plasmonic nanostructures with polarization-modulation infrared linear dichroism microscopy (μ PM-IRLD). *Adv. Opt. Mater.*, **2018**, *6*, 1701336.

Dr. Stuart T. Read is the support scientist for the mid-infrared beamline at the CLS. He was responsible for the μ PM-IRLD setup and developing the program used to acquire and analyze the data. Danielle M. McRae performed some of the FDTD calculations. Dr. Scott M. Rosendahl oversaw the mid-infrared measurements at the CLS.

Chapter 7: Wallace, G.Q.; McRae, D.M.; McConnell, E.M.; Therien, D.A.B.; DeRosa, M.C.; Lagugné-Labarthe, F. Plasmonic properties of lithographically prepared metallic dendrimers and their applicability to SERS-based sensing. *Manuscript in Preparation*.

Danielle M. McRae performed some of the FDTD calculations and will be involved in the data analysis of the experiments involving the aptamer. Dr. Erin M. McConnell is a Post-Doctoral Fellow in the lab of Prof. Maria C. DeRosa (Carleton University). Dr. McConnell performed the synthesis of the dopamine aptamer used. D. Alexander B. Therien performed some of the absorbance measurements.

Acknowledgments

To be frank, none of this would have happened if it wasn't for my supervisor, Prof. François Lagugné-Labarthet. Some people say that they work for their supervisor, I am fortunate to say that I worked with my supervisor. Time and time again, François gave me the opportunity to explore my research and pursue my own ideas. Because of François, I worked on a series of collaborative projects, including international collaborations. Thanks to François, I was given opportunities to present my research from coast-to-coast, and to go to Paris to perform experiments. I would not be the researcher that I am if it wasn't for François, and for that, I am eternally grateful.

With François comes the FLL group. I have had the distinct pleasure of working with and alongside some amazing people. When I first joined the group as an undergrad, Dr. Mohammadali Tabatabaei took me under his wing. Although only one chapter may list his contributions; his support, guidance, and friendship played a role at the beginning and throughout my graduate studies. As well, I want to specifically acknowledge Danielle McRae. Our friendship may have been expedited due to the group dramatically shrinking in size, but, I am sure glad that it happened.

I must also thank all of those that have played a role in my research. Without the help of Tim Goldhawk and Dr. Todd Simpson of the Western Nanofabrication Facility, the platforms shown in this thesis would have never made it past the drawing phase. Whenever I went to the CLS, it was always great to be able to work with Drs. Scott Rosendahl and Stuart Read, and have visits from Tyler Morhart and Prof. Ian Burgess (University of Saskatchewan). We are unable to know and do everything. I have worked with a fantastic group of collaborators: Prof. Mark Workentin, Dr. Pierangelo Gobbo, and Mariachiara Zuin (Western Chemistry); Prof. Harvey Goldberg, Dr. Yohannes Soenjaya, and Ryan Marinovich (Schulich); Prof. Maria DeRosa, and Dr. Erin McConnell (Carleton University); Prof. Alexandre Merlen (Université de Toulon); Prof. Nordin Félidj, Prof. Claire Mangeney, and Issam Kherbouche (Université Paris Diderot).

During my graduate studies, I was fortunate enough to receive funding at various levels that helped to support my research, and my attendance at conferences. I would like to specifically

acknowledge the CLS as they gave me two student travel grants to perform my research at the CLS in Saskatoon.

Over the years, I have made friendships with people across the Chemistry Department. To those on the other side of the wardrobe, I say this, you have made my time in the MSA an interesting one. Overhearing bits of the conversation coming from the Ding lab often lead to me having quite a laugh. Always remember, beware of backyard ziplines!

Lastly, I want to thank my entire family. When I first came to Western, there was an expectation of a long-haul education, and they have been nothing but supportive of it even if that had no clue what I was doing. In the brightest of days and the darkest of nights, it has been comforting knowing that they were always there for me. I always looked forward to coming home as it meant movies with dad, genealogy research with mom, games of Ticket to Ride with Patrick and Brooke, and some really messed up games of Cards Against Humanity while sitting at the dinner table.

Table of Contents

Abstract.....	i
Keywords.....	ii
Dedication.....	iii
Co-Authorship Statement.....	iv
Acknowledgments.....	vi
Table of Contents.....	viii
List of Tables.....	xiv
List of Figures.....	xv
List of Abbreviations, Symbols, and Nomenclature.....	xxv
List of Appendices.....	xxvii
Chapter 1.....	1
1 General Introduction.....	1
1.1 Applications Involving Plasmonic Nanostructures.....	1
1.1.1 Performing Chemistry at the Nanoscale.....	2
1.1.2 Enhanced Vibrational Spectroscopy for On-Chip Sensing.....	5
1.2 Scope of Thesis.....	6
1.3 References.....	8
Chapter 2.....	12
2 Design, Fabrication, and Characterization of Plasmonic Nanostructures.....	12
2.1 Plasmonic Resonances in Metals.....	12
2.1.1 Plasmon.....	12
2.1.2 Surface Plasmon.....	13
2.1.3 Localized Surface Plasmon Resonance.....	14
2.1.4 Modelling the Plasmonic Properties of Nanostructures.....	16

2.2	General Considerations for Fabricating Nanostructures	17
2.3	Plasmonic Platforms Prepared by Lithography	19
2.3.1	Nanosphere Lithography (NSL)	20
2.3.2	Electron-Beam Lithography (EBL)	22
2.4	Probing the Plasmonic Properties in the Visible to Near-Infrared Spectral Regions	25
2.4.1	Visible Near-Infrared Absorption Measurements.....	25
2.4.2	Surface-Enhanced Raman Spectroscopy (SERS) Measurements.....	27
2.5	Probing the Plasmonic Properties in the Near- to Mid-Infrared Spectral Regions.....	29
2.5.1	Sources of Mid-Infrared Light	30
2.5.2	Near- to Mid-Infrared Absorption Measurements	31
2.5.3	Surface-Enhanced Infrared Absorption (SEIRA) Measurements.....	32
2.6	References	34
Chapter 3.....		40
3	Achieving High Hot-Spot Densities in Anisotropic Nanostructures Compatible with Plasmon-Enhanced Spectroscopies.....	40
3.1	Introduction.....	40
3.2	Experimental.....	43
3.2.1	Materials	43
3.2.2	Electron-Beam Lithography.....	44
3.2.3	Visible to Near-Infrared Absorption.....	44
3.2.4	Near- to Mid-Infrared Absorption	44
3.2.5	Surface-Enhanced Raman Measurements.....	44
3.2.6	Surface-Enhanced Fluorescence Measurements.....	45
3.2.7	Electromagnetic Field Modelling	45
3.3	Results and Discussion	45
3.3.1	Singlet and Doublet Nanorods	45

3.3.2	Multimer Configurations of Nanoprisms.....	49
3.3.3	Superimposing Nanoprisms to Generate Nanoarrowheads	53
3.3.4	Response of Multimer Configurations.....	55
3.3.5	Sierpiński Hexagonal Gasket.....	57
3.4	Conclusions.....	60
3.5	References.....	61
Chapter 4.....		66
4	Superimposed Arrays of Nanoprisms for Multispectral Molecular Plasmonics.....	66
4.1	Introduction.....	66
4.2	Experimental.....	69
4.2.1	Materials	69
4.2.2	Nanosphere Lithography.....	70
4.2.3	Electron-Beam Lithography.....	70
4.2.4	Visible and Near-Infrared Absorption	70
4.2.5	Surface-Enhanced Fluorescence	70
4.2.6	Surface-Enhanced Raman.....	71
4.2.7	Infrared Absorption and Surface-Enhanced Infrared Absorption.....	71
4.2.8	Electromagnetic Field Modelling	71
4.3	Results and Discussion	72
4.3.1	Superimposed Fischer's Patterns	72
4.3.2	Optical Properties of the Superimposed Patterns in the Visible Region ..	74
4.3.3	SEF Compatibility	77
4.3.4	SERS Compatibility.....	80
4.3.5	Optical Properties of the Superimposed Patterns from Near- to Mid-IR Regions	83
4.3.6	SEIRA Compatibility.....	87

4.3.7	Multispectral Platform Comparison.....	88
4.4	Conclusions.....	89
4.5	References.....	90
Chapter 5	94
5	Dendritic Plasmonics for Mid-Infrared Spectroscopy	94
5.1	Introduction.....	94
5.2	Experimental.....	98
5.2.1	Materials	98
5.2.2	Electron-Beam Lithography.....	98
5.2.3	Infrared Absorption and Surface-Enhanced Infrared Absorption.....	99
5.2.4	Electromagnetic Field Modelling	99
5.3	Results and Discussion	99
5.3.1	General Optical Properties of Dendritic Fractals.....	99
5.3.2	Increasing the Size of the Dendritic Fractal.....	108
5.3.3	Increasing the Number of Branches.....	110
5.3.4	Surface-Enhanced Infrared Absorption of a Thin Film	114
5.3.5	Surface-Enhanced Infrared Absorption of a Monolayer.....	118
5.4	Conclusion	119
5.5	References.....	120
Chapter 6	124
6	Exploiting Anisotropy of Plasmonic Nanostructures with Polarization-Modulation Infrared Linear Dichroism Microscopy (μ PM-IRLD)	124
6.1	Introduction.....	124
6.2	Experimental.....	127
6.2.1	Materials	127
6.2.2	Electron-Beam Lithography.....	127

6.2.3	Static Polarization Infrared Measurements	127
6.2.4	Polarization-Modulated Infrared Linear Dichroism Microscopy Measurements	127
6.2.5	Surface-Enhanced Infrared Absorption	128
6.2.6	Electromagnetic Field Modelling	128
6.3	Results and Discussion	129
6.3.1	Polarization Dependence of Dendritic Fractals	129
6.3.2	Polarization-Modulated Measurements of Dendritic Structures.....	130
6.3.3	Polarization-Modulation and Optical Tuning	133
6.3.4	Increasing the Side Lengths of the Nanorods	133
6.3.5	Increasing the Number of Inner Branches	135
6.3.6	Third-Order Generation Dendritic Fractals	139
6.3.7	Polarization-Modulated Surface-Enhanced Infrared Absorption	141
6.4	Conclusions.....	143
6.5	References.....	144
Chapter 7.....		148
7	Plasmonic Properties of Lithographically Prepared Dendrimers and their Applicability to SERS-Based Sensing	148
7.1	Introduction.....	148
7.2	Experimental.....	151
7.2.1	Materials	151
7.2.2	Electron-Beam Lithography.....	151
7.2.3	Visible to Near-Infrared (400-1000 nm) Absorption.....	151
7.2.4	Electromagnetic Field Calculations	151
7.2.5	Surface-Enhanced Raman Measurements with 4-NTP.....	152
7.2.6	Raman and Surface-Enhanced Raman Measurements with Dopamine..	152
7.2.7	Surface-Enhanced Raman Measurements with Aptamer	152

7.3 Results and Discussion	153
7.3.1 Optical Properties of Dendritic Fractals in the Visible to Near-Infrared Region.....	153
7.3.2 Further Tuning the Spectral Positions of the Localized Surface Plasmon Resonances.....	160
7.3.3 SERS Compatibility of the Dendritic Fractals.....	162
7.3.4 Direct SERS-Based Detection of Dopamine	164
7.3.5 Indirect SERS-Based Detection of Dopamine.....	166
7.4 Conclusion	168
7.5 References.....	169
Chapter 8.....	173
8 Conclusions and Outlook.....	173
8.1 References.....	179
Appendix A – Details for FDTD Calculations	181
Appendix B – Fabrication Details for Nanosphere Lithography	183
Appendix C – Fabrication Details for Electron-Beam Lithography.....	184
Appendix D – Copyrights.....	185
Curriculum Vitae	194

List of Tables

Table 5.1 SEIRA vibrational mode assignment for PMMA.....	117
---	-----

List of Figures

Figure 1.1 A) Changes to the scattering spectra of a AuNPoM platform with increasing irradiation time. *T*: transverse mode; *L*: dipolar mode. B) Prediction of coupled plasmon resonance wavelength with changing gap size. The inset scheme depicts the polymer growth between the AuNP and the mirror.²⁷ C-F) SEM images of gold nanostructures coated with a PMMA thin film followed by irradiation.²⁸ For C and D) the light is polarized along the length of nanorod. G) AFM image of a AuNR prior to grafting with an aryl diazonium salt. H) AFM image of the AuNR after grafting and the formation of the poly(aryl) layer. I) Subtracted AFM image of G) and H) revealing the location of the grafted film. J) Electric field distribution around a rectangular rod with rounded edges.²⁹ Adapted with permission from references 27, 28 and 29. Copyright 2017 American Chemical Society and 2017 Royal Society of Chemistry..... 4

Figure 2.1 Illustration of a propagating surface plasmon at the interface between a metal surface and a dielectric..... 13

Figure 2.2 Complex dielectric constants of A) gold and silver, and B) copper and aluminum according to the Drude-Lorentz model. 14

Figure 2.3 Model of a localized surface plasmon resonance (LSPR) for a metallic nanosphere. 15

Figure 2.4 Illustration of a standard Cartesian Yee cell used for FDTD calculations and how the electric (red circles and arrows, E_x , E_y , E_z) and magnetic (blue circles and arrows, H_x , H_y , H_z) field components are distributed across the cell. 17

Figure 2.5 Schematic illustration of the general NSL process. Polystyrene or silica particles are deposited onto a substrate, such as a glass cover slip, and eventually form a monolayer. Thin films of metals (adhesion followed by plasmonic) are deposited onto the surface by electron-beam evaporation. The particles are then removed by sonication in ethanol to reveal the nanostructures formed between the gaps of the particles. 21

Figure 2.6 Scanning electron micrographs for different examples of nanostructures prepared by nanosphere lithography: A) film over nanospheres, B) nanoprisms, C) tetrahedral

nanopyramids, D) nanohole arrays, E) Moiré patterns, and F) nanocrescents. Adapted with permission from refs 78 , 79 , 83 Copyright 2014 American Chemical Society and 2015 American Chemical Society. 22

Figure 2.7 Schematic illustration for the general EBL process. An electron-beam sensitive resist is spin-coated onto the surface of a cleaned substrate. If the substrate is non-conductive, a conductive polymer is spin-coated onto the resist and is further baked. Following exposure to the electron-beam (darker regions), the sample is developed, the resulting patterned resist will depend on the type of resist. Once the metal is deposited and the excess resist is lifted-off, the final structure is revealed. 23

Figure 2.8 SEM images highlighting examples of gold nanostructures prepared in the Lagugné-Labarthe group using electron-beam lithography: A) box of nanorods, B) arrays of the boxes of nanorods, C) Cesaro-like fractal, D) Sierpiński triangle, E) snowflake-like nanostructures, and F) arrays of nanoholes. A-E) were prepared using a positive resist, and F) was prepared using a negative resist. 24

Figure 2.9 Schematic representation of different order LSPR modes for a metallic nanosphere. 25

Figure 2.10 Schematic illustration of the absorbance setup used in this thesis. 26

Figure 2.11 Schematic illustration of the Raman and SERS setup used in this thesis. The green arrows indicate the optical path of the incident (excitation) photons, and those in red correspond to the Raman scattered photons. 29

Figure 2.12 Comparison of the normalized infrared absorbance spectra for superimposed arrays of gold nanoprisms with side lengths of 2 and 0.25 μm obtained using different infrared sources. 31

Figure 2.13 Schematic illustration of the general mid-infrared absorption and SEIRA set-up used in this thesis. The components in the dashed lines were used in the anisotropy measurements described in Chapter 6. 32

Figure 3.1 SEM images of gold nanorods arranged as A) singlets, and B) doublets. C) and D) are the corresponding visible to near-IR absorbance spectra of the nanorods at orthogonal polarizations, where 0° matches the long axis of the nanorods. 46

Figure 3.2 FDTD calculations for singlet and doublet configurations under polarizations that are A) and B) parallel (0°), and C and D) perpendicular (90°) to the long axis of the nanorods. The SERS spectra correspond to 4-NTP functionalized E) singlets, and F) doublets. The colours correspond to the orthogonal polarizations of light. The dotted spectra were obtained on 4-NTP functionalized flat gold. 48

Figure 3.3 SEM images of gold nanoprisms with side lengths of 125 nm arranged in different configurations, A) dimer, B) trimer, C) tetramer, D) pentamer, and E) hexamer. Corresponding experimental absorption spectra are shown in F-J). The scale bar in the inset SEM images is 100 nm. 50

Figure 3.4 A) Absorbance spectra of gold nanoprisms written with specified lengths and arranged in trimer configurations. The pattern was written with a gap of 50 nm. B) Absorbance spectra of gold nanoprisms written with varying gap sizes, fixed side lengths of 200 nm, and arranged in dimer configurations. 51

Figure 3.5 FDTD calculations of the electric field $(|E/E_0|)^2$: log scale representation at wavelengths corresponding to the dominant absorption of the gold nanoprisms A) dimer, B) trimer, C) tetramer, D) pentamer, and E) hexamer. F) Electric field at the highest energy resonance of the hexamer. The side lengths of the nanoprisms is 135 nm. 52

Figure 3.6 Absorbance spectra for A) double, and B) triple nanoarrowheads. The lengths mentioned refer to the side lengths of the nanoprisms used to prepare the arrowheads. The inset SEM images correspond to the double and triple nanoarrowheads written with the nanoprisms having a side length of 150 nm. The scale bar in the inset SEM images is 200 nm. 53

Figure 3.7 FDTD calculations of the electric field $(|E/E_0|)^2$: log scale representation at wavelengths corresponding to the absorptions for A-C) double and D-F) triple nanoarrowheads prepared in a pentamer configuration. The side lengths of the nanoprisms of the arrowheads are 135 nm. 55

Figure 3.8 SERS measurements performed on nanoprisms and nanoarrowheads with side lengths of 135 nm functionalized in a 10^{-3} M solution of 4-NTP. The spectra in A-C) were acquired with an excitation wavelength of 633 nm, and D-F) used an excitation of 785 nm. 57

Figure 3.9 A) SEM image of a pseudo-Sierpiński Hexagon fabricated on a silicon substrate. The inset image shows that the base unit hexagon is a hexamer configuration of gold nanoprisms. B) Visible to near-IR absorbance spectra taken at orthogonal polarizations of the fractal prepared on a CaF_2 window. C) SEF image of a functionalized fractal prepared on CaF_2 . D) Near-IR to mid-IR absorption spectrum of a non-functionalized fractal on CaF_2 . . 59

Figure 3.10 SEF image overlaid onto the SEM image of the pseudo-Sierpiński Hexagon. The bright red regions correspond to the regions of enhanced fluorescence. 60

Figure 4.1 SEM images of superimposed nanoprisms fabricated on silicon. A) Local region highlighting the overlap of the two patterns prepared by NSL. Superimposed arrays of nanoprisms prepared by EBL with small nanoprisms (coloured red) of $0.25 \mu\text{m}$ side length and large nanoprisms (coloured green) with B) $1 \mu\text{m}$, C) $1.25 \mu\text{m}$, D) $1.5 \mu\text{m}$, E) $1.75 \mu\text{m}$, and F) $2 \mu\text{m}$ sidelengths. 73

Figure 4.2 SEM images of large regions of superimposed arrays of nanoprisms fabricated on silicon prepared by A) NSL, and B) EBL. 74

Figure 4.3 Visible and near-IR absorption of the Fischer's pattern, and the superimposed structures with the indicated side lengths. 75

Figure 4.4 FDTD calculations of the transverse components of the electric field ($|E/E_0|^2$, log scale representation at wavelengths of 633 nm (A,B), and 950 nm (C,D) for superimposed nanoprism patterns with side lengths of 1 and $0.25 \mu\text{m}$ 76

Figure 4.5 Scattering (A-D) and SEF (E-H) images of Fischer's patterns with dimension of $0.25 \mu\text{m}$ (A,E), $1 \mu\text{m}$ (B,F), and superimposed patterns with side lengths of 1 and $0.25 \mu\text{m}$ (C,G), 2 and $0.25 \mu\text{m}$ (D,H). 78

Figure 4.6 SEF analysis, and hot-spot representations of the superimposed patterns. 79

Figure 4.7 A) Scattering, and B) SEF images of a patch of superimposed 2 and 0.25 μm nanoprisms with regions of un-lifted gold present.	80
Figure 4.8 Integrated SERS maps from 1300-1350 cm^{-1} for 4-NTP functionalized patterns with side lengths of 0.25 μm (A), and for superimposed patterns with side lengths of 2 and 0.25 μm (B), 1.75 and 0.25 μm (C). Individual SERS spectra corresponding to the indicated regions from A-C are shown in D. Triangles matching the dimensions described are overlaid in A and B, and the SERS map of C is overlaid on an SEM micrograph to relate the SERS map to the structures.	81
Figure 4.9 A) Raman spectra for CaF_2 and 4-NTP functionalized flat gold, and a SERS spectrum of 4-NTP functionalized superimposed nanoprisms. B) SERS analysis of 25 individual spectra on each of the superimposed patterns.....	82
Figure 4.10 Infrared absorption of single Fischer's patterns and superimposed patterns for various sizes. A) Comparison between non-superimposed (0.25, and 1 μm prisms) and superimposed patterns (1 and 0.25 μm prisms). B) Influence of different electron exposure doses during lithography on the absorptions. C) Effect of increasing the size of the larger triangles in the superimposed patterns.....	84
Figure 4.11 FDTD calculations of the transverse components of the electric field ($ E/E_0 ^2$), log scale representation at wavelengths of 2.1 μm (A and B), and 3.8 μm (C and D) for superimposed nanoprisms with side lengths of 1 and 0.25 μm	85
Figure 4.12 FDTD calculations of the transverse components of the electric field ($ E/E_0 ^2$), log scale representation, for the superimposed patterns at the maximum absorbance at the stated wavelengths. Superimposed patterns of nanoprisms with side lengths of 0.25 μm and A) 1.25 μm , B) 1.5 μm , C) 1.75 μm , and D) 2 μm	86
Figure 4.13 Comparison of infrared absorption 2 and 0.25 μm superimposed nanoprisms before and after functionalization with A) 4-NTP, B) 4-NTP, and C) 4-MPBA at the indicated exposure doses.....	88
Figure 5.1 Scanning electron micrograph of dendritic fractals in the A) first, B) second, C) third, and D) fourth-order generations. E-H) Corresponding experimental (solid line) and	

calculated (dashed line) absorption spectra for each of the generations. The scale bar in the inset SEM images is 200 nm.....	101
Figure 5.2 A) Scanning electron micrograph of fifth order generation three branched dendritic fractal and B) the corresponding absorption spectrum.	103
Figure 5.3 Normalized extinction spectra for first, second, third, and fourth-order generation dendritic structures with individual rod lengths of 200 nm. For each generation, the normalized electric field distribution $(E/E_0)^2$ under horizontal polarization was calculated for each resonance and displayed using log scale for clarity. The plasmon hybridization (red dashed line) is shown upon iteration of the fractal generation.	104
Figure 5.4 Hybridization model for the dendritic fractal at the second- through fourth-order generations. For each model, the electric field maps are shown at the energies corresponding to the resonances of the structure. In addition, a schematic illustration of the structure used in the model is shown.....	105
Figure 5.5 FDTD calculations of the transverse components of the electric field $(E/E_0)^2$: log scale representation at wavelengths corresponding to the absorptions of the fourth-order generation dendritic fractal comprised of gold nanorods with side lengths of 200 nm.....	106
Figure 5.6 A) SEM image of the fourth-order generation fractal where the side lengths are 200 nm. Colour coded map of iso-wavelength distribution representing the distribution of the maximum electric field for a B) x - and C) y -polarized input field.	107
Figure 5.7 Infrared absorption of three-branched dendritic fractal at the A) first, B) second, and C) third-order generations with the side lengths indicated in A).	109
Figure 5.8 Infrared absorption spectra of dendritic fractals with the indicated number of inner branches probed with orthogonal polarizations for A) first and B) second-order generations with side lengths of 300 nm.	111
Figure 5.9 SEM images of the third-order generation of a five-branched dendritic fractal that is A) original and B) truncated. C) Absorption spectra of the fractals from A and B. The dashed spectrum corresponds to the second-order generation five branched dendritic fractal.	

D and E) SEM images of truncated second-order generation of an eight-branched dendritic fractal. F) Absorption spectra of the truncated fractals from D and E. The dashed spectrum corresponds to the first order generation eight branched dendritic fractal. The fractals are comprised of nanorods with lengths of 400 nm. The scale bar in the SEM images is 400 nm. 113

Figure 5.10 Comparison between bare and PMMA coated dendritic fractals for side lengths varying from 200 to 400 nm. A) Five-branched second-order generation, and B) three-branched fifth-order generation. 115

Figure 5.11 Absorbance measurements on PMMA coated dendritic fractals for A) five-branched second-order and B) three-branched fifth order generation dendritic fractals. Resulting absorbance difference spectra of C) five-branched second-order and D) three-branched fifth-order generation dendritic fractals. 116

Figure 5.12 SEIRA measurements of 4-NTP functionalized dendritic fractals. A) Truncated 8 branched second-order generation dendritic fractal (same as Figure 6D). The inset in the figure highlights the symmetric stretch of NO₂. B) SEIRA spectra of 4-NTP on different dendritic fractals with a polynomial fit having been removed. The spectra are offset for clarity and the ratios of $\omega_{\text{vib}}/\omega_{\text{res}}$ are included. 119

Figure 6.1 A) Scanning electron micrograph of three-branched second-order generation dendritic fractals prepared by electron-beam lithography. B) Experimental absorbance spectra obtained using orthogonal polarizations on the same sample as A). The scale bar on the inset SEM image is 350 nm. The arrows in the inset correspond to the polarization directions reported in A). 129

Figure 6.2 A) Comparison of the absorbance spectrum taken with the PEM (from the sum interferogram) and the average absorbance spectrum of the static polarization measurements (0 and 90°) from Figure 1. B) Comparison of the dichroic spectra obtained using the μ PM-IRLD (with a modulation centered at $\lambda = 1500 \text{ cm}^{-1}$) and the sequential measurement of A_{0° and A_{90° . The μ PM-IRLD spectrum is shown after calibration. 131

Figure 6.3 A) Raw PM absorption ratio spectra needed to perform the calibration. These were obtained by introducing a polarizer that was positioned parallel (C_{\parallel}) or perpendicular (C_{\perp})

with respect to the polarizer direction positioned in front of the PEM. B) Calculated dichroic spectrum from FDTD calculations. The points indicated by LE and HE correspond to the low energy and high resonance positions used to generate the EM field maps..... 132

Figure 6.4 A-D) FDTD calculations of the electric field $(|E/E_0|)^2$: log scale representation at the high energy (HE) and low energy (LE) wavelengths where the absorbance spectra overlap at orthogonal polarizations for a second-order generation dendritic fractal composed of gold nanorods with side lengths of 350 nm. 133

Figure 6.5 Changes to the absorbance (A and B), and the calibrated PM absorption spectra (C and D) because of altering the side length of the gold nanorods in the dendritic fractal..... 135

Figure 6.6 Influence of increasing the number of inner branches on the A-C) absorbance, and D-F) calibrated PM absorption spectra. Shown as insets in A-C) are SEM images corresponding to A) four-, B) five-, and C) six-branched second-order generation dendritic fractals. The scale bar of the inset images is 350 nm..... 136

Figure 6.7 Calibrated PM spectrum obtained on CaF_2 137

Figure 6.8 FDTD calculations of the electric field $(|E/E_0|)^2$: log scale representation at the A) high energy (HE) and B) low energy (LE) resonance wavelengths for a four-branched second-order generation dendritic fractal composed of gold nanorods with side lengths of 360 nm. C) SEM image of the four-branched second-order dendritic fractal with side lengths of 360 nm. The scale bar in the SEM image is 350 nm. 138

Figure 6.9 A) Absorbance and B) calibrated PM measurements for a three-branched third-order dendritic fractal. Included as an inset of A) in an SEM image of the structure with a scale bar of 200 nm. 140

Figure 6.10 A) Absorbance and B) PM calibrated measurements of a 4-NTP functionalized sample (three-branched second-order generation). Vibrational intensity spectra obtained from C) the absorbance spectrum, and D) the PM calibrated spectrum. E) PM calibrated spectra for a series of three-branched second-order dendritic fractals functionalized with 4-NTP, and F) the corresponding integrated peak area from $1328 - 1346 \text{ cm}^{-1}$, corresponding to the symmetric NO_2 stretch as indicated by the shaded region of E)..... 142

Figure 7.1 SEM images of first-order dendritic fractals with A) three, B) four, and C) five inner branches. The scale bar in the SEM images is 200 nm. D) Absorbance spectra of the first-order dendritic fractals with side lengths of 175 nm. E) Absorbance spectra of four-branched first-order dendritic fractals with side lengths from 150 to 250 nm..... 154

Figure 7.2 Absorbance spectra from finite-difference time-domain (FDTD) calculations of four-branched first-order dendritic fractals with side lengths from 175 nm and varying widths..... 154

Figure 7.3 FDTD calculations of the electric field $(|E/E_0|)^2$: log scale representation at the observed resonance for first-order generation dendritic fractals with A) three, B) four, and C) five inner branches..... 155

Figure 7.4 SEM images of second-order dendritic fractals with A) three, B) four, and C) five inner branches. The scale bar in the SEM images is 200 nm. D) Absorbance spectra of the second-order dendritic fractals with side lengths of 175 nm. 156

Figure 7.5 FDTD calculations of the electric field $(|E/E_0|)^2$: log scale representation at the resonances of a four-branched second-order dendritic fractal with side lengths of 175 nm. The numbers correspond to those indicated in Figure 7.4D. 157

Figure 7.6 SEM images of third-order dendritic fractals with A) three, B) four inner branches. C) SEM images of a truncated version of B). The scale bar in the SEM images is 200 nm. D) Absorbance spectra of the third-order dendritic fractals with side lengths of 175 nm. 158

Figure 7.7 FDTD calculations of the electric field $(|E/E_0|)^2$: log scale representation at the resonances of a four-branched third-order dendritic fractal with side lengths of 175 nm. The numbers correspond to the indicated resonances in Figure 7.6. 159

Figure 7.8 SEM images of 6-branched A) first-order, B and C) truncated second-order generation fractals. The scale bar in the SEM images is 200 nm. D) Absorbance spectra of the second-order dendritic fractals with side lengths of 175 nm. 159

Figure 7.9 A) Absorbance spectra of four-branched second-order generation dendritic fractals with side lengths ranging from 150 to 250 nm. B) Absorbance spectra of five-branched second-order generation dendritic fractals with written widths ranging from 30 to 50 nm. 161

Figure 7.10 Absorbance spectra of A) four-branched second-order generation, B) five-branched second-order generation, and C) four-branched third-order generation dendritic fractals with rod side lengths of 200 nm. D-F) Changes in the spectral position of the indicated resonances as the side length of the nanorods is altered. 162

Figure 7.11 SERS response of 4-NTP functionalized dendritic fractals. A) First-order generation fractals where the number above the spectrum indicates the number of inner branches. B) Four-branched dendritic fractals in the indicated order generation. 164

Figure 7.12 Raman spectrum obtained of a 10 mM solution of dopamine (DA) on glass. SERS spectrum obtained of the dopamine solution using a four-branched third-order dendritic fractal. Included as an inset is the chemical structure of dopamine. A polynomial baseline correction has been applied to the spectra. 165

Figure 7.13 SERS spectra obtained on the dendritic fractals under various conditions involving the dopamine binding aptamer and dopamine. The peaks indicated by * and ** correspond to peaks that appear once dopamine is introduced. A polynomial baseline correction has been applied to the spectra. 167

Figure 8.1 SEM images of other structures that have been prepared by EBL for different applications in plasmonics. A) Dashed H-tree fractal, and B) chiral spiral metasurface composed of 1 μm diameter gold nanodisks. 176

List of Abbreviations, Symbols, and Nomenclature

χ	shape factor of a nanoparticle
ϵ_0	dielectric constant of free-space
ϵ_d	dielectric constant of a dielectric
ϵ_m	complex dielectric of a metal
λ	wavelength
$\sigma_{\text{abs/ext/sca}}$	absorption/extinction/scattering cross-section
ω_p	plasmon frequency
$\mu\text{PM-IRLD}$	polarization-modulation infrared linear dichroism microscopy
4-MPBA	4-mercaptophenylboronic acid
4-NTP	4-nitrothiophenol
<i>A</i>	absorbance
AFM	atomic force microscopy
CCD	charge-coupled device
CLS	Canadian Light Source
Cy5	cyanine 5
DA	dopamine
<i>e</i>	charge of an electron
E_0	incident electric field
$ E/E_0 ^2$	total electric field intensity
e-beam	electron-beam
EBL	electron-beam lithography
EF	enhancement factor
EHT	extra high tension
EM	electromagnetic

FDTD	finite-difference time-domain
FT-IR	Fourier transform infrared
I	light intensity
IR	infrared
LSPR	localized surface plasmon resonance
MCH	6-mercaptohexanol
MCT	mercury cadmium telluride
m_e	effective mass of an electron
N.A.	numerical aperture
n_e	number of electrons
NPoM	nanoparticle-on-mirror
NSL	nanosphere lithography
PEG	polyethylene glycol
PML	perfectly matched layer
PMMA	poly(methyl methacrylate)
PMT	photomultiplier tube
SE-CARS	surface-enhanced coherent anti-Stokes Raman spectroscopy
SEF	surface-enhanced fluorescence
SEIRA	surface-enhanced infrared absorption
SEM	scanning electron microscopy
SERS	surface-enhanced Raman spectroscopy
R-SH	thiol or thiol functional group
TERS	tip-enhanced Raman spectroscopy

List of Appendices

Appendix A – Details for FDTD Calculations	181
Appendix B – Fabrication Details for Nanosphere Lithography	183
Appendix C – Fabrication Details for Electron-Beam Lithography	184
Appendix D – Copyrights	185

Chapter 1

1 General Introduction

In the mid-1970's, various researchers reported large enhancement of Raman spectra of pyridine molecules adsorbed onto the surface of roughened silver electrodes.¹⁻³ This effect would later lead to the birth of an entire new field of research referred to as surface-enhanced Raman spectroscopy (SERS).⁴ Since then, in parallel to the continuous development of SERS from both fundamental and experimental perspectives, other spectroscopic techniques have benefited from this type of enhancement mediated by a surface, most notably infrared (surface-enhanced infrared absorption, SEIRA),⁵⁻⁷ and fluorescence (surface-enhanced fluorescence, SEF).⁸⁻¹¹

Although studies involving roughened metal surfaces are still being performed,¹²⁻¹⁴ advancements in syntheses and nanofabrication processes has enabled the preparation of a wide variety of nanostructures. Noticeably, these structures can be finely tailored to exhibit optical properties that are tuned to specific spectral regions for specific applications.

1.1 Applications Involving Plasmonic Nanostructures

Whether prepared by synthetic or lithographic means, plasmonic nanostructures have been utilized for a variety of different applications. In solar cell technology, metallic nanoparticles have been incorporated by varying means so as to improve the efficiency of the energy conversion processes.¹⁵ In the field of medicine, nanoparticles have shown promise for both the diagnosis and treatment of disease through photothermal therapy.¹⁶ By adding gold nanoshells functionalized with the a pH sensitive molecule (4-mercaptobenzoic acid) to the end of an endoscope, it is possible to determine the pH of specific portions of the body, such as alveolae in the lungs, using SERS.¹⁷ More specifically, this section further explores two critical areas of plasmonics research in the field of chemistry. The two topics chosen are specifically highlighted as they can be readily applied to the structures discussed in this thesis.

1.1.1 Performing Chemistry at the Nanoscale

Upon light absorption and the corresponding excitation of the localized surface plasmon resonance (LSPR) of the nanostructure, the resulting electromagnetic decay can result in the formation of hot-electrons by transferring the energy to electrons in the conduction band of the metal.¹⁸ An important feature of the hot-electrons is that they can be used to perform plasmon-mediated chemical reactions at the nanoscale. Examples of these reactions include hydrogenation of carbonyls,¹⁹ water reduction to produce hydrogen,²⁰ and the demethylation of methylene blue.²¹ Throughout the literature, the quintessential plasmon-mediated reactions are the oxidative coupling reactions between self-assembled amino or nitro-terminated molecules adsorbed onto the surface of the structures.²²⁻²⁵

Similar to the plasmon-mediated dimerization reactions, plasmon-driven polymerization reactions can also be performed. A recent study from the Deckert group used tip-enhanced Raman spectroscopy (TERS) to perform plasmon-catalyzed reactions of dibenzo(1,2)dithiine-3,8-diamine (D3ATP) at the nanoscale.²⁶ In their work, a silver coated atomic force microscopy (AFM) tip is placed near the surface of a gold nanoplate coated with a monolayer of D3ATP. Upon illumination, the amino groups undergo coupling to form azo groups, as verified by the TERS spectra. As the nanoplate is scanned, the polymerization reactions occur over the entire surface. By instead performing the TERS measurements on only portions of the nanoplate, it may become possible to generate local 1-dimensions materials.

Another important feature of plasmon-mediated polymerization reactions is that they can be used to both tune and visualize the plasmonic properties of metallic nanostructures (Figure 1.1).²⁷⁻²⁹ Coupling plasmonic nanostructures with metal films (described as mirrors) yields platforms with geometries known as structure-on-mirror.³⁰⁻³⁵ When irradiated with a proper excitation wavelength, arrays such as nanoparticle-on-mirror (NPoM) exhibit a strong local field enhancement in the nanoscale gap located between the particle and the mirror. In a work from the Baumberg group,²⁷ polymerization of divinylbenzene was performed with NPoM structures using a continuous wave laser with an excitation wavelength of 635 nm that matches the plasmon resonance of the structure.

As the polymerization reaction progresses, the position of the transverse (T) and longitudinal (L) resonances undergo blue-shifts (shifts to shorter wavelengths) (Figure 1.1A). These changes are the result of the polymer increasing the gap between the nanoparticle and the mirror (Figure 1.1B), as opposed to the changes in the refractive index of the surrounding material. As the degree of polymerization changes with time, it is possible to finely tune the spectral position of the resonances. In addition to the changing the spectral position of resonances, polymers and polymerization can also be used to experimentally visualize the hot-spots or electric-field resonances associated with the structures or metasurfaces.³⁶⁻³⁹ In these studies, both the nanostructures and the polymer are sensitive to the excitation wavelength used. When irradiated, the polymer that is located within a hot-spot undergoes a significant migration away from the hot-spot. The resulting change in topography can then be observed by AFM, providing important information about the spatial distribution of hot-spots. In the context of plasmon-mediated reactions, polymers can be used to visualize the individual hot-spots. By spin coating a polymer thin film over the surface of the nanostructures, followed by irradiating the sample, it is possible for the generated hot-electrons to alter the chemical composition of the polymer.²⁸ This approach is analogous to the technique of electron-beam lithography that is discussed in greater detail in Chapter 2. When the irradiated sample is placed into a developing solution, areas of the polymer exposed to the hot-electrons are readily observed (Figure 1.1C-F). Depending on the laser power, the polymer may be decomposed (Figure 1.1C, E, and F) or crosslinked (Figure 1.1D). As opposed to relating changes in a polymer film to the spatial distribution of hot-spots, it is also possible to induce localized polymerization within the hot-spots. In these methods developed by Mangeney and Félidj,^{29, 40-41} the nanostructure is exposed to a solution of an analyte (diazonium salt) and is irradiated using a laser. Although spontaneous functionalization will occur, the polymerization will only occur in the regions of EM enhancement. The thickness of the grafted layer will depend on the strength of the EM enhancement and irradiation time. Depending on the plasmonic properties of the nanostructure, and polarization of the input light, the poly(aryl) layer will form in distinct spatial regions of the structure.

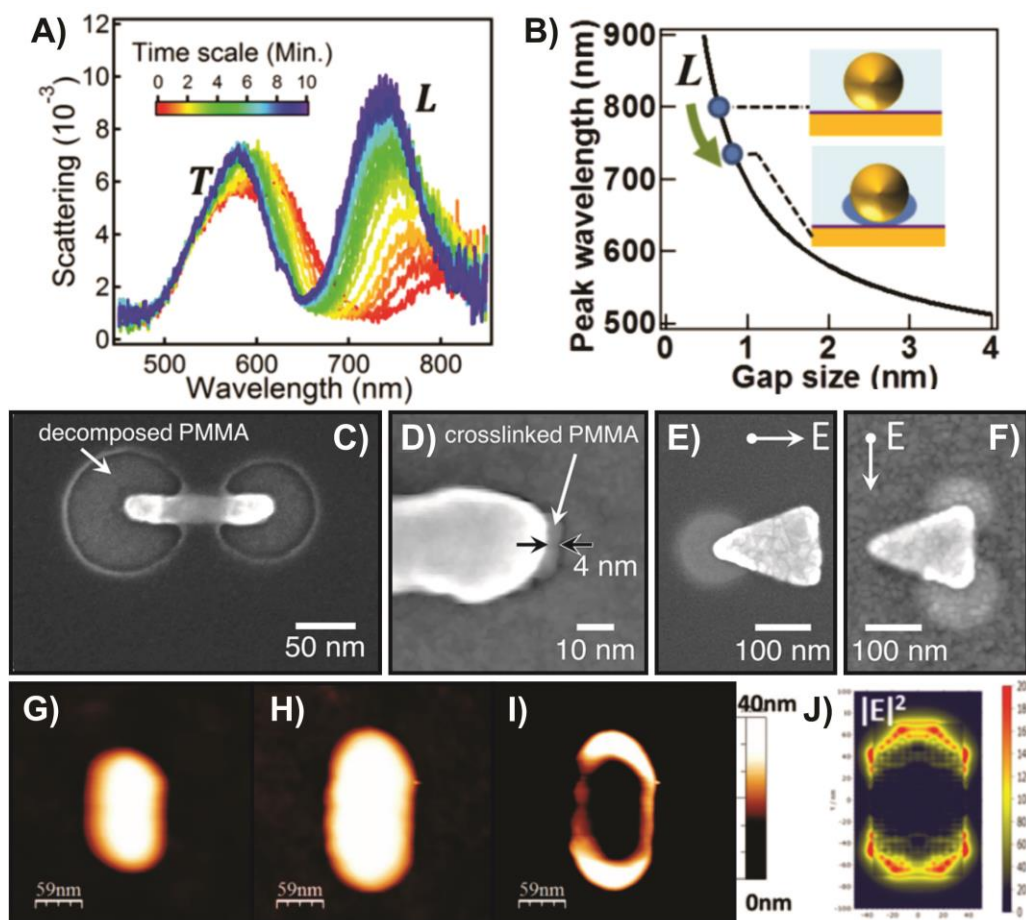


Figure 1.1 A) Changes to the scattering spectra of a AuNPoM platform with increasing irradiation time. *T*: transverse mode; *L*: dipolar mode. B) Prediction of coupled plasmon resonance wavelength with changing gap size. The inset scheme depicts the polymer growth between the AuNP and the mirror.²⁷ C-F) SEM images of gold nanostructures coated with a PMMA thin film followed by irradiation.²⁸ For C and D) the light is polarized along the length of nanorod. G) AFM image of a AuNR prior to grafting with an aryl diazonium salt. H) AFM image of the AuNR after grafting and the formation of the poly(aryl) layer. I) Subtracted AFM image of G) and H) revealing the location of the grafted film. J) Electric field distribution around a rectangular rod with rounded edges.²⁹ Adapted with permission from references 27, 28 and 29. Copyright 2017 American Chemical Society and 2017 Royal Society of Chemistry.

1.1.2 Enhanced Vibrational Spectroscopy for On-Chip Sensing

By far, the largest portion of published manuscripts in the field focusses on the use of plasmonic and surface-enhanced related effects for sensing applications. Of interest is on-chip sensing, where the nanostructures are fabricated on a substrate and integrated in a device. For these types of sensors, the nanostructures are often incorporated into nano- or microfluidic channels or are designed to be scanned using common technology such as smartphones.⁴²⁻⁴⁴ Another approach to on-chip sensing is to alter the substrate used.⁴⁵ As opposed to traditional inflexible substrates (i.e. glass), flexible substrates are emerging as alternatives for analysis in the field. In the case of metal coated sandpaper,¹² the intrinsic roughness provides the enhancement needed for SERS-based sensing. Metallic nanoparticles can be assembled onto or embedded into polymeric films,⁴⁶⁻⁴⁷ or fibers so that they substrate can be directly applied to a surface of interest.⁴⁸ More common is to incorporate the add the nanostructures into paper,⁴⁹⁻⁵¹ yielding a low-cost and readily-accessible plasmonic substrate.

The use of SERS platforms for on-chip sensing covers a wide range of target analytes including: ions,⁵² bacteria,⁵³ illicit drugs,⁵⁴ toxins,⁵⁵ and explosives.⁵⁶ The detection of the analyte is often based on the occurrence of vibrational markers associated with the analyte, changes in the SERS spectrum of an analyte-binding molecule, or both. SERS sensors can also be used to probe target molecules, such as explosives, when they are airborne.⁵⁷ Quantitatively determining the concentration of an analyte remains a significant challenge as any variability in the density of hot-spots or the enhancement at a hot-spot will yield SERS spectra with different intensities. When preparing calibration plots based on these results, large error bars are often observed. New methods for quantitatively determining the concentration of analytes are being explored, including measuring the ratio between the enhanced elastic and inelastic scattering.⁵⁸ This lowers the coefficient of variation from 10 – 60% to 2 – 7%. Expanding to other optical processes, particularly those that are inherently normalized, such as absorption, may provide more accurate quantitative measurements.

The development of SEIRA for sensing applications has more recently emphasized protein detection.⁵⁹⁻⁶² To improve detection, the nanostructures can be surrounded with

superhydrophobic and hydrophilic regions,⁵⁹ or integrated into fluidic channels.⁶¹⁻⁶² Both approaches allow for the low concentration of analyte to be localized at the sensing regions. Another interesting application of SEIRA is for gas sensing. Much like working with analytes at low concentration in solution, the greatest challenge is to develop a means of confining the gas near the metal surface so that it can be within the sensing volume of the platform. The current approach is to add a film of a metal-organic framework to the metal structures.⁶³⁻⁶⁴ As the gas pressure increases, the gas molecules move deeper into the film, and therefore closer to the metal surface. Thus far, the studies have focussed on CO₂, with the vibrational bands between 2.65 and 2.8 μm (3575 – 3775 cm⁻¹) being used for detection.

By performing correlative measurements, it is possible to obtain more sensitive results, and/or new chemical information about the analyte. For these types of measurements, it is necessary that the platform exhibit compatibility with the techniques of interest. Combining surface plasmon resonance with SERS,⁶⁵ or SEF with SERS is relatively straightforward as the techniques often rely on the same wavelengths of light.⁶⁶ Performing subsequent SERS and SEIRA measurements using the same platform requires that the structure exhibit compatibility an extremely broad resonance or a series of resonances.⁶⁷⁻⁷⁰

Whether the aim is to perform qualitative or quantitative measurements, reproducible results are critical. In this regard, dependable fabrication and generation of hot-spots is necessary, otherwise, complicated normalization procedures are required.⁵⁸ Lithographic techniques have been shown to offer reliable fabrication of nanostructures with idealized optical properties.⁷¹⁻⁷² These nanostructures can be designed so that they exhibit dependable resonances, including multiple resonances within narrow or broad spectral ranges.

1.2 Scope of Thesis

In the context of developing plasmonic nanostructures, this thesis aims to bridge the spectral gap by: (i) fabricating plasmonic platforms that exhibit multiple resonances that

span the visible through mid-infrared spectra regions, and (ii) use these platforms for a variety of plasmon-enhanced spectroscopies, notably SERS, SEF, and SEIRA.

A summary of the subjects covered in each chapter is as follows:

In Chapter 2, the necessary design considerations for the fabrication of plasmonic platforms is discussed. Different fabrication methodologies are explored in detail, along with a means of calculating the EM field enhancement of the structure is explained. This chapter then goes into detail on the experimental procedures used to characterize the plasmonic properties of the fabricated nanostructures.

Chapter 3 explores the relationship between the arrangement of individual nanostructures and the resulting densities of hot-spots over the platform. By altering the configurations of the nanostructures, it is possible to broaden the resonances, and more importantly, introduce additional resonances in the visible to near-infrared. This chapter also introduces the concept of superimposing nanostructures as a means of increasing the number of resonances. This concept is explored in greater detail in Chapter 4 as a means of performing a variety of plasmon-enhanced techniques using a single plasmonic platform.

Chapters 5, 6, and 7 explore the multi-resonant properties of dendritic fractals. Fractal structures are interesting alternatives to increase the number of resonances by varying the number of generations of the fractal pattern. Chapter 5 focusses on the plasmonic properties in the near- to mid-IR, with the aim of introducing resonances in the fingerprint region so that SEIRA measurements are possible using the structure. As the structures exhibit a polarization dependence, Chapter 6 explores the linear dichroism associated with the structure using polarization modulation infrared linear dichroism microscopy (μ PM-IRLD). Chapter 7 then develops a means of using the dendritic fractals for molecular plasmonics in the visible region while maintaining their multiresonant properties.

In the final chapter, a summary of the presented work is provided, along with a critical review of some of the emerging fields that would benefit from the use of multiple

spectroscopic techniques. We finally conclude by discussing the potential future areas of research projects derived from those presented in this thesis.

1.3 References

1. Fleischmann, M.; Hendra, P. J.; McQuillan, A. J., *Chem. Phys. Lett.* **1974**, *26*, 163-166.
2. Albrecht, M. G.; Creighton, J. A., *J. Am. Chem. Soc.* **1977**, *99*, 5215-5217.
3. Jeanmaire, D. L.; Van Duyne, R. P., *J. Electroanal. Chem. Interfacial Electrochem.* **1977**, *84*, 1-20.
4. Van Duyne, R. P., Laser Excitation of Raman Scattering from Adsorbed Molecules on Electrode Surfaces. In *Chemical and Biochemical Applications of Lasers*, Academic Press: 1979; pp 101-185.
5. Hartstein, A.; Kirtley, J. R.; Tsang, J. C., *Phys. Rev. Lett.* **1980**, *45*, 201-204.
6. Hatta, A.; Ohshima, T.; Suëtaka, W., *Appl. Phys. A: Solids Surf.* **1982**, *29*, 71-75.
7. Osawa, M., Surface-Enhanced Infrared Absorption. In *Near-Field Optics and Surface Plasmon Polaritons*, Kawata, S., Ed. Springer Berlin Heidelberg: Berlin, Heidelberg, 2001; pp 163-187.
8. Glass, A. M.; Liao, P. F.; Bergman, J. G.; Olson, D. H., *Opt. Lett.* **1980**, *5*, 368-370.
9. Chen, C. Y.; Davoli, I.; Ritchie, G.; Burstein, E., *Surf. Sci.* **1980**, *101*, 363-366.
10. Weitz, D. A.; Garoff, S.; Hanson, C. D.; Gramila, T. J.; Gersten, J. I., *J. Lumin.* **1981**, *24-25*, 83-86.
11. Moskovits, M., *Rev. Mod. Phys.* **1985**, *57*, 783-826.
12. Fan, M.; Zhang, Z.; Hu, J.; Cheng, F.; Wang, C.; Tang, C.; Lin, J.; Brolo, A. G.; Zhan, H., *Mater. Lett.* **2014**, *133*, 57-59.
13. Wang, W.; Huang, Y.-F.; Liu, D.-Y.; Wang, F.-F.; Tian, Z.-Q.; Zhan, D., *J. Electroanal. Chem.* **2016**, *779*, 126-130.
14. Sun, M.; Qian, H.; Liu, J.; Li, Y.; Pang, S.; Xu, M.; Zhang, J., *RSC Adv.* **2017**, *7*, 7073-7078.
15. Enrichi, F.; Quandt, A.; Righini, G. C., *Renew. Sust. Energ. Rev.* **2018**, *82*, 2433-2439.
16. Cialla-May, D.; Zheng, X. S.; Weber, K.; Popp, J., *Chem. Soc. Rev.* **2017**, *46*, 3945-3961.
17. Choudhury, D.; Tanner, M. G.; McAughtrie, S.; Yu, F.; Mills, B.; Choudhary, T. R.; Seth, S.; Craven, T. H.; Stone, J. M.; Mati, I. K.; Campbell, C. J.; Bradley, M.; Williams, C. K. I.; Dhaliwal, K.; Birks, T. A.; Thomson, R. R., *Biomed. Opt. Express* **2017**, *8*, 243-259.

18. Clavero, C., *Nat. Photon.* **2014**, *8*, 95-103.
19. Landry, M. J.; Gellé, A.; Meng, B. Y.; Barrett, C. J.; Moores, A., *ACS Catal.* **2017**, *7*, 6128-6133.
20. Wu, B.; Liu, D.; Mubeen, S.; Chuong, T. T.; Moskovits, M.; Stucky, G. D., *J. Am. Chem. Soc.* **2016**, *138*, 1114-1117.
21. Tesema, T. E.; Kafle, B.; Tadesse, M. G.; Habteyes, T. G., *J. Phys. Chem. C* **2017**, *121*, 7421-7428.
22. Brandt, N. C.; Keller, E. L.; Frontiera, R. R., *J. Phys. Chem. Lett.* **2016**, *7*, 3179-3185.
23. Zhang, Z.; Merk, V.; Hermanns, A.; Unger, W. E. S.; Kneipp, J., *ACS Catal.* **2017**, *7*, 7803-7809.
24. Ding, Q.; Chen, M.; Fang, Y.; Zhang, Z.; Sun, M., *J. Phys. Chem. C* **2017**, *121*, 5225-5231.
25. Kafle, B.; Poveda, M.; Habteyes, T. G., *J. Phys. Chem. Lett.* **2017**, *8*, 890-894.
26. Zhang, Z.; Richard-Lacroix, M.; Deckert, V., *Faraday Discuss.* **2017**, *205*, 213-226.
27. Ding, T.; Mertens, J.; Lombardi, A.; Scherman, O. A.; Baumberg, J. J., *ACS Photonics* **2017**, *4*, 1453-1458.
28. Hobbs, R. G.; Putnam, W. P.; Fallahi, A.; Yang, Y.; Kärtner, F. X.; Berggren, K. K., *Nano Lett.* **2017**, *17*, 6069-6076.
29. Nguyen, M.; Kherbouche, I.; Gam-Derouich, S.; Ragheb, I.; Lau-Truong, S.; Lamouri, A.; Levi, G.; Aubard, J.; Decorse, P.; Felidj, N.; Mangeney, C., *Chem. Commun.* **2017**, *53*, 11364-11367.
30. Mubeen, S.; Zhang, S.; Kim, N.; Lee, S.; Krämer, S.; Xu, H.; Moskovits, M., *Nano Lett.* **2012**, *12*, 2088-2094.
31. Li, L.; Hutter, T.; Steiner, U.; Mahajan, S., *Analyst* **2013**, *138*, 4574-4578.
32. Wallace, G. Q.; Tabatabaei, M.; Zuin, M. S.; Workentin, M. S.; Lagugné-Labarthe, F., *Anal. Bioanal. Chem.* **2016**, *408*, 609-618.
33. Benz, F.; Chikkaraddy, R.; Salmon, A.; Ohadi, H.; de Nijs, B.; Mertens, J.; Carnegie, C.; Bowman, R. W.; Baumberg, J. J., *J. Phys. Chem. Lett.* **2016**, *7*, 2264-2269.
34. Lum, W.; Bruzas, I.; Gorunmez, Z.; Unser, S.; Beck, T.; Sagle, L., *J. Phys. Chem. Lett.* **2017**, *8*, 2639-2646.
35. Qin, J.; Chen, Y.-H.; Ding, B.; Blaikie, R. J.; Qiu, M., *J. Phys. Chem. C* **2017**, *121*, 24740-24744.
36. Hubert, C.; Rumyantseva, A.; Lerondel, G.; Grand, J.; Kostcheev, S.; Billot, L.; Vial, A.; Bachelot, R.; Royer, P.; Chang, S.-h.; Gray, S. K.; Wiederrecht, G. P.; Schatz, G. C., *Nano Lett.* **2005**, *5*, 615-619.

37. Galarreta, B. C.; Rugar, I.; Young, A.; Lagurné-Labarthe, F., *J. Phys. Chem. C* **2011**, *115*, 15318-15323.
38. Tabatabaei, M.; Sangar, A.; Kazemi-Zanjani, N.; Torchio, P.; Merlen, A.; Lagurné-Labarthe, F., *J. Phys. Chem. C* **2013**, *117*, 14778-14786.
39. Kim, M.; Huh, J.-H.; Lee, J.; Woo, H. J.; Kim, K.; Jung, D.-W.; Yi, G.-R.; Jeong, M. S.; Lee, S.; Song, Y. J., *J. Phys. Chem. Lett.* **2017**, *8*, 3745-3751.
40. Nguyen, M.; Lamouri, A.; Salameh, C.; Levi, G.; Grand, J.; Boubekeur-Lecaque, L.; Mangeney, C.; Felidj, N., *Nanoscale* **2016**, *8*, 8633-8640.
41. Tijunelyte, I.; Kherbouche, I.; Gam-Derouich, S.; Nguyen, M.; Lidgi-Guigui, N.; de la Chapelle, M. L.; Lamouri, A.; Levi, G.; Aubard, J.; Chevillot-Biraud, A.; Mangeney, C.; Felidj, N., *Nanoscale Horiz.* **2018**, *3*, 53-57.
42. Ayas, S.; Cupallari, A.; Ekiz, O. O.; Kaya, Y.; Dana, A., *ACS Photonics* **2014**, *1*, 17-26.
43. Wei, Q.; Acuna, G.; Kim, S.; Vietz, C.; Tseng, D.; Chae, J.; Shir, D.; Luo, W.; Tinnefeld, P.; Ozcan, A., *Sci. Rep.* **2017**, *7*, 2124.
44. Wang, X.; Chang, T.-W.; Lin, G.; Gartia, M. R.; Liu, G. L., *Anal. Chem.* **2017**, *89*, 611-615.
45. Aksu, S.; Huang, M.; Artar, A.; Yanik, A. A.; Selvarasah, S.; Dokmeci, M. R.; Altug, H., *Adv. Mater.* **2011**, *23*, 4422-4430.
46. Zhong, L.-B.; Yin, J.; Zheng, Y.-M.; Liu, Q.; Cheng, X.-X.; Luo, F.-H., *Anal. Chem.* **2014**, *86*, 6262-6267.
47. Xing, C.; Yan, Y.; Feng, C.; Xu, J.; Dong, P.; Guan, W.; Zeng, Y.; Zhao, Y.; Jiang, Y., *ACS Appl. Mater. Interfaces* **2017**, *9*, 32896-32906.
48. K, J.; S, B.; Ganiga, M.; R, D.; S, A.; Cyriac, J.; George, B. K., *Anal. Methods* **2017**, *9*, 3998-4003.
49. Sánchez-Purrà, M.; Carré-Camps, M.; de Puig, H.; Bosch, I.; Gehrke, L.; Hamad-Schifferli, K., *ACS Infect. Dis.* **2017**, *3*, 767-776.
50. Park, M.; Hwang, C. S. H.; Jeong, K.-H., *ACS Appl. Mater. Interfaces* **2018**, *10*, 290-295.
51. Lee, M.; Oh, K.; Choi, H.-K.; Lee, S. G.; Youn, H. J.; Lee, H. L.; Jeong, D. H., *ACS Sens.* **2018**, *3*, 151-159.
52. Guselnikova, O.; Postnikov, P.; Erzina, M.; Kalachyova, Y.; Švorčík, V.; Lyutakov, O., *Sens. Actuator B-Chem.* **2017**, *253*, 830-838.
53. Choi, N.; Lee, J.; Ko, J.; Jeon, J. H.; Rhie, G.-e.; deMello, A. J.; Choo, J., *Anal. Chem.* **2017**, *89*, 8413-8420.
54. Dies, H.; Raveendran, J.; Escobedo, C.; Docoslis, A., *Sens. Actuator B-Chem.* **2018**, *257*, 382-388.
55. Gillibert, R.; Triba, M. N.; Lamy de la Chapelle, M., *Analyst* **2018**, *143*, 339-345.

56. Chen, N.; Ding, P.; Shi, Y.; Jin, T.; Su, Y.; Wang, H.; He, Y., *Anal. Chem.* **2017**, *89*, 5072-5078.
57. Piorek, B. D.; Lee, S. J.; Moskovits, M.; Meinhart, C. D., *Anal. Chem.* **2012**, *84*, 9700-9705.
58. Wei, H.; Leng, W.; Song, J.; Willner, M. R.; Marr, L. C.; Zhou, W.; Vikesland, P. J., *Anal. Chem.* **2018**, *90*, 3227-3237.
59. De Ninno, A.; Ciasca, G.; Gerardino, A.; Calandrini, E.; Papi, M.; De Spirito, M.; Nucara, A.; Ortolani, M.; Businaro, L.; Baldassarre, L., *Phys. Chem. Chem. Phys.* **2015**, *17*, 21337-21342.
60. Chen, K.; Guo, P.; Dao, T. D.; Li, S.-Q.; Ishiii, S.; Nagao, T.; Chang, R. P. H., *Adv. Opt. Mater.* **2017**, *5*, 1700091.
61. Le, T. H. H.; Tanaka, T., *ACS Nano* **2017**, *11*, 9780-9788.
62. Etezadi, D.; Warner Iv, J. B.; Ruggeri, F. S.; Dietler, G.; Lashuel, H. A.; Altug, H., *Light Sci. Appl.* **2017**, *6*, e17029.
63. Kim, K.-J.; Chong, X.; Kreider, P. B.; Ma, G.; Ohodnicki, P. R.; Baltrus, J. P.; Wang, A. X.; Chang, C.-H., *J. Mater. Chem. C* **2015**, *3*, 2763-2767.
64. Chong, X.; Zhang, Y.; Li, E.; Kim, K.-J.; Ohodnicki, P. R.; Chang, C.-h.; Wang, A. X., *ACS Sens.* **2018**, *3*, 230-238.
65. Kim, J.-Y.; Zeng, Z.-C.; Xiao, L.; Schultz, Z. D., *Anal. Chem.* **2017**, *89*, 13074-13081.
66. Chang, S.; Eichmann, S. L.; Huang, T.-Y. S.; Yun, W.; Wang, W., *J. Phys. Chem. C* **2017**, *121*, 8070-8076.
67. D'Andrea, C.; Bochterle, J.; Toma, A.; Huck, C.; Neubrech, F.; Messina, E.; Fazio, B.; Maragò, O. M.; Di Fabrizio, E.; Lamy de La Chapelle, M.; Gucciardi, P. G.; Pucci, A., *ACS Nano* **2013**, *7*, 3522-3531.
68. Aouani, H.; Rahmani, M.; Šípová, H.; Torres, V.; Hegnerová, K.; Beruete, M.; Homola, J.; Hong, M.; Navarro-Cía, M.; Maier, S. A., *J. Phys. Chem. C* **2013**, *117*, 18620-18626.
69. Bibikova, O.; Haas, J.; Lopez-Lorente, A. I.; Popov, A.; Kinnunen, M.; Meglinski, I.; Mizaikoff, B., *Analyst* **2017**, *142*, 951-958.
70. Tan, C.; Zhang, Z.; Qu, Y.; He, L., *Langmuir* **2017**, *33*, 5345-5352.
71. Cottat, M.; D'Andrea, C.; Yasukuni, R.; Malashikhina, N.; Grinyte, R.; Lidgi-Guigui, N.; Fazio, B.; Sutton, A.; Oudar, O.; Charnaux, N.; Pavlov, V.; Toma, A.; Di Fabrizio, E.; Gucciardi, P. G.; Lamy de la Chapelle, M., *J. Phys. Chem. C* **2015**, *119*, 15532-15540.
72. Flauraud, V.; Regmi, R.; Winkler, P. M.; Alexander, D. T. L.; Rigneault, H.; van Hulst, N. F.; García-Parajo, M. F.; Wenger, J.; Brugger, J., *Nano Lett.* **2017**, *17*, 1703-1710.

Chapter 2

2 Design, Fabrication, and Characterization of Plasmonic Nanostructures

This chapter focusses on the plasmonic properties of metallic nanostructures, their fabrication and characterization. Comprehensive details associated with the fabrication and characterization of the various nanostructures used throughout this thesis are provided. Both optical characterization of the plasmon resonances of the structures and spectroscopic characterization using a variety of surface-enhanced techniques are provided.

2.1 Plasmonic Resonances in Metals

The field of plasmonics aims at controlling the coupling between an electromagnetic (EM) wave and the free electrons of a metal. Plasmonics is often coupled with spectroscopy and is often referred to as molecular plasmonics. Techniques used in molecular plasmonics include: surface- and tip-enhanced Raman spectroscopy (SERS and TERS), surface-enhanced fluorescence (SEF), and surface-enhanced infrared absorption (SEIRA). These surface-enhanced techniques rely on the nanoscale EM field enhancements that occur in nanostructured metals. To acquire a better understanding of the surface-enhanced spectroscopies discussions in this thesis, plasmon resonances in metal surfaces are introduced in the subsequent sections.

2.1.1 Plasmon

The interaction of EM radiation (i.e. light) with metallic structures excites the oscillation of the free conduction electrons of the metal out of phase relative to the driving electric field of the incident radiation.¹ The collective oscillation of the conduction electrons in a metal in response to an EM disturbance, such as an optical field, is referred to as a plasmon. For a bulk plasmon, these oscillations occur at the plasma frequency (ω_p), as described in (2.1).²

$$\omega_p = \frac{1}{2\pi} \sqrt{\frac{n_e e^2}{m_e \epsilon_0}} \quad (2.1)$$

Where ϵ_0 is the dielectric constant of free space, n_e is the electron density of the metal, e is the electron charge, and m_e is the effective mass of an electron.

2.1.2 Surface Plasmon

When at the interface between a metal surface and a dielectric material, such as air or glass, plasmon modes are classified as surface plasmons.² A surface plasmon refers to the collective oscillations of the electron density at the metal surface. These electron oscillations are driven by the oscillating electric field of the incident light. The most effective coupling between the incident light and the surface plasmon occurs when the wavevector is nearly parallel to the surface. Figure 2.1 depicts that surface plasmons are a combination of EM wave and surface charges. Importantly, the surface plasmon that occurs between a metal structure and a dielectric can greatly enhance the optical near-field at or very near the metal surface. However, this enhancement decays exponentially above the metal surface.³⁻⁴

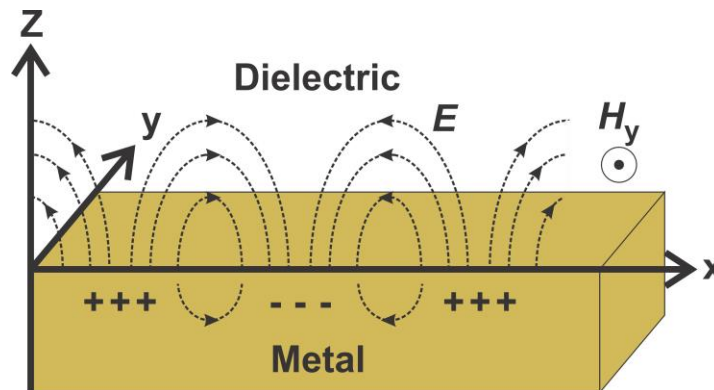


Figure 2.1 Illustration of a propagating surface plasmon at the interface between a metal surface and a dielectric.

To model the plasmon properties of a metal, one must consider the complex index of refraction of the considered metal and the dielectric interface. A metal, or in more general terms, a conductive material has a negative real, and a positive imaginary part.⁵ The complex dielectric functions of four noble metals; gold, silver, copper and aluminum, are shown in Figure 2.2. The complex dielectric functions are calculated using the Drude-Lorentz model, which is widely used to characterize the motion of the free electrons

inside an EM field.⁶ Of the metals highlighted in Figure 2.2, silver and gold are the most common choices for exciting surface plasmons in the ultraviolet (UV)-visible region.

As shown in Figure 2.2A, the imaginary part of the dielectric constants for gold and silver are quite similar. However, the minor differences of these values at each wavelength give rise to significant differences in the plasmonic behavior of the two metals. Therefore, it is critical to consider how the metal composition of the structure influences the resulting plasmonic properties, especially when working with nanostructures.

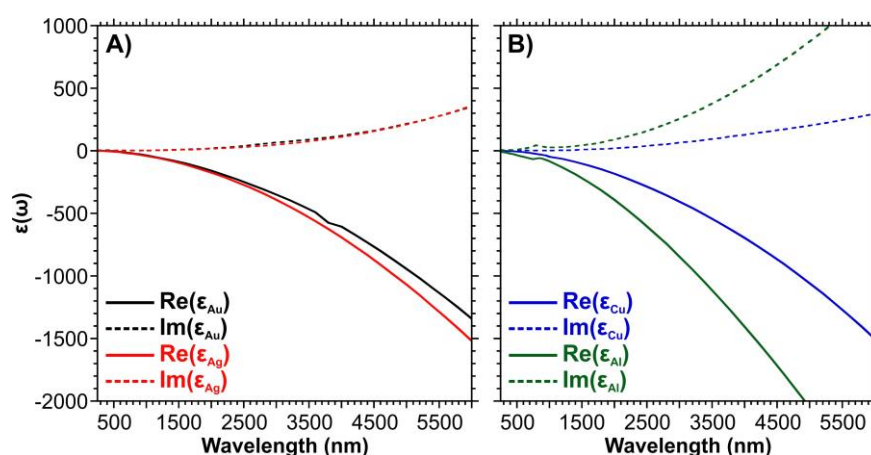


Figure 2.2 Complex dielectric constants of A) gold and silver, and B) copper and aluminum according to the Drude-Lorentz model.

2.1.3 Localized Surface Plasmon Resonance

A localized surface plasmon resonance (LSPR) arises when a surface plasmon is confined to a structure that is smaller than the incident wavelength of light.² The impinging light promotes the free electrons of the metallic nanostructure to collectively oscillate with respect to the incident electric field yielding an accumulation of charge at the surface of the structure (Figure 2.3). This leads to an enhancement of the electric field in nanoscale regions known as hot-spots. Similar to the surface plasmon, the intensity of these fields rapidly decays away from the surface. For SERS, the little enhancement is typically observed past a length of 5 nm above the surface,⁷⁻⁸ though when the dimensions of the structures are tuned, longer lengths have been reported.⁹⁻¹⁰ In a typical SEIRA

configuration, the near-field enhancement extends up to 100 nm above the metal surface.¹¹ The electric field can be further enhanced by introducing nanostructures near each other, as is observed for dimer structures.¹²

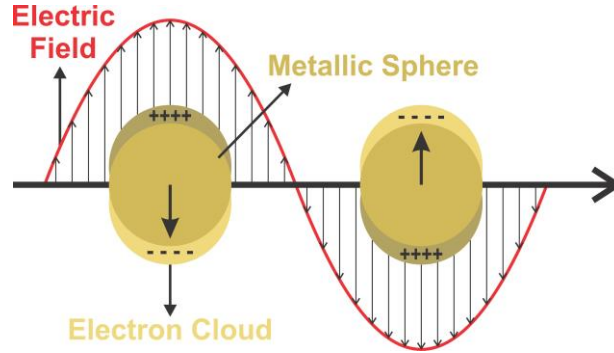


Figure 2.3 Model of a localized surface plasmon resonance (LSPR) for a metallic nanosphere.

To characterize the spectral position of an LSPR, Mie's analytical solution to Maxwell's equations for the scattering and absorption of light by spherical particles is typically used. For nanoparticles that are considerably smaller than the incident wavelength of light ($d \ll \lambda$), Mie's theory defines the total scattering (σ_{ext}), extinction (σ_{sca}), and absorption cross-sections (σ_{abs}) of a nanosphere as:²

$$\sigma_{ext} = \frac{18\pi\epsilon_d^{\frac{3}{2}}V}{\lambda} \times \frac{Im(\epsilon_m)}{[Re(\epsilon_m) + \chi\epsilon_d]^2 + [Im(\epsilon_m)]^2} \quad (2.2)$$

$$\sigma_{sca} = \frac{32\pi^4\epsilon_d^2V^2}{\lambda^4} \times \frac{[Re(\epsilon_m) - \epsilon_d]^2 + [Im(\epsilon_m)]^2}{[Re(\epsilon_m) + \chi\epsilon_d]^2 + [Im(\epsilon_m)]^2} \quad (2.3)$$

$$\sigma_{abs} = \sigma_{ext} - \sigma_{sca} \quad (2.4)$$

Equations (2.2 – 2.4) provide critical information regarding the parameters needed to tune the spectral positions of LSPRs. The optical properties of metallic nanoparticles depend on the dielectric constants of the metal and the environment (ϵ_d), and the geometric parameters of the nanoparticle, specifically the shape factor (χ) and volume (V). For a gold nanosphere ($\chi = 2$) with a radius of 20 nm in a solution of water ($\epsilon_d = 1.7$), the LSPR

is predicted to be near 520 nm.² This is consistent with the experimental observations, including those of Michael Faraday in the mid-nineteenth century where his gold colloid solution was “a beautiful ruby fluid.”¹³ Furthermore, Faraday noted that by varying the size of the particles, it was possible to observe solutions with different colours. This historical example demonstrates the influence of tuning the opto-geometric properties of the structure and surrounding environment to tune the plasmonic properties.

In short, plasmons, and more specifically LSPRs, can guide and enhance the surrounding EM field at the interface between metals and a dielectric. Since the plasmonic properties are dependent on various opto-geometric conditions, further detail is provided in the subsequent sections on how the geometric parameters of the nanostructures can be altered.

2.1.4 Modelling the Plasmonic Properties of Nanostructures

There are limited suggested theories for more complex structures beyond nanospheres and spheroids. As such, numerical methods are generally required to predict their optical properties.¹⁴⁻¹⁵ Specifically, electrodynamic calculations, such as finite-difference time-domain (FDTD) method,¹⁶ discrete dipole approximation,¹⁷ or finite element method are used to model the LSPR spectrum and to spatially determine the EM enhancement over the surface of the structure.¹⁸ In this thesis FDTD calculations are performed for the various fabricated nanostructures.

The FDTD method solves Maxwell’s equations using finite-difference algorithms that discretize the space and time.¹⁹ The spatial domain uses a uniform Cartesian grid, based on Yee’s algorithm,²⁰ known as a Yee cell (Figure 2.4). The unit cell is composed of individual electric and magnetic pointing vector components, shifted by half-grid points relative to each other. During the calculation, the excitation wavelength is treated as a short pulse as opposed to a plane wave, and the difference in the field components before and after being used is calculated.²¹ This process repeats continuously until the field converges and reaches a steady-state solution. Converting the time-domain results to frequency domain spectra is performed using Fourier transformations.

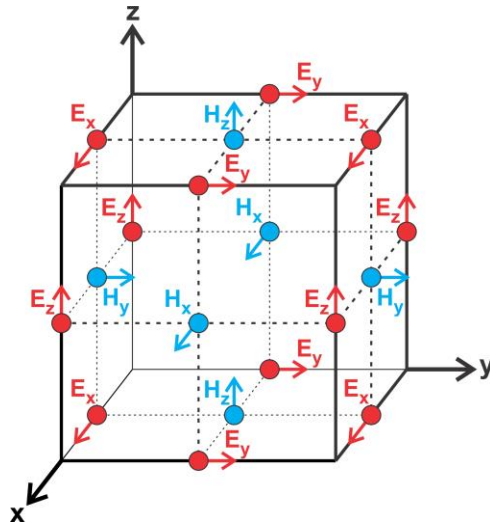


Figure 2.4 Illustration of a standard Cartesian Yee cell used for FDTD calculations and how the electric (red circles and arrows, E_x, E_y, E_z) and magnetic (blue circles and arrows, H_x, H_y, H_z) field components are distributed across the cell.

FDTD calculations are readily performed on non-spherical structures, even though the use of a grid-like mesh can lead to stair casing errors. Importantly, relative to other computational methods, such as FEM, FDTD is less computationally expensive. In this thesis, FDTD calculations are performed using the commercial software FDTD Solutions from Lumerical. A description of how the simulations are built is provided in Appendix A. For the FDTD calculations in this thesis, a plane wave source is most often used, along with the default intensity (E_0) equal to 1 is used. As such, all the electric field components ($E_x, E_y, and E_z$) are already normalized to the intensity of the source. The normalized electric field magnitude ($|E_{x,y,z}/E_0|^2$) can then be determined simply by squaring the obtained E values. This is the approach used to generate the EM field maps of the polarized component shown throughout the thesis. Other relevant experimental details regarding specific meshing parameters is provided in the experimental sections of Chapters 3 – 7.

2.2 General Considerations for Fabricating Nanostructures

When determining what nanostructure to prepare and by what means, is to necessary consider what the desired outcome is. As the nanostructure plays a fundamental role in

determining the applicability of different spectroscopic technique(s), and potentially the applications of the nanostructure, carefully selecting the appropriate fabrication parameters is crucial.

As was discussed in the previous section, different metals exhibit different plasmonic properties in the UV and visible regions. This means that depending on the excitation source, the likely number of metal choices becomes smaller. For the visible region, silver and gold are by far the most common metals used. It is important to note that by tuning the dimensions of the structure, it is possible to perform SERS measurements in the visible region ($\lambda_{\text{exc}} = 633 \text{ nm}$) using other metals (copper, aluminum, and nickel).²² For UV-plasmonics, metals such as aluminum,²³ indium,²⁴ and rhodium,²⁵ have emerged as popular choices. In the mid-infrared, gold is the most commonly used metal for SEIRA,²⁶ with aluminum becoming an alternative choice.²⁷⁻²⁹

Beyond its critical role in the tuning of the spectral position of the resonances, the choice of plasmonic metal(s) may also influence the potential application of the nanostructure. A classic example of this is the common use of gold as opposed to silver for applications involving biological systems. When silver nanoparticles are internalized by cells, they undergo oxidative dissolution, yielding toxic Ag (I) species.³⁰ Approaches such as chemical surface modification,³¹ or by encapsulating the silver in a chemically stable metallic shell, like gold, can be used to minimize the toxicity of silver nanoparticles.³² Beyond biosensing applications, nanostructures are often used to perform plasmon-mediated catalysis and photocatalysis of chemical reactions at the metal surface.³³ To perform these reactions, a variety of metal and material compositions have been explored including: Ag,³⁴ Pd,³⁵ Au@AgAu,³⁶ graphene/Ag,³⁷ Au/TiO₂,³⁸ Au/Pd,³⁹⁻⁴⁰ and Pd/Ag.⁴⁰ In this thesis, gold was chosen as the plasmonic metal for all of the fabricated nanostructures due to its chemical inertness, ease of functionalization, but more importantly, its applicability to both the visible and mid-infrared spectral regions.

The fabrication methodology is another important factor that must be considered. For the preparation of nanostructures, both bottom-up and top-down approaches are commonly used. One means of deciding on the best approach is to consider what the end goal

application is. In some cases, either approach can be used, such as for the detection of glycans on the surface of cells.⁴¹⁻⁴² If the objective is to internalize the nanoparticle into a cell, a bottom-up or synthetic approach, is likely to be preferable.⁴³⁻⁴⁵ Alternatively, top-down or lithographic fabrication is particularly well suited for on-chip sensing applications that require a high-degree of reproducibility.⁴⁶⁻⁴⁹ More important to the scope of this thesis is the relationship between the fabrication methodology and the control of the plasmonic properties of the nanostructure. Although both methods have merit and can be used to prepare an incredibly large catalogue of nanostructures, in this thesis we have selected lithographic-based fabrication. These technologies provide exquisite control over the precise dimensions of the resulting nanostructure(s) as well as high sample-to-sample reproducibility.

2.3 Plasmonic Platforms Prepared by Lithography

Depending on the desired shape, and dimensions of the nanostructure, along with the necessary array size of the pattern, different lithographic techniques can be used. Some notable lithographic techniques for the high-throughput fabrication of plasmonic structures are: nanostencil,⁵⁰⁻⁵² laser-interference,⁵³⁻⁵⁴ direct laser writing,⁵⁵⁻⁵⁶ nanoimprint,⁵⁷⁻⁵⁹ and photolithography.^{46, 60-61} Although high-throughput fabrication may be ideal for large scale fabrication, it often limits the types of structures that can be fabricated. For example, techniques requiring the use of a template or mask, result in structures derived from the template itself. Although the masks are reusable, the initial process of preparing a wide arrange of sizes and geometries is time consuming as unique templates would be required. Thus, such an approach should only be used once an ideal geometry has been determined. Techniques derived from colloidal lithography,⁶²⁻⁶⁴ including angled nanospherical-lens lithography,⁶⁵ provide the capability of using a simple mask to prepare a variety of nanostructures. Another limitation to high-throughput fabrication is the resolution of the fabrication. In the case of laser-based or mask-based lithographic methods, best-case structure diameters ranging from 100 to 400 nm are often reported.⁵⁵⁻⁵⁶ Depending on the desired dimensions and geometries of the structure, such a resolution may not be ideal. In this thesis, two lithographic techniques are used to

prepare the nanostructures benefitting from the ability to fabricate a variety of nanostructures with a high resolution.

2.3.1 Nanosphere Lithography (NSL)

Derived from natural lithography,⁶⁶ colloidal lithography commonly referred to as nanosphere lithography (NSL),⁶⁷ is a benchtop lithographic technique that is used to prepare plasmonic nanostructures. An advantage of this technique is that it can prepare nanostructures over surface areas commonly on the order of several mm², but also up to 1 m².⁶⁸ During the NSL process, a monolayer of polystyrene or silica spheres is added to the surface of a clean and hydrophilic surface, most commonly glass, silicon, or other conductive surfaces. To best achieve the necessary monolayer over the surface, a variety of approaches have been developed including drop-casting,⁶⁹⁻⁷⁰ spin-coating,⁷¹ and air-water interface methods.⁷²⁻⁷³ Once the particle solution is dried, a thin layer of metal is deposited over the surface, followed by the removal of the particles. A general scheme of the NSL process is shown in Figure 2.5.

Using any of the mentioned methods for depositing a monolayer onto the surface it is possible to prepare a variety of nanostructures, some of which are highlighted in Figure 2.6. The simplest plasmonic nanostructure fabricated by NSL are film over nanospheres (Figure 2.6A), where the coated particles are left on the surface of the substrate. Since the particles form a hexagonal close packed monolayer, small triangular gaps are present between the particles. As the metal is deposited, it reaches the surface of the substrate. Removal of the particles reveals the resulting structures, and is the most-commonly used approach by the Lagugné-Labarthe group. By depositing thin layer(s) of metal(s), nanoprisms are formed (Figure 2.6B).^{41, 74-77} As the amount of metal approaches 0.4D (D = diameter of the particle), tetrahedral nanopyramids are formed (Figure 2.6C).^{72, 76} Alternatively, by altering the etching the particles prior to metal deposition, followed by the subsequent lift-off of the particles, arrays of nanoholes are revealed (Figure 2.6D).⁷⁸ Adding two monolayers on top of each other, followed by etching and metal deposition can yield a variety of Moiré patterns with resonances that span the visible through mid-infrared spectral regions,⁷⁹⁻⁸² an example of which is shown in (Figure 2.6E). If the sample is tilted during the metal deposition, it is possible to prepare even more

geometries,⁸³ including crescents (Figure 2.6F). After revealing the nanostructures, a thin dielectric layer, such as SiO₂, can be sputtered over the surface of the platforms. These platforms could then be used for surface-enhanced fluorescence (SEF), since the dielectric layer prevents the quenching of a fluorophore when it is in the vicinity of the metal surface.^{75, 84}

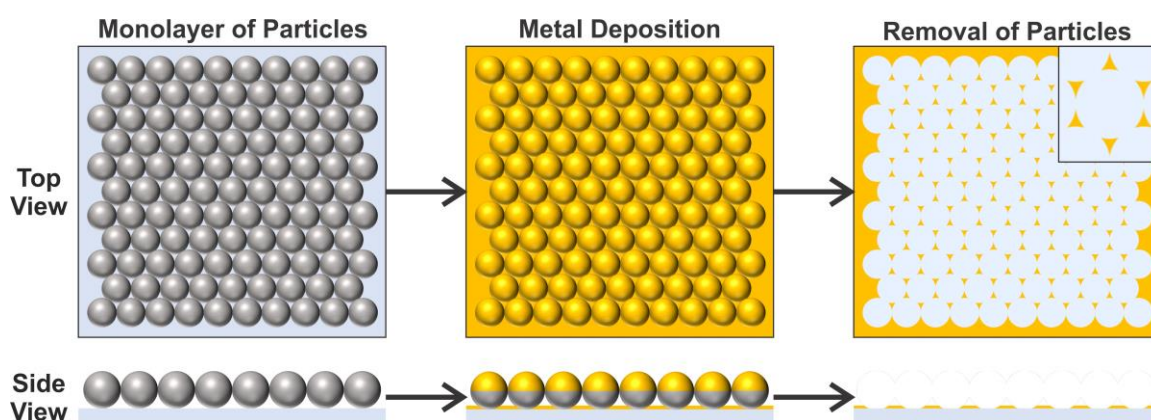


Figure 2.5 Schematic illustration of the general NSL process. Polystyrene or silica particles are deposited onto a substrate, such as a glass cover slip, and eventually form a monolayer. Thin films of metals (adhesion followed by plasmonic) are deposited onto the surface by electron-beam evaporation. The particles are then removed by sonication in ethanol to reveal the nanostructures formed between the gaps of the particles.

For structures prepared by NSL, the dominant means of tuning the spectral position of the LSPRs is by altering the size of the particles. This effect was well demonstrated by Hoffmann *et al.* where when fabricated on CaF₂ substrates, increasing the diameter of the polystyrene particles from 3 to 8 μm resulted in resonances that spanned from 4 to 8 μm ($1250 - 2500 \text{ cm}^{-1}$).⁸⁵ By coupling the changes in particle diameter with changes in the refractive index, resonances were introduced over a broad spectral range (3 to 13 μm). These larger nanoprisms were then coated with a thin layer of PMMA, and the C=O stretch at 1730 cm^{-1} was detected using surface-enhanced infrared absorption (SEIRA). Alternatively, altering the metal composition of the nanostructures can broaden the plasmonic properties of the nanostructures.⁸⁶ Previous work in the Lagugn -Labarhet group has explored this effect by fabricating heterometallic nanoprisms prepared by

depositing alternating layers of gold and silver during the electron-beam evaporation steps of the NSL process.⁷⁴ The resulting heterometallic nanoprisms exhibited optical resonances from 400 to 800 nm.

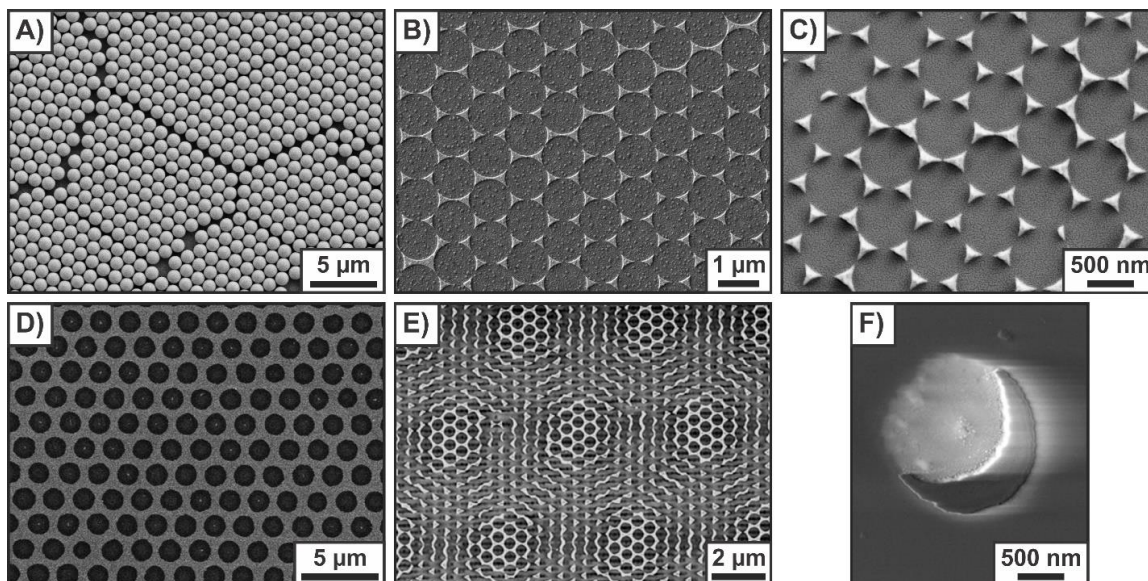


Figure 2.6 Scanning electron micrographs for different examples of nanostructures prepared by nanosphere lithography: A) film over nanospheres, B) nanoprisms, C) tetrahedral nanopryramids, D) nanohole arrays, E) Moiré patterns, and F) nanocrescents. Adapted with permission from refs 78 , 79 , 83 Copyright 2014 American Chemical Society and 2015 American Chemical Society.

In this thesis, NSL is used in Chapter 4 to prepare a plasmonic platform composed of superimposed arrays of nanoprisms with different side lengths. Details regarding the experimental procedure used can be found in Appendix B.

2.3.2 Electron-Beam Lithography (EBL)

Although NSL can be used to prepare a variety of nanostructures, it is often difficult to accurately control the final dimensions of the structure. Often, a distribution of sizes and interstructure gaps are reported. Therefore, in order to finely control the plasmonic nanostructures, an alternative technique is used throughout this thesis. EBL relies on the use of an electron-beam to write a desired pattern onto a photoresist. This enables the fabrication of an incredibly diverse range of nanostructures, with plasmonic properties

ranging from the visible through the mid-IR spectral regions.⁸⁷ Importantly, these nanostructures can be fabricated with a resolution of at least 10 nm using conventional systems and resists,⁸⁸ and can be further improved to 1-2 nm given specific set-ups.⁸⁹

A general scheme of the EBL fabrication process is shown in Figure 2.7. Depending on the desired purpose of the sample, different substrates can be used. Silicon wafers are often ideal for imaging the samples, glass cover slips for applications in the visible region, and CaF₂ windows for near- to mid-IR measurements.

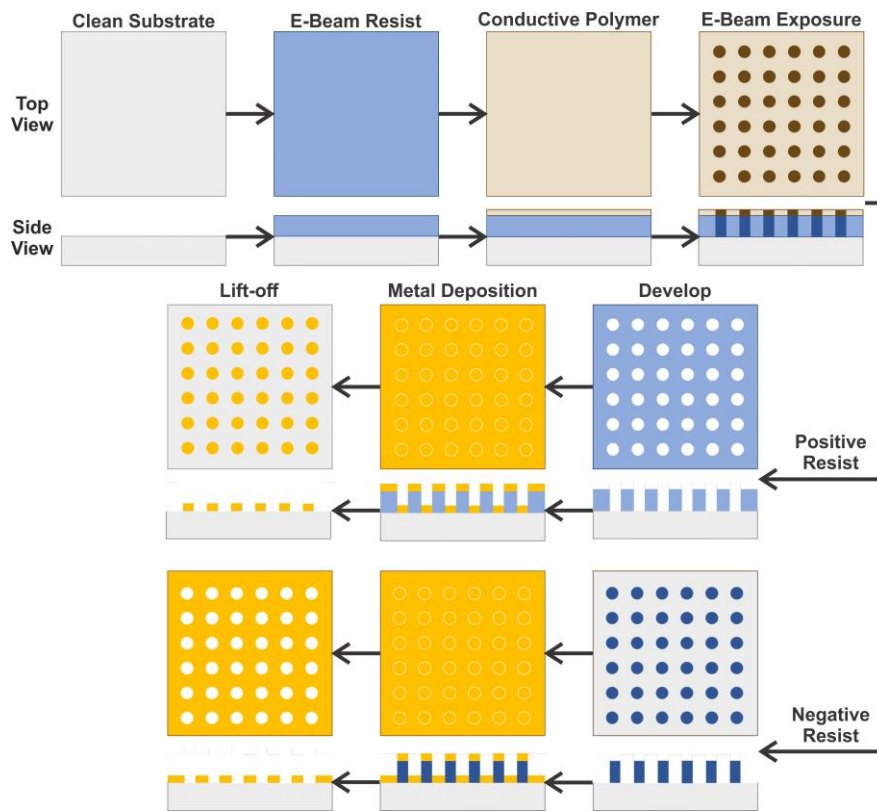


Figure 2.7 Schematic illustration for the general EBL process. An electron-beam sensitive resist is spin-coated onto the surface of a cleaned substrate. If the substrate is non-conductive, a conductive polymer is spin-coated onto the resist and is further baked. Following exposure to the electron-beam (darker regions), the sample is developed, the resulting patterned resist will depend on the type of resist. Once the metal is deposited and the excess resist is lifted-off, the final structure is revealed.

With the capability of preparing a wide-range of structures, with precise geometries and position, EBL has become a technique of choice used in the Lagugn -Labarthe group for preparing nanostructures with specific optical and physical properties (Figure 2.8). As opposed to preparing traditional arrays of isolated nanorods, nanorods with different side lengths can be arranged into a box configuration (Figure 2.8A). These boxes can be subsequently arranged into arrays (Figure 2.8B), where the arrays sizes can be between $50 \times 50 \mu\text{m}^2$ to $100 \times 100 \mu\text{m}^2$ to perform microscopy measurements. Furthermore, simple geometries coupled with complex arrangements can yield fractal geometries (Figure 2.8C and D). Structures with complex geometries can be arranged into varying configurations (Figure 2.8E), enabling the formation of high-densities of hot-spots. By changing the nature of the resist from a positive resist (Figure 2.8A-E) to a negative resist (Figure 2.8F), it is possible to fabricate arrays of holes, without the use of a mask,⁴⁶ or ion milling steps.⁹⁰

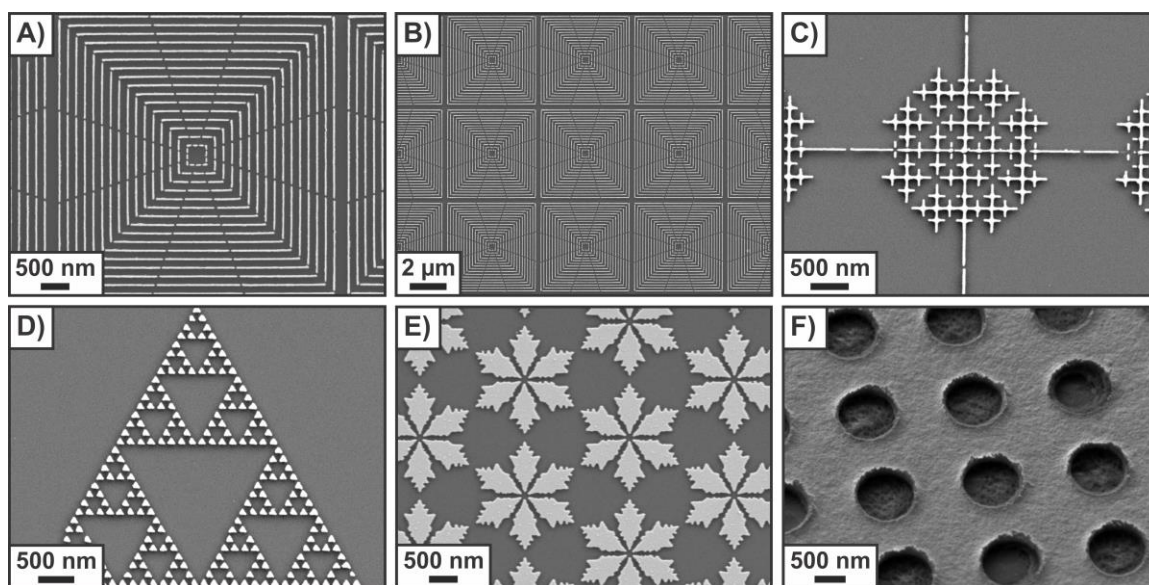


Figure 2.8 SEM images highlighting examples of gold nanostructures prepared in the Lagugn -Labarthe group using electron-beam lithography: A) box of nanorods, B) arrays of the boxes of nanorods, C) Cesaro-like fractal, D) Sierpiński triangle, E) snowflake-like nanostructures, and F) arrays of nanoholes. A-E) were prepared using a positive resist, and F) was prepared using a negative resist.

In this thesis, EBL was used in Chapters 3 – 7 to prepare the nanostructures, with a positive resist being exclusively used. Full experimental details are provided in Appendix C.

2.4 Probing the Plasmonic Properties in the Visible to Near-Infrared Spectral Regions

Throughout this thesis, the fabricated nanostructures exhibit plasmonic properties in the visible and near-infrared spectral regions. This section describes the various techniques used to probe those properties.

2.4.1 Visible Near-Infrared Absorption Measurements

To determine the LSPR wavelengths from the nanostructures, the absorption, scattering, or extinction spectra are generally measured experimentally.^{2,5} This can be done by performing far-field optical transmission measurements using a spectrometer combined with a microscope. The spectral resonances obtained by performing these measurements can then be related to the different LSPR modes that the structure can support by calculation or by using other techniques.⁹¹⁻⁹² For a simple geometry, such as a spherical nanoparticle, the assignment is relatively straightforward, and is described in Figure 2.9. Qualitatively, the lowest energy mode ($l = 1$), described as the dipole mode, relates to the collective oscillation of the electron cloud that is in-phase with the input electromagnetic wave. Depending on the size and geometry of the nanostructure, it is possible to observe different LSPR modes.⁹³⁻⁹⁴ The quadrupole mode ($l = 2$) relies on the oscillation of half of the conduction electrons, and the higher-order modes, such as hexapolar modes, will represent other oscillations of the free electrons driven by the impinging light.

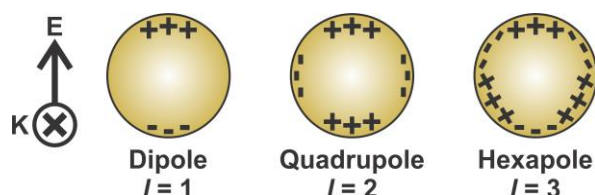


Figure 2.9 Schematic representation of different order LSPR modes for a metallic nanosphere.

In this thesis, absorption measurements to determine the spectral position of LSPRs in the visible to near-infrared spectral regions are performed in Chapters 3, 4, and 7. In Chapters 3 and 4, a halogen lamp with a 100 μm optical fiber coupled to an Olympus IX71 inverted optical microscope was used. A 10 \times (N.A. = 0.25) objective was used to collimate (i.e. to make parallel) the source beam exiting from the fiber, and a 20 \times (N.A. = 0.4) objective to focus the beam onto the sample. This resulted in a spot size of approximately 50 μm (comparable to the size of the patches of nanostructures prepared by EBL). After the sample, the transmitted light was collected by a 20 \times (N.A. = 0.5) objective prior to analysis by the spectrometer, equipped with a liquid nitrogen cooled charge coupled device (CCD, HR LabRam, Horiba-Jobin-Yvon, Kyoto, Japan, focal length of 800 mm). A confocal pinhole of 200 μm and a grating of 150 grooves/mm was used for these measurements. A representative schematic of the set-up is shown in Figure 2.10. In Chapter 7, a Nikon Diaphot inverted optical microscope, along with a USB 4000-VIS-NIR-ES spectrometer (Ocean Optics, FL, USA) were used instead and built on the same principle.

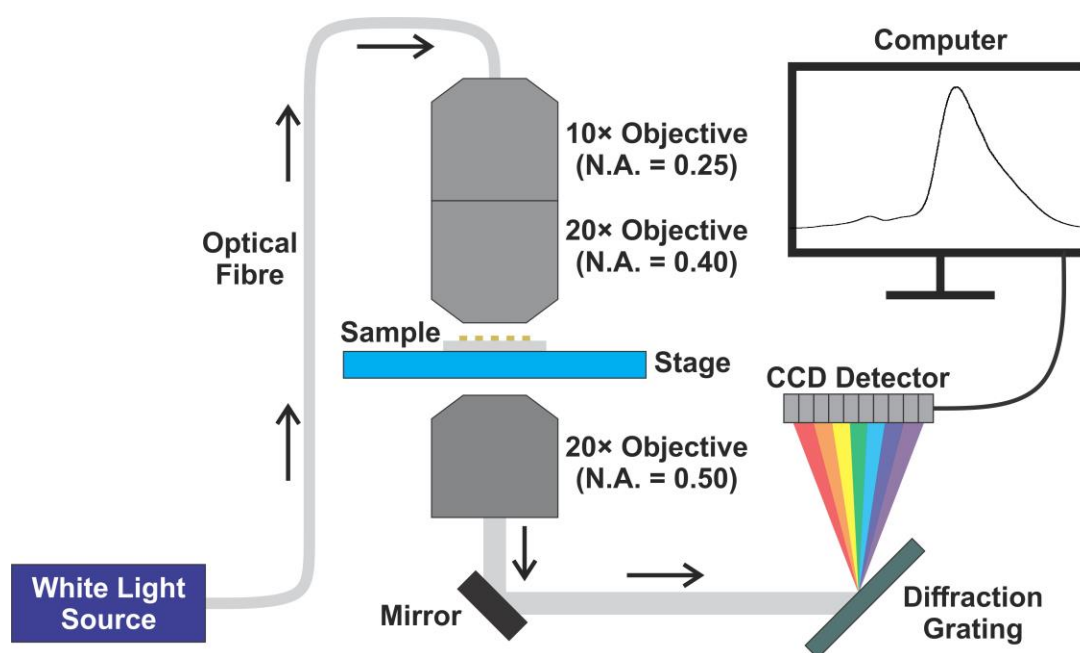


Figure 2.10 Schematic illustration of the absorbance setup used in this thesis.

2.4.2 Surface-Enhanced Raman Spectroscopy (SERS) Measurements

SERS relies on the combination of EM and chemical enhancement mechanisms.⁹⁵ As was discussed earlier in this chapter, the EM enhancement derives from the hot-spots found at the surface, and more specifically, from the edges and/or sharp tips of the nanostructures. For SERS the intensity of the EM field from the LSPR is highly dependent on the wavelength of light ($E_{LSPR}(\lambda)$). When irradiated with an excitation source, the intensity of the incident field ($E_0(\lambda)^2$) is enhanced with respect to $E_{LSPR}(\lambda)$, as well as the Raman scattered light ($E_{LSPR}(\lambda \pm \lambda_R)$). The enhancement factor results from the product of both enhancements at the LSPR frequency and at the Raman shifted frequency as described by (2.5):²

$$EF_{EM}(\lambda) = \frac{|E_{LSPR}(\lambda)|^2 |E_{LSPR}(\lambda \pm \lambda_R)|^2}{|E_0(\lambda)|^4} \quad (2.5)$$

Since the Raman frequencies of the fingerprint regions are generally within 100 nm of the Rayleigh scattering, it is often assumed that $E_{LSPR}(\lambda \pm \lambda_R)$ is similar to $E_{LSPR}(\lambda)$, resulting in a commonly simplified equation (2.6):⁹⁶

$$EF_{EM}(\lambda) = \frac{|E_{LSPR}(\lambda)|^4}{|E_0(\lambda)|^4} \quad (2.6)$$

Here, the enhancement factor scales to the fourth power, implying that a minimal increase in intensity of the electric field (factor of 10) can yield a sufficiently large EM enhancement factor (EF, 10000). Of course, the farther the considered vibrational mode is from the Rayleigh scattering, the more deviation from (2.6) will be observed. It is also important to note that in SERS, there also exists a second enhancement method known as chemical enhancement. This enhancement is described as the combination of charge transfer, resonance Raman, and non-resonance Raman enhancements.⁹⁷ These contributions, especially resonance Raman, are most often observed when working with dye molecules (rhodamine, crystal violet, malachite green, methylene blue) under electronic resonance conditions. If both enhancement contributions are to be considered,

an alternative equation for describing the EF is required and is classically described as (2.7).⁹⁸⁻⁹⁹

$$EF = \frac{I_{SERS}}{I_{Raman}} \times \frac{n_{Raman}}{n_{SERS}} \quad (2.7)$$

where, I_{SERS} and I_{Raman} are the observed intensities for a specific vibrational mode, and n_{SERS} and n_{Raman} are the number of molecules present contributing to the SERS and normal Raman scattering respectively. Importantly, unlike EM enhancement that is based on the properties of the nanostructure, chemical enhancement is dependent on the analyte.¹⁰⁰ In this thesis, any contributions associated to chemical enhancement are not discussed, as it is believed that the analytes used exhibit little to no chemical enhancement. As opposed to comparing Raman and SERS responses, the intensity of the EF as determined by the FDTD calculations is used to estimate the EF of the prepared structures.

In this thesis, SERS measurements are reported in Chapters 3, 4, and 7. For these measurements, a commercial Raman spectrometer (HR LabRam, Horiba-Jobin-Yvon, Kyoto, Japan, focal length of 800 mm) is used to perform the SERS measurements. The spectrometer is connected to an inverted optical microscope (IX71, Olympus, Tokyo, Japan) that is interfaced with a 5-axis atomic force microscope (AFM) system (AFM, NanoWizard II Bioscience, JPK Instruments Inc., Berlin, Germany). A bottom illumination configuration with a backscattering collection geometry is used, and a schematic representation of the optical pathway is shown in Figure 2.11. The setup can be configured for different excitation wavelengths (532, 632.8, and 785 nm) by changing the laser, interference filter, and the notch filter. In this thesis, only 632.8 and 785 nm excitation wavelengths were used, and the wavelengths were chosen based on the plasmonic properties of the nanostructures. For all SERS measurements, a confocal pinhole of 200 μm , and a diffraction grating of 600 grooves/mm were used. The acquisition time used for each experiment was dependent on the obtained signal-to-noise ratio for the probe molecule.

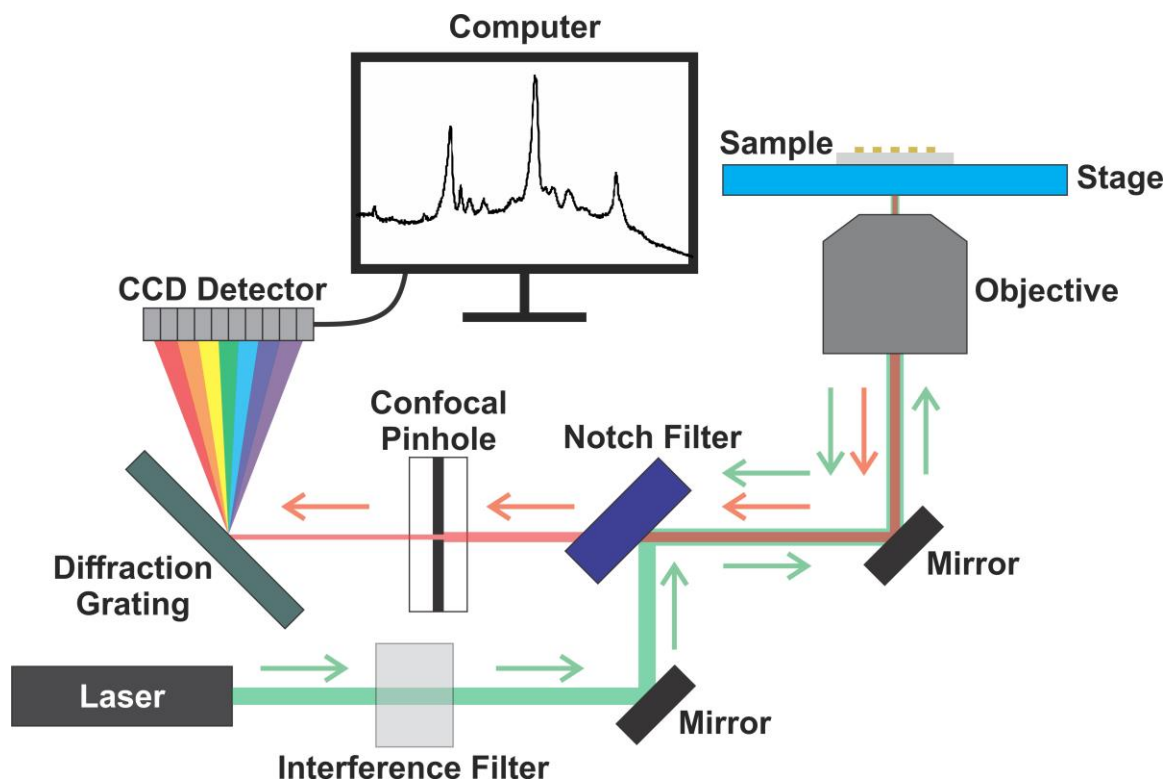


Figure 2.11 Schematic illustration of the Raman and SERS setup used in this thesis. The green arrows indicate the optical path of the incident (excitation) photons, and those in red correspond to the Raman scattered photons.

2.5 Probing the Plasmonic Properties in the Near- to Mid-Infrared Spectral Regions

Brightness, often referred to as brilliance, is a measure of the intensity of light for a unit area of the source. As different sources offer different brightness, it is necessary to consider the source to be used. For example, small samples often require the use of a source that provides a higher brilliance to obtain a sufficient signal-to-noise ratio. In Raman spectroscopy, as bright monochromatic sources such as lasers are used, the collected signal is generally optimized. However, in the mid-IR, the Globar source used in most common infrared spectrometers is generally weak, often leading to the need for longer acquisition times.

2.5.1 Sources of Mid-Infrared Light

Commercial FT-IR spectrometers are often equipped with a conventional infrared Globar source (such as an ETC EverGlo®). With a Globar source, a sintered silicon-carbide element is heated to a high temperature (>1350 K) by passing an electrical current through it.¹⁰¹⁻¹⁰² The result from the blackbody emission is infrared radiation in all directions.¹⁰³ Parabolic mirrors are used to collect the light, collimate it and send it towards an interferometer.

An alternative source of mid-infrared light is synchrotron light. Synchrotron light is produced by the interaction between charged particles (typically electrons) with a magnetic field as the charged particles travel. As the charged particle interacts with the magnetic field, energy is lost. Some of this lost energy is given off in the form of synchrotron light. This light spans the electromagnetic spectrum from the far-infrared to higher energy x-rays, and is given off tangentially to the particles path in the magnetic field.¹⁰⁴ Importantly, the synchrotron light beam is highly collimated, resulting in a brightness that is orders of magnitude higher than a conventional infrared source.¹⁰⁴⁻¹⁰⁵

As measurements involving infrared light are used throughout this thesis for SEIRA measurements (Chapters 3, 4, 5, and 6), determining the ideal source for those experiments was necessary. A comparison between the normalized absorbance spectra obtained for an array of plasmonic nanostructures obtained using different infrared sources is shown in Figure 2.12. For these measurements, the infrared light was directed onto the sample using a microscope. Under these conditions, the diameter of the beam was comparable to the dimensions of the patch fabricated by EBL ($50 \times 50 \mu\text{m}^2$).

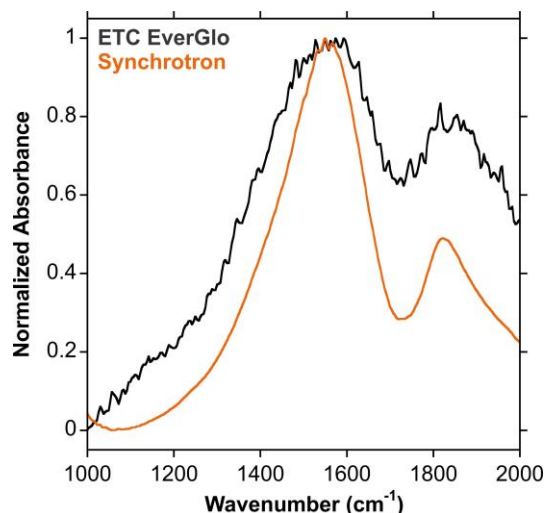


Figure 2.12 Comparison of the normalized infrared absorbance spectra for superimposed arrays of gold nanoprisms with side lengths of 2 and 0.25 μm obtained using different infrared sources.

Importantly, distinct absorbances corresponding to the localized surface plasmon resonances of the structure were observed for both sources. As mentioned, the signal-to-noise ratio can be improved by performing measurements using sources that have a higher brightness. This is clearly the case for the spectra of Figure 2.12, as the spectrum obtained using a synchrotron source has significantly less noise than the spectrum acquired with a Globar source. It is also important to note that the synchrotron spectrum is the average of 512 spectra, whereas the conventional source, with a poorer signal-to-noise ratio is the average of 1000 spectra. Since the synchrotron source provided less noise in the spectra, and the spectra could be acquired in a shorter acquisition time, it was used for all mid-infrared absorption and SEIRA measurements in this thesis.

2.5.2 Near- to Mid-Infrared Absorption Measurements

In this thesis, near- to mid-IR absorption measurements are shown in Chapters 3 – 6. Fourier transform infrared (FT-IR) spectroscopy measurements were performed at the Mid-IR beamline synchrotron facility located at the Canadian Light Source (Beamline 01B-01). The beamline end station consists of a Bruker Optics Vertex 70v FT-IR Spectrometer coupled to a Hyperion 3000 IR Microscope (Bruker Optics, MA, USA). Light was focused and collected in absorbance mode using a 36 \times objective (N.A. 0.65).

The input source coming from the synchrotron beam was linearly polarized. The collected light was measured using a narrowband fast DC coupled mercury cadmium telluride (MCT) (liquid nitrogen cooled) Kolmar (Kolmar Technologies, Inc., MA, USA) detector. A schematic representation of the set-up is shown in Figure 2.13. All measurements were collected from $8000\text{-}800\text{ cm}^{-1}$ with a spectral resolution of 4 cm^{-1} . In Chapter 6, a photoelastic modulator (PEM) was added onto the beam path to perform anisotropic measurements. Greater details regarding the adapted set-up are described in Chapter 6.

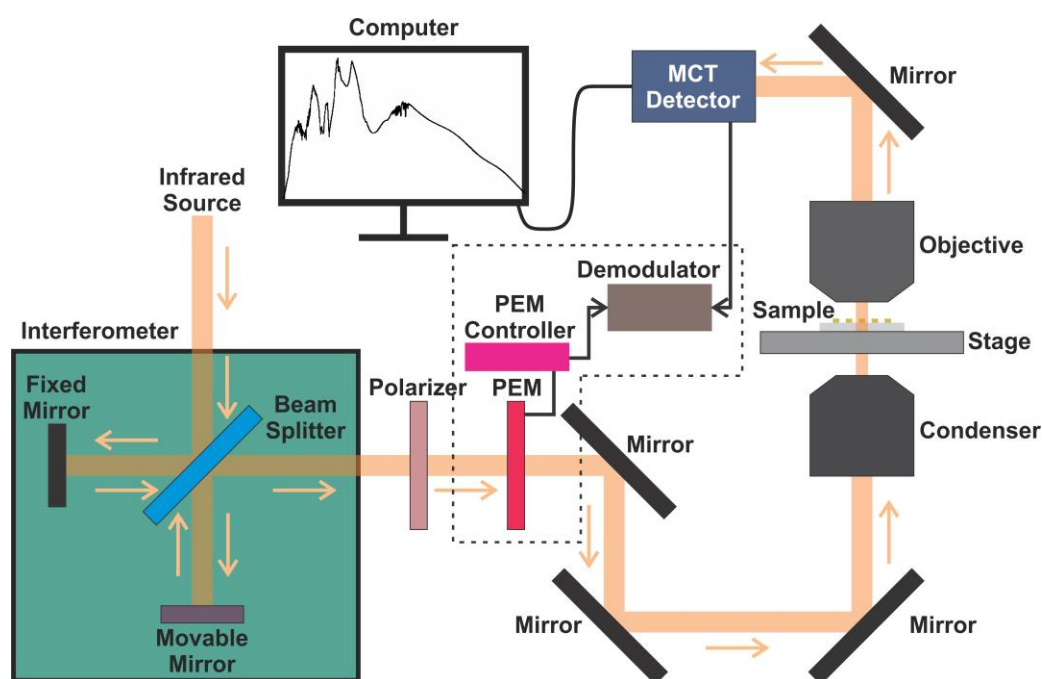


Figure 2.13 Schematic illustration of the general mid-infrared absorption and SEIRA set-up used in this thesis. The components in the dashed lines were used in the anisotropy measurements described in Chapter 6.

2.5.3 Surface-Enhanced Infrared Absorption (SEIRA) Measurements

The dominant enhancement mechanism for SEIRA is based on the EM enhancement offered by the nanostructures. Maximizing SEIRA enhancement involves tuning the optical properties of the nanostructures, often referred to in the literature as antennas, so that both the absorption and scattering cross-sections of the structure are similar.¹⁰⁶

Unlike in SERS where the excitation light and the Raman scattered light contribute to the

enhancement, SEIRA only involves the use of the excitation light.¹⁰⁷ When considering only the EM enhancement, the equation used is **(2.8)**:

$$EF_{EM}(\lambda) = \frac{|E_{LSPR}(\lambda)|^2}{|E_0(\lambda)|^2} \quad (2.8)$$

As in SERS, chemical enhancement can play a factor for specific vibrational modes of some analytes. The chemical enhancement is the result coupling between vibrational and electron-hole pair excitations.¹⁰⁸⁻¹⁰⁹ Once again, a more complete equation combining all mechanisms can be used, and is denoted as **(2.9)**.²⁶

$$EF = \frac{I_{SEIRA}}{I_0} \times \frac{A_0}{A_{SEIRA}} \quad (2.9)$$

where I_{SEIRA} and I_0 are the intensities of the vibrational modes associated with the SEIRA and normal infrared measurements, and A_{SEIRA} and A_0 are relate to the number of molecules that are absorbing the infrared light. It can often be a challenge to obtain the number of molecules present in the non-resonant IR measurements, as monolayers and thin films less than 100 nm are often used for the SEIRA measurements. Measurements at these levels often rely on the use of other techniques, such as polarization-modulation infrared reflection absorption spectroscopy, to obtain an absorbance. As these methods yield distinct signals, this can influence the observed absorbance, and thus, the determination of the EF. For this thesis, only the EM SEIRA enhancement is considered. Interestingly, in SEIRA measurements, the enhanced vibrational resonance appears as an asymmetric dip in the plasmon resonance of the structure. These types of asymmetric resonances are known as Fano resonances.¹¹⁰ The intensity of these Fano resonances is highly dependent on the position of the vibrational resonance of the analyte with respect to the plasmon resonances.¹¹¹ In this thesis, SEIRA measurements were performed in Chapters 4 – 6, with Chapter 6 introducing the relationship between linear dichroism measurements and SEIRA. To perform these measurements, the set-up shown in Figure 2.13 was used.

2.6 References

1. Kreibig, U.; Vollmer, M., *Optical Properties of Metal Clusters*; Springer: Berlin, 1995; Vol. 25.
2. Mayer, K. M.; Hafner, J. H., *Chem. Rev.* **2011**, *111*, 3828-3857.
3. Sambles, J. R.; Bradbery, G. W.; Yang, F., *Contemp. Phys.* **1991**, *32*, 173-183.
4. Barnes, W. L.; Dereux, A.; Ebbesen, T. W., *Nature* **2003**, *424*, 824.
5. Willets, K. A.; Duynes, R. P. V., *Annu. Rev. Phys. Chem.* **2007**, *58*, 267-297.
6. Yang, H. U.; D'Archangel, J.; Sundheimer, M. L.; Tucker, E.; Boreman, G. D.; Raschke, M. B., *Phys. Rev. B* **2015**, *91*, 235137.
7. Kennedy, B. J.; Spaeth, S.; Dickey, M.; Carron, K. T., *J. Phys. Chem. B* **1999**, *103*, 3640-3646.
8. Dieringer, J. A.; McFarland, A. D.; Shah, N. C.; Stuart, D. A.; Whitney, A. V.; Yonzon, C. R.; Young, M. A.; Zhang, X.; Van Duyne, R. P., *Faraday Discuss.* **2006**, *132*, 9-26.
9. Singh, A. K.; Khan, S. A.; Fan, Z.; Demeritte, T.; Senapati, D.; Kanchanapally, R.; Ray, P. C., *J. Am. Chem. Soc.* **2012**, *134*, 8662-8669.
10. Wei, W.; Li, S.; Millstone, J. E.; Banholzer, M. J.; Chen, X.; Xu, X.; Schatz, G. C.; Mirkin, C. A., *Angew. Chem. Int. Ed.* **2009**, *48*, 4210-4212.
11. Limaj, O.; Etezadi, D.; Wittenberg, N. J.; Rodrigo, D.; Yoo, D.; Oh, S.-H.; Altug, H., *Nano Lett.* **2016**, *16*, 1502-1508.
12. Zhao, Y.; Sun, M.; Ma, W.; Kuang, H.; Xu, C., *J. Phys. Chem. Lett.* **2017**, *8*, 5633-5642.
13. Faraday, M., *Phil. Trans. R. Soc. Lond.* **1857**, *147*, 145-181.
14. Myroshnychenko, V.; Rodriguez-Fernandez, J.; Pastoriza-Santos, I.; Funston, A. M.; Novo, C.; Mulvaney, P.; Liz-Marzan, L. M.; Garcia de Abajo, F. J., *Chem. Soc. Rev.* **2008**, *37*, 1792-1805.
15. Yu, R.; Liz-Marzan, L. M.; Garcia de Abajo, F. J., *Chem. Soc. Rev.* **2017**, *46*, 6710-6724.
16. Oubre, C.; Nordlander, P., *J. Phys. Chem. B* **2004**, *108*, 17740-17747.
17. Draine, B. T.; Flatau, P. J., *J. Opt. Soc. Am. A* **1994**, *11*, 1491-1499.
18. Christopher, G. K.; Stephen, J. N.; Tuan, V.-D., *Nanotechnology* **2010**, *21*, 315203.
19. Zhao, J.; Pinchuk, A. O.; McMahon, J. M.; Li, S.; Ausman, L. K.; Atkinson, A. L.; Schatz, G. C., *Acc. Chem. Res.* **2008**, *41*, 1710-1720.
20. Kane, Y., *IEEE Trans. Antennas Propag.* **1966**, *14*, 302-307.
21. Parsons, J.; Burrows, C. P.; Sambles, J. R.; Barnes, W. L., *J. Mod. Opt.* **2010**, *57*, 356-365.

22. Kanipe, K. N.; Chidester, P. P. F.; Stucky, G. D.; Meinhart, C. D.; Moskovits, M., *J. Phys. Chem. C* **2017**, *121*, 14269-14273.
23. Tian, S.; Neumann, O.; McClain, M. J.; Yang, X.; Zhou, L.; Zhang, C.; Nordlander, P.; Halas, N. J., *Nano Lett.* **2017**, *17*, 5071-5077.
24. Asselin, J.; Lambert, M.-P.; Fontaine, N.; Boudreau, D., *Chem. Commun.* **2017**, *53*, 755-758.
25. Watson, A. M.; Zhang, X.; Alcaraz de la Osa, R.; Sanz, J. M.; González, F.; Moreno, F.; Finkelstein, G.; Liu, J.; Everitt, H. O., *Nano Lett.* **2015**, *15*, 1095-1100.
26. Neubrech, F.; Huck, C.; Weber, K.; Pucci, A.; Giessen, H., *Chem. Rev.* **2017**, *117*, 5110-5145.
27. Ayas, S.; Topal, A. E.; Cupallari, A.; Güner, H.; Bakan, G.; Dana, A., *ACS Photonics* **2014**, *1*, 1313-1321.
28. Chen, K.; Dao, T. D.; Ishii, S.; Aono, M.; Nagao, T., *Adv. Funct. Mater.* **2015**, *25*, 6637-6643.
29. Cerjan, B.; Yang, X.; Nordlander, P.; Halas, N. J., *ACS Photonics* **2016**, *3*, 354-360.
30. Hsiao, I. L.; Hsieh, Y.-K.; Wang, C.-F.; Chen, I. C.; Huang, Y.-J., *Environ. Sci. Technol.* **2015**, *49*, 3813-3821.
31. Das, B.; Tripathy, S.; Adhikary, J.; Chattopadhyay, S.; Mandal, D.; Dash, S. K.; Das, S.; Dey, A.; Dey, S. K.; Das, D.; Roy, S., *J. Biol. Inorg. Chem.* **2017**, *22*, 893-918.
32. Jiang, X.; Wang, L.; Ji, Y.; Tang, J.; Tian, X.; Cao, M.; Li, J.; Bi, S.; Wu, X.; Chen, C.; Yin, J.-J., *Small* **2017**, *13*, 1602855.
33. Ren, X.; Cao, E.; Lin, W.; Song, Y.; Liang, W.; Wang, J., *RSC Adv.* **2017**, *7*, 31189-31203.
34. Landry, M. J.; Gellé, A.; Meng, B. Y.; Barrett, C. J.; Moores, A., *ACS Catal.* **2017**, *7*, 6128-6133.
35. Wu, B.; Lee, J.; Mubeen, S.; Jun, Y.-S.; Stucky, G. D.; Moskovits, M., *Adv. Opt. Mater.* **2016**, *4*, 1041-1046.
36. da Silva, A. G. M.; Rodrigues, T. S.; Correia, V. G.; Alves, T. V.; Alves, R. S.; Ando, R. A.; Ornellas, F. R.; Wang, J.; Andrade, L. H.; Camargo, P. H. C., *Angew. Chem. Int. Ed.* **2016**, *55*, 7111-7115.
37. Ding, Q.; Chen, M.; Fang, Y.; Zhang, Z.; Sun, M., *J. Phys. Chem. C* **2017**, *121*, 5225-5231.
38. Tan, T. H.; Scott, J.; Ng, Y. H.; Taylor, R. A.; Aguey-Zinsou, K.-F.; Amal, R., *ACS Catal.* **2016**, *6*, 8021-8029.
39. Klinkova, A.; Ahmed, A.; Choueiri, R. M.; Guest, J. R.; Kumacheva, E., *RSC Adv.* **2016**, *6*, 47907-47911.

40. Verma, P.; Kuwahara, Y.; Mori, K.; Yamashita, H., *J. Mater. Chem. A* **2016**, *4*, 10142-10150.
41. Tabatabaei, M.; Wallace, G. Q.; Caetano, F. A.; Gillies, E. R.; Ferguson, S. S. G.; Lagugne-Labarthe, F., *Chem. Sci.* **2016**, *7*, 575-582.
42. Craig, D.; McAughtrie, S.; Simpson, J.; McCraw, C.; Faulds, K.; Graham, D., *Anal. Chem.* **2014**, *86*, 4775-4782.
43. Suvarna, S.; Das, U.; Kc, S.; Mishra, S.; Sudarshan, M.; Saha, K. D.; Dey, S.; Chakraborty, A.; Narayana, Y., *PLOS ONE* **2017**, *12*, e0178202.
44. Ma, N.; Wu, F.-G.; Zhang, X.; Jiang, Y.-W.; Jia, H.-R.; Wang, H.-Y.; Li, Y.-H.; Liu, P.; Gu, N.; Chen, Z., *ACS Appl. Mater. Interfaces* **2017**, *9*, 13037-13048.
45. Huefner, A.; Kuan, W.-L.; Müller, K. H.; Skepper, J. N.; Barker, R. A.; Mahajan, S., *ACS Nano* **2016**, *10*, 307-316.
46. Couture, M.; Ray, K. K.; Poirier-Richard, H.-P.; Crofton, A.; Masson, J.-F., *ACS Sens.* **2016**, *1*, 287-294.
47. Li, X.; Soler, M.; Ozdemir, C. I.; Belushkin, A.; Yesilkoy, F.; Altug, H., *Lab Chip* **2017**, *17*, 2208-2217.
48. Yang, L.; Fu, C.; Wang, H.; Xu, S.; Xu, W., *Anal. Bioanal. Chem.* **2017**, *409*, 235-242.
49. Hong, K. Y.; Brolo, A. G., *Anal. Chim. Acta* **2017**, *972*, 73-80.
50. Aksu, S.; Huang, M.; Artar, A.; Yanik, A. A.; Selvarasah, S.; Dokmeci, M. R.; Altug, H., *Adv. Mater.* **2011**, *23*, 4422-4430.
51. Aksu, S.; Yanik, A. A.; Adato, R.; Artar, A.; Huang, M.; Altug, H., *Nano Lett.* **2010**, *10*, 2511-2518.
52. Yesilkoy, F.; Flauraud, V.; Rugg, M.; Kim, B. J.; Brugger, J., *Nanoscale* **2016**, *8*, 4945-4950.
53. Bagheri, S.; Giessen, H.; Neubrech, F., *Adv. Opt. Mater.* **2014**, *2*, 1050-1056.
54. Bagheri, S.; Strohfeldt, N.; Sterl, F.; Berrier, A.; Tittl, A.; Giessen, H., *ACS Sens.* **2016**, *1*, 1148-1154.
55. Bagheri, S.; Weber, K.; Gissibl, T.; Weiss, T.; Neubrech, F.; Giessen, H., *ACS Photonics* **2015**, *2*, 779-786.
56. Braun, A.; Maier, S. A., *ACS Sens.* **2016**, *1*, 1155-1162.
57. Zhang, M.; Large, N.; Koh, A. L.; Cao, Y.; Manjavacas, A.; Sinclair, R.; Nordlander, P.; Wang, S. X., *ACS Nano* **2015**, *9*, 9331-9339.
58. Xiao, B.; Pradhan, S. K.; Santiago, K. C.; Rutherford, G. N.; Pradhan, A. K., *Sci. Rep.* **2016**, *6*, 24385.
59. Tseng, S.-Y.; Li, S.-Y.; Yi, S.-Y.; Sun, A. Y.; Gao, D.-Y.; Wan, D., *ACS Appl. Mater. Interfaces* **2017**, *9*, 17306-17316.

60. Stewart, J. W.; Akselrod, G. M.; Smith, D. R.; Mikkelsen, M. H., *Adv. Mater.* **2017**, *29*, 1602971.
61. Fang, M.; Lin, H.; Cheung, H.-Y.; Yip, S.; Xiu, F.; Wong, C.-Y.; Ho, J. C., *Adv. Opt. Mater.* **2014**, *2*, 855-860.
62. Zhao, Z.; Cao, Y.; Cai, Y.; Yang, J.; He, X.; Nordlander, P.; Cremer, P. S., *ACS Nano* **2017**, *11*, 6594-6604.
63. Ogier, R.; Fang, Y.; Svedendahl, M.; Johansson, P.; Käll, M., *ACS Photonics* **2014**, *1*, 1074-1081.
64. Wang, L.; Ai, B.; Möhwald, H.; Yu, Y.; Zhang, G., *Adv. Opt. Mater.* **2016**, *4*, 906-916.
65. Chien, Y.-H.; Wang, C.-H.; Liu, C.-C.; Chang, S.-H.; Kong, K. V.; Chang, Y.-C., *ACS Appl. Mater. Interfaces* **2017**, *9*, 24917-24925.
66. Deckman, H. W.; Dunsmuir, J. H., *Appl. Phys. Lett.* **1982**, *41*, 377-379.
67. Hulteen, J. C.; Duyne, R. P. V., *J. Vac. Sci. Technol.* **1995**, *13*, 1553-1558.
68. Gao, P.; He, J.; Zhou, S.; Yang, X.; Li, S.; Sheng, J.; Wang, D.; Yu, T.; Ye, J.; Cui, Y., *Nano Lett.* **2015**, *15*, 4591-4598.
69. Haynes, C. L.; McFarland, A. D.; Smith, M. T.; Hulteen, J. C.; Van Duyne, R. P., *J. Phys. Chem. B* **2002**, *106*, 1898-1902.
70. Choi, Y.; Hong, S.; Lee, L. P., *Nano Lett.* **2009**, *9*, 3726-3731.
71. Chandramohan, A.; Sibirev, N. V.; Dubrovskii, V. G.; Petty, M. C.; Gallant, A. J.; Zeze, D. A., *Sci. Rep.* **2017**, *7*, 40888.
72. Tabatabaei, M.; Sangar, A.; Kazemi-Zanjani, N.; Torchio, P.; Merlen, A.; Lagugné-Labarthe, F., *J. Phys. Chem. C* **2013**, *117*, 14778-14786.
73. Lotito, V.; Zambelli, T., *Langmuir* **2016**, *32*, 9582-9590.
74. Garreau, A.; Tabatabaei, M.; Hou, R.; Wallace, G. Q.; Norton, P. R.; Lagugné-Labarthe, F., *J. Phys. Chem. C* **2016**, *120*, 20267-20276.
75. Fayyaz, S.; Tabatabaei, M.; Hou, R.; Lagugné-Labarthe, F., *J. Phys. Chem. C* **2012**, *116*, 11665-11670.
76. Cheng, X. R.; Wallace, G. Q.; Lagugné-Labarthe, F.; Kerman, K., *ACS Appl. Mater. Interfaces* **2015**, *7*, 4081-4088.
77. Wallace, G. Q.; Tabatabaei, M.; Lagugné-Labarthe, F., *Can. J. Chem.* **2014**, *92*, 1-8.
78. Wang, J.; Duan, G.; Li, Y.; Liu, G.; Cai, W., *ACS Appl. Mater. Interfaces* **2014**, *6*, 9207-9213.
79. Chen, K.; Rajeeva, B. B.; Wu, Z.; Rukavina, M.; Dao, T. D.; Ishii, S.; Aono, M.; Nagao, T.; Zheng, Y., *ACS Nano* **2015**, *9*, 6031-6040.
80. Wu, Z.; Chen, K.; Menz, R.; Nagao, T.; Zheng, Y., *Nanoscale* **2015**, *7*, 20391-20396.

81. Wu, Z.; Kelp, G.; Yogeesh, M. N.; Li, W.; McNicholas, K. M.; Briggs, A.; Rajeeva, B. B.; Akinwande, D.; Bank, S. R.; Shvets, G.; Zheng, Y., *Nanoscale* **2016**, *8*, 18461-18468.
82. Wu, Z.; Zheng, Y., *Adv. Opt. Mater.* **2017**, *5*, 1700034.
83. Cooper, C. T.; Rodriguez, M.; Blair, S.; Shumaker-Parry, J. S., *J. Phys. Chem. C* **2015**, *119*, 11826-11832.
84. Flynn, J. D.; Haas, B. L.; Biteen, J. S., *J. Phys. Chem. C* **2016**, *120*, 20512-20517.
85. Hoffmann, J. M.; Yin, X.; Richter, J.; Hartung, A.; Maß, T. W. W.; Taubner, T., *J. Phys. Chem. C* **2013**, *117*, 11311-11316.
86. Guisbiers, G.; Mendoza-Cruz, R.; Bazán-Díaz, L.; Velázquez-Salazar, J. J.; Mendoza-Perez, R.; Robledo-Torres, J. A.; Rodriguez-Lopez, J.-L.; Montejano-Carrizales, J. M.; Whetten, R. L.; José-Yacamán, M., *ACS Nano* **2016**, *10*, 188-198.
87. Aouani, H.; Rahmani, M.; Šípová, H.; Torres, V.; Hegnerová, K.; Beruete, M.; Homola, J.; Hong, M.; Navarro-Cía, M.; Maier, S. A., *J. Phys. Chem. C* **2013**, *117*, 18620-18626.
88. Lehmann, F.; Richter, G.; Borzenko, T.; Hock, V.; Schmidt, G.; Molenkamp, L. W., *Microelectron. Eng.* **2003**, *65*, 327-333.
89. Manfrinato, V. R.; Stein, A.; Zhang, L.; Nam, C.-Y.; Yager, K. G.; Stach, E. A.; Black, C. T., *Nano Lett.* **2017**, *17*, 4562-4567.
90. Andrade, G. F. S.; Hayashi, J. G.; Rahman, M. M.; Salcedo, W. J.; Cordeiro, C. M. B.; Brolo, A. G., *Plasmonics* **2013**, *8*, 1113-1121.
91. Bellido, E. P.; Manjavacas, A.; Zhang, Y.; Cao, Y.; Nordlander, P.; Botton, G. A., *ACS Photonics* **2016**, *3*, 428-433.
92. Hobbs, R. G.; Manfrinato, V. R.; Yang, Y.; Goodman, S. A.; Zhang, L.; Stach, E. A.; Berggren, K. K., *Nano Lett.* **2016**, *16*, 4149-4157.
93. Kelly, K. L.; Coronado, E.; Zhao, L. L.; Schatz, G. C., *J. Phys. Chem. B* **2003**, *107*, 668-677.
94. Payne, E. K.; Shuford, K. L.; Park, S.; Schatz, G. C.; Mirkin, C. A., *J. Phys. Chem. B* **2006**, *110*, 2150-2154.
95. Moskovits, M., *Rev. Mod. Phys.* **1985**, *57*, 783-826.
96. Le Ru, E. C.; Etchegoin, P. G., *Chem. Phys. Lett.* **2006**, *423*, 63-66.
97. Jensen, L.; Aikens, C. M.; Schatz, G. C., *Chem. Soc. Rev.* **2008**, *37*, 1061-1073.
98. Félidj, N.; Truong, S. L.; Aubard, J.; Lévi, G.; Krenn, J. R.; Hohenau, A.; Leitner, A.; Aussenegg, F. R., *J. Chem. Phys.* **2004**, *120*, 7141-7146.
99. Tabatabaei, M.; Najiminaini, M.; Davieau, K.; Kaminska, B.; Singh, M. R.; Carson, J. J. L.; Lagugné-Labarthe, F., *ACS Photonics* **2015**, *2*, 752-759.

100. Maitani, M. M.; Ohlberg, D. A. A.; Li, Z.; Allara, D. L.; Stewart, D. R.; Williams, R. S., *J. Am. Chem. Soc.* **2009**, *131*, 6310-6311.
101. Silverman, S., *J. Opt. Soc. Am.* **1948**, *38*, 989-989.
102. McIntosh, A. L.; Wofford, B. A.; Lucchese, R. R.; Bevan, J. W., *Infrared Phys. Technol.* **2001**, *42*, 509-514.
103. Childs, D. T. D.; Hogg, R. A.; Revin, D. G.; Rehman, I. U.; Cockburn, J. W.; Matcher, S. J., *Appl. Spectrosc. Rev.* **2015**, *50*, 822-839.
104. Marcelli, A.; Cinque, G., Chapter 3 Infrared Synchrotron Radiation Beamlines: High Brilliance Tools for IR Spectromicroscopy. In *Biomedical Applications of Synchrotron Infrared Microspectroscopy: A Practical Approach*, The Royal Society of Chemistry: 2011; pp 67-104.
105. Miller, L. M.; Smith, R. J., *Vib. Spectrosc.* **2005**, *38*, 237-240.
106. Neuman, T.; Huck, C.; Vogt, J.; Neubrech, F.; Hillenbrand, R.; Aizpurua, J.; Pucci, A., *J. Phys. Chem. C* **2015**, *119*, 26652-26662.
107. Brown, L. V.; Yang, X.; Zhao, K.; Zheng, B. Y.; Nordlander, P.; Halas, N. J., *Nano Lett.* **2015**, *15*, 1272-1280.
108. Langreth, D. C., *Phys. Rev. Lett.* **1985**, *54*, 126-129.
109. Priebe, A.; Pucci, A.; Otto, A., *J. Phys. Chem. B* **2006**, *110*, 1673-1679.
110. Fano, U., *Phys. Rev.* **1961**, *124*, 1866-1878.
111. Vogt, J.; Huck, C.; Neubrech, F.; Toma, A.; Gerbert, D.; Pucci, A., *Phys. Chem. Chem. Phys.* **2015**, *17*, 21169-21175.

Chapter 3

3 Achieving High Hot-Spot Densities in Anisotropic Nanostructures Compatible with Plasmon-Enhanced Spectroscopies

The design and fabrication of metallic nanostructures that exhibit tailored optical resonances is a requirement for plasmon-enhanced spectroscopies. To enable the detection of an analyte located near the surface of the structure, a large local enhancement of the electromagnetic field is required. The degree of this enhancement varies on the spectroscopic technique, but, more importantly, on the nature of the plasmonic nanostructures. Depending on the spectroscopic technique of interest, these resonances need to be in specific spectral domains. Surface-enhanced Raman spectroscopy, and surface-enhanced fluorescence, commonly rely on resonances in the visible to near-infrared spectral regions. Expanding resonances into the mid-infrared can lead to compatibility with surface-enhanced infrared absorption. To modify the spectral location of the resonances, the nanostructures can be modified by altering the metal composition, size and shape of the structure, and the refractive index of the surrounding material. This Chapter explores how the configuration of the nanostructures influences the resulting plasmonic properties. Prepared by electron-beam lithography, two different base unit structures (nanorods, and nanoprisms) are fabricated into different array geometries. The different configurations are then evaluated for their compatibility in the visible through mid-infrared spectral regions, along with the corresponding plasmon-enhanced techniques.

3.1 Introduction

With plasmon-enhanced techniques becoming more relevant for a variety of applications ranging from ultra-sensitive sensing to high spatial resolution spectroscopy,¹⁻¹² the development of plasmonic structures with tailored optical properties has become of greater importance. The greatest challenge in this field is to ensure that the localized surface plasmon resonances (LSPRs) of the nanostructure are in resonance or pre-resonance conditions with the excitation wavelength corresponding to the optical process

of interest. The visible region is the dominant spectral domain of interest as plasmon-enhanced techniques such as surface-enhanced Raman spectroscopy (SERS), and surface-enhanced fluorescence (SEF), most often rely on visible excitations. If the nanostructures support LSPRs in the mid-infrared, measurements involving surface-enhanced infrared absorption (SEIRA) can be performed. Other techniques, including non-linear optical processes, such as coherent anti-Stokes Raman spectroscopy and sum frequency generation can benefit from plasmon-mediated enhancement.¹³ This electromagnetic (EM) enhancement is localized to nanoscale regions, known as hot-spots, that are found at the surface of the structure.¹⁴ In addition to EM enhancement, chemical enhancement will also aid in the detection of analytes adsorbed surface of the nanostructure.¹⁵ However, chemical enhancement is analyte dependent,¹⁶ whereas EM is not. Therefore, exploring the development of plasmonic nanostructures is the necessary first step before examining applications involving plasmonic nanostructures.¹⁷

The EM enhancement from the generation of hot-spots is related to multiple factors, including various structural parameters associated with the nanostructure. First is the nature of the material to be used. Although silver and gold are by far the most common, other metals have been shown to be compatible with SERS.¹⁸ The spatial distribution of hot-spots over a nanostructure is most often determined based on the structure's geometry. An incredibly diverse range of nanostructures have been prepared using various bottom-up (synthetic),¹⁹⁻²² and top-down (lithographic) approaches.²³⁻²⁶ By controlling the fabrication methodology, it is possible to prepare nanostructures with particular characteristics such as anisotropy,²⁷⁻²⁸ or to have structures capable of supporting a high density of hot-spots. As the number of hot-spots increases, there exists a greater probability that an analyte of interest will be present, and can therefore be detected. Once a desired shape has been achieved, altering the dimensions of the structure allows for the tuning of the LSPR(s). Changes in the refractive indices of the substrate and/or the surrounding media will alter the spectral position of the LSPR.²⁴ Much like increasing the size of the nanostructure, increasing the refractive index leads to a red-shift. Therefore, it is important to consider both parameters concurrently.

The enhancement is further influenced by the polarization of the impinging light with respect to the symmetry of the structure, and on the considered optical process. Depending on the shape of the structure, the number of resonances and their spectral positions will depend on the polarization of the incident light. Metallic nanorods are a classical example, where gold nanorods with a length of 1410 nm, a height of 55 nm, and a width of 60 nm, support resonances at a wavelength of 5.61 μm when the light is polarized along the length of the rod, and a second resonance at 641 nm when the light is polarized along the width.²⁹ The observed enhancement is also dependent on the technique that is used. The EM enhancement factor for SERS commonly described as $|E/E_0|^4$.³⁰ As a result, a small increase in the ratio of E/E_0 , such as 10, will yield an enhancement of 10^4 . If the ratio is further increased to 100, the generated Raman enhancement will be 10^8 . In the absence of additional electronic resonance effects, the common range of EM enhancement for SERS is 10^4 - 10^8 .³¹⁻³² Meanwhile other processes, such as SEIRA have different enhancement factors ($|E/E_0|^2$),³³ and have different common ranges for reported EM enhancement (10^3 - 10^5).³³ A recent study involving SEIRA antenna calculated an EM enhancement of 10^7 for bowtie-shaped nanostructures with sub-3 nm gaps.³⁴ By tailoring the optical requirements with the dimensions of the nanostructure, it is possible to achieve idealized opto-geometric properties yielding enhancement sufficient for the detection of analytes.

Lithographic fabrication processes, such as electron-beam lithography (EBL), allow for controlling the arrangement of the nanostructures into well-organized patterns and arrays.^{23, 35-38} With a spatial resolution better than 10 nm,³⁹ the position and the density of hot-spots can be controlled. By decreasing the gap between adjacent nanostructures, it is possible to couple the structures along different axes to generate additional enhancement that can be accessed by altering the polarization of the input excitation with respect to the structural symmetry. Furthermore, by incorporating additional structures, the density and total number of hot-spots increases, leading to a stronger average spectroscopic signal. As EBL can fabricate the nanostructures and the arrays with a high degree of precision and reproducibility, the required opto-geometric properties necessary for the selected surface-enhanced technique (SERS, SEF, SEIRA) can be achieved reproducibly.

Herein, we explore the plasmonic properties of a series of nanostructures prepared by EBL that have been arranged into different patterns. Special attention will be placed on the spatial distribution of the hot-spots across the various arrangements of the nanostructures, and how the resulting SERS signal varies from configuration-to-configuration. For this study, two model structures are used: nanorods, and nanoprisms. Since nanorods are most often configured as lines, we begin with this arrangement, and expand the array design to incorporate a second set of nanorods. This yields a linear arrangement of nanorods described a doublet. Since nanoprisms are often arranged as a dimer (commonly referred to as a “bowtie” assembly), we chose here to increase the number of nanoprisms in the ensemble to form a series of multimer configurations. With each subsequent structure, more hot-spots were introduced into the array. To further illustrate the control of hot-spot generation, nanoarrowhead structures were fabricated by superimposing the nanoprisms. Without dramatically altering the optical properties in the visible region, these new structures offered a greater SERS signal than the traditional nanoprisms. Last, using the hexamer configuration of nanoprisms, we demonstrate the fabrication of a Sierpiński Hexagonal Gasket-type fractal. This fractal maintains its plasmonic properties in the visible region associated with the individual hexamers, as evidenced by SEF, while also supporting additional resonances that expand into the near- and mid-infrared.

3.2 Experimental

3.2.1 Materials

Glass microscope cover slips ($22 \times 22 \times 0.15$ mm) were purchased from Fisher Scientific (ON, CAN). Silicon and CaF_2 substrates (13 mm diameter \times 2 mm) were acquired from Spectral Systems LLC (NY, USA). Poly(methyl methacrylate) A2 950 resist and isopropanol were purchased from MicroChem Corp. (MA, USA). AquaSave was obtained from Mitsubishi Rayon America Inc. (NY, USA). Acetone (CHROMASOLV) and 4-nitrothiophenol (4-NTP) were procured from Sigma-Aldrich (MO, USA). Cyanine 5 labelled polyethylene glycol with a thiol (Cy5-PEG-SH, MW 5000 DA) was purchased from Nanocs Inc. (NY, USA).

3.2.2 Electron-Beam Lithography

Glass microscope cover slips, silicon and CaF₂ substrates were cleaned using reactive O₂ plasma for 20 minutes. Details of the process for EBL are described in detail in Appendix C. To maintain the same size as the patch of structures, the Sierpiński Hexagon-like fractal was fabricated such that the total size of the fractal did not exceed 50 × 50 μm². Scanning electron micrographs of the structures were then obtained using the Leo Zeiss 1530 SEM used to prepare the structures by EBL.

3.2.3 Visible to Near-Infrared Absorption

The set-up for obtaining the visible to near-infrared absorption spectra is described in 2.4.1 and shown in Figure 2.10. An acquisition time of 1 second per spectrum was used. Each spectrum shown is the result of 50 accumulations.

3.2.4 Near- to Mid-Infrared Absorption

Fourier transform infrared (FT-IR) spectroscopy measurements were performed at the Mid-IR beamline synchrotron facility located at the Canadian Light Source (Beamline 01B-01). Information regarding the set-up at the beamline end station is provided in 2.5.2 and Figure 2.13. The apertures size chosen (1.5) allowed for the beam diameter to be slightly smaller than the 50 × 50 μm² patch. Measurements were collected from 8000-800 cm⁻¹ with a spectral resolution of 4 cm⁻¹. Each spectrum is the average of 512 spectra.

3.2.5 Surface-Enhanced Raman Measurements

Samples were functionalized in a 10⁻³ M solution of 4-NTP prepared in ethanol for 24 hours. Information regarding the Raman spectrometer used is provided in 2.4.2 and Figure 2.11. A helium neon laser (λ = 632.8 nm, power of ~500 μW at the sample) or a near-infrared laser (λ = 785 nm, power of ~1.5 mW at the sample) were used as excitation sources, and a 100× (NA = 0.9) objective was used to collect the back scattered light. An acquisition time of 10 seconds per spectrum was used for all measurements.

3.2.6 Surface-Enhanced Fluorescence Measurements

Samples were functionalized in a 10^{-5} M solution of Cy5-PEG-SH prepared in Milli-Q water for 24 hours. Fluorescence imaging was performed with a Zeiss LSM 510 META Multiphoton Confocal Laser Scanning Microscope. A helium neon laser ($\lambda = 632.8$ nm) along with a $63\times$ (N.A. = 0.75) objective was used, with the scanning area for the image set to 512×512 . The fluorescence images were obtained by examining the emission of the dye from 650-700 nm using the fluorescence microscope.

3.2.7 Electromagnetic Field Modelling

Idealized and dimensions based on those observed after fabrication were used for finite-difference time-domain (FDTD) modelling (Lumerical). CRC dielectric values for gold and titanium were used. Periodic boundaries conditions were used on the x and y axes, and perfectly matched layer (PML) was used in the z axis.

3.3 Results and Discussion

3.3.1 Singlet and Doublet Nanorods

As a plasmonic nanostructure of interest, metallic nanorods have been used for a variety of plasmon-mediated techniques including SERS,^{1, 7, 40} SEF,^{3, 6, 41} SEIRA,⁴²⁻⁴⁴ and plasmonic circular dichroism.^{8, 45} Preparing nanostructures by lithographic techniques allows for reproducible fabrication and greater control of the structures dimensions. Nanorods have been prepared by a variety of procedures, such as direct laser writing,⁴⁶⁻⁴⁷ nanoimprint,⁴⁸⁻⁴⁹ and nanostencil lithographies.⁵⁰⁻⁵¹ For this study, electron-beam lithography (EBL) was used to prepare the nanostructures because of it offers a high resolution (~ 10 nm), and is a template-free approach allowing for a wide arrange of configurations and parameters to be prepared without having to make a large quantity of masks or stencils. Nanorods are commonly prepared as isolated nanostructures, or in a single line with a narrow gap between adjacent structures. We will use the term singlet to describe the latter configuration (Figure 3.1A). Different configurations of nanorods have been explored for different applications, however, we have chosen to just explore a

doublet configuration (Figure 3.1B). In the doublet, a second nanorod is placed with a small gap next to the nanorods of the singlet.

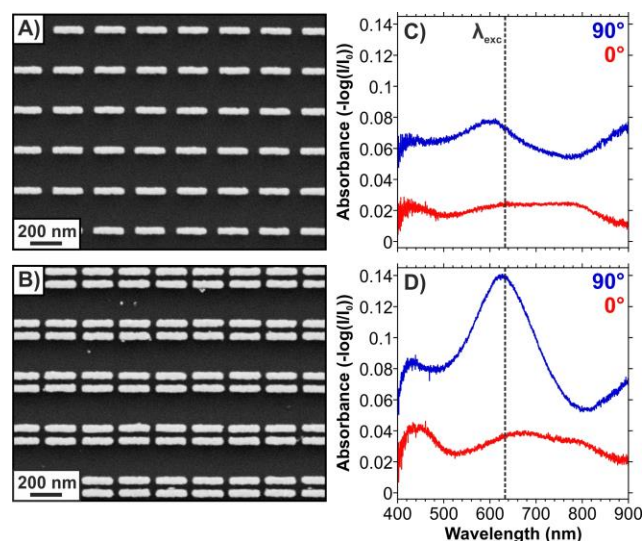


Figure 3.1 SEM images of gold nanorods arranged as A) singlets, and B) doublets. C) and D) are the corresponding visible to near-IR absorbance spectra of the nanorods at orthogonal polarizations, where 0° matches the long axis of the nanorods.

Nanorods are inherently anisotropic structures, and therefore, the LSPRs exhibit a polarization dependence (Figure 3.1C). When the impinging light is polarized along the long axis of the nanorod (0°), a broad combination of resonances is observed spanning from nearly 500 to 850 nm. This is likely the result of less discrete higher-order plasmonic modes. When the light is polarized perpendicular to the nanorod (90°), a distinct mode near 600 nm was observed. The absorbance spectra for the parallel excitation of the doublet configuration (Figure 3.1D), is similar to the singlet (Figure 3.1C), though the absorbance is marginally higher. However, for the perpendicular polarization, the weak resonance near 600 nm for the singlet (Figure 3.1C) becomes significantly stronger and shifts closer to 620 nm (Figure 3.1D).

To correlate the spatial distribution of the resonances with the spectral response of the structure, a series of FDTD calculations were performed. As the purpose of these structures was for visible spectroscopies, and an excitation wavelength of 633 nm was to

be used, this wavelength was chosen for all calculations (Figure 3.2A-D). For the calculations, the following parameters were used: length of 200 nm, width of 60 nm, height composed of 3 nm of Ti and 20 nm of Au, and a gap of 30 nm between adjacent nanorods. For a polarization along the length of the nanorods, very little enhancement of the EM field was observed for the singlet (Figure 3.2A) or doublet (Figure 3.2B) configurations. This is consistent with the absorbance spectra of Figure 3.1C and D, where no significant resonances were observed near 633 nm. The EM fields for the polarization along the width do show local enhancement near the apices of the nanorods, with additional enhancement along the outer edges of the nanorods. Figure 3.2C, corresponding to the singlets, shows similar enhancement relative to the doublet configuration (Figure 3.2D). Based on the EM field maps, it appears that a doublet configuration of nanostructures is preferable to the traditional singlet configuration as the second row of nanorods introduces twice the number of hot-spots as seen by the greater number of red regions. Additionally, there is a slight increase in the intensity of the enhancement due to slight coupling between the adjacent nanostructures due to the small gap (30 nm). Further decreasing of this gap may lead to greater coupling of the nanostructures.

After functionalizing the surface of the nanorods a SERS reporter (4-nitrothiophenol, 4-NTP), the different configurations were tested under distinct polarization excitations. The concentration used (10^{-3} M) is sufficient to form a self-assembled monolayer over the gold surfaces. The SERS spectra obtained using both polarizations are found in Figure 3.2E for the singlets, and in Figure 3.2F for the doublets. Compared to the spectra obtained on flat gold (dotted spectra), the spectra obtained on the nanostructures clearly show an enhanced signal. The well-defined peaks at 1078, 1333, 1570 cm^{-1} correspond to the S–C stretching, symmetric NO_2 stretching, and C=C stretching respectively.^{4, 52} Minimal SERS enhancement was measured using a polarization of 0° as expected from results of the EM calculations.

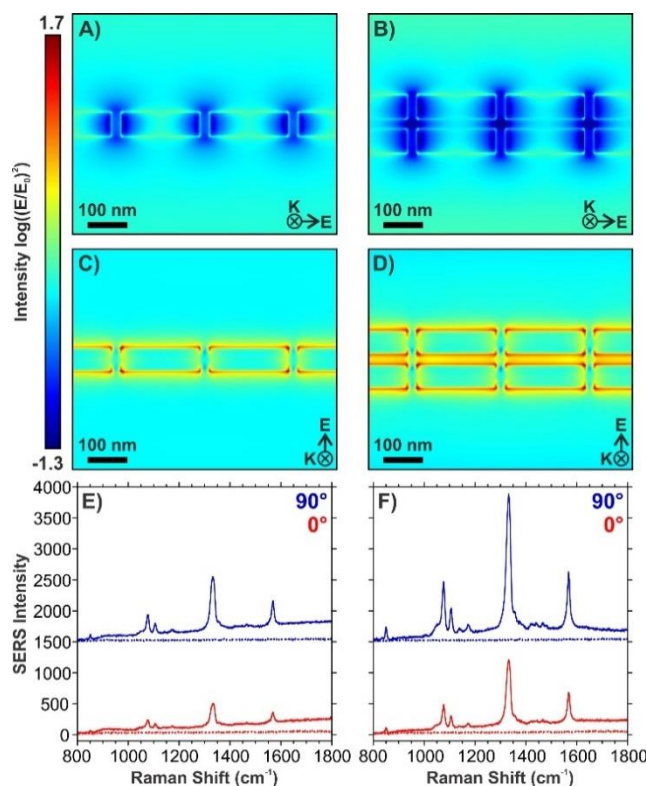


Figure 3.2 FDTD calculations for singlet and doublet configurations under polarizations that are A) and B) parallel (0°), and C) and D) perpendicular (90°) to the long axis of the nanorods. The SERS spectra correspond to 4-NTP functionalized E) singlets, and F) doublets. The colours correspond to the orthogonal polarizations of light. The dotted spectra were obtained on 4-NTP functionalized flat gold.

Comparing the obtained results from the singlets and doublets shows trends consistent with what is expected based on the FDTD calculations. The second set of nanorods in the doublet introduces twice the number of structures. Since the corners of the nanorods yield the greatest nanoscale enhancement, doubling the number of structures similarly doubles the number of hot-spots. This is further evidenced in the SERS spectra (Figure 3.2E, F) where the doublet has an average intensity that is better than double the average intensity of the singlet. It was previously demonstrated by D'Andrea *et al.* that gold nanorods exhibit multispectral compatibility, enabling analyte detection by SERS and SEIRA.²⁹ Subsequent studies have focused on optimizing the SEIRA enhancement of the nanorods.⁵³⁻⁵⁴ However, it is unknown if these changes have improved the SERS

enhancement above the initial results (5×10^2).²⁹ Our proposed doublet configuration marginally improves the SERS EM enhancement (10^3), but more importantly, provides a means of increasing the SERS response and sharper resonances. This is a critical design parameter to further improve the detection of analytes located on such a surface of a structure, especially if the structure can be used with correlative spectroscopies.

3.3.2 Multimer Configurations of Nanoprisms

Much like the nanorods, metallic nanoprisms are a commonly prepared nanostructure for plasmon-enhanced techniques.^{2, 9, 38} Arguably the most common configuration is a dimer (bow-tie, Figure 3.3A), as this configuration can be readily prepared by different lithographic techniques, such as EBL, and nanosphere lithography.^{2, 9, 55-57} Fabrication by EBL offers the option of preparing the nanoprisms in different configurations. To this end, we have prepared arrays of plasmonic nanoprisms in configurations ranging from dimers to hexamers (Figure 3.3A-E). Each configuration was placed into a $50 \times 50 \mu\text{m}^2$ patch, where a fixed number of patterns (1444) were prepared, and as evidenced in the SEM images, were well spaced from one another. Unlike the nanorods where the lines of structures were placed close together to enable coupling between the nanorods, the large spacing was chosen to avoid any plasmonic coupling between adjacent arrays and minimize any contributions from other arrays when performing SERS measurements. Visible to near-IR microspectroscopy measurements were performed to identify the spectral position of the LSPR(s) of the structure (Figure 3.3F-J). Beginning with the dimer configuration, a well-defined resonance was observed near 800 nm. Due to the size of the nanoprisms, it was believed that this corresponds to the dipolar resonance of the structures. As well, a small shoulder near 650 nm was also observed, and is assigned as a higher-order mode (quadrupolar). It was observed that as the number of nanoprisms increased, higher-order mode was minimally affected, whereas the dipolar resonance became broader (Figure 3.3H-J). The broadness is the result of the superimposition of two resonances and is best shown in the spectrum of the hexamer configuration (Figure 3.3J). The inset SEM images clearly show that as the number of nanoprisms increases in the array, the gap between adjacent nanoprisms decreases. This decrease in the gap likely

leads to secondary coupling between the nanostructures, resulting in the presence of a new lower energy peak.

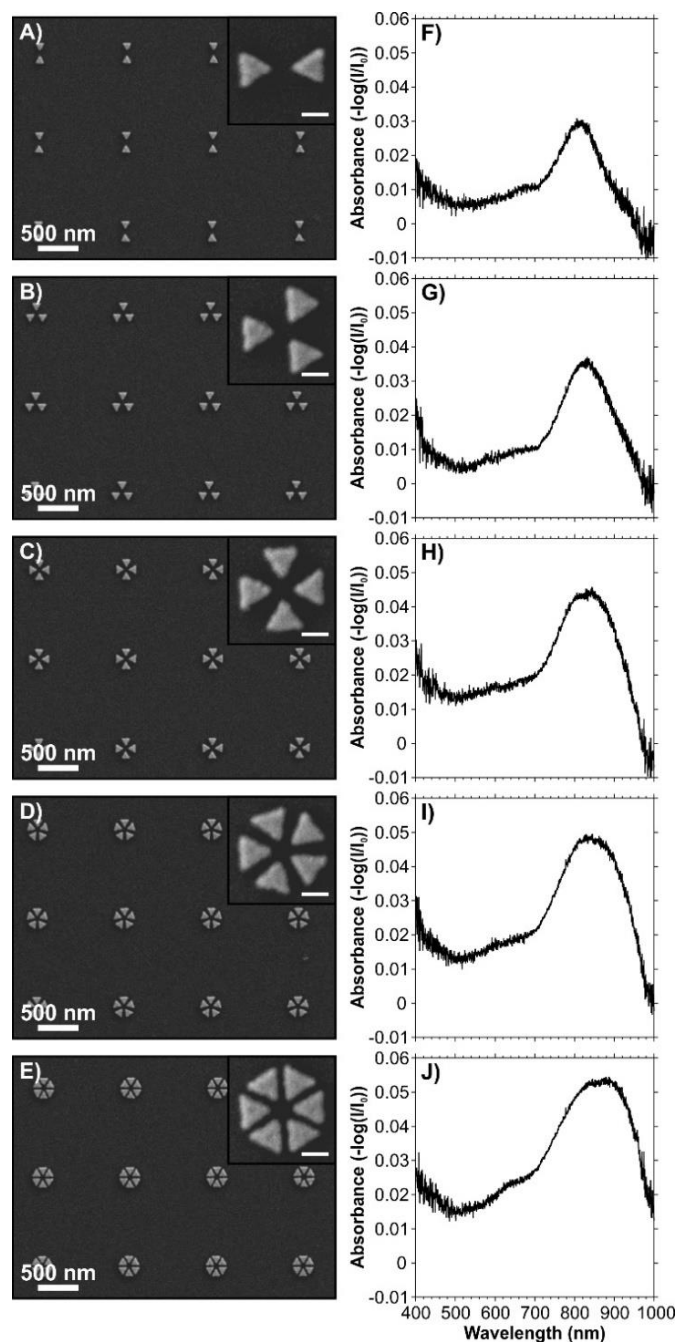


Figure 3.3 SEM images of gold nanoprisms with side lengths of 125 nm arranged in different configurations, A) dimer, B) trimer, C) tetramer, D) pentamer, and E) hexamer. Corresponding experimental absorption spectra are shown in F-J). The scale bar in the inset SEM images is 100 nm.

Increasing the size of the nanoprisms results in a red-shift of the resonances (Figure 3.4A), and increasing the gap between adjacent nanostructures yields a blue-shift (Figure 3.4B). When working with equilateral nanoprisms (as shown in this study), the gap between the tips of the equatorial nanoprisms is different than the gap between the sides of the adjacent nanoprisms. As the equatorial gap decreases, so will the side gap, and eventually, the sides of the nanoprisms will overlap. By switching to an isosceles nanoprism, it will become possible to have gaps that are closer in size, thus preventing overlap. These design considerations for the nanoprisms should also be considered when preparing array configurations involving a greater number of nanoprisms.

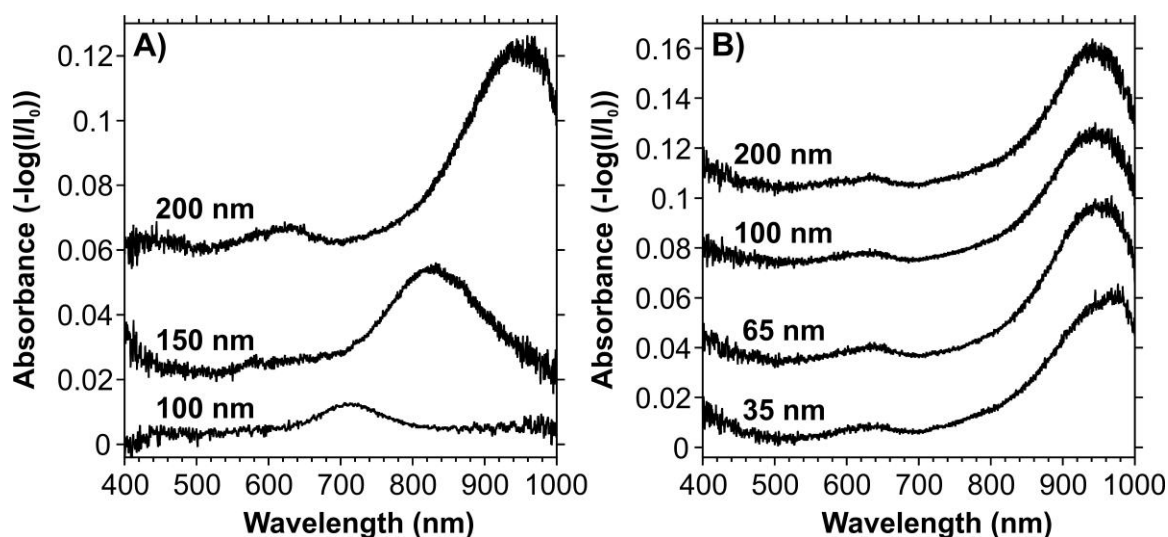


Figure 3.4 A) Absorbance spectra of gold nanoprisms written with specified lengths and arranged in trimer configurations. The pattern was written with a gap of 50 nm. B) Absorbance spectra of gold nanoprisms written with varying gap sizes, fixed side lengths of 200 nm, and arranged in dimer configurations.

To visualize the spatial distribution of the hot-spots across the nanostructures, FDTD calculations were performed on the various array configurations based on the experimentally observed lengths and gaps (Figure 3.5). For the calculations, only a horizontal polarization is considered for the EM field maps as this is the ideal optogeometric alignment for the dimer configuration. The spatial distribution of the hot-spots for the dimer configuration at the wavelength for the dominant resonance is consistent with a dipolar mode. Consistent with multibranch structures,²⁵ increasing the

number of nanoprisms introduces a greater number of hot-spots across the surface of the structure (Figure 3.5A-E). Furthermore, consistent with the broadening observed in the absorbance spectra, coupling is clearly observed between the adjacent nanoprisms for the pentamer and hexamer configurations (Figure 3.5D, E). This coupling is important as it leads to an improved EM enhancement (darkest red regions of any EM field maps). The EM field map for the higher energy resonance (720 nm, Figure 3.5F) shows that the distribution of enhancement is predominantly localized to the tips nearest to the center of the pattern.

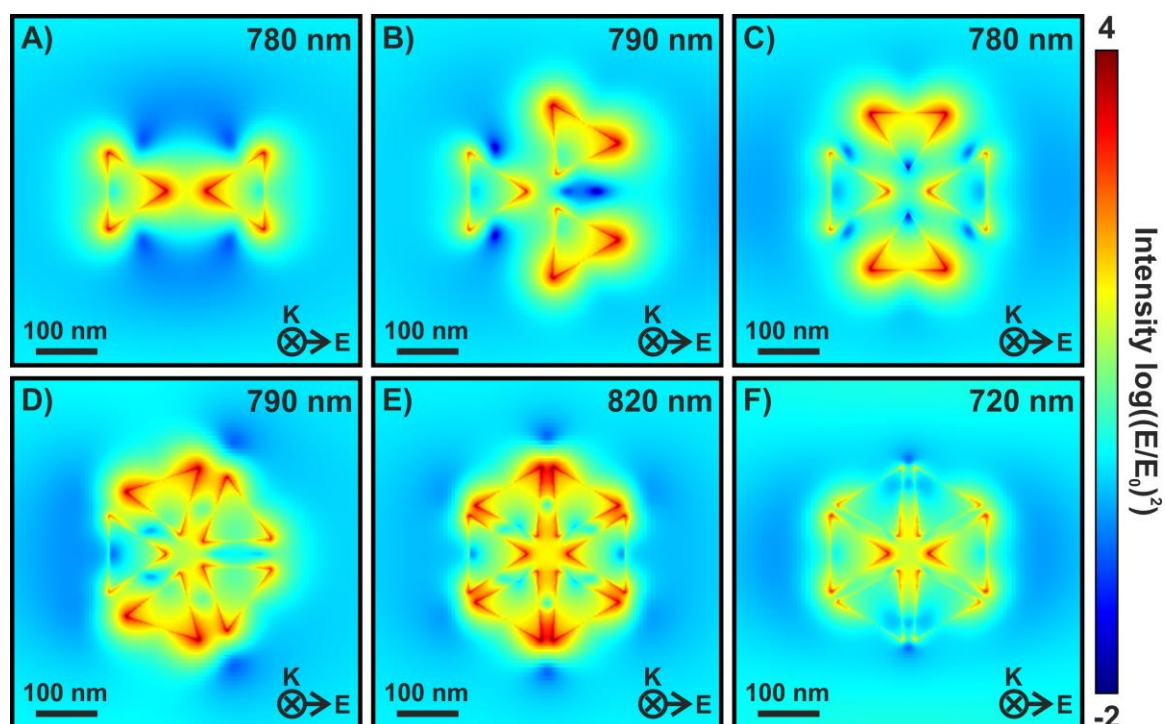


Figure 3.5 FDTD calculations of the electric field $(|E/E_0|)^2$: log scale representation at wavelengths corresponding to the dominant absorption of the gold nanoprisms A) dimer, B) trimer, C) tetramer, D) pentamer, and E) hexamer. F) Electric field at the highest energy resonance of the hexamer. The side lengths of the nanoprisms is 135 nm.

3.3.3 Superimposing Nanoprisms to Generate Nanoarrowheads

In a previous study,³⁸ we demonstrated that the superimposition of arrays large and small nanoprisms can be used to introduce additional resonances and hot-spots in the near- to mid-IR. Here, we show how the superimposition of gold nanoprisms coupled with the pattern configurations can be used to introduce new resonances in the visible to near-IR, and more importantly, generate additional hot-spots. Interestingly, a similar type of structure, though exclusively prepared as a dimer, can also be fabricated using nanosphere lithography.⁵⁶ These new nanostructures are described as nanoarrowheads with double or triple corresponding to the number of nanoprisms used in the preparation of the arrowhead.

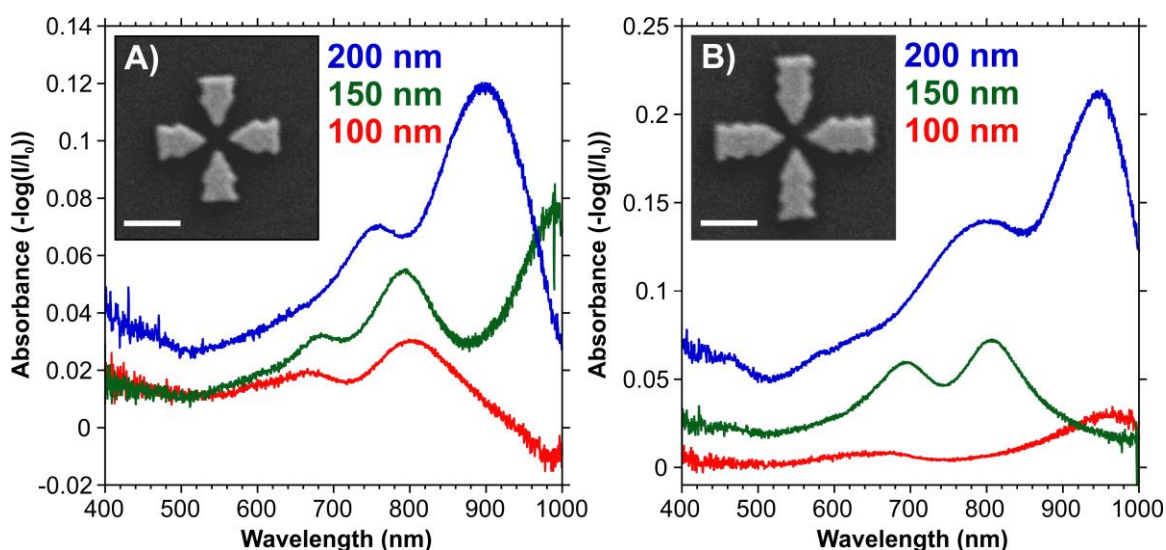


Figure 3.6 Absorbance spectra for A) double, and B) triple nanoarrowheads. The lengths mentioned refer to the side lengths of the nanoprisms used to prepare the arrowheads. The inset SEM images correspond to the double and triple nanoarrowheads written with the nanoprisms having a side length of 150 nm. The scale bar in the inset SEM images is 200 nm.

Examples of the resulting nanoarrowheads are shown in the SEM inset images of Figure 3.6. The side lengths reported refer to the side lengths used in the individual nanoprisms that were superimposed. The corresponding absorbance spectra for arrays of double arrowheads (Figure 3.6A) and triple arrowheads (Figure 3.6B), shown that the structures

exhibit multiple resonances in the visible to near-IR. For the 150 nm double arrowhead, three modes were observed from 500 to 1000 nm. Increasing the size resulted in only two of the resonances appearing due to the red-shift of the resonances. By adding in another nanoprism and forming the triple arrowhead (Figure 3.6B), only two modes were ever observed, with minimal shift differences between resonances of the double and triple arrowheads.

To understand the relationship between the spatial geometry of the arrowheads and the position of the resonances, FDTD calculations were performed (Figure 3.7). Since only two resonances were observed from 500 to 1000 nm, we chose to expand the range of the FDTD calculations to 1500 nm to determine if additional resonances were present. Interestingly, the EM field maps for the double and triple arrowheads show nearly identical spatial distributions for the hot-spots. At the highest-energy resonance (Figure 3.7A, D), the EM enhancement is highly localized to just the tips of the nanoprisms of the arrowheads. The second resonance (Figure 3.7B, E) has the dominant enhancement from the tips and sides of the outermost nanoprisms, along with some contributions from the tips of the inner nanoprisms. The lowest energy resonance (Figure 3.7C, F) exhibits a distribution that incorporates the apex of the inner nanoprisms with the apices and edges of the outermost nanoprisms. No significant contribution from the central nanoprism in the triple arrowhead was observed. This resonance can be described as the global resonance of the arrowhead and is therefore most susceptible to change by increasing the number of nanoprisms. As the number of nanoprisms in the arrowhead increases, so does the overall size, resulting in a significant red-shift in the position of the LSPR. With a sufficient number of nanoprisms, this resonance could be shifted into the mid-IR, and could then be used for applications involving SEIRA. Furthermore, the addition of more nanoprisms would likely also lead to the formation of additional resonances in the near-to mid-IR. This effect was previously observed for microwave antennae-like structures, where by tuning the dimensions of the protrusions, like the tips of the nanoprisms, the number and spectral position of the resonances could be tuned. Such structures were shown to exhibit optical properties compatible with linear and non-linear optical processes spanning the visible through mid-infrared spectral regions.^{37, 58-59}

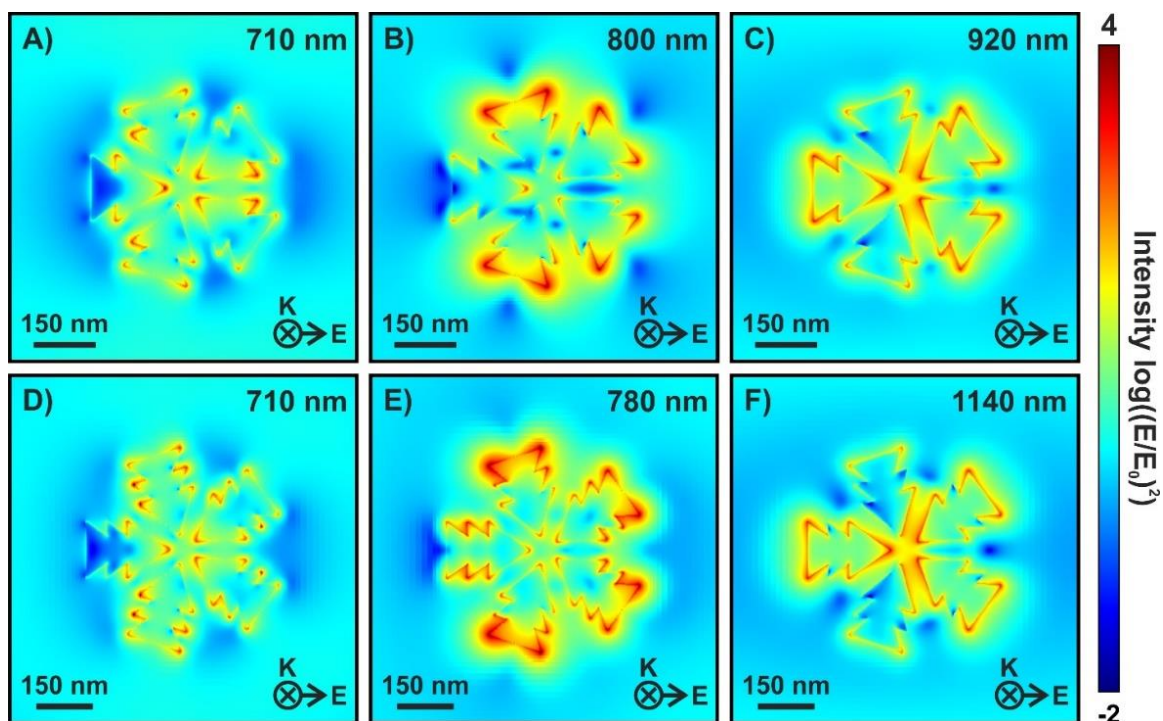


Figure 3.7 FDTD calculations of the electric field $(|E/E_0|)^2$: log scale representation at wavelengths corresponding to the absorptions for A-C) double and D-F) triple nanoarrowheads prepared in a pentamer configuration. The side lengths of the nanoprisms of the arrowheads are 135 nm.

Importantly, the highest energy resonances exhibit the greatest number of hot-spots. These hot-spots could then be used to enhance the signal from a spectroscopic technique, such as SERS. The spectral position of the resonances also lends themselves to the excitation wavelengths ($\lambda = 633, 785 \text{ nm}$) that are common for SERS studies. The lowest energy resonance could potentially be used for SERS with wavelengths in the near-IR, however, this was beyond the scope of this work.

3.3.4 Response of Multimer Configurations

As was done for the singlet and doublet nanorods, the arrays of nanoprisms and nanoarrowheads were functionalized in a 10^{-3} M solution of 4-NTP. The averaged SERS spectra of Figure 3.8 indicate that the nanoprisms and nanoarrowheads prepared using side lengths of 135 nm are SERS active for both 633 and 785 nm excitations. This is verified by comparing to regions of functionalized flat gold, where no signal related to

the 4-NTP was observed. Relative to the classical configuration of dimers, the trimer through hexamer arrangements offer an improved SERS signal. As we have described for the nanoprisms and nanoarrowheads, increasing the number of structures results in a greater number of hot-spots. It has previously been shown that for silver nanoprisms that 98% of the SERS signal is related to just 2% of the total molecules.⁶⁰ Thus, increasing the number of hot-spots will increase the likelihood that more molecules will be enhanced, leading to a stronger SERS signal. Based on the results of Figure 3.8, the ideal configurations for SERS appears to be the tetramer through hexamer arrangements. Increasing the number of structures is also beneficial as the polarization dependence will decrease. The SERS measurements for the trimer and pentamer configurations are also promising for further study. A trimer-like configuration of nanoprisms has previously shown compatibility with plasmon-enhanced second harmonic generation.⁶¹

The multiwavelength compatibility of the nanostructures (Figure 3.8), coupled with the differences in the hot-spot distribution (Figure 3.7), may lead to other areas of study. Of note is photochemical and plasmon-mediated chemical reactions. The SERS experiments of Figure 3.8 show not only the characteristic peaks of 4-NTP, but also peaks because of the dimerization of 4-NTP, resulting in the formation of an azo group and the molecule 4,4'-dimercaptoazobenzene (1140, 1390, and 1435 cm^{-1}).⁶²⁻⁶³ The use of plasmon-mediated chemistry can also be used to drive the selective surface functionalization of analytes.⁶⁴ By using different excitation wavelengths, it may be possible to locally functionalize different analytes at different positions of the nanostructures. The nanoarrowheads are especially well suited for this technique as they show strong SERS responses for both 633 and 785 nm. By introducing a series of molecules that can interact with specific target analyte, it would be possible to perform multiplexing measurements on a single array. Additionally, if the grafted molecule is capable of undergoing plasmon-mediated polymerization, the polymerized analyte will increase the width and height of the AFM image only in the areas where the hot-spots are present.⁶⁴ This would provide a means of experimentally identifying the spatial distribution of hot-spots of complex multiwavelength compatible nanostructures. Alternatively, mapping the surface by tip-enhanced Raman spectroscopy (TERS) can also be used to experimentally determine the spatial distribution of the hot-spots across the nanostructures.⁶⁵

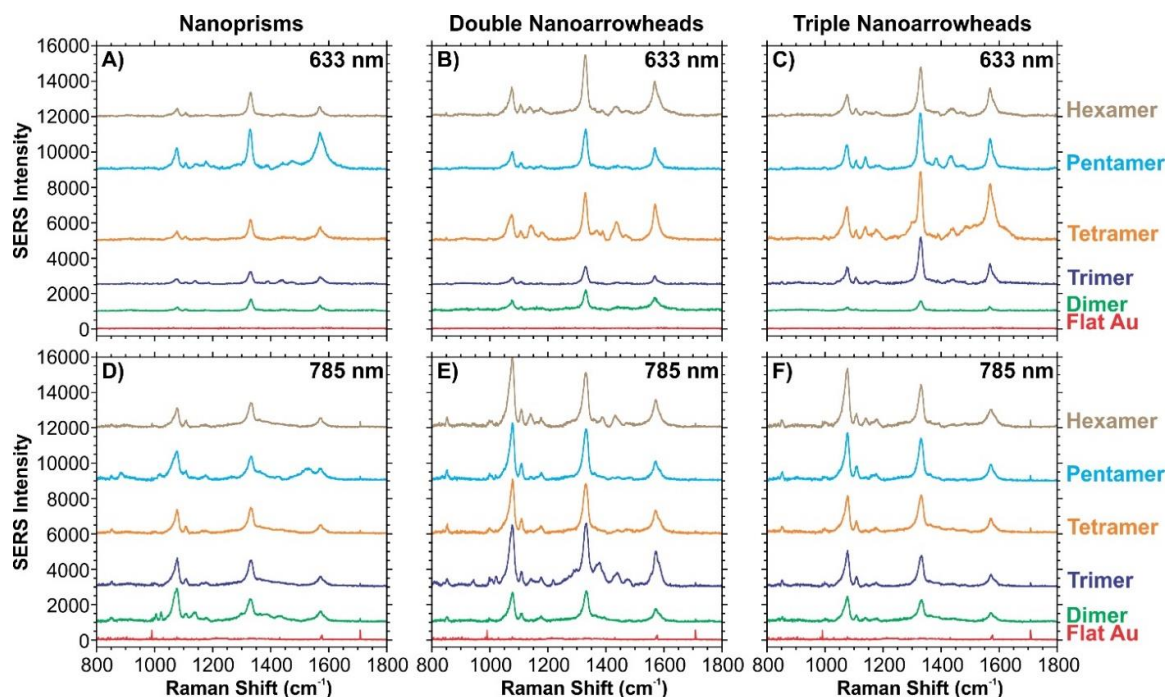


Figure 3.8 SERS measurements performed on nanoprisms and nanoarrowheads with side lengths of 135 nm functionalized in a 10^{-3} M solution of 4-NTP. The spectra in A-C) were acquired with an excitation wavelength of 633 nm, and D-F) used an excitation of 785 nm.

3.3.5 Sierpiński Hexagonal Gasket

One of the current challenges in the fabrication of plasmonic structures and devices, is the introduction of resonances that span broad spectral domains. For instance, to perform SERS and SEIRA measurements, resonances must be present in the visible and mid-infrared spectral regions. Gold nanorods,²⁹ superimposed arrays of nanoprisms,³⁸ and highly tuned optical antennae have been previously prepared to have both SERS and SEIRA compatibility.⁵⁸ Alternatively, fractal and fractal-like structures can also support resonances that span large spectral domains.^{35, 66-71} By beginning with a base unit structure that is compatible in one spectral region, and then subsequently repeating the base unit, additional resonances at longer wavelengths can be introduced. As we have shown, hexamer configurations of gold nanoprisms can support resonances in the visible and near-IR. To prepare a fractal based on this structure, the hexamers were further arranged into hexagonal configurations, resulting in a fractal that resembles a Sierpiński

hexagonal gasket (Figure 3.9A).⁷² Other configurations could also be considered, such as a Sierpiński carpet using the tetramer configuration,⁷³⁻⁷⁴ and a Sierpiński pentagon with the pentamers. Furthermore, the nanoarrowheads may also be used. Traditionally for the Sierpiński class of fractals, a large structure is subdivided into smaller and smaller structures, yielding multiple generations.⁷⁵⁻⁷⁷

For the fabrication of our Sierpiński hexagonal gasket, we chose to use an iterative approach where the base unit configuration is repeated outwards to form the higher-order generations. This approach was chosen as we had already probed the optical properties of the hexamer configuration. It was also believed that the relatively small nanoprisms prepared in the previous sections would require a significantly high number of generations to introduce mid-IR resonances. Therefore, the outer side lengths of the nanoprisms were increased to 1 μm . Interestingly, even though this size is sufficiently large, resonances were observed in the visible to near-IR (Figure 3.9B). These likely correspond to higher order modes of the nanoprisms. To experimentally visualize the various hot-spots across the surface of the fractal, a sample was functionalized with a fluorophore to perform SEF measurements.

The molecule chosen (Cy5-PEH-SH) had cyanine 5 (Cy5) as the fluorophore, along with a polyethylene glycol (PEG) side chain to spatially offset the Cy5 from the gold surface preventing the effects of quenching from the metal surface, and a thiol (SH) to form a covalent bond to the gold surface. Cy5 was chosen as the fluorophore as it has a maximum absorption band at 650 nm, and an emission centered at 670 nm. This along with the excitation wavelength used ($\lambda = 632.8$ nm) agree with the LSPR of the base unit hexamer configuration. Figure 3.9C shows that an enhanced fluorescence signal is observed (red regions) only in specific locations of the structure. By overlaying the SEF

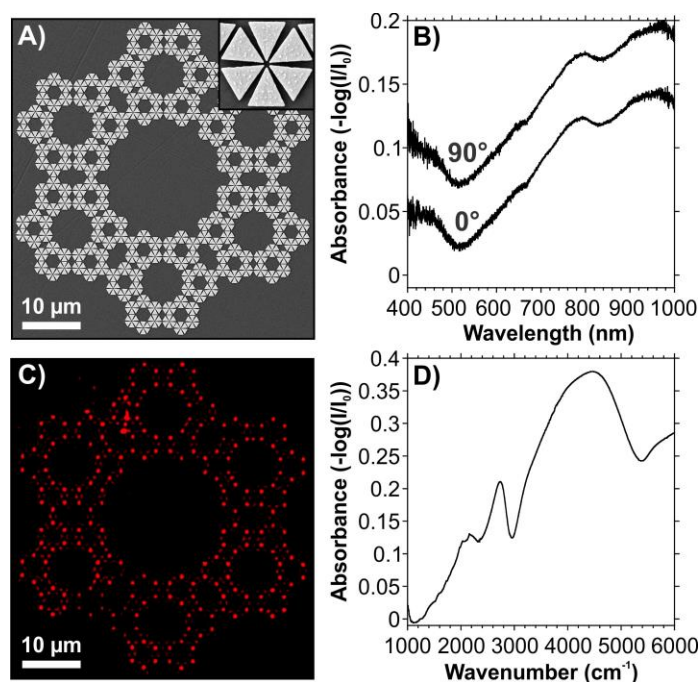


Figure 3.9 A) SEM image of a pseudo-Sierpiński Hexagon fabricated on a silicon substrate. The inset image shows that the base unit hexagon is a hexamer configuration of gold nanoprisms. B) Visible to near-IR absorbance spectra taken at orthogonal polarizations of the fractal prepared on a CaF₂ window. C) SEF image of a functionalized fractal prepared on CaF₂. D) Near-IR to mid-IR absorption spectrum of a non-functionalized fractal on CaF₂.

The molecule chosen (Cy5-PEH-SH) had cyanine 5 (Cy5) as the fluorophore, along with a polyethylene glycol (PEG) side chain to spatially offset the Cy5 from the gold surface preventing the effects of quenching from the metal surface, and a thiol (SH) to form a covalent bond to the gold surface. Cy5 was chosen as the fluorophore as it has a maximum absorption band at 650 nm, and an emission centered at 670 nm. This along with the excitation wavelength used ($\lambda = 632.8$ nm) agree with the LSPR of the base unit hexamer configuration. Figure 3.9C shows that an enhanced fluorescence signal is observed (red regions) only in specific locations of the structure. By overlaying the SEF image with the SEM image, it is possible to correlate the regions of enhancement with the structure (Figure 3.10). As expected, a bright spot is observed in the center of the hexamer structures. It is important to note that although the light is polarized along the y-

axis, all the hexamers were plasmonically active, consistent with the polarization measurements of Figure 8B that show little polarization dependence. Additional regions of enhancement were observed along the edges and outer tips of adjacent of nanoprisms in adjacent hexamers.

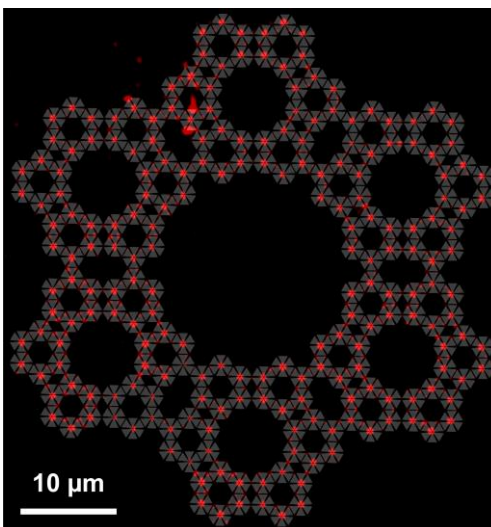


Figure 3.10 SEF image overlaid onto the SEM image of the pseudo-Sierpiński Hexagon. The bright red regions correspond to the regions of enhanced fluorescence.

A non-functionalized sample was also probed in the near- to mid-IR spectral range, where a series of resonances were observed (Figure 3.9D). The base unit hexamer yields the broad resonance from 3000 to 5400 cm^{-1} , and the lower energy resonances are attributed to the hybridization of the resonances introduced with each generation. This effect has been previously numerically demonstrated for Sierpiński fractals.⁷⁶⁻⁷⁷

Optimizing the configuration of the base-unit structures (hexamers) and the overall fractal configuration (number of generations) may lead to the introduction of resonances in the fingerprint region (1000 – 1800 cm^{-1}) leading to compatibility with SEIRA.

3.4 Conclusions

Tuning the optical properties of plasmonic nanostructures is a necessary pre-requisite for performing plasmon-enhanced measurements. Classical methods, such as changing size, offer the greatest ability to tune the spectral position of the resonances. However, no

additional hot-spots are introduced, thus lowering probability of a molecule being detected by spectroscopic means, such as SERS. Increasing the enhancement factor of a structure does not guarantee an improved likelihood that a molecule will be in the hot-spot, only that if it is, the intensity of the signal will be greater. To improve the probability of an analyte being in a probed hot-spot, it is necessary to increase the density of hot-spots. In this work, we have shown by performing series of FDTD calculations and SERS measurements, that altering the arrangement of the nanostructures in an array is critical to the number of hot-spots, and the observed SERS intensity. For classical structures like nanorods, a doublet arrangement is preferable to a singlet arrangement. Although dimer, or bow-tie, configurations of nanoprisms are well established in the literature, increasing to a trimer through hexamer, increases the number of hot-spots. Furthermore, additional hot-spots can be introduced by overlapping the nanoprisms to form arrow-head like structures, leading to not only a greater SERS signal, but also compatibility with additional wavelengths. By working with a simple array base unit, such as a hexamer, and creating a fractal pattern derived from the structure, compatibility is expanded from the visible into the mid-IR spectral ranges. This approach lends itself to correlative detection of analytes using a variety of complementary spectroscopic techniques including SERS and SEIRA.

3.5 References

1. Cottat, M.; D'Andrea, C.; Yasukuni, R.; Malashikhina, N.; Grinyte, R.; Lidgi-Guigui, N.; Fazio, B.; Sutton, A.; Oudar, O.; Charnaux, N.; Pavlov, V.; Toma, A.; Di Fabrizio, E.; Gucciardi, P. G.; Lamy de la Chapelle, M., *J. Phys. Chem. C* **2015**, *119*, 15532-15540.
2. Flynn, J. D.; Haas, B. L.; Biteen, J. S., *J. Phys. Chem. C* **2016**, *120*, 20512-20517.
3. Khatua, S.; Paulo, P. M. R.; Yuan, H.; Gupta, A.; Zijlstra, P.; Orrit, M., *ACS Nano* **2014**, *8*, 4440-4449.
4. Li, J.; Liu, J.; Yang, Y.; Qin, D., *J. Am. Chem. Soc.* **2015**, *137*, 7039-7042.
5. Li, X.; Soler, M.; Ozdemir, C. I.; Belushkin, A.; Yesilkoy, F.; Altug, H., *Lab Chip* **2017**, *17*, 2208-2217.
6. Mei, Z.; Tang, L., *Anal. Chem.* **2017**, *89*, 633-639.
7. Rodal-Cedeira, S.; Montes-García, V.; Polavarapu, L.; Solís, D. M.; Heidari, H.; La Porta, A.; Angiola, M.; Martucci, A.; Taboada, J. M.; Obelleiro, F.; Bals, S.; Pérez-Juste, J.; Pastoriza-Santos, I., *Chem. Mater.* **2016**, *28*, 9169-9180.

8. Shinmori, H.; Mochizuki, C., *Chem. Commun.* **2017**, *53*, 6569-6572.
9. Tabatabaei, M.; Wallace, G. Q.; Caetano, F. A.; Gillies, E. R.; Ferguson, S. S. G.; Lagugne-Labarthe, F., *Chem. Sci.* **2016**, *7*, 575-582.
10. Wallace, G. Q.; Tabatabaei, M.; Zuin, M. S.; Workentin, M. S.; Lagugne-Labarthe, F., *Anal. Bioanal. Chem.* **2016**, *408*, 609-618.
11. Bruzas, I.; Unser, S.; Yazdi, S.; Ringe, E.; Sagle, L., *Anal. Chem.* **2016**, *88*, 7968-7974.
12. Olson, A. P.; Ertsgaard, C. T.; Elliott, S. N.; Lindquist, N. C., *ACS Photonics* **2016**, *3*, 329-336.
13. Kauranen, M.; Zayats, A. V., *Nat. Photon.* **2012**, *6*, 737-748.
14. Ding, S.-Y.; You, E.-M.; Tian, Z.-Q.; Moskovits, M., *Chem. Soc. Rev.* **2017**, *46*, 4042-4076.
15. Alvarez-Puebla, R. A.; Liz-Marzán, L. M., *Angew. Chem. Int. Ed.* **2012**, *51*, 11214-11223.
16. Kneipp, K., *J. Phys. Chem. C* **2016**, *120*, 21076-21081.
17. Cardinal, M. F.; Vander Ende, E.; Hackler, R. A.; McAnally, M. O.; Stair, P. C.; Schatz, G. C.; Van Duyne, R. P., *Chem. Soc. Rev.* **2017**, *46*, 3886-3903.
18. Kanipe, K. N.; Chidester, P. P. F.; Stucky, G. D.; Meinhart, C. D.; Moskovits, M., *J. Phys. Chem. C* **2017**, *121*, 14269-14273.
19. Yan, Y.; Radu, A. I.; Rao, W.; Wang, H.; Chen, G.; Weber, K.; Wang, D.; Ciialla-May, D.; Popp, J.; Schaaf, P., *Chem. Mater.* **2016**, *28*, 7673-7682.
20. Jorgenson, E.; Ianoul, A., *J. Phys. Chem. B* **2017**, *121*, 967-974.
21. Kariuki, V. M.; Hoffmeier, J. C.; Yazgan, I.; Sadik, O. A., *Nanoscale* **2017**, *9*, 8330-8340.
22. Sheen Mers, S. V.; Umadevi, S.; Ganesh, V., *ChemPhysChem* **2017**, *18*, 1358-1369.
23. Gopalakrishnan, A.; Chirumamilla, M.; De Angelis, F.; Toma, A.; Zaccaria, R. P.; Krahe, R., *ACS Nano* **2014**, *8*, 7986-7994.
24. Tabatabaei, M.; Najiminaini, M.; Davieau, K.; Kaminska, B.; Singh, M. R.; Carson, J. J. L.; Lagugne-Labarthe, F., *ACS Photonics* **2015**, *2*, 752-759.
25. Chirumamilla, M.; Chirumamilla, A.; Roberts, A. S.; Zaccaria, R. P.; De Angelis, F.; Kjær Kristensen, P.; Krahe, R.; Bozhevolnyi, S. I.; Pedersen, K.; Toma, A., *Adv. Opt. Mater.* **2017**, *5*, 1600836.
26. Wallace, G. Q.; Foy, H. C.; Rosendahl, S. M.; Lagugne-Labarthe, F., *J. Phys. Chem. C* **2017**, *121*, 9497-9507.
27. Reguera, J.; Langer, J.; Jimenez de Aberasturi, D.; Liz-Marzán, L. M., *Chem. Soc. Rev.* **2017**, *46*, 3866-3885.

28. Simon, S.; Olumorin, T. I.; Guo, B.; Burgess, I. J., *J. Phys. Chem. C* **2016**, *120*, 26150-26158.
29. D'Andrea, C.; Bochterle, J.; Toma, A.; Huck, C.; Neubrech, F.; Messina, E.; Fazio, B.; Maragò, O. M.; Di Fabrizio, E.; Lamy de La Chapelle, M.; Gucciardi, P. G.; Pucci, A., *ACS Nano* **2013**, *7*, 3522-3531.
30. Le Ru, E. C.; Etchegoin, P. G., *Chem. Phys. Lett.* **2006**, *423*, 63-66.
31. Moskovits, M., *Phys. Chem. Chem. Phys.* **2013**, *15*, 5301-5311.
32. Radziuk, D.; Moehwald, H., *Phys. Chem. Chem. Phys.* **2015**, *17*, 21072-21093.
33. Neubrech, F.; Huck, C.; Weber, K.; Pucci, A.; Giessen, H., *Chem. Rev.* **2017**, *117*, 5110-5145.
34. Dong, L.; Yang, X.; Zhang, C.; Cerjan, B.; Zhou, L.; Tseng, M. L.; Zhang, Y.; Alabastri, A.; Nordlander, P.; Halas, N. J., *Nano Letters* **2017**, *17*, 5768-5774.
35. Aslan, E.; Turkmen, M., *Sens. Actuators A Phys.* **2017**, *259*, 127-136.
36. Gottheim, S.; Zhang, H.; Govorov, A. O.; Halas, N. J., *ACS Nano* **2015**, *9*, 3284-3292.
37. Navarro-Cia, M.; Maier, S. A., *ACS Nano* **2012**, *6*, 3537-3544.
38. Wallace, G. Q.; Tabatabaei, M.; Hou, R.; Coady, M. J.; Norton, P. R.; Simpson, T. S.; Rosendahl, S. M.; Merlen, A.; Lagugné-Labarthe, F., *ACS Photonics* **2016**, *3*, 1723-1732.
39. Lehmann, F.; Richter, G.; Borzenko, T.; Hock, V.; Schmidt, G.; Molenkamp, L. W., **2003**, *65*, 327-333.
40. Dai, L.; Song, L.; Huang, Y.; Zhang, L.; Lu, X.; Zhang, J.; Chen, T., *Langmuir* **2017**, *33*, 5378-5384.
41. Wang, L.; Song, Q.; Liu, Q.; He, D.; Ouyang, J., *Adv. Funct. Mater.* **2015**, *25*, 7017-7027.
42. Cetin, A. E.; Korkmaz, S.; Durmaz, H.; Aslan, E.; Kaya, S.; Paiella, R.; Turkmen, M., *Adv. Opt. Mater.* **2016**, *4*, 1274-1280.
43. Li, Y.; Simeral, M. L.; Natelson, D., *J. Phys. Chem. C* **2016**, *120*, 22558-22564.
44. Weber, K.; Nesterov, M. L.; Weiss, T.; Scherer, M.; Hentschel, M.; Vogt, J.; Huck, C.; Li, W.; Dressel, M.; Giessen, H.; Neubrech, F., *ACS Photonics* **2017**, *4*, 45-51.
45. Jin, X.; Jiang, J.; Liu, M., *ACS Nano* **2016**, *10*, 11179-11186.
46. Bagheri, S.; Weber, K.; Gissibl, T.; Weiss, T.; Neubrech, F.; Giessen, H., *ACS Photonics* **2015**, *2*, 779-786.
47. Braun, A.; Maier, S. A., *ACS Sensors* **2016**, *1*, 1155-1162.
48. James, T. D.; Mulvaney, P.; Roberts, A., *Nano Lett.* **2016**, *16*, 3817-3823.

49. Krishnamoorthy, S.; Krishnan, S.; Thoniyot, P.; Low, H. Y., *ACS Appl. Mater. Interfaces* **2011**, *3*, 1033-1040.
50. Aksu, S.; Cetin, A. E.; Adato, R.; Altug, H., *Adv. Opt. Mater.* **2013**, *1*, 798-803.
51. Aksu, S.; Yanik, A. A.; Adato, R.; Artar, A.; Huang, M.; Altug, H., *Nano Lett.* **2010**, *10*, 2511-2518.
52. Kiran, V.; Sampath, S., *ACS Appl. Mater. Interfaces* **2012**, *4*, 3818-3828.
53. Huck, C.; Neubrech, F.; Vogt, J.; Toma, A.; Gerbert, D.; Katzmann, J.; Härtling, T.; Pucci, A., *ACS Nano* **2014**, *8*, 4908-4914.
54. Huck, C.; Toma, A.; Neubrech, F.; Chirumamilla, M.; Vogt, J.; De Angelis, F.; Pucci, A., *ACS Photonics* **2015**, *2*, 497-505.
55. Garreau, A.; Tabatabaei, M.; Hou, R.; Wallace, G. Q.; Norton, P. R.; Lagugné-Labarthe, F., *J. Phys. Chem. C* **2016**, *120*, 20267-20276.
56. Hoffmann, J. M.; Janssen, H.; Chigrin, D. N.; Taubner, T., *Opt. Express* **2014**, *22*, 14425-14432.
57. Nguyen, M.; Kanaev, A.; Sun, X.; Lacaze, E.; Lau-Truong, S.; Lamouri, A.; Aubard, J.; Felidj, N.; Mangeney, C., *Langmuir* **2015**, *31*, 12830-12837.
58. Aouani, H.; Rahmani, M.; Šípová, H.; Torres, V.; Hegnerová, K.; Beruete, M.; Homola, J.; Hong, M.; Navarro-Cía, M.; Maier, S. A., *J. Phys. Chem. C* **2013**, *117*, 18620-18626.
59. Aouani, H.; Šípová, H.; Rahmani, M.; Navarro-Cia, M.; Hegnerová, K.; Homola, J.; Hong, M.; Maier, S. A., *ACS Nano* **2013**, *7*, 669-675.
60. Le Ru, E. C.; Etchegoin, P. G.; Meyer, M., *J. Chem. Phys.* **2006**, *125*, 204701.
61. Hou, R.; Shynkar, V.; Lafargue, C.; Kolkowski, R.; Zyss, J.; Lagugne-Labarthe, F., *Phys. Chem. Chem. Phys.* **2016**, *18*, 7956-7965.
62. Sun, M.; Xu, H., *Small* **2012**, *8*, 2777-2786.
63. Xia, L.; Ma, C.; Wang, J.; Wu, S.; Liu, Y.; Zhang, Q.; Song, P., *Chem. Commun.* **2017**, *53*, 9582-9585.
64. Nguyen, M.; Lamouri, A.; Salameh, C.; Levi, G.; Grand, J.; Boubekour-Lecaque, L.; Mangeney, C.; Felidj, N., *Nanoscale* **2016**, *8*, 8633-8640.
65. Awada, C.; Plathier, J.; Dab, C.; Charra, F.; Douillard, L.; Ruediger, A., *Phys. Chem. Chem. Phys.* **2016**, *18*, 9405-9411.
66. Agrawal, A.; Matsui, T.; Zhu, W.; Nahata, A.; Vardeny, Z. V., *Phys. Rev. Lett.* **2009**, *102*, 113901.
67. Ahmadvand, A.; Gerislioglu, B.; Sinha, R.; Vabbina, P. K.; Karabiyik, M.; Pala, N., *J. Infrared Milli. Terahz. Waves* **2017**, *38*, 992-1003.
68. Aslan, E.; Aslan, E.; Wang, R.; Hong, M. K.; Erramilli, S.; Turkmen, M.; Saracoglu, O. G.; Dal Negro, L., *ACS Photonics* **2016**, *3*, 2102-2111.

69. De Zuani, S.; Reindl, T.; Rommel, M.; Gompf, B.; Berrier, A.; Dressel, M., *ACS Photonics* **2015**, *2*, 1719-1724.
70. Hasan, D.; Ho, C. P.; Lee, C., *ACS Omega* **2016**, *1*, 818-831.
71. Hegde, R. S.; Khoo, E. H., *Plasmonics* **2016**, *11*, 465-473.
72. Newkome, G. R.; Wang, P.; Moorefield, C. N.; Cho, T. J.; Mohapatra, P. P.; Li, S.; Hwang, S.-H.; Lukoyanova, O.; Echegoyen, L.; Palagallo, J. A.; Iancu, V.; Hla, S.-W., *Science* **2006**, *312*, 1782-1785.
73. Hsu, K. H.; Back, J. H.; Fung, K.-H.; Ferreira, P. M.; Shim, M.; Fang, N. X., *J. Raman Spectrosc.* **2010**, *41*, 1124-1130.
74. Volpe, G.; Volpe, G.; Quidant, R., *Opt. Express* **2011**, *19*, 3612-3618.
75. Sederberg, S.; Elezzabi, A. Y., *Opt. Express* **2011**, *19*, 10456-10461.
76. Cakmakyapan, S.; Cinel, N. A.; Cakmak, A. O.; Ozbay, E., *Opt. Express* **2014**, *22*, 19504-19512.
77. Rosa, L.; Sun, K.; Juodkazis, S., *Phys. Status Solidi RRL* **2011**, *5*, 175-177.

Chapter 4

4 Superimposed Arrays of Nanoprisms for Multispectral Molecular Plasmonics

(A version of this work has been published in the journal *ACS Photonics*: Wallace, G.Q.; Tabatabaei, M.; Hou, R.; Coady, M.J.; Norton, P.R.; Rosendahl, S.M.; Merlen, A.; Lagurné-Labarthe, F. *ACS Photonics*, **2016**, 3, 1723-1732.)

Molecular plasmonics relies on the development of conductive nanostructures to yield large local electromagnetic enhancement enabling the detection of molecules located in their vicinity. Although various spectroscopic techniques benefit from such enhancement, performing different spectroscopic measurements on the same platform remains a challenge. As such, the rational design of structures capable of enhancement effects over a large spectral range, particularly from the visible to the mid-infrared, is of great interest. In this Chapter, we develop a series of metallic patterns, consisting of superimposed arrays of gold nanoprisms, that have the potential for surface-enhanced Raman spectroscopy (SERS), surface-enhanced fluorescence (SEF), and surface-enhanced infrared absorption (SEIRA). We first demonstrate that a modified version of the nanosphere lithography method can be used to fabricate such platforms. Patterns with selected sizes can further be produced by electron-beam lithography with virtually no defects, thus yielding tunable and precise optical resonances from the visible to the mid-infrared range. The hexagonal lattices were composed of smaller prisms (0.25 μm prism base length) incorporated for SERS and SEF applications, and larger triangles (1-2 μm base size) for SEIRA purposes. The superimposed patterns display regions that are compatible with SEF, SERS, and SEIRA, thus opening promising applications for multispectral detection of molecules.

4.1 Introduction

Upon illumination, conductive nanostructures with proper opto-geometric parameters can be of great use to locally enhance electromagnetic (EM) fields.¹ Such localized confinement can further be exploited for a variety of applications in spectroscopy, pushing the limits of detection to the single-molecule level.²⁻⁵ Surface-enhanced Raman

spectroscopy (SERS) was the first observation of a highly magnified spectroscopic signal,⁶⁻⁸ that has since been exploited over four decades for a variety of applications ranging from fundamental catalytic surface-mediated processes,⁹⁻¹¹ to accessing intimate biochemical mechanisms.¹²⁻¹⁴ Beyond SERS, molecular plasmonics has been successfully used to access other linear optical processes, such as surface-enhanced fluorescence (SEF) and surface-enhanced infrared absorption (SEIRA),¹⁵⁻¹⁸ as well as nonlinear optical phenomena.¹⁹⁻²²

Although the physical underlying processes are distinct, the enhancement of the linear and nonlinear optical processes occurs when the excitation wavelength is in resonance or pre-resonance with the localized surface plasmon resonances of a given platform. The strength, along with the spectral and spatial location of these resonances depend on several parameters. These include the conductive material used to make the structure, the structure's size and shape, the orientation of the structures with respect to each other and with respect to the polarization of the impinging light.²³ The spectral location of the resonances can be further altered by changing the dielectric constant of the media surrounding the platform (i.e. air vs. water).²⁴

In this context, a variety of approaches have been used to fabricate and tune 2-dimensional platforms that exhibit resonances in selected spectral domains of interest.²⁵ Lithographic techniques ranging from lab bench approaches, such as nanosphere lithography,²⁶⁻²⁷ to nanofabrication technology including focused ion beam or electron-beam lithography,²⁸⁻²⁹ are often used to prepare these platforms.

Electron-beam lithography (EBL) is particularly valuable owing to its ability to create structures with high resolutions (~10 nm).³⁰ Since this fabrication process requires the use of a pattern generating software, it is possible to create structures and platforms with tailored opto-geometric properties. To this end, structures comprised of multiple plasmon compatible metals have been readily prepared and studied.³¹⁻³³ Moreover, it is possible to achieve multiple resonances using a monometallic structure of fixed dimensions simply by altering the configurations of the structures with respect to each other. This is the concept of plasmonic oligomer clusters. Such platforms have been comprised of

nanorods,³⁴ nanodiscs,³⁵⁻³⁶ and split nanorings.³⁷ For these platforms, resonances in the visible and near-IR can be generated with excellent reproducibility.

Extending the multiwavelength compatibility beyond the visible and near-IR is more challenging. Critical to the field of molecular plasmonics for SEIRA is generating surface plasmon resonances in the same spectral region as the absorptions of an analyte. Since these absorptions cover a broad spectral range (2.5-20 μm , 500-4000 cm^{-1}), it is necessary to have structures that exhibit either extremely broad resonances or multiple resonances. One means of generating multiple resonances in the near and mid-IR is through the use of fractal patterns.³⁸⁻³⁹ As the number of generations in the fractal increases, so does the number of resonances. The challenge with such structures is to rationally design the size of the fractal so as to have resonances in the spectral regions of interest of great interest, such as 1000-1800 cm^{-1} and 2800-3100 cm^{-1} , that cover the fingerprint region along with C-H vibrational modes.

Introducing multispectral compatibility into the mid-IR has become of greater interest due to the increase in research involving SEIRA. Unlike SERS and SEF where the individual conductive structures generally have dimensions in the 20-300 nm range, resulting in a quadrupolar resonance in the visible, SEIRA often requires the use of nanostructures that have considerably larger dimensions to yield resonances over a larger spectral range. To achieve this multispectral compatibility, platforms can be fabricated that rely on the polarization of the incoming light or can be rationally designed.

Metallic nanorods, with lengths ranging from 1-2 μm and widths of 60 nm were shown to exhibit two plasmon resonances.⁴⁰ A plasmon resonance in the infrared was present when illuminated with light polarized parallel to the nanorod, while a plasmon resonance in the visible was observed when illuminated with perpendicularly polarized light. Another multispectral compatible structure are optical nanoantennas that mimic microwave antennas.⁴¹ By varying the length of the protruding teeth,³⁴ plasmons in both visible and infrared regions were generated. Although the compatibility for SEF, SERS, and SEIRA was explored, the platform's use was restricted due to the limited transmission of quartz in the vibrational fingerprint region (1000 – 1800 cm^{-1}) of the mid-IR.⁴² In this context,

the development of structures that feature either a broad resonance or several resonances matching the spectral domains of interest, fabricated on a substrate with optical transparency in these regions, is critical to combining complementary spectroscopic techniques.

In the present work, we develop a platform with resonances that allow one to conduct a variety of spectroscopic measurements. This was achieved through the use of superimposed gold nanoprisms with distinct dimensions. By orientating larger nanoprisms in a hexagonal lattice, there was sufficient space to incorporate smaller nanoprisms also in a hexagonal lattice. For demonstration of the principle, nanosphere lithography (NSL) was used with polystyrene particles of two diameters. A first NSL step yielded small prisms arranged in a hexagonal fashion mean while a second NSL step with a larger sphere yielded larger prisms that superimposed with some of the arrays of smaller nanoprisms. In order to refine the structure, and to control the respective orientation of the superimposed patterns, EBL was used. By incorporating nanoprisms with a side length of $0.25\ \mu\text{m}$, along with larger $1\text{-}2\ \mu\text{m}$ prisms, the superimposed prisms were capable of exhibiting resonances across the visible, near-IR, and mid-IR spectral regions. By fabricating the structures on CaF_2 windows, we minimized substrate interference effects across our multispectral ranges. The optical response and field distribution of the resulting platforms were modelled using finite difference time domain calculations highlighting the density and locations of hot-spots. Microspectroscopy experiments combining SERS and SEIRA, as well as SEF were demonstrated, highlighting the versatility of our platforms that could find applications in correlative microscopy where distinct microcopy techniques are used on an identical sample.

4.2 Experimental

4.2.1 Materials

Silicon and CaF_2 substrates ($13\ \text{mm}$ diameter \times $2\ \text{mm}$) were purchased from Spectral Systems LLC (NY, USA). Polystyrene spheres (10% w/w) with a diameter of $1\ \mu\text{m}$ were acquired from ThermoScientific Co. (CA, USA). Polystyrene spheres (2.5% w/w) with a diameter of $6\ \mu\text{m}$ were purchased from Corpuscular Inc. (NY, USA). Poly(methyl

methacrylate) A2 950 resist and isopropanol were purchased from MicroChem Corp. (MA, USA). AquaSave was obtained from Mitsubishi Rayon America Inc. (NY, USA). Acetone (CHROMASOLV), 4-nitrothiophenol (4-NTP) and 4-mercaptophenylboronic acid (4-MPBA) were procured from Sigma-Aldrich (MO, USA). Cyanine 5 labelled polyethylene glycol with a thiol (Cy5-PEG-SH, MW 5000 DA) was purchased from Nanocs Inc. (NY, USA).

4.2.2 Nanosphere Lithography

The cleaning procedure for the silicon substrates along with the complete nanosphere lithography protocol is described with considerable detail in Appendix A. Scanning electron micrographs of the prepared samples were obtained using a LEO Zeiss 1530 SEM (Oberkochen, Germany).

4.2.3 Electron-Beam Lithography

Silicon and CaF₂ substrates were cleaned using reactive O₂ plasma for 20 minutes. Details of the process for EBL are described in detail in Appendix C. Scanning electron micrographs of the structures were then obtained using the Leo Zeiss 1530 SEM used to prepare the structures by EBL.

4.2.4 Visible and Near-Infrared Absorption

The set-up for obtaining the visible to near-infrared absorption spectra is described in 2.4.1 and shown in Figure 2.10. An acquisition time of 1 second per spectrum was used. Each spectrum shown is the result of 50 accumulations.

4.2.5 Surface-Enhanced Fluorescence

Samples were functionalized in a 10⁻⁵ M solution of Cy5-PEG-SH prepared in Milli-Q water for 24 hours. Fluorescence imaging was performed with a Zeiss LSM 510 META Multiphoton Confocal Laser Scanning Microscope. A helium neon laser ($\lambda = 632.8$ nm) along with a 63 \times (N.A. = 0.75) objective was used, with the scanning area for the image set to 512 \times 512. The fluorescence images were obtained by examining the emission of the dye from 650-700 nm using the fluorescence microscope.

4.2.6 Surface-Enhanced Raman

Samples were functionalized in a 10^{-3} M solution of 4-NTP prepared in ethanol for 24 hours. Information regarding the Raman spectrometer used is provided in 2.4.2 and Figure 2.11. A helium neon laser ($\lambda = 632.8$ nm, power of ~ 500 μ W at the sample) was used as the excitation source, and a $100\times$ (NA = 0.9) objective was used to collect the back scattered light. An acquisition time of 10 seconds per spectrum was used for spot analyses, and for mapping, an acquisition time of 1 second per spectrum was used.

4.2.7 Infrared Absorption and Surface-Enhanced Infrared Absorption

Fourier transform infrared (FT-IR) spectroscopy measurements were performed at the Mid-IR beamline synchrotron facility located at the Canadian Light Source (Beamline 01B-01). Information regarding the set-up at the beamline end station is provided in 2.5.2 and Figure 2.13. The apertures size chosen (1.5) allowed for the beam diameter to be slightly smaller than the 50×50 μm^2 patch. Measurements were collected from 8000 - 800 cm^{-1} with a spectral resolution of 4 cm^{-1} . Each spectrum is the average of 512 spectra. For SEIRA measurements, the samples were functionalized for 6-12 hours in a freshly prepared 10^{-3} M solution of either 4-NTP or 4-MPBA prepared in ethanol.

4.2.8 Electromagnetic Field Modelling

Finite-difference time-domain (FDTD) modelling (Lumerical) was used to simulate the absorption and electromagnetic fields of the patterns. Dimensions and metal thicknesses were based on the idealized geometry and metal thicknesses. CRC and Palik dielectric values for gold and titanium for visible, and infrared extinction cross sections respectively.⁴⁴⁻⁴⁵ The structures were placed on a substrate of CaF_2 with a thickness of 250 nm. Periodic boundaries on the x and y axes conditions were reflective of the overall size of the periodic structure used, and perfectly matched layer (PML) was used in the z axis.

4.3 Results and Discussion

4.3.1 Superimposed Fischer's Patterns

The Fischer's pattern coining refers to the seminal work that first used a layer of compactly arranged microspheres as a template to form an ensemble of prisms arranged in a hexagonal lattice with a narrow distribution of inter-prism gaps.⁴⁶ To fabricate the superimposed patterns by NSL, polystyrene spheres with diameters of 1 and 6 μm were used, resulting in prisms with base lengths of 0.3 and 1.75 μm respectively. The typical structure is shown in Figure 4.1A. By adjusting the size of the spheres used, it is possible to tailor the dimensions of the resulting structures that can be used for targeted spectral measurements. Smaller prisms formed using smaller sphere sizes are compatible with the visible spectral range enabling SEF,⁴⁷⁻⁴⁸ and SERS.^{43, 49-50} Increasing the sphere size results in larger prisms compatible with plasmon resonances in the mid-infrared range and are ideal for SEIRA measurements.^{26, 51} An interesting advantage of using two consecutive steps during fabrication is the possibility to use different metals or metal oxides for each of the structures. However, as shown in Figure 4.1A, this approach presents several drawbacks, such as a broad distribution in the size of the prisms and spacing between them, a random orientation overlap of the nanoprisms, as well as structural defects. Therefore, the use of EBL was investigated as an alternative technique to the fabrication of the superimposed patterns.

EBL offers the ability to overcome many of the issues observed with NSL. It yields structures with defined sizes, inter-prism gaps, and orientation of the features that can be homogeneously fabricated (Figure 4.1B, C). As such, for the desired superimposed patterns, the location of the overlapping prisms is consistent and can be finely tuned. Overall, two different types of samples were prepared with variable dimension of the larger set of prisms. In the first series of samples, when the prisms overlap, one apex of the smaller prism is embedded into the larger prism (Figure 4.1B), and the second series has two apices embedded (Figure 4.1C). The former allowed an apex of the smaller prisms near the apices of the larger prism, while the latter did not. The first series was fabricated for prisms with sizes of 1, 1.5, and 2 μm (Figure 4.1B,D, and F), while the second series was obtained with prism side lengths of 1.25 and 1.75 μm (Figure 4.1C,

and E). Although NSL does allow for large areas ($100 \times 100 \mu\text{m}^2$ or greater) to be fabricated (Figure 4.2A), another advantage of EBL over NSL is that the size ($50 \times 50 \mu\text{m}^2$) and position of the platforms is easily controlled (Figure 4.2B). This leads to the potential of automation of spectral measurements over an ensemble of plasmonic patches defined by a series of x and y coordinates.

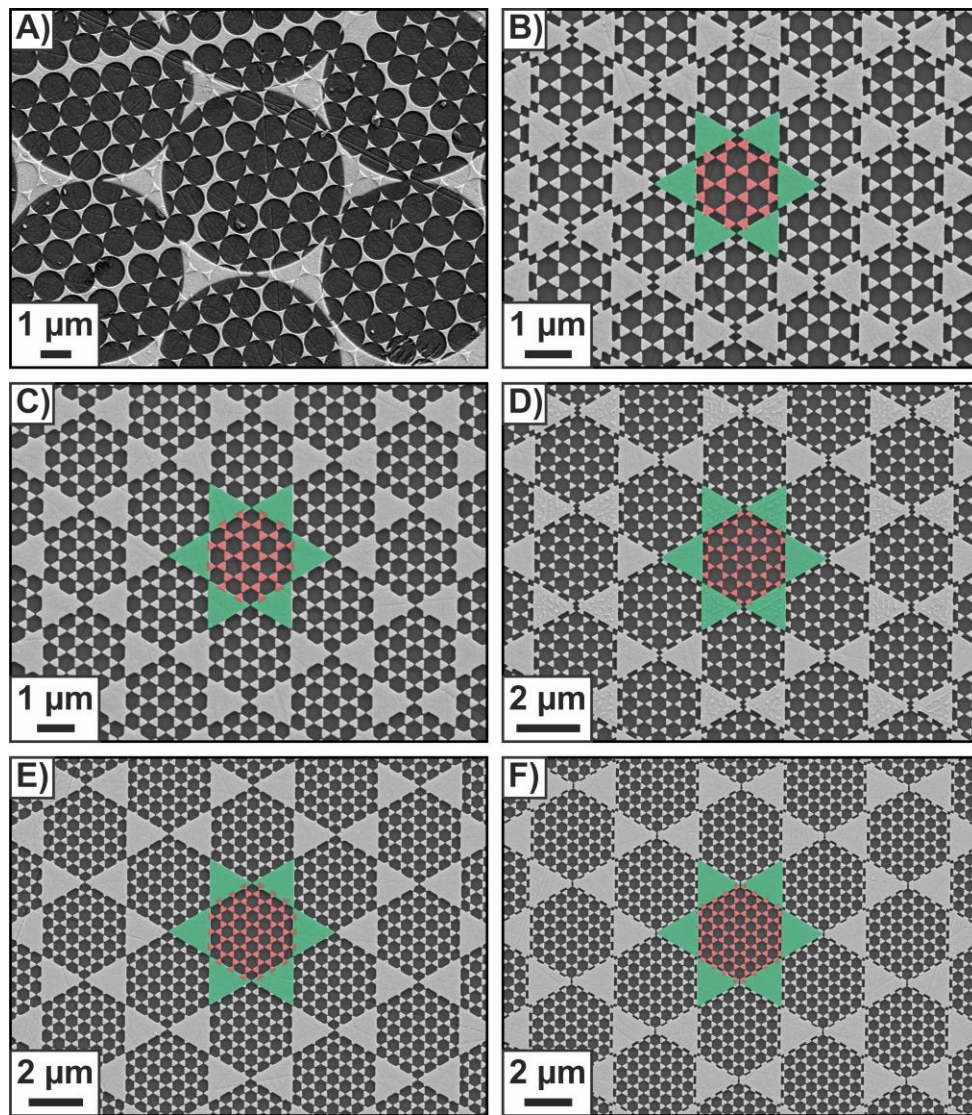


Figure 4.1 SEM images of superimposed nanoprisms fabricated on silicon. A) Local region highlighting the overlap of the two patterns prepared by NSL. Superimposed arrays of nanoprisms prepared by EBL with small nanoprisms (coloured red) of $0.25 \mu\text{m}$ side length and large nanoprisms (coloured green) with B) $1 \mu\text{m}$, C) $1.25 \mu\text{m}$, D) $1.5 \mu\text{m}$, E) $1.75 \mu\text{m}$, and F) $2 \mu\text{m}$ sidelengths.

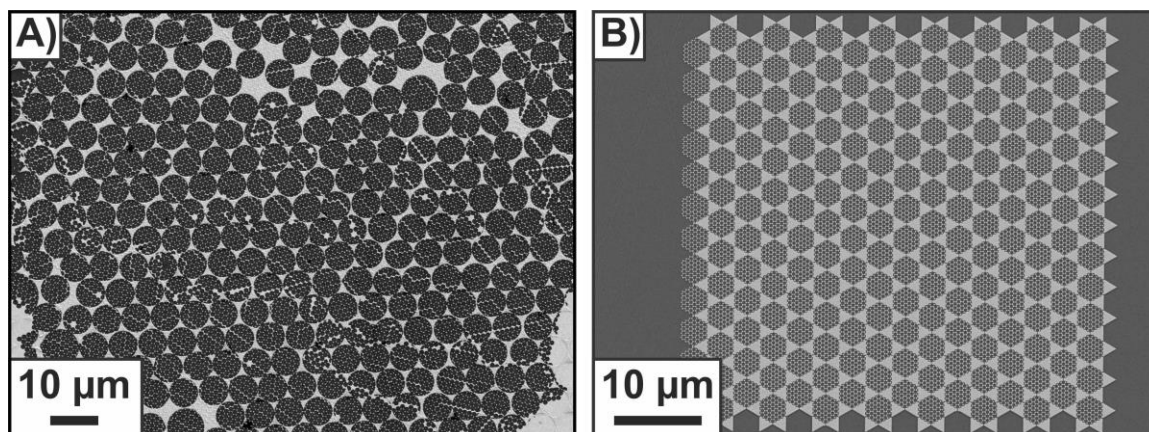


Figure 4.2 SEM images of large regions of superimposed arrays of nanoprisms fabricated on silicon prepared by A) NSL, and B) EBL.

4.3.2 Optical Properties of the Superimposed Patterns in the Visible Region

Extinction measurements were conducted on the superimposed prisms to determine the optical resonances and compare with non-superimposed arrays. Since one of the objectives of this work was to have the same platform compatible with visible and mid-infrared spectral domains, CaF_2 was selected as the substrate for its optical compatibility with SEF, SERS, and SEIRA measurements. As shown in Figure 4.3, the pattern made with arrays of $0.25 \mu\text{m}$ triangles exhibit a dipolar mode at 950 nm , and a multipolar mode near 640 nm . For the superimposed patterns, the resonances maintain similar spectral positions. This implies that the superimposed platforms are compatible with excitations in the visible, and more specifically 632.8 nm would be a suitable wavelength to perform plasmon-mediated fluorescence and Raman measurements.

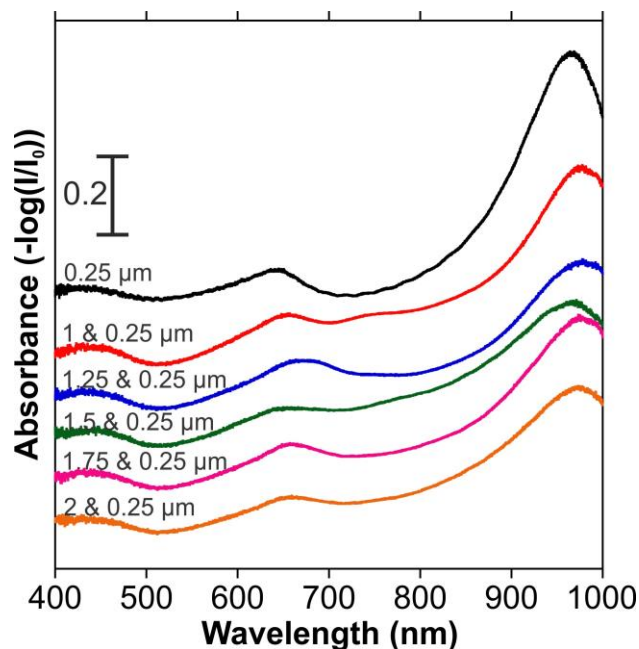


Figure 4.3 Visible and near-IR absorption of the Fischer's pattern, and the superimposed structures with the indicated side lengths.

By performing finite-difference time-domain (FDTD) simulations on the superimposed patterns, it is possible to identify the structures contributing to the observed resonances. Figure 4.4 shows the EM field distribution for the superimposed pattern comprised of 1 and 0.25 μm prisms upon excitation with linearly polarized light. At the wavelength used for the SEF and SERS measurements ($\lambda = 632.8 \text{ nm}$, Figure 4.4A, B), the contribution to the absorption comes from the smaller triangles located in the middle of the lattice, and from the edges of the overlap between the large and small triangles.

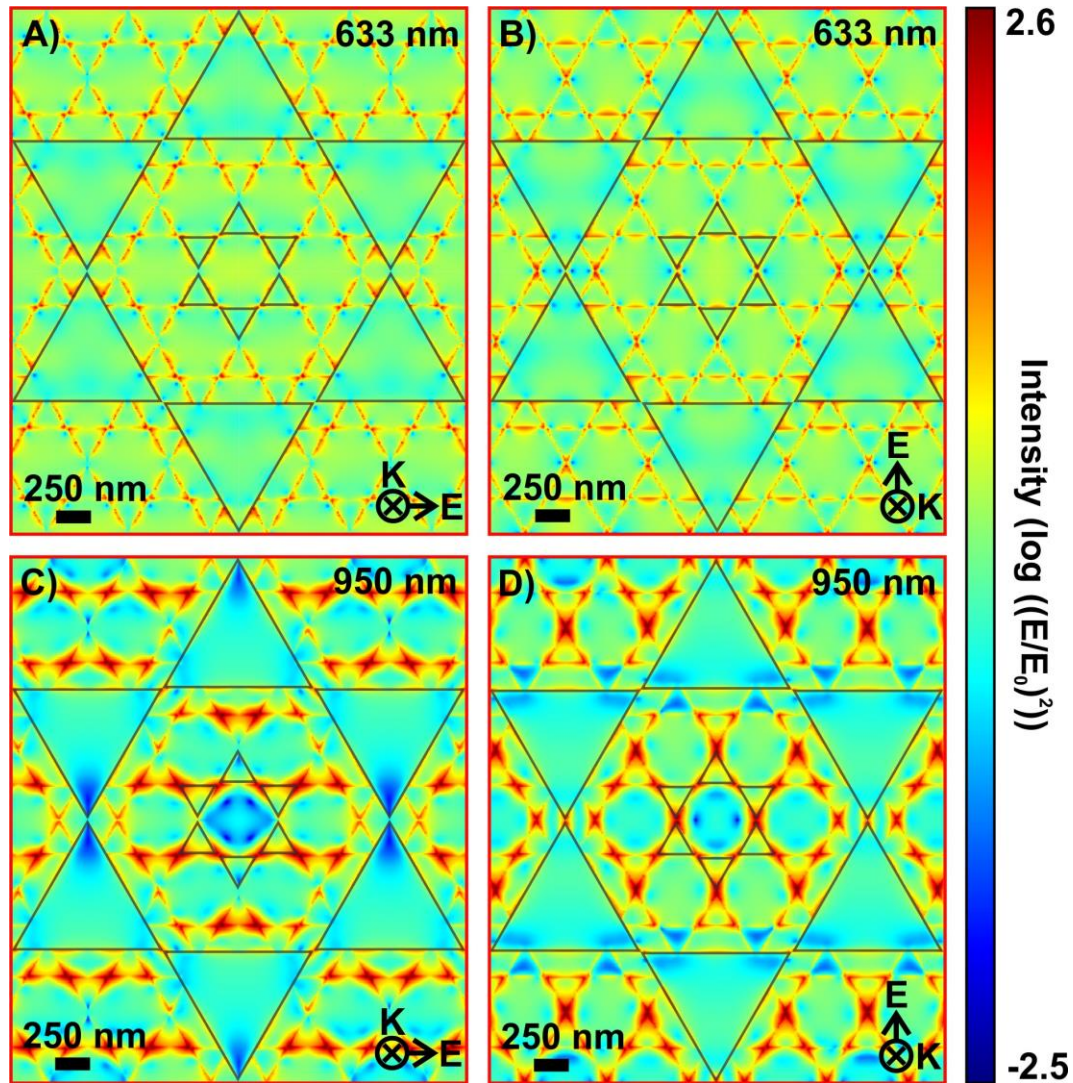


Figure 4.4 FDTD calculations of the transverse components of the electric field ($|E/E_0|^2$, log scale representation at wavelengths of 633 nm (A,B), and 950 nm (C,D) for superimposed nanoprism patterns with side lengths of 1 and 0.25 μm .

The intensity of the local enhancement ($|E/E_0|^2$) is $10^{2.6}$. This yields a theoretical enhancement factor of and $10^{5.2}$ for SERS assuming an $|E/E_0|^4$ dependence.⁵² It is important to note that for SERS, there is also a contribution from chemical enhancement (10^1 - 10^2),⁵³ that is not taken into account in the FDTD modeling. Near the dipolar mode at 950 nm (Figure 4.4C, D), there is still the contribution from the smaller triangles, however, the contribution from the intersection of the smaller and larger triangles is weaker. Instead, a contribution from the larger triangles is now observed. With $|E/E_0|^2$

being $10^{3.5}$, a greater enhancement would occur for both SEF and SERS upon near-IR excitation. However, in this work, the benefit of this enhancement was not examined as both SEF and SERS measurements were performed at an excitation of 632.8 nm. By changing the input polarization from horizontal (Figure 4.4A, C), to vertical (Figure 4.4B, D), the enhancements are localized in distinct regions of the platform that correspond to the hot-spots of interest.

4.3.3 SEF Compatibility

The superimposed platforms were first tested against SEF. To minimize the quenching of the fluorescence by the gold structure, the fluorophore used in this study was physically separated from the metal surface using a polymer side-chain.

Specifically, the selected molecule (Cy5-PEG-SH) had cyanine 5 (Cy5) as the fluorophore, along with a polyethylene glycol (PEG) side chain as the protection layer, and finally a thiol (SH) added to the end of the PEG chain so the molecule could covalently bond to the gold surface. With a total molecular weight of 5000 Da, the PEG chain was long enough to minimize the fluorophore-gold proximity and allow for enhancement of the fluorescence signal. Cy5 has a maximum absorption band at 650 nm, and an emission centered at 670 nm. This allows for an excitation wavelength of 632.8 nm to be used, a wavelength that as we have previously described as being compatible with our platforms.

Figure 4.5A-D shows the Rayleigh scattering images for the EBL patterns inscribed on CaF₂. For the smaller size prisms (0.25 μm), it is difficult to observe the scattering (Figure 4.5A), whereas for the larger triangles, the structures can be easily identified (Figure 4.5B-D). SEF is observed for both the non-superimposed (Figure 4.5E-F) and superimposed platforms (Figure 4.5G-H). When the horizontally polarized light interacts with the nanostructure, the dominant enhancement occurs with prisms aligned along the same direction. Although such dependence is difficult to observe with the 0.25 μm prisms, it is clear for the 1 μm prisms as shown from the SEF map displayed in Figure 4.5F. Furthermore, the SEF results in Figure 4.5F indicate that the 1 μm prisms also exhibit SEF compatibility. By combining the 1 and 0.25 μm prisms, it is possible to

introduce coupling in the regions where the apices of the small and large prisms are in close proximity.

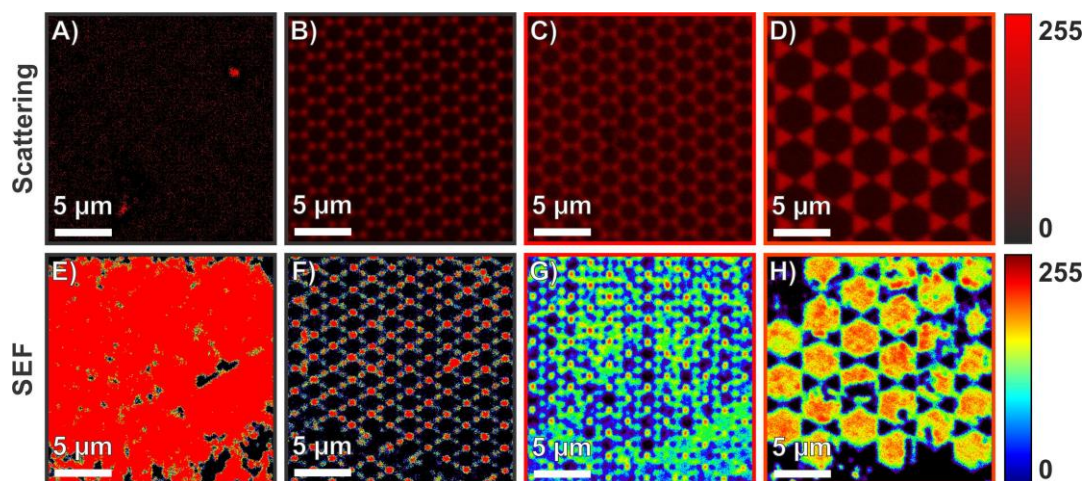


Figure 4.5 Scattering (A-D) and SEF (E-H) images of Fischer's patterns with dimension of 0.25 μm (A,E), 1 μm (B,F), and superimposed patterns with side lengths of 1 and 0.25 μm (C,G), 2 and 0.25 μm (D,H).

This effect is also highlighted in Figure 4.6 along with a complete representation of the SEF results merged with the SEM images of all the structures and the representation of the hot-spots. As the size of the prisms increases, the degree of the coupling decreases. Moreover, the space inside the center of the lattice of larger prisms increases. This increase allows for a greater number of the smaller prisms. During the SEF study, this enabled a stronger SEF signal as more of the SEF compatible 0.25 μm prisms were being illuminated. Therefore, to maximize the SEF signal, it is recommended that a sufficient number of hot-spot generating structures are present. In the case of the superimposed prisms, this was achieved when the larger prisms were 1.25 μm or greater in side length. Furthermore, as the size of the larger prisms increases, it becomes easier to observe the structure. For example, Figure 4.5H and Figure 4.6 clearly show that the majority of the 2 μm prisms do not enhance the fluorescence signal as they appear darkly coloured, whereas the enhancement is only observed at the outer edge and tip apices.

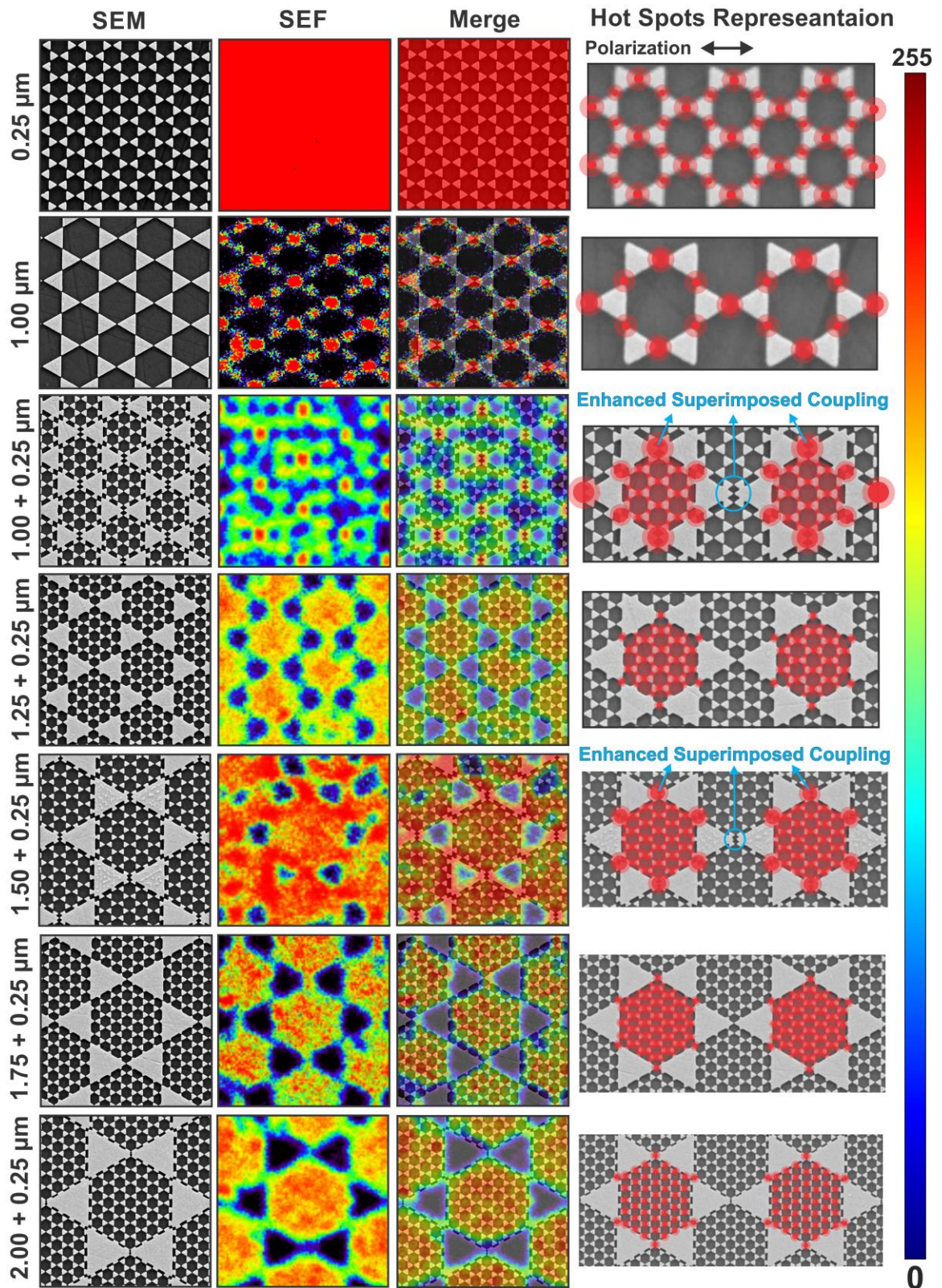


Figure 4.6 SEF analysis, and hot-spot representations of the superimposed patterns.

To verify that the enhancement of the fluorescence signal is the result of the smaller prisms, a comparison between patterned regions and regions with gold that was not removed during the lift-off process was performed. Figure 4.7A shows the Rayleigh scattering images of a patch of superimposed 2 and 0.25 μm prisms that contains un-lifted gold and the revealed patterns. The areas of un-lifted gold are clearly visible along with the larger 2 μm prisms. The SEF image (Figure 4.7B) indicates that the regions of un-lifted gold do not exhibit an enhanced fluorescence signal, whereas the 0.25 μm prisms within the superimposed structure do.

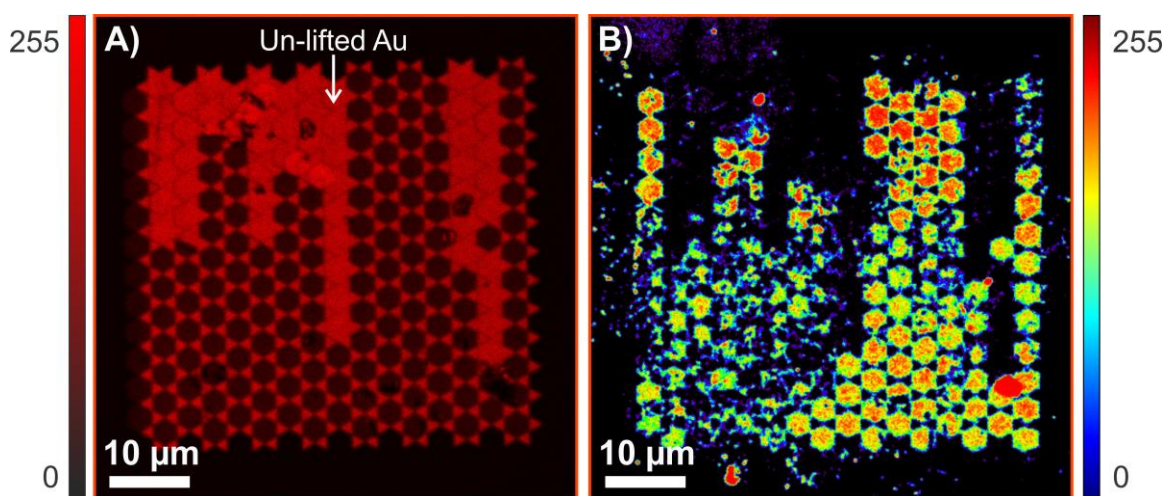


Figure 4.7 A) Scattering, and B) SEF images of a patch of superimposed 2 and 0.25 μm nanoprisms with regions of un-lifted gold present.

4.3.4 SERS Compatibility

To further examine the compatibility of the platform, SERS measurements were performed on a sample functionalized with 4-nitrothiophenol (4-NTP). A SERS map was generated by collecting a series of spectra over the surface with a 750 nm step size and integrating each spectrum from 1325-1350 cm^{-1} , corresponding to the symmetric NO_2 stretch. As such, it was once again possible to spatially correlate the enhancement to the different sizes of the prisms (Figure 4.8A-C). Figure 4.8D indicates that even with an acquisition time of 1 second per spectrum, the SERS spectrum of 4-NTP could be observed. Similar to the SEF study, the 0.25 μm prisms show significant enhancement. With the larger nanoprisms, the middle portions do not offer significant enhancement,

much like the SEF results. This is highlighted by overlaying the generated SERS map over a SEM image from the same type of structure (Figure 4.8C).

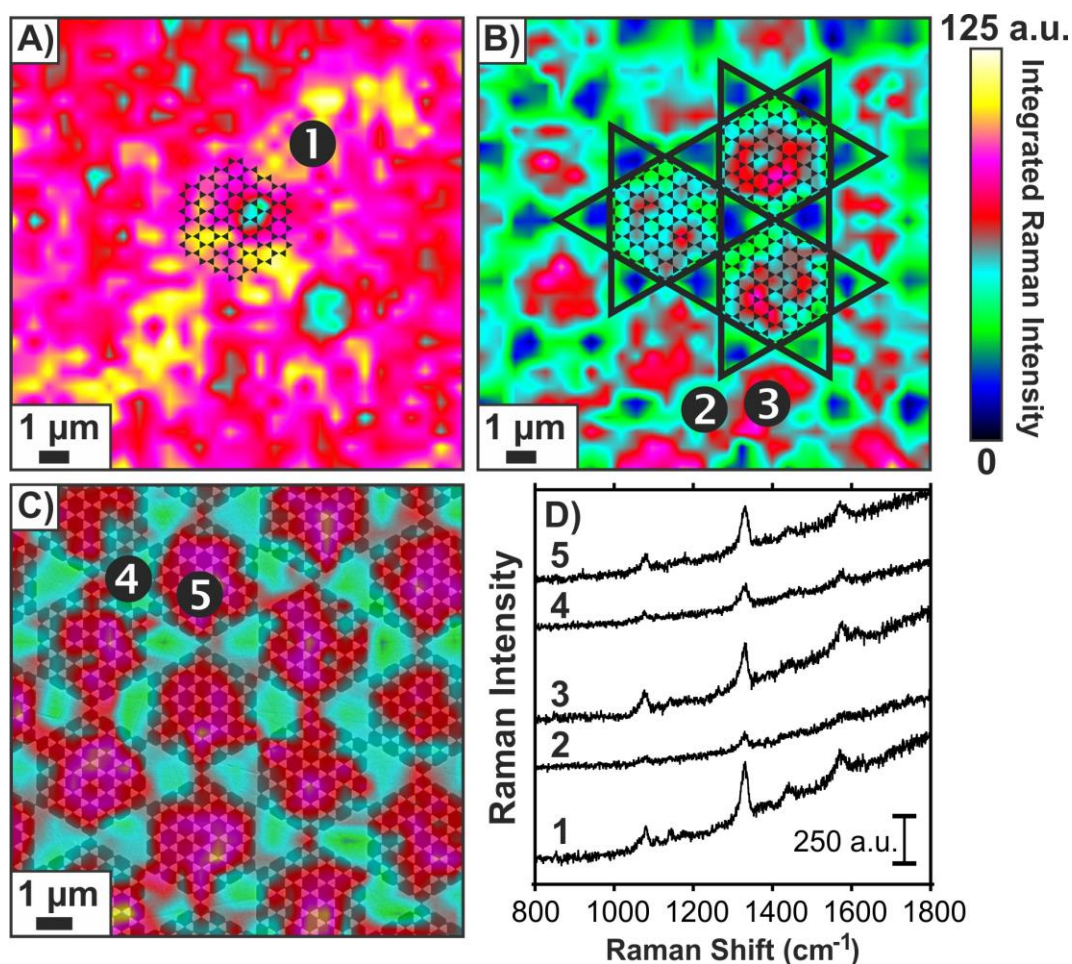


Figure 4.8 Integrated SERS maps from 1300-1350 cm^{-1} for 4-NTP functionalized patterns with side lengths of 0.25 μm (A), and for superimposed patterns with side lengths of 2 and 0.25 μm (B), 1.75 and 0.25 μm (C). Individual SERS spectra corresponding to the indicated regions from A-C are shown in D. Triangles matching the dimensions described are overlaid in A and B, and the SERS map of C is overlaid on an SEM micrograph to relate the SERS map to the structures.

As can be seen in the SERS spectra of Figure 4.8D, along with the spectra in Figure S5A, there is a fair amount of background. This can be attributed to the CaF_2 substrate used in the superimposed platforms. Although this background could be decreased by altering the substrate, doing so could potentially hinder the multispectral compatibility as the

substrate would still need to be compatible with both the visible and mid-IR ranges. A comparison between the nanostructures and non-structured gold was performed to verify that the observed enhancement was the result of the nanostructures. As shown in Figure 4.9A, regions of flat gold functionalized with the probe molecule do not show a Raman or SERS spectra of the analyte, whereas the nanoprisms do.

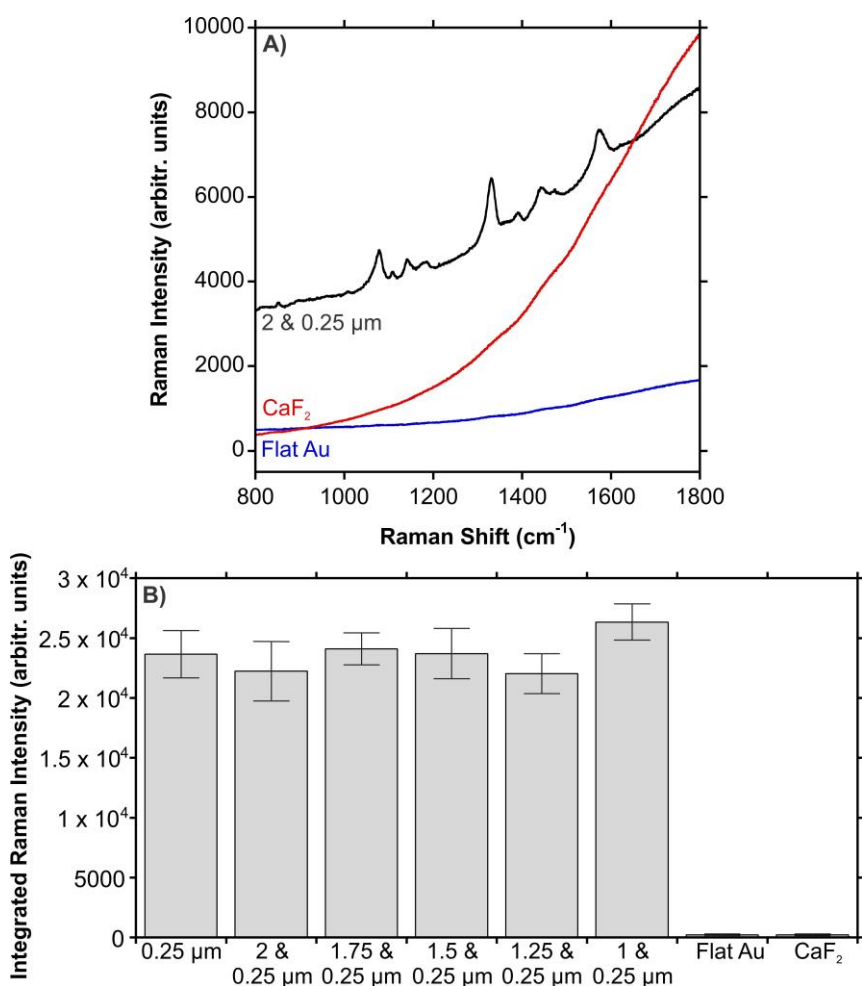


Figure 4.9 A) Raman spectra for CaF₂ and 4-NTP functionalized flat gold, and a SERS spectrum of 4-NTP functionalized superimposed nanoprisms. B) SERS analysis of 25 individual spectra on each of the superimposed patterns.

One crucial aspect of a SERS compatible platform is reproducibility of the measurements over the whole surface of the platform. The consistency of the SERS measurements was statistically verified by analyzing 25 distinct areas for each pattern. For the superimposed structures, the center of the Fischer's pattern from the larger triangle was selected, as this

area contains the 0.25 μm prisms. As the size of the larger prisms increased, due to the increase in the size of the center region, it became easier to probe the smaller prisms. The results of these analyses are shown in Figure 4.9B. So long as the probed region contains the 0.25 μm prisms, the results are comparable. As such, the superimposed nanoprisms are compatible for SERS based studies.

4.3.5 Optical Properties of the Superimposed Patterns from Near- to Mid-IR Regions

Some metallic nanostructures have been designed to have Fano and Fano-like resonances in the near and mid-IR regions.⁵⁴⁻⁵⁵ These asymmetric resonances occur due to the interference between two resonances, a broad resonance and a narrower discrete resonance. In this work, all the spectra collected in the mid-infrared range were collected using microscopy conditions in conjunction with a synchrotron light source due to the limited area of the platforms ($50 \times 50 \mu\text{m}^2$, see experimental section for the FTIR measurements). The patterns comprised of just 0.25 μm triangles do not exhibit any resonances in the near or mid-IR, whereas broad, asymmetric resonance in the mid-IR range can be observed for the 1 μm prisms. The dual absorptions in close proximity to each other, such as 3100 and 3600 cm^{-1} in the spectra from the 1 μm prisms in Figure 4.10A, are the result of both the impure and unknown polarization of the input infrared light. It has previously been observed that this phenomenon can be introduced by having the polarized light introduced at an off-axis angle with respect to the structure.³⁸ For the superimposed patterns with the 1 and 0.25 μm prisms, a red shift of the resonance can be observed together with the introduction of a new resonance.

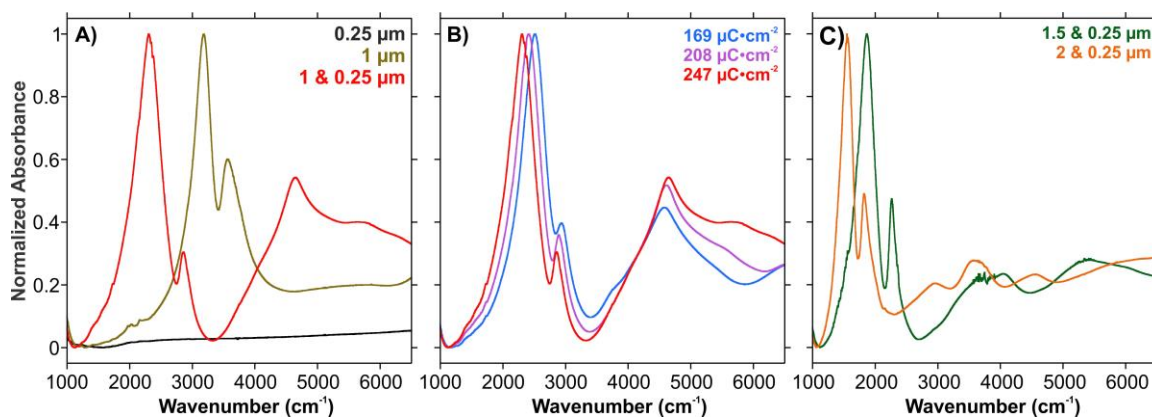


Figure 4.10 Infrared absorption of single Fischer's patterns and superimposed patterns for various sizes. **A)** Comparison between non-superimposed (0.25, and 1 μm prisms) and superimposed patterns (1 and 0.25 μm prisms). **B)** Influence of different electron exposure doses during lithography on the absorptions. **C)** Effect of increasing the size of the larger triangles in the superimposed patterns.

Furthermore, it is possible to tune the position of the resonances simply by adjusting the area dose ($\mu\text{C}\cdot\text{cm}^{-2}$) of the electron beam during the exposure process. When the exposure is increased, the size of the resulting structure increases, and the gaps between the metallic structures are subsequently narrowed. As a result of these changes, it has previously been observed that the absorptions in the visible region for Fischer's patterns can be finely tailored.⁵⁶ Figure 4.10B illustrates that this is also true for the mid-IR spectral range. By increasing the area dose, a red shift for the dominant resonance occurs, while the minor resonance exhibits a blue shift.

In order to achieve a greater shift in the spectral position of the resonances, it is necessary to alter the size of the triangles by a greater amount than what can be achieved just by adjusting the area dose. Figure 4.10C illustrates this phenomenon by increasing the size of the larger triangles to 1.5, and 2 μm . By increasing the size of the structure, a more significant red shift occurs. Furthermore, additional absorptions are introduced at higher wavenumbers (shorter wavelengths).

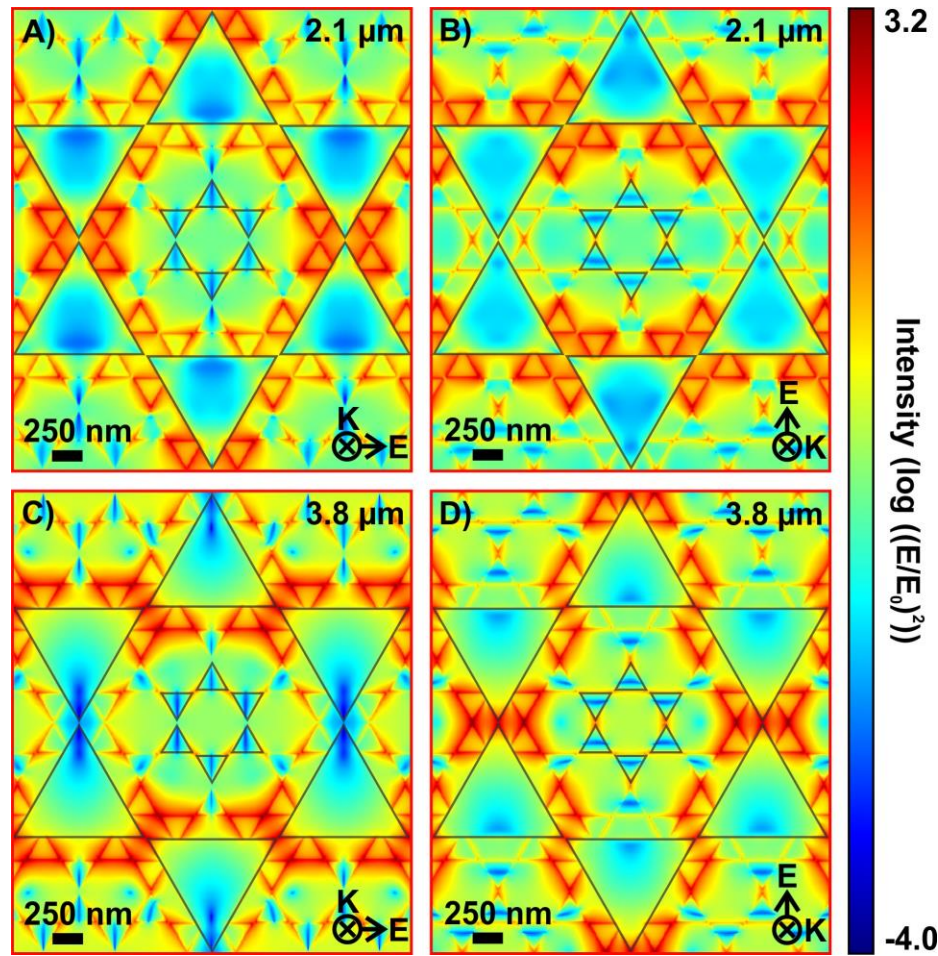


Figure 4.11 FDTD calculations of the transverse components of the electric field ($|E/E_0|^2$), log scale representation at wavelengths of 2.1 μm (A and B), and 3.8 μm (C and D) for superimposed nanoprisms with side lengths of 1 and 0.25 μm .

As was done for the visible region, FDTD modelling was performed to spatially correlate the infrared resonances with respect to the structure (Figure 4.11). Near the wavelength corresponding to the near-infrared resonance at 2.1 μm (4760 cm^{-1}) for the 1 and 0.25 μm superimposed patterns, the triangles contributing to the enhancement of the EM field are the 0.25 μm prisms that are superimposed onto the 1 μm prisms (Figure 4.11A and B). Additionally, no significant contribution from the 1 μm triangles is observed for either horizontally or vertically polarized light. Near the dominant resonance at 3.8 μm (2630 cm^{-1}), contributions from both the superimposed small and large prisms can be observed for both input polarizations (Figure 4.11C and D). With enhancement for $|E/E_0|^2$

corresponding to $10^{3.2}$ and $10^{3.6}$, comparable enhancements of the infrared absorption occur for both resonances. It is noteworthy that enhancements limited to 10^2 - 10^4 are commonly observed for structures compatible with SEIRA. This range is consistent with the superimposed nanoprisms (Figure 4.12) For the superimposed patterns a predicted maximum enhancement of $10^{4.3}$ was calculated at a wavelength of $5.6 \mu\text{m}$ (1786 cm^{-1}) for the superimposed 2 and $0.25 \mu\text{m}$ prisms (Figure 4.12D). This particular platform is of interest not only because it yielded the largest enhancement, but also because the dominant absorption lies in the region of $1000 - 1800 \text{ cm}^{-1}$, corresponding to the molecular fingerprint spectral region.

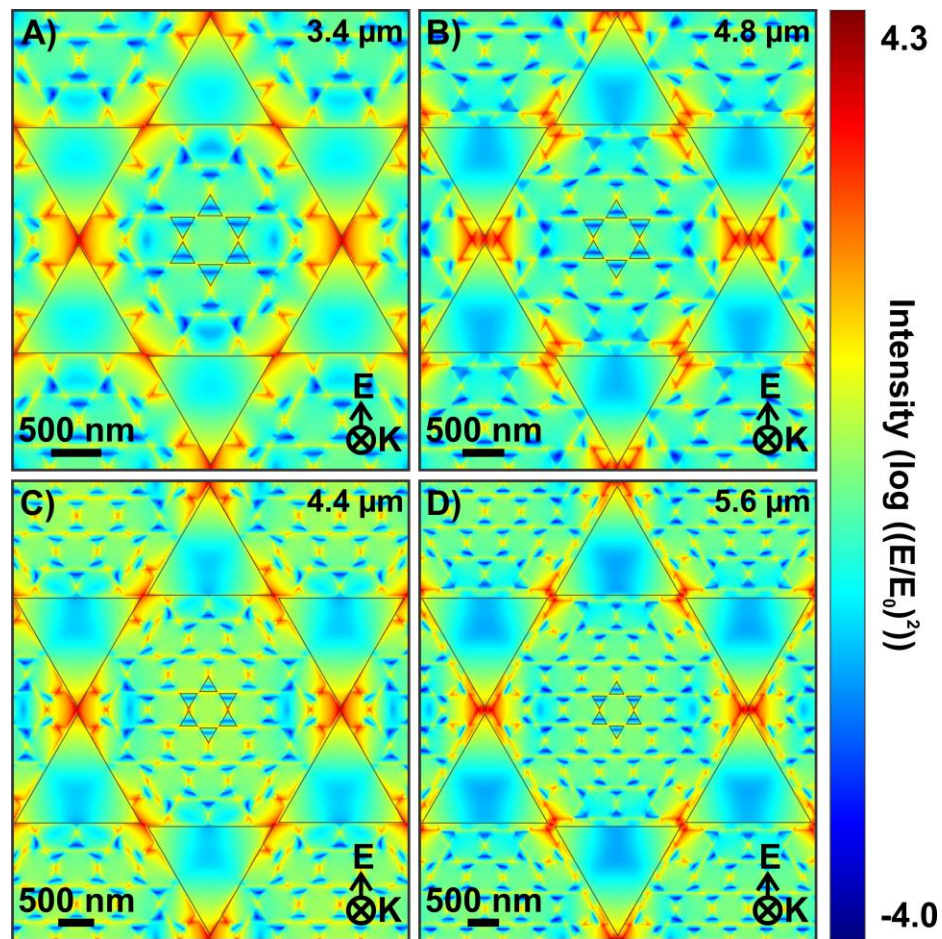


Figure 4.12 FDTD calculations of the transverse components of the electric field ($|E/E_0|^2$), log scale representation, for the superimposed patterns at the maximum absorbance at the stated wavelengths. Superimposed patterns of nanoprisms with side lengths of $0.25 \mu\text{m}$ and A) $1.25 \mu\text{m}$, B) $1.5 \mu\text{m}$, C) $1.75 \mu\text{m}$, and D) $2 \mu\text{m}$.

4.3.6 SEIRA Compatibility

SEIRA measurements were conducted on the 2 and 0.25 μm superimposed patterns functionalized with 4-NTP, or 4-mercaptophenylboronic acid (4-MPBA). 4-NTP was selected since it was the same molecule used in the SERS studies, whereas 4-MPBA, an alternative model molecule, although not probed by SERS in this study, has previously been used as a reporter for the detection of glucose, and glycans by SERS.⁵⁷⁻⁵⁸ The bright synchrotron source used with a FTIR microscope enabled high signal-to-noise ratio with fewer number of scans. Furthermore, due to the large density of hot-spots over the superimposed platforms, probing the full area with an intense beam yield intense signal with short collection time. For example, the spectrum shown in Figure 4.13A for the platform functionalized with a monolayer of NTP was acquired in 3 minutes only with 512 scans and with a 4 cm^{-1} spectral resolution.

As previously mentioned, altering the exposure dose during the EBL process allows for tuning of the resonance. Figure 4.13A and B highlight that these small differences lead to noticeably different enhancements of the SEIRA signal. In both cases, peaks corresponding to 4-NTP can be observed, with the two dominant absorptions corresponding to the symmetric NO_2 (1340 cm^{-1}) and antisymmetric NO_2 (1510 cm^{-1}) stretches. As well, two less intense absorptions near 1580 and 1595 cm^{-1} correspond to C=C stretching of the ring.⁵⁹⁻⁶⁰ Although the absorptions in Figure 4.13C are weaker, several characteristic peaks of 4-MPBA are present. These include stretches with contributions from the B-O of the boronic acid (1340 , 1370 , and 1405 cm^{-1}), and much like 4-NTP, an absorption near 1595 cm^{-1} corresponding to the C=C stretching of the ring.⁶¹

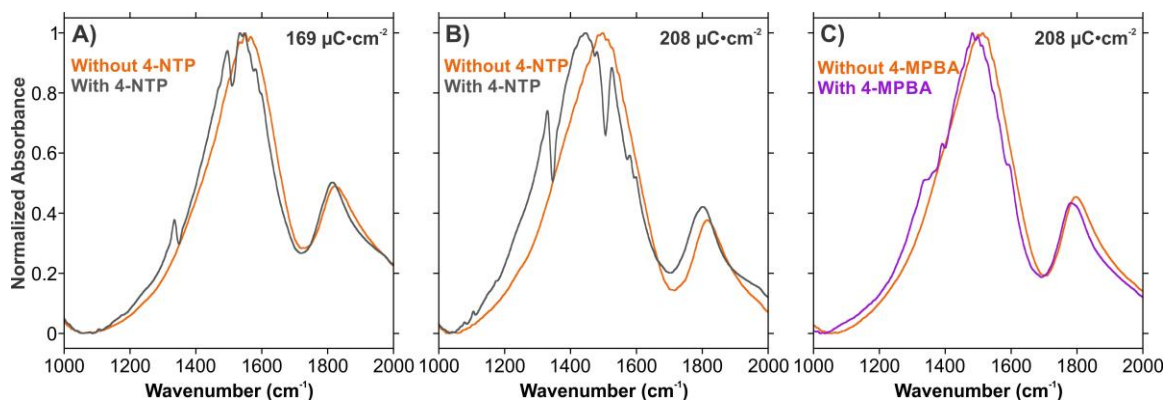


Figure 4.13 Comparison of infrared absorption 2 and 0.25 μm superimposed nanoprisms before and after functionalization with A) 4-NTP, B) 4-NTP, and C) 4-MPBA at the indicated exposure doses.

Although we are able to have enhancement of the vibrational signals in the fingerprint region, it should be possible to enhance vibrational signals at lower wavenumbers by increasing the size of the larger prisms. Such advancements are of interest as it would allow for the detection of key vibrational modes for amino acids, such as the ring of phenylalanine near 1000 cm^{-1} .⁶² Since our platform is both SERS and SEIRA compatible, it would be possible to acquire a more complete vibrational assignment for a molecule of interest. As well, changes to the vibrational fingerprint of a reporter molecule during guest-host interactions may also be probed. This would allow for the superimposed nanoprisms to act as a platform for multispectral sensing applications.

4.3.7 Multispectral Platform Comparison

One of the concerns when developing a structure or platform that has multispectral compatibility are enhancements that are lower than the commonly observed enhancements for an individual technique. As previously mentioned, gold nanorods exhibit multispectral compatibility depending on the wavelength of light, and the polarization of the incident light with respect to the orientation of the structure.⁴⁰ In addition, the Raman results may be biased considering that electronic resonances from the used of dyes are involved.³³ Although their SEIRA enhancement of 10^4 - 10^5 is comparable with both the literature and with the result from the present work, the SERS enhancement reported by d'Andrea *et al.* is $\sim 10^2$ which is lower than the 10^4 - 10^8 factor

often reported as a SERS enhancement factor.⁶³ Our modelling results that consider solely a EM contribution provide values for the SERS enhancement factor of $\sim 10^5$. Thus, our proposed structure offers a more consistent enhancement for the complimentary spectroscopic techniques of SERS and SEIRA.

Our superimposed pattern offers comparable enhancements for applications in SEF, SERS, and SEIRA with the three-arm log-periodic gold nanoantenna from Aouani *et al.*⁴¹ Although the platforms are both fabricated by EBL, ours is a relatively straightforward structure that can be fabricated by NSL thus reducing preparation time and fabrication cost. Instead of having to optimize the overall size of the antenna along with the number and dimensions of teeth, our structure is based on simple nanoprisms. The only parameters that need to be optimized are the side lengths of the triangles and the size of the inter-prism gaps. As shown in this work, altering the size of the triangles is a straightforward process, yielding only two series of platforms. Whereas a more complex structure would likely require significantly more optimization in order to achieve a homogeneous enhancement from the visible to mid-IR regions.

4.4 Conclusions

We have demonstrated the fabrication, characterization, and use of a multiresonant plasmonic platform with resonances spanning the visible to mid-IR regions. This is achieved by combining arrays of prisms comprised of small ($0.25 \mu\text{m}$) and large prisms ($1\text{-}2 \mu\text{m}$). Such patterns can be fabricated by NSL, or EBL. Once prepared, SEF, SERS, and SEIRA can all be performed on a single pattern, and as we have shown, all on the same substrate. By overlapping the structures, the intersection of the small and large prisms introduces new regions of EM enhancement in the visible region that further enhanced plasmon-mediated fluorescence and Raman scattering. Furthermore, the superimposed patterns offer comparable results between their non-superimposed counterparts in the visible region. The benefit of the superimposed patterns is best highlighted in the mid-IR region, as the overlap of the triangles introduces new resonances that may be used for SEIRA. By tailoring the size of the triangles, and the fabrication procedure, it is possible to finely optimize the resonance position of SEIRA. Further development of the superimposed patterns by optimizing the size of the small

nanoprisms will allow for even greater tunability in the visible and IR regions. As well, the incorporation of a reflective surface located beneath a dielectric layer may enable an increase in the SEIRA enhancement.⁶⁴ By embedding these structures within microfluidic channels,⁶⁵⁻⁶⁶ it may be possible to develop a multispectral and multi-technique platform for the detection of analytes at low concentrations.

4.5 References

1. Shimada, T.; Nakashima, H.; Kumagai, Y.; Ishigo, Y.; Tsushima, M.; Ikari, A.; Suzuki, Y., *J. Phys. Chem. C* **2016**, *120*, 534-541.
2. Kneipp, K.; Wang, Y.; Kneipp, H.; Perelman, L. T.; Itzkan, I.; Dasari, R. R.; Feld, M. S., *Phys. Rev. Lett.* **1997**, *78*, 1667-1670.
3. Nie, S.; Emory, S. R., *Science* **1997**, *275*, 1102-1106.
4. Wertz, E.; Isaacoff, B. P.; Flynn, J. D.; Biteen, J. S., *Nano Lett.* **2015**, *15*, 2662-2670.
5. Zheng, Y.; Soeriyadi, A. H.; Rosa, L.; Ng, S. H.; Bach, U.; Justin Gooding, J., *Nat. Commun.* **2015**, *6*.
6. Fleischmann, M.; Hendra, P. J.; McQuillan, A. J., *Chem. Phys. Lett.* **1974**, *26*, 163-166.
7. Albrecht, M. G.; Creighton, J. A., *J. Am. Chem. Soc.* **1977**, *99*, 5215-5217.
8. Jeanmaire, D. L.; Van Duyne, R. P., *J. Electroanal. Chem.* **1977**, *84*, 1-20.
9. Wang, H.; Liu, T.; Huang, Y.; Fang, Y.; Liu, R.; Wang, S.; Wen, W.; Sun, M., *Sci. Rep.* **2014**, *4*, 7087.
10. Choi, H.-K.; Park, W.-H.; Park, C.-G.; Shin, H.-H.; Lee, K. S.; Kim, Z. H., *J. Am. Chem. Soc.* **2016**, *138*, 4673-4684.
11. Hartman, T.; Wondergem, C. S.; Kumar, N.; van den Berg, A.; Weckhuysen, B. M., *J. Phys. Chem. Lett.* **2016**, *7*, 1570-1584.
12. Pallaoro, A.; Hoonejani, M. R.; Braun, G. B.; Meinhart, C. D.; Moskovits, M., *ACS Nano* **2015**, *9*, 4328-4336.
13. Cui, L.; Zhang, Y.-J.; Huang, W. E.; Zhang, B.-F.; Martin, F. L.; Li, J.-Y.; Zhang, K.-S.; Zhu, Y.-G., *Anal. Chem.* **2016**, *88*, 3164-3170.
14. Huefner, A.; Kuan, W.-L.; Müller, K. H.; Skepper, J. N.; Barker, R. A.; Mahajan, S., *ACS Nano* **2016**, *10*, 307-316.
15. Yang, Y.-Y.; Ren, J.; Li, Q.-X.; Zhou, Z.-Y.; Sun, S.-G.; Cai, W.-B., *ACS Catal.* **2014**, *4*, 798-803.
16. Hamad, S.; Krishna Podagatlapalli, G.; Ahamad Mohiddon, M.; Venugopal Rao, S., *Chem. Phys. Lett.* **2015**, *621*, 171-176.

17. Li, C.-Y.; Meng, M.; Huang, S.-C.; Li, L.; Huang, S.-R.; Chen, S.; Meng, L.-Y.; Panneerselvam, R.; Zhang, S.-J.; Ren, B.; Yang, Z.-L.; Li, J.-F.; Tian, Z.-Q., *J. Am. Chem. Soc.* **2015**, *137*, 13784-13787.
18. Wu, L.; Zeng, L.; Jiang, X., *J. Am. Chem. Soc.* **2015**, *137*, 10052-10055.
19. Arfaoui, I.; Bermúdez, V.; Bottari, G.; De Nadai, C.; Jalkanen, J.-P.; Kajzar, F.; Leigh, D. A.; Lubomska, M.; Mendoza, S. M.; Niziol, J.; Rudolf, P.; Zerbetto, F., *J. Phys. Chem. B* **2006**, *110*, 7648-7652.
20. Renger, J.; Quidant, R.; van Hulst, N.; Novotny, L., *Phys. Rev. Lett.* **2010**, *104*, 046803.
21. Yampolsky, S.; Fishman, D. A.; Dey, S.; Hulkko, E.; Banik, M.; Potma, E. O.; Apkarian, V. A., *Nat. Photon.* **2014**, *8*, 650-656.
22. Butet, J.; Brevet, P.-F.; Martin, O. J. F., *ACS Nano* **2015**, *9*, 10545-10562.
23. Ross, M. B.; Mirkin, C. A.; Schatz, G. C., *J. Phys. Chem. C* **2016**, *120*, 816-830.
24. Tabatabaei, M.; Najiminaini, M.; Davieau, K.; Kaminska, B.; Singh, M. R.; Carson, J. J. L.; Lagugné-Labarthet, F., *ACS Photonics* **2015**, *2*, 752-759.
25. Jahn, M.; Patze, S.; Hidi, I. J.; Knipper, R.; Radu, A. I.; Muhlig, A.; Yuksel, S.; Peksa, V.; Weber, K.; Mayerhofer, T.; Cialla-May, D.; Popp, J., *Analyst* **2016**, *141*, 756-793.
26. Hoffmann, J. M.; Yin, X.; Richter, J.; Hartung, A.; Maß, T. W. W.; Taubner, T., *J. Phys. Chem. C* **2013**, *117*, 11311-11316.
27. Zrimsek, A. B.; Henry, A.-I.; Van Duyne, R. P., *J. Phys. Chem. Lett.* **2013**, *4*, 3206-3210.
28. Aksu, S.; Cetin, A. E.; Adato, R.; Altug, H., *Adv. Optic. Mater.* **2013**, *1*, 798-803.
29. Huck, C.; Toma, A.; Neubrech, F.; Chirumamilla, M.; Vogt, J.; De Angelis, F.; Pucci, A., *ACS Photonics* **2015**, *2*, 497-505.
30. Lehmann, F.; Richter, G.; Borzenko, T.; Hock, V.; Schmidt, G.; Molenkamp, L. W., *Microelectron. Eng.* **2003**, *65*, 327-333.
31. Mayer, M.; Scarabelli, L.; March, K.; Altantzis, T.; Tebbe, M.; Kociak, M.; Bals, S.; García de Abajo, F. J.; Fery, A.; Liz-Marzán, L. M., *Nano Lett.* **2015**, *15*, 5427-5437.
32. da Silva, A. G. M.; Rodrigues, T. S.; Correia, V. G.; Alves, T. V.; Alves, R. S.; Ando, R. A.; Ornellas, F. R.; Wang, J.; Andrade, L. H.; Camargo, P. H. C., *Angew. Chem. Int. Ed.* **2016**, *55*, 7111-7115.
33. Genç, A.; Patarroyo, J.; Sancho-Parramon, J.; Arenal, R.; Duchamp, M.; Gonzalez, E. E.; Henrard, L.; Bastús, N. G.; Dunin-Borkowski, R. E.; Puentes, V. F.; Arbiol, J., *ACS Photonics* **2016**, *3*, 770-779.
34. Liu, S.-D.; Leong, E. S. P.; Li, G.-C.; Hou, Y.; Deng, J.; Teng, J. H.; Ong, H. C.; Lei, D. Y., *ACS Nano* **2016**, *10*, 1442-1453.

35. Hentschel, M.; Dregely, D.; Vogelgesang, R.; Giessen, H.; Liu, N., *ACS Nano* **2011**, *5*, 2042-2050.
36. Cherqui, C.; Bigelow, N. W.; Vaschillo, A.; Goldwyn, H.; Masiello, D. J., *ACS Photonics* **2014**, *1*, 1013-1024.
37. Liu, S.-D.; Yang, Z.; Liu, R.-P.; Li, X.-Y., *ACS Nano* **2012**, *6*, 6260-6271.
38. Gottheim, S.; Zhang, H.; Govorov, A. O.; Halas, N. J., *ACS Nano* **2015**, *9*, 3284-3292.
39. Hegde, R. S.; Khoo, E. H., *Plasmonics* **2016**, *11*, 465-473.
40. D'Andrea, C.; Bochterle, J.; Toma, A.; Huck, C.; Neubrech, F.; Messina, E.; Fazio, B.; Maragò, O. M.; Di Fabrizio, E.; Lamy de La Chapelle, M.; Gucciardi, P. G.; Pucci, A., *ACS Nano* **2013**, *7*, 3522-3531.
41. Aouani, H.; Rahmani, M.; Šípová, H.; Torres, V.; Hegnerová, K.; Beruete, M.; Homola, J.; Hong, M.; Navarro-Cía, M.; Maier, S. A., *J. Phys. Chem. C* **2013**, *117*, 18620-18626.
42. Kischkat, J.; Peters, S.; Gruska, B.; Semtsiv, M.; Chashnikova, M.; Klinkmüller, M.; Fedosenko, O.; Machulik, S.; Aleksandrova, A.; Monastyrskiy, G.; Flores, Y.; Ted Masselink, W., *Appl. Opt.* **2012**, *51*, 6789-6798.
43. Tabatabaei, M.; Sangar, A.; Kazemi-Zanjani, N.; Torchio, P.; Merlen, A.; Lagugné-Labarthe, F., *J. Phys. Chem. C* **2013**, *117*, 14778-14786.
44. Palik, E. D., Preface. In *Handbook of Optical Constants of Solids*, Academic Press: Burlington, 1997.
45. Lide, D. R.; Haynes, W. M., *CRC Handbook of Chemistry and Physics: A Ready-Reference Book of Chemical and Physical Data*; CRC Press: Boca Raton, 2009.
46. Fischer, U. C.; Zingsheim, H. P., *J. Vac. Sci. Technol.* **1981**, *19*, 881-885.
47. Fayyaz, S.; Tabatabaei, M.; Hou, R.; Lagugné-Labarthe, F., *J. Phys. Chem. C* **2012**, *116*, 11665-11670.
48. Flynn, J. D.; Haas, B. L.; Biteen, J. S., *J. Phys. Chem. C* **2015**.
49. Chen, K.; Rajeeva, B. B.; Wu, Z.; Rukavina, M.; Dao, T. D.; Ishii, S.; Aono, M.; Nagao, T.; Zheng, Y., *ACS Nano* **2015**, *9*, 6031-6040.
50. Nguyen, M.; Kanaev, A.; Sun, X.; Lacaze, E.; Lau-Truong, S.; Lamouri, A.; Aubard, J.; Felidj, N.; Mangeney, C., *Langmuir* **2015**, *31*, 12830-12837.
51. Jensen, T. R.; Duyne, R. P. V.; Johnson, S. A.; Maroni, V. A., *Appl. Spectrosc.* **2000**, *54*, 371-377.
52. Le Ru, E. C.; Etchegoin, P. G., *Chem. Phys. Lett.* **2006**, *423*, 63-66.
53. Valley, N.; Greeneltch, N.; Van Duyne, R. P.; Schatz, G. C., *J. Phys. Chem. Lett.* **2013**, *4*, 2599-2604.
54. Fano, U., *Phys. Rev.* **1961**, *124*, 1866-1878.

55. Luk'yanchuk, B.; Zheludev, N. I.; Maier, S. A.; Halas, N. J.; Nordlander, P.; Giessen, H.; Chong, C. T., *Nat. Mater.* **2010**, *9*, 707-715.
56. Galarreta, B. C.; Harte, E.; Marquestaut, N.; Norton, P. R.; Lagugne-Labarthe, F., *Phys. Chem. Chem. Phys.* **2010**, *12*, 6810-6816.
57. Tabatabaei, M.; Wallace, G. Q.; Caetano, F. A.; Gillies, E. R.; Ferguson, S. S. G.; Lagugne-Labarthe, F., *Chem. Sci.* **2016**, *7*, 575-582.
58. Wallace, G. Q.; Tabatabaei, M.; Zuin, M. S.; Workentin, M. S.; Lagugne-Labarthe, F., *Anal. Bioanal. Chem.* **2016**, *408*, 609-618.
59. Merklin, G. T.; He, L.-T.; Griffiths, P. R., *Appl. Spectrosc.* **1999**, *53*, 1448-1453.
60. Verger, F.; Nazabal, V.; Colas, F.; Némec, P.; Cardinaud, C.; Baudet, E.; Chahal, R.; Rinnert, E.; Boukerma, K.; Peron, I.; Deputier, S.; Guilloux-Viry, M.; Guin, J. P.; Lhermite, H.; Moreac, A.; Compère, C.; Bureau, B., *Opt. Mater. Express* **2013**, *3*, 2112-2131.
61. Parlak, C.; Ramasami, P.; Tursun, M.; Rhyman, L.; Kaya, M. F.; Atar, N.; Alver, Ö.; Şenyel, M., *Spectrochim. Acta A* **2015**, *144*, 131-138.
62. Wallace, G. Q.; Zuin, M. S.; Tabatabaei, M.; Gobbo, P.; Lagugne-Labarthe, F.; Workentin, M. S., *Analyst* **2015**, *140*, 7278-7282.
63. Le Ru, E. C.; Blackie, E.; Meyer, M.; Etchegoin, P. G., *J. Phys. Chem. C* **2007**, *111*, 13794-13803.
64. Brown, L. V.; Yang, X.; Zhao, K.; Zheng, B. Y.; Nordlander, P.; Halas, N. J., *Nano Lett.* **2015**, *15*, 1272-1280.
65. Galarreta, B. C.; Tabatabaei, M.; Guieu, V.; Peyrin, E.; Lagugne-Labarthe, F., *Anal. Bioanal. Chem.* **2013**, *405*, 1613-1621.
66. Limaj, O.; Etezadi, D.; Wittenberg, N. J.; Rodrigo, D.; Yoo, D.; Oh, S.-H.; Altug, H., *Nano Lett.* **2016**, *16*, 1502-1508.

Chapter 5

5 Dendritic Plasmonics for Mid-Infrared Spectroscopy

(A version of this work has been published in the *Journal of Physical Chemistry C*: Wallace, G.Q.; Foy, H.C.; Rosendahl, S.M.; Lagugné-Labarthe, F. *J. Phys. Chem. C*, **2017**, *121*, 9497-9507. This Chapter also contains work for a manuscript in preparation: Wallace, G.Q.; Eisele, M.; McRae, D.M., Lagugné-Labarthe, F.)

Metallic nanostructures that exhibit tailored optical resonances spanning from the near to mid-infrared spectral range are of particular interest for spectroscopic and optical measurements in these spectral domains that can benefit from localized surface-enhancement effects. Plasmon resonances shifted in the near or mid-infrared range could be used to further enhance the excitation and/or the emission of an optical process. Surface-enhanced infrared absorption (SEIRA) is one of such processes and can particularly benefit from plasmon-enhanced local fields yielding an increase in sensitivity towards the detection of an analyte. In this Chapter, fabricate a series of gold dendritic nanostructures, prepared by electron-beam lithography, that exhibit plasmon resonances spanning the near and mid-infrared spectral regions. We explore the influence of the number of branches of the dendritic structures, as well as the length of each generation together with the overall effect of the shape and symmetry on the resulting optical resonances. The creation of new resonances that appear upon newer fractal generation are explained using a hybridization model. Selected structures were then evaluated for SEIRA measurements towards analytes as either thin films or as a monolayer.

5.1 Introduction

The design and fabrication of conductive nanostructures for plasmon-enhanced spectroscopy has become a field of intense research due to their application in molecular sensing and biosensing.¹⁻⁵ Under ideal conditions, extreme sensitivity can be reached, pushing the performances of optical measurements in terms of spatial resolution,⁶⁻⁷ and sensitivity down to the single molecule level.⁸⁻¹⁰ Metallic nanostructures with rational dimensions and shapes can, in ideal experimental conditions, locally enhance and confine

an electromagnetic field that can be used as a local antenna either in collection (enhancement of the impinging light) or in emission (enhancement of the emitted field).¹¹ When a molecule of interest is placed in these nanoscale regions of electromagnetic enhancement, the magnitude of the enhanced vibrational spectra depends on numerous factors, including geometrical factors (i.e. the design of the structure with respect to an excitation wavelength and an input polarization), distribution and density of the molecular species over the structure and of the considered optical process. The field of molecular plasmonics relies on this interaction, and has been exploited to a variety of spectroscopic techniques, most notably for surface-enhanced Raman spectroscopy (SERS), tip-enhanced Raman spectroscopy (TERS) and surface-enhanced infrared absorption (SEIRA).¹²⁻¹⁴ In SERS or TERS, since the enhancement factor varies with the fourth power of E/E_0 , a minimal local field enhancement of a 10 fold factor will therefore yield a predicted enhancement of 10^4 .¹⁵ Many other linear or nonlinear optical measurements can benefit from such enhancement that scales with the considered optical process.¹⁶⁻¹⁸ In multiple waves mixing processes, the first difficulty is to enhance multiple wavelengths on distinct spectral ranges with a given structure. Being coherent processes, the second difficulty in diffraction limited nonlinear waves is to keep phase matching conditions: the nonlinear sources enhanced by the nanostructure must add up in phase to enable frequency conversion.¹⁹ Last, depending on the considered nonlinear process, this enhancement may depend on the symmetry of the metallic nanostructure.^{18, 20} Keeping in mind all these spatio-temporal critical factors, the possibility to tune multiple resonances over a large spectral domain could be further exploited in nonlinear optical vibrational spectroscopy such as sum-frequency generation or coherent anti-stokes Raman processes, yielding higher sensitivity.²¹

Critical to the field of molecular plasmonics is the tailoring of the localized surface plasmon resonance (LSPR) of the nanostructure such that it is in resonance or pre-resonance conditions with the impinging and or the emitted light. This is commonly achieved through a variety of methods including the alteration the chemical nature of the conductive metal, adjusting the size and shape of the nanostructures, the configuration of the nanostructures arrangement or changing the dielectric constant of the media that surrounds the platform. The development of plasmonic structures that exhibit SERS

compatibility is relatively straightforward as it is only necessary to have a resonance that covers a narrow spectral region that both overlaps the excitation and the Raman shifted photons. Expanding into the infrared remains a greater challenge as it is necessary to have enhancement over a broader spectral region ($500 - 4000 \text{ cm}^{-1}$, $2.5 - 20 \text{ }\mu\text{m}$).

To achieve the enhancement in the infrared range, different conceptual approaches can be undertaken. One means of achieving enhancement in the mid-infrared is by using colloidal metallic nanoparticles and forming a film.²²⁻²⁴ Although these platforms can be readily prepared, they often suffer from low enhancement and offer poor reproducibility. In addition, the use of a solvent to keep the integrity of the colloidal particles can be detrimental to the optical measurement. To overcome these limitations, structures prepared by lithographic techniques have emerged as means of fabricating structures that have LSPRs in the infrared. One of the most common classes of structures are nanorods. An advantage of this type of structure is that they can be readily produced using a variety of lithographic techniques including electron-beam lithography (EBL),^{13, 25-28} nanostencil lithography,²⁹⁻³⁰ nanoimprint lithography,³¹ and direct laser writing lithography.³²⁻³³ When fabricated as isolated structures, or as dashed lines, a single absorption is most often observed. Although it can be possible to tune the absorptions of such structures to a narrow portion of the infrared spectral region, introducing additional resonances, beyond the multipolar resonances, using a single rod is not possible.

Introducing multiple absorptions in the infrared spectral region can be achieved by incorporating structures with distinct sizes within the probed region.³⁴⁻³⁵ In these studies, the absorption of a given structure is individually tailored to a particular wavelength. By having multiples structures, multiple resonances are introduced. Another alternative to introducing multiple absorptions is to superimpose the nanostructures orthogonally to each other.³⁶ The resulting structure is capable of generating different absorptions simply by rotating the polarization of the impinging light. Although these methodologies have been successfully applied to measurements involving SEIRA, the resulting absorptions of the nanostructure are generally too narrow for the mid-infrared range, thus requiring many variations of the structure to yield multiple resonances with optimized spectral overlap. SEIRA has followed the early developments of SERS,³⁷⁻³⁹ but only recent work

by Neuman *et al.* has shed a new light on the mechanism of SEIRA.⁴⁰ Briefly, the role of scattering and absorption by the nanostructured metallic antenna were elegantly modelled highlighting that maximum enhancement was observed when both mechanisms, i.e. scattering and absorption, had similar spectral maxima magnitude. From such modelling work on linearly shaped antennas, it was concluded that tailoring the ratio between absorption and scattering losses could yield optimal structures for SEIRA. Such tailoring could be done by tuning the dimension and the aspect ratio of the antenna.⁴⁰

In the context of nanomaterials with resonances in the infrared spectral range and keeping in mind the observations reported above for vibrational spectroscopy applications, fractal and fractal-like structures have emerged as an interesting class of structure that are capable of exhibiting a greater number of resonances.⁴¹⁻⁴⁸ For many of these structures, nanorods and rod-like structures are used as the base units and are repeated radially, such as in the example of the Cayley Tree.⁴² Introduced as a plasmonic fractal, the Cayley Tree structures inscribed on quartz substrates showed spectral resonances that could be finely tuned between 880 and 4500 nm. However, no resonances were observed beyond 4500 nm due to the use of a quartz substrate that fully absorbs infrared light beyond this wavelength.⁴⁹ Furthermore, it is likely that due to the overall small size of the individual nanorods (100 – 180 nm) comprising the Cayley Tree, a significantly high number of generations would have been required to prepare structures with compatibility in the mid-infrared range. Finally, although the optical properties were well explored, no measurements were performed to ascertain the applicability of such a structure to analyte detection by SEIRA. In this study, we further expand on the use of nanorods as a means of generating dendritic fractals. In particular, we explore larger sized nanorods with different number of branches for the starting generation, along with the higher order generations as a means of preparing dendritic fractals that are compatible with SEIRA spectroscopy.

Here, EBL is used to prepare these structures onto CaF₂ optical windows that are mid-infrared compatible. With a resolution between 10-20 nm,⁵⁰ EBL is ideally suited to the fabrication of dendritic fractals in particular for the smallest structures present on the highest generations. Utilizing synchrotron radiation as the source of infrared light for our

measurements, we begin by using a three-branched dendritic fractal to explore how the optical properties of the dendritic fractal are altered as higher-order generations are developed. Through the use of finite difference time domain (FDTD) calculations, we evaluate the absorption spectra of the structure to the fractal composition at the fourth-order generation and we establish the wavelength spatial distribution of the plasmon resonances over the selected structure. We then introduce various means of tailoring the optical properties of the dendritic fractal across the near- and mid-infrared spectral regions. This is achieved by not only altering the size of the individual nanorods, but also by increasing the number of branches in the first-order generation. It was found that increasing the number of branches results can result in the branches becoming too tightly packed. Therefore, we also prepare truncated dendritic fractals as a means of further tuning the optical properties and measured their mid-infrared resonances. Last, the prepared platforms were functionalized with an analyte to demonstrate the compatibility of the structures for molecular plasmonics in the mid-infrared.

5.2 Experimental

5.2.1 Materials

CaF₂ substrates (13 mm diameter × 2 mm) were purchased from Spectral Systems LLC (NY, USA). Poly(methyl methacrylate) A2 950 resist and isopropanol were purchased from MicroChem Corp. (MA, USA). AquaSave was obtained from Mitsubishi Rayon America Inc. (NY, USA). Acetone (CHROMASOLV), and 4-nitrothiophenol (4-NTP) were procured from Sigma-Aldrich (MO, USA).

5.2.2 Electron-Beam Lithography

CaF₂ windows were first cleaned by reactive O₂ plasma for 20 minutes to ensure adhesion of the thin film of resist. Details of the process for EBL are described in detail in Appendix C. Prior to imaging the structures by SEM, the sample was coated with 5 nm of osmium. The sample used for imaging was the sample used to acquire the infrared absorption spectra.

5.2.3 Infrared Absorption and Surface-Enhanced Infrared Absorption

Fourier transform infrared (FT-IR) spectroscopy measurements were performed at the Mid-IR beamline synchrotron facility located at the Canadian Light Source (Beamline 01B-01). Information regarding the set-up at the beamline end station is provided in section 2.5.2 and Figure 2.13. The apertures size chosen (1.5) allowed for the beam diameter to be slightly smaller than the $50 \times 50 \mu\text{m}^2$ patch. Measurements were collected from $8000\text{-}800 \text{ cm}^{-1}$ with a spectral resolution of 4 cm^{-1} . Each spectrum is the average of 512 spectra. For SEIRA, the samples were coated with a thin layer of PMMA or functionalized for 6 hours in a freshly prepared 10^{-3}M solution of 4-nitrothiophenol (4-NTP) prepared in dry ethanol. After 6 hours, the solution was dipped in dry ethanol to remove any unbound 4-NTP and was dried under air.

5.2.4 Electromagnetic Field Modelling

Finite-difference time-domain (FDTD) modelling (Lumerical) was used to simulate the absorption and electromagnetic fields of the dendritic fractals. Shown in the text, the individual nanorods that the dendritic fractal was comprised of had lengths of 200 nm, widths of 50 nm, heights of 20 nm for gold, and 3 nm of titanium placed beneath the gold. Palik dielectric values for gold and titanium were used for the FDTD calculations.⁵¹ The structures were placed on a substrate with a constant refractive index of 1.42 representing the CaF_2 window, and had a thickness of 250 nm. Periodic boundaries on the x and y axes conditions were no smaller than 700 nm, and were representative of the periodicity of the fabricated structure. Last, a perfectly matched layer (PML) was used in the z axis. Mesh sizes of 7.5 nm were used in the x and y axis and 4 nm in the z axis.

5.3 Results and Discussion

5.3.1 General Optical Properties of Dendritic Fractals

The dendritic fractals shown in Figure 1 are based on the Cayley Tree structures first used by Halas *et al.*⁴² In their work, the structures, that were inscribed up to the 3rd generation, did not show any resonance in the mid-infrared range due to the cut-off wavelength of the quartz substrates ($4.5 \mu\text{m}$).⁴⁹ Here, we have made use of CaF_2 that has

a cut-off closer to 10 μm , providing access to the fingerprint region from 1000 to 1800 cm^{-1} .^{33, 35}

To investigate the influence of fractal generation on the optical properties, structures were fabricated up to the fourth-order generation, as shown in the SEM images Figure 5.1A-D. Each gold rod of the dendritic fractal had a thickness of 20 nm, a width of 50 nm, and the rod elements forming the fractals shown in Figure 5.1A-D had lengths of 200 nm. Beneath each structure was a titanium adhesion layer of 3 nm. The structures were fabricated in $(50 \times 50) \mu\text{m}^2$ arrays, with varying periodicities. A sufficiently large gap (at least 700 nm) between the adjacent fractals was used to ensure that no plasmon coupling occurred between fractals.

The infrared absorption measurements taken for each sample shown in Figure 5.1A-D are shown in Figure 5.1E-H together with the calculated spectra. In order to maximize the signal-to-noise ratio of our infrared measurements, the mid-infrared beamline of a synchrotron was used. In a previous study done by our group, a comparison between the use of the CLS mid-infrared beamline synchrotron source and a conventional FT-IR source showed no change in the spectral position for the absorptions of superimposed nanoprisms.³⁵ Thus, the spectral location of the absorptions can be described as being source independent.

Beginning with the first-order generation, a single absorption at 5500 cm^{-1} was observed. Although such an absorption is not particularly relevant for SEIRA, it may be of value for other surface-enhanced spectroscopies, specifically surface-enhanced near-infrared absorption (SENIRA),⁵² and surface-enhanced Raman spectroscopy (SERS).⁵³ As a technique, SENIRA probes the vibrational overtones associated with the infrared vibrational modes that can be probed by SEIRA.⁵² Although not explored in this study, the ability to have a plasmonic platform that is compatible with both SEIRA and SENIRA may be of interest, as it could provide a more complete vibrational fingerprint for a molecule of interest. SERS measurements predominantly rely on the use of visible light. More recently, there has been an interest in developing platforms compatible with longer wavelengths, such as 1550 nm (6452 cm^{-1}) because these longer wavelengths are

retina-safe.⁵³ Although the results of the dendritic fractal (Figure 5.1E-H) do not have absorptions at such a wavelength, it should be possible to tune the absorptions to such a wavelength. In doing so, the dendritic fractal could then potentially be used for SEIRA, SENIRA, and SERS.

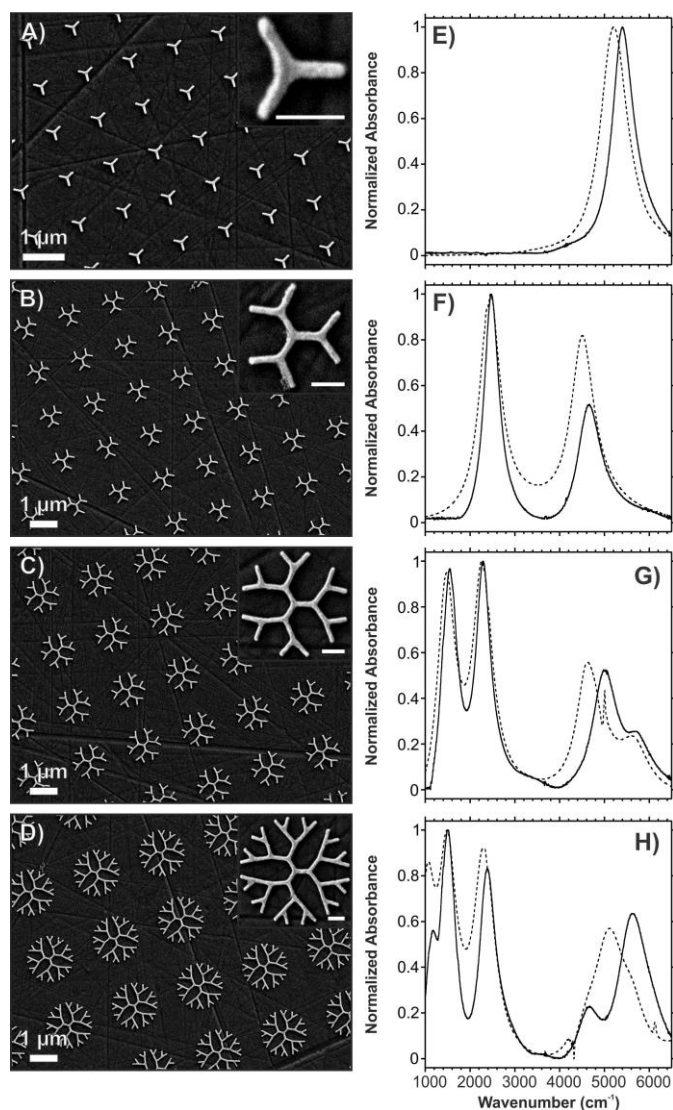


Figure 5.1 Scanning electron micrograph of dendritic fractals in the A) first, B) second, C) third, and D) fourth-order generations. E-H) Corresponding experimental (solid line) and calculated (dashed line) absorption spectra for each of the generations. The scale bar in the inset SEM images is 200 nm.

Beginning with the first-order generation, a single absorption at 5500 cm^{-1} was observed. Although such an absorption is not particularly relevant for SEIRA, it may be of value for other surface-enhanced spectroscopies, specifically surface-enhanced near-infrared absorption (SENIRA),⁵² and surface-enhanced Raman spectroscopy (SERS).⁵³ As a technique, SENIRA probes the vibrational overtones associated with the infrared vibrational modes that can be probed by SEIRA.⁵² Although not explored in this study, the ability to have a plasmonic platform that is compatible with both SEIRA and SENIRA may be of interest, as it could provide a more complete vibrational fingerprint for a molecule of interest. SERS measurements predominantly rely on the use of visible light. More recently, there has been an interest in developing platforms compatible with longer wavelengths, such as 1550 nm (6452 cm^{-1}) because these longer wavelengths are retina-safe.⁵³ Although the results of the dendritic fractal (Figure 5.1E-H) do not have absorptions at such a wavelength, it should be possible to tune the absorptions to such a wavelength. In doing so, the dendritic fractal could then potentially be used for SEIRA, SENIRA, and SERS.

For the dendritic fractals, we observed that in the N^{th} generation, the infrared spectra were dominated by N resonances. As higher-order generations were probed ($N > 1$), additional resonances were found at lower wavenumbers. As it has been previously described, the dominant absorptions presumably correspond to various dipolar modes of the structure at each generation. Reciprocally, the weaker absorptions near 5800 cm^{-1} and 4700 cm^{-1} , were observed for the third-order generation (Figure 5.1G) and fourth-order generation (Figure 5.1H) respectively, and are assigned to the quadrupolar resonances of the structure. The dendritic fractal was also inscribed for the fifth-order generation, shown in Figure 5.2A. However, we were unable to introduce any new dominant absorption bands at lower wavenumbers (Figure 5.2B). This is most probably because in the fourth-order generation, the lowest energy absorption was near 1200 cm^{-1} , very close to the cut-off limitation of the CaF_2 substrate. At the fifth-order generation, the new low energy absorption would likely be lower than 1000 cm^{-1} , and could not be probed. So, although higher-order generations are within the fabrication limitations, they cannot be exploited in the mid-infrared range.

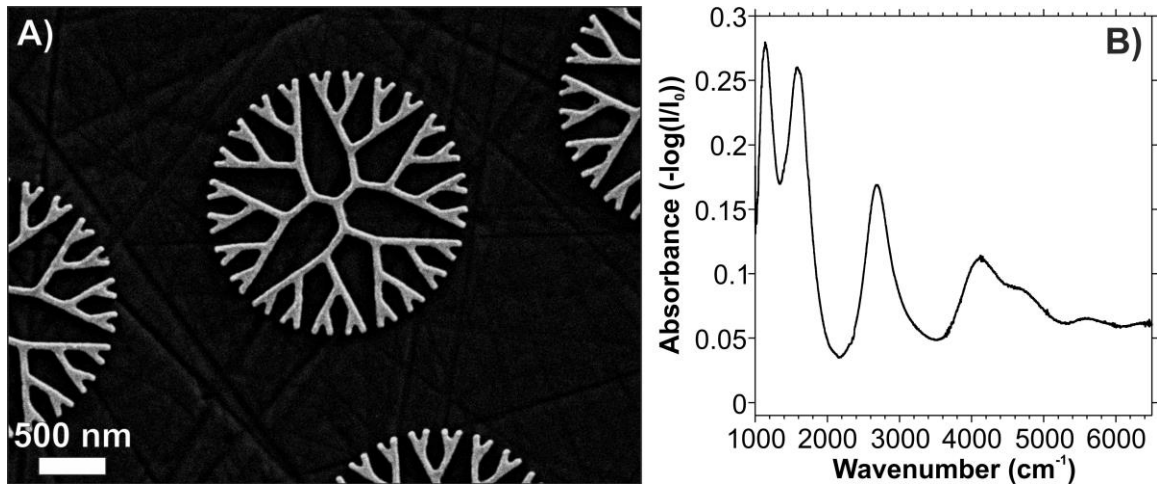


Figure 5.2 A) Scanning electron micrograph of fifth order generation three branched dendritic fractal and B) the corresponding absorption spectrum.

In order to correlate the resonances and their spatial localization with the generation order of the dendritic fractal, a plasmon hybridization model was used.⁵⁴⁻⁵⁶ In Figure 5.3, the calculated spectra and associated field enhancements for the first four generations of the dendritic fractals are calculated between 1000 and 7000 cm^{-1} using finite difference time domain (FDTD) calculations. When going from the first-order generation to the fourth-order generation, the number of resonances increases from 1 to 5. Since these structures are composed of concentric features (i.e. the dendron that forms the iterative fractal components), the hybridization model appears relevant to explain the major resonances together with the electric field distribution. For the lower-order generations of the fractal, the initial resonance(s) splits into two resonances with high (HE) and low (LE) energies (Figure 5.3). When going from the first to the second-order generations, the initial single mode that appears at $\lambda=1.92 \mu\text{m}$ is split into two modes with wavelengths of $\lambda=2.22 \mu\text{m}$ (HE) and $\lambda=4.06 \mu\text{m}$ (LE). To better understand this splitting, we proposed a hybridization model that combines the structure from the first-order generation (G1), along with the outer-most structures that were introduced in the second-order generation (G2-G1) (Figure 5.4). This approach provides the most physically acceptable energetic assignments accounting for the modes of G1 and G2-G1.

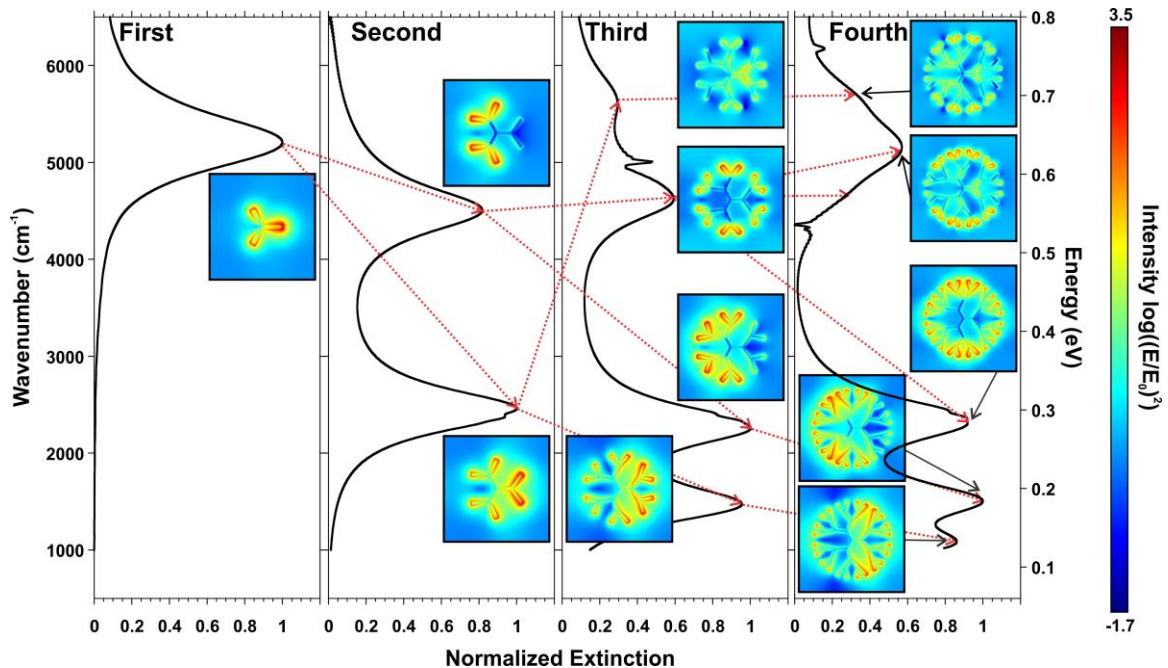


Figure 5.3 Normalized extinction spectra for first, second, third, and fourth-order generation dendritic structures with individual rod lengths of 200 nm. For each generation, the normalized electric field distribution $(E/E_0)^2$ under horizontal polarization was calculated for each resonance and displayed using log scale for clarity. The plasmon hybridization (red dashed line) is shown upon iteration of the fractal generation.

The third-order generation shows four modes hybridized from the second-order generation structure located at $\lambda=1.75 \mu\text{m}$ (HE1) and $\lambda=6.62 \mu\text{m}$ (LE1) as well as $\lambda=2.14 \mu\text{m}$ (HE2) and $\lambda=4.42 \mu\text{m}$ (LE2), respectively (Figure 2). A similar approach was used for the hybridization model (Figure 5.4), where the parent structures of the second-order generation (G2) and the outer-most structures of the third-order generation (G3-G2) were combined. Moving to the fourth-order generation shows a more complex spectrum with overlapping resonances. Here, the electric field enhancement is calculated only for the five major resonances derived from the previous generation. Once again, the hybridization of the plasmon modes between the previous generation and that of the newly introduced structures can tentatively be used to explain the newer resonances that appear at $\lambda=1.78, 1.95, 4.38, 6.72$ and $9.36 \mu\text{m}$. When higher order generations above the

fourth-order are calculated, very little spectral difference can be observed experimentally (Figure 5.2A) or from calculation (not shown).

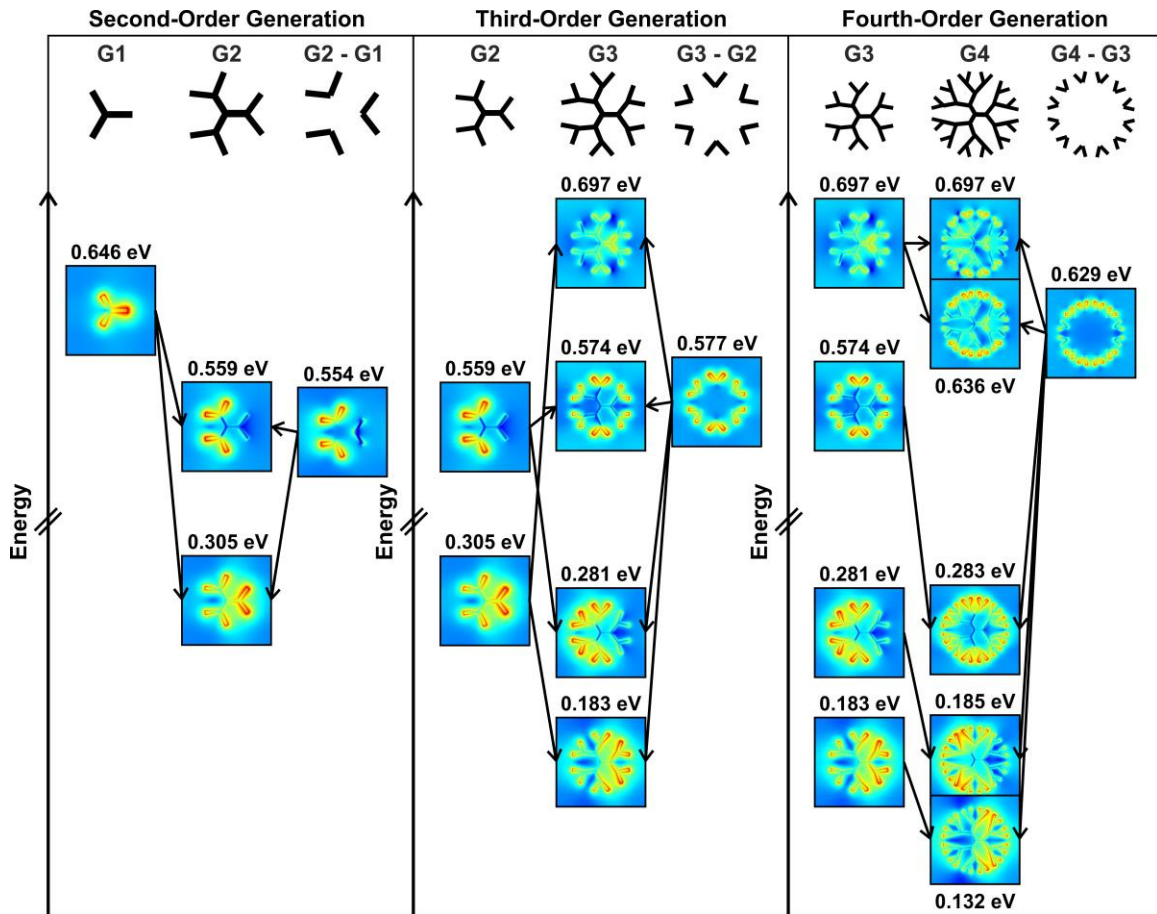


Figure 5.4 Hybridization model for the dendritic fractal at the second- through fourth-order generations. For each model, the electric field maps are shown at the energies corresponding to the resonances of the structure. In addition, a schematic illustration of the structure used in the model is shown.

Details on the resonances observed in the fourth-order generations structures are provided in Figure 5.5. The electric field distribution over the structure were calculated for selected input wavelengths that correspond to the four major resonances as shown in the spectrum of Figure 1H and Figure 2. Two orthogonal polarizations (0° and 90°) were selected for these calculations.

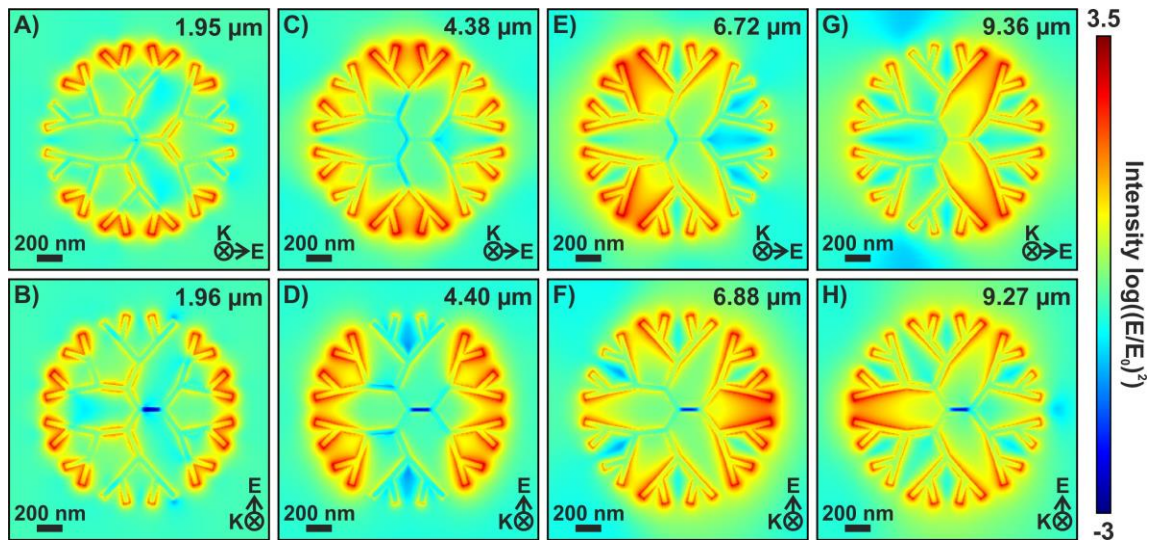


Figure 5.5 FDTD calculations of the transverse components of the electric field $(E/E_0)^2$: log scale representation at wavelengths corresponding to the absorptions of the fourth-order generation dendritic fractal comprised of gold nanorods with side lengths of 200 nm.

Examining the electric field distribution maps, shown in Figure 5.5, highlights a well-defined relationship between the fractal order and the spatial distribution. Starting with the highest energy absorptions (Figure 5.5A,B), the electric field is enhanced in the branches introduced in the fourth generation. By altering the polarization of the impinging light, it is possible to selectively excite the LSPRs across the entirety of the outer periphery of the structure. Moving to the second highest energy (Figure 5.5C,D), the enhancement now incorporates the branches from the third and fourth generations. As the absorptions move to lower energies (Figure 5.5E-H), each absorption incorporates the branches from an additional generation, until as shown in Figure 5.5G,H, the LSPR is spread over the whole structure. It is necessary to note that in this work, the absorptions closer to the fingerprint region are the most important since they will be used to enhance the absorption fingerprint of the analyte. Therefore, ensuring that absorption(s) of the structure are in this region is critical. Furthermore, the intensity of the electric field at these regions must also be considered. The electric field distribution map of Figure 5.5 provides an estimated (E^2/E_0^2) enhancement of $10^{3.5}$. This enhancement lies within the range of 10^2 - 10^5 that is experimentally observed for SEIRA compatible nanostructures.

To better visualize the spatial distribution of the multiple resonances, the iso-wavelength maps at the orthogonal polarizations were calculated (Figure 5.6).⁵⁷ In this representation, each map is first calculated at 44 discrete wavelengths over a spectral range of 1.4 – 10 μm . For each polarization, this forms a 3rd rank tensor of dimensions X(308), Y(308) and $\lambda(44)$. For each (x,y) spatial location, the tensor is then analyzed along the λ direction, and the λ max is extracted and assigned to an (x,y) spatial position. This representation forms a new matrix of (X,Y) that represents the distribution of the λ_{max} associated with the multiple resonances and that we refer to as the iso-wavelength maps.

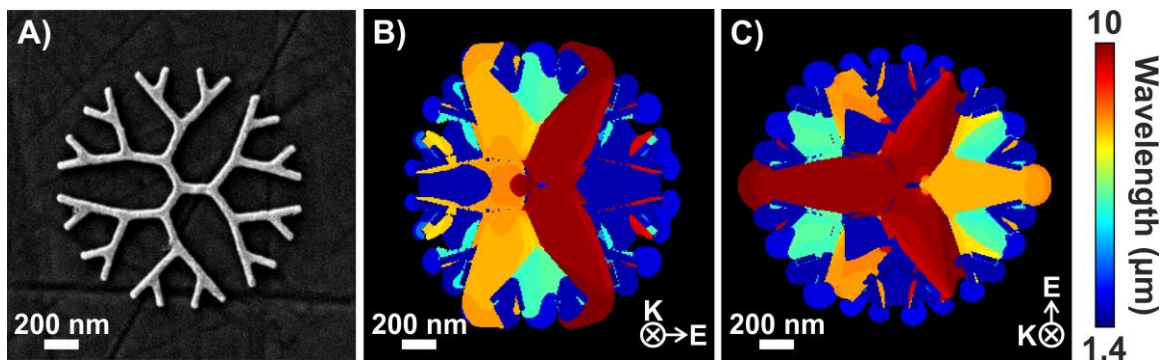


Figure 5.6 A) SEM image of the fourth-order generation fractal where the side lengths are 200 nm. Colour coded map of iso-wavelength distribution representing the distribution of the maximum electric field for a B) x - and C) y -polarized input field.

These iso-wavelength maps are shown for both orthogonally-polarized input sources (Figure 5.6B and C). Using the SEM image in Figure 5.6A for reference, the variation of the wavelength corresponding to the electric field maximum can be seen as an overlap of the results shown in Figure 5.5. Under varying polarizations of the input electric field, it is once again observed that the outer branches correspond to higher energy wavelengths, whereas the inner most branches coupled with the outer branches exhibit stronger electric fields at lower energies. Owing to the configuration of the three-branched dendritic fractal, only a few branches of the structure contribute to the enhancement of the electric field. As such, the fabrication of dendritic fractals with a greater number of initial branches may lead to improved enhancement of the electric field, yielding greater enhancement for measurements in molecular plasmonics. Importantly, the iso-wavelength

maps show an interesting polarization-dependence that can be further exploited. In Figure 5.6B, the distribution of maximum wavelength is asymmetric with respect to the polarization direction. This implies that the left part of the structure is predominantly subject to shorter wavelength resonances meanwhile the right part display resonances at longer wavelengths. For the orthogonal polarization direction, that does not match any symmetry axes of the structure, the iso-wavelength map shows that longer wavelengths are confined in the inner cavity formed by the longer branches of the structure. Such symmetry effects could potentially be used for optical processes where symmetry of the structure is critical with respect to the input field. The proposed structure could potentially be active for second-order non-linear optical processes due to its absence of an inversion center. This also implies that the rotation of the input polarization in this structure with 3-fold symmetry will enable each plasmon resonance to be tuned on demand in selected part(s) of the structure.

5.3.2 Increasing the Size of the Dendritic Fractal

As has been described, the spatial location of the absorptions is related to the overall shape of the dendritic fractal and the input polarization direction. However, tuning the absorptions of the structure based exclusively on the number of generations is not ideal as it may not be possible to tune absorptions across spectral range spanning from near to mid-infrared. Therefore, to bridge the spectral gap, it is necessary to turn to alternative means for spectral tuning.

A common procedure for tuning plasmonic properties is by altering the size of the individual building blocks that compose the nanostructure.⁵⁸ In this study, the lengths of the individual rods of the dendritic fractal were varied from 200 – 400 nm. This range of size was selected as it was believed that such structures would offer the ability to have a greater number of absorptions closer to the fingerprint region, as opposed to the sizes previously studied for the Cayley Tree fractal (100 – 180 nm).⁴²

As expected, increasing the size of the individual nanorods within the dendritic fractal results in a red-shift of the absorptions (Figure 5.7). It was found that for the structures probed, a spectral shift of 6-7 nm was introduced for every 1 nm increase in the length of

the nanorods. With such a high degree of spectral tunability, it was possible to shift the absorption of the first-order generation absorption from 5500 cm^{-1} to 3150 cm^{-1} simply by increasing the size of the nanorods from 200 to 400 nm (Figure 5.7A). It is important to note that in studies involving isolated nanorods for applications involving SEIRA, the lengths of the rods are required to be longer. For example, gold nanorods with lengths of 710 nm, widths of 60 nm, heights of 55 nm, with a spacing of 50 nm between adjacent nanorods, had an absorption at 3093 cm^{-1} .⁵⁹ With the dendritic fractals, it is possible to achieve a similar absorption using nanorods that are approximately half the size. This is because in the dendritic fractal, the nanorods are connected to each other. As such, although the individual nanorods are 400 nm, the entire length of the resulting first-order dendritic fractal is 600 nm along the x -, and 692 nm along the y -directions.

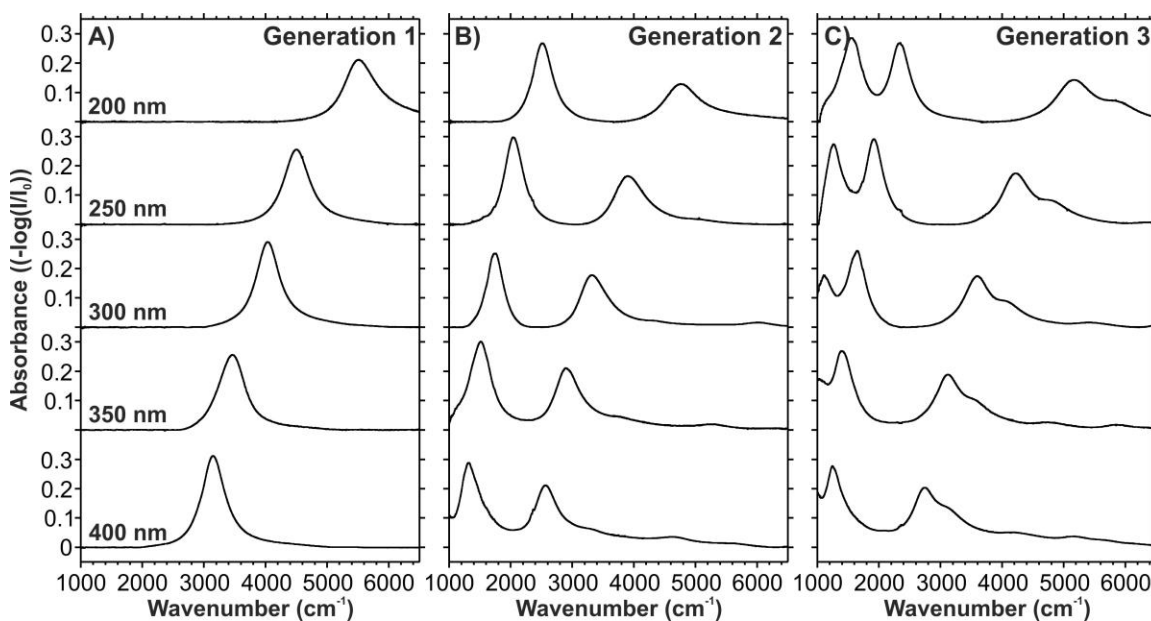


Figure 5.7 Infrared absorption of three-branched dendritic fractal at the A) first, B) second, and C) third-order generations with the side lengths indicated in A).

Examining the second-order generation dendritic fractal (Figure 5.7B), the same red-shift of 6-7 nm spectral shift for every 1 nm increase in length, is observed for each absorption. The same spectral shift is also observed for the third-order generation in Figure 5.7C. However, it is necessary to note that increasing the size of the nanorods too much eventually leads to a diminishing return. As was the case for expanding beyond the

fourth-order generation, if the individual nanorods become too large (such as 350 and 400 nm), it is no longer possible to observe all the absorptions. The absorption corresponding to the global plasmon resonance of the structure is lost due to the CaF_2 cut-off. Therefore, in addition to the limitation of the number of generations, there is a limitation in terms of structure size that must also be considered when fabricating dendritic structures for applications in plasmonics.

Further tuning of the spectral positions of the absorption could be investigated in future work. For example, when the lengths of the nanorods were increased, this was applied to all rods within the structure. One can envision a structure where the branches corresponding to each generation are of different lengths. The likely result of such a structure is that the total number of absorptions would remain the same whilst a spectral shift is observed for each absorption. If the desire is to have the greatest number of absorptions, an alternative method would be required. Here, each arm of the dendritic fractal would have nanorods with different lengths. The resulting absorption spectrum of such a structure could be viewed as a combination of the spectra obtained when each individual length was studied, as was done in this study (Figure 5.7).

5.3.3 Increasing the Number of Branches

Thus far, the emphasis of spectral tuning has been placed on the generation order and the size of the individual nanorods within the structure. Since the shape of the dendritic fractal can be altered by increasing the number of branches within the first generation, there may exist yet another means of tuning the absorptions. Figure 5.8A shows that as the number of branches in the first-order generation increases from 3 to 8, a noticeable blue shift from 4428 cm^{-1} to 4815 cm^{-1} is observed. For the second-order generation fractals, the number of branches is still based on $n - 1$. This implies that the second-order generation for the dendritic fractal would only be explored for up to $n = 6$. This is because as n increases, the available space decreases for the outer generations. At $n = 8$, there is likely to be insufficient space to have 7 branches that are fully resolved. The second-order generation fractals exhibit a significant blue-shift for the higher energy absorptions (Figure 5.8B). The lower energy absorption, corresponding the global plasmon resonance is less influenced by the increase in the number of branches in the

first generation. Beyond introducing a blue-shift, increasing the number of branches has an additional benefit to the plasmon tuning ability of the structure. As shown in Figure 6A, increasing the number of branches from 3 to 8 decreases the polarization dependence for both orthogonal polarizations. This can be explained based on the overall size of the structure. As the number of branches increases, the resulting dendritic fractal adopts a structure that bears a stronger resemblance to a circle. Since structures such as plasmonic nanodiscs do not exhibit a strong dependence on the input polarization, it is unsurprising that the dendritic fractals with a greater number of branches would exhibit similar optical properties.

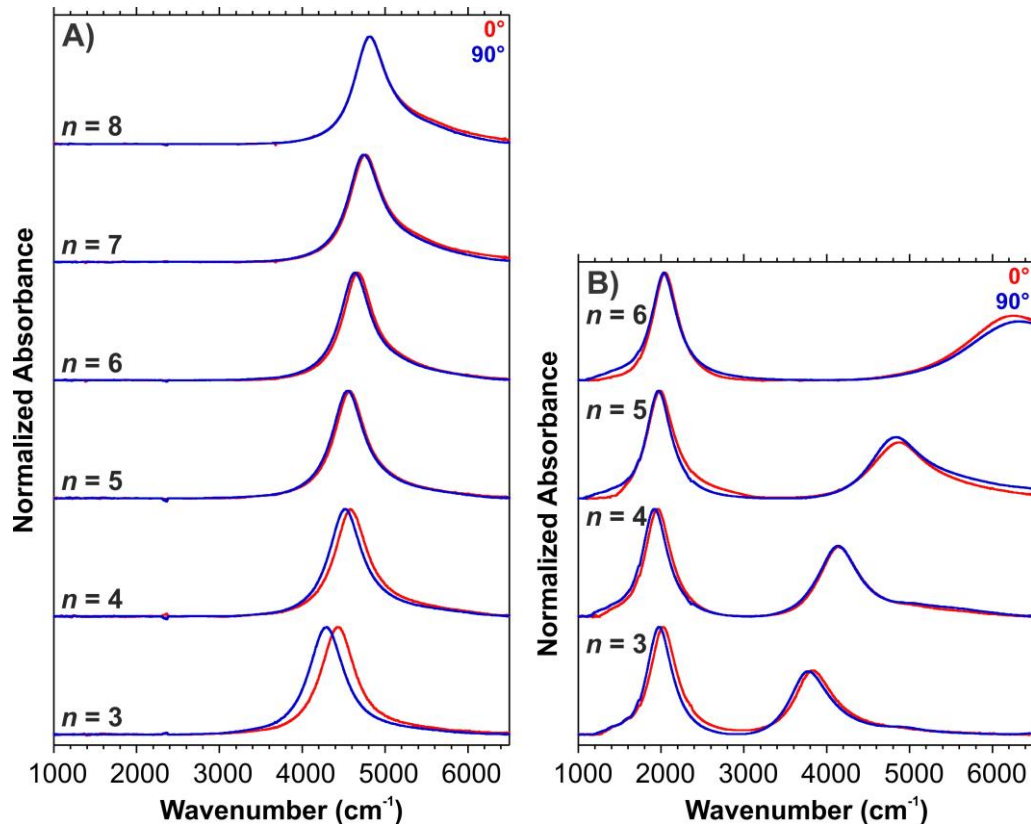


Figure 5.8 Infrared absorption spectra of dendritic fractals with the indicated number of inner branches probed with orthogonal polarizations for A) first and B) second-order generations with side lengths of 300 nm.

It was possible to fabricate the typical second-order generation dendritic fractal comprised of 5 inner branches (Figure 5.8B). When fabricated, increasing to the third-

order generation results in a dendritic fractal such as the one that is shown in Figure 5.9A. The branches of the outer generation are not fully resolved, due to a limitation during the fabrication process. As the pattern is being written, rods that are overlapping or are very close together, are exposed to the electron beam multiple times. This yields an effective dose that is greater than the nominal exposure dose. Instead of having isolated branches, the branches are instead connected, yielding a “duck foot” like structure. Since it is not possible to add additional space to the pattern, the only means to solve this issue is to remove branches in the outer generation. These new dendritic patterns are hereby described as being truncated dendritic fractals.

Truncating the outer generation of the third-order generation dendritic fractal yields the structure in Figure 5.9B. A comparison of the absorption spectra of the original and truncated from Figure 5.9A,B is shown in Figure 5.9C. Examining the spectra shows that truncating the fractal does not alter the spectral position of the lower energy absorption. The higher energy absorptions are significantly different between the two spectra. For the original fractal, the higher energy absorptions do not bear a resemblance to the spectral pattern from the second-order generation absorption spectrum. By truncating the fractal, we not only have our nanorod structure, we also have higher energy absorptions that are closer to those that were observed in the second-order generation dendritic fractal.

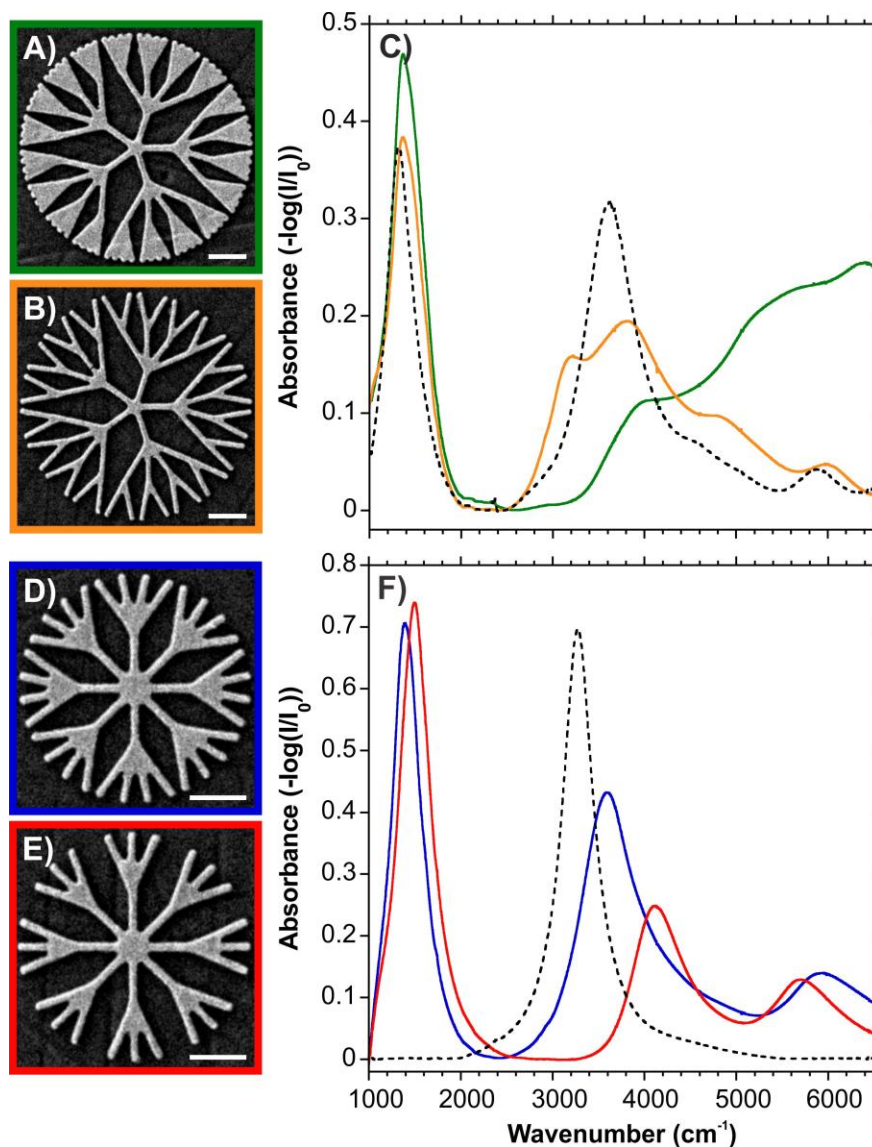


Figure 5.9 SEM images of the third-order generation of a five-branched dendritic fractal that is A) original and B) truncated. C) Absorption spectra of the fractals from A and B. The dashed spectrum corresponds to the second-order generation five branched dendritic fractal. D and E) SEM images of truncated second-order generation of an eight-branched dendritic fractal. F) Absorption spectra of the truncated fractals from D and E. The dashed spectrum corresponds to the first order generation eight branched dendritic fractal. The fractals are comprised of nanorods with lengths of 400 nm. The scale bar in the SEM images is 400 nm.

The process of truncating the dendritic fractal was also performed on second-order generation structures. This was necessary when the number of inner branches was high. Figure 5.9D,E show two possible configurations for truncated 8 branched second-order generation dendritic fractals. In the first configuration, three of the outer seven branches are removed (Figure 5.9D), and in the second four of the branches are removed (Figure 5.9E). The comparison of the absorption spectra of the resulting structures once again shows that the lower energy absorption, here corresponding to the global plasmon resonance of the structure, is only marginally altered (Figure 5.9F). Much like the case for the 5 branched structures, the absorptions at higher wavenumbers are altered, most notably the absorptions near 3600 and 4200 cm^{-1} . It is important to note that although there is a spectral location difference between these absorptions relative the first order generation, the overall profile of the absorption remains similar. Much like the case of the third order truncated dendritic fractal from Figure 5.9B, the truncation prevents the formation of duck feet, allowing for an absorption spectrum that bears a stronger resemblance to the previous generation. When structures are brought in closer proximity to each other, there is a red-shift in the LSPR. In the case of the truncated fractal shown in Figure 5.9D, the outer branches of each arm are close together (<50 nm). As such, those branches can couple together, and would yield a red-shift in the LSPR relative to a structure that has the rods placed further apart (Figure 5.9E). For both sets of structures, there are more resonances observed than what would be expected based on the prior results (Figure 5.1). This is attributed to the increase in size of the nanorods from 200 to 400 nm, which doubles the overall size of the fractal. Due to the overall size of the resulting structures (2.4 μm for Figure 5.9A,B and 1.6 μm for Figure 5.9D,E), we attribute these other absorptions to the multipolar resonances of the fractal.

5.3.4 Surface-Enhanced Infrared Absorption of a Thin Film

To correlate the regions of electromagnetic enhancement to the detection of an analyte, a 30 nm thin film of PMMA was spin coated onto the surface. PMMA thin films are well established probe analytes for SEIRA measurements due to the intense C=O stretching mode between 1720-1740 cm^{-1} . This vibrational mode can either be looked at exclusively,⁶⁰⁻⁶³ or with other vibrational modes in the fingerprint (1000-1800 cm^{-1})

and/or asymmetric C–H stretching (2950–3000 cm^{-1}) regions.^{26, 33–34, 36, 43, 64} A comparison between the normalized absorbance spectra for the dendritic fractals before and after coated with PMMA shows that there is a noticeable red-shift in the resonance positions once coated with a 30 nm thin film of PMMA (Figure 5.10). This is to be expected due to the change in refractive index of the media surrounding the dendritic fractals

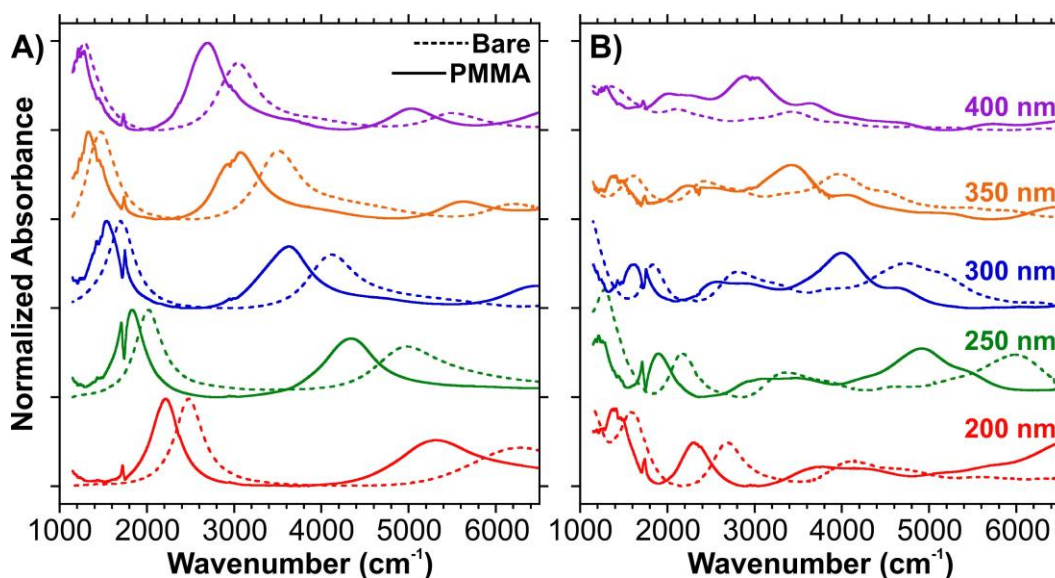


Figure 5.10 Comparison between bare and PMMA coated dendritic fractals for side lengths varying from 200 to 400 nm. A) Five-branched second-order generation, and B) three-branched fifth-order generation.

To obtain the absorbance difference spectra, a running average fit is applied to the absorbance spectra (Figure 5.11A,B). In experimental conditions where the plasmonic resonance is tuned with the vibrational oscillation of the molecule, a sharp negative dip appears at the molecular vibration frequency.^{65–66} Such coupling is referred to as a Fano resonance, and is the result of interference between the background of the plasmonic excitation mode and the vibrationally induced molecular dipole governed by the optical near-field confined in the vicinity of the structure.⁶⁷ An anti-resonance (sharp dip) is generally observed for weak coupling, as in the case of organic molecules. The observed magnitude of the anti-resonance in the resulting extinction spectra depends on the individual contributions of both absorption and scattering processes, which are mostly dependent on the parameters of the structure.⁴⁰

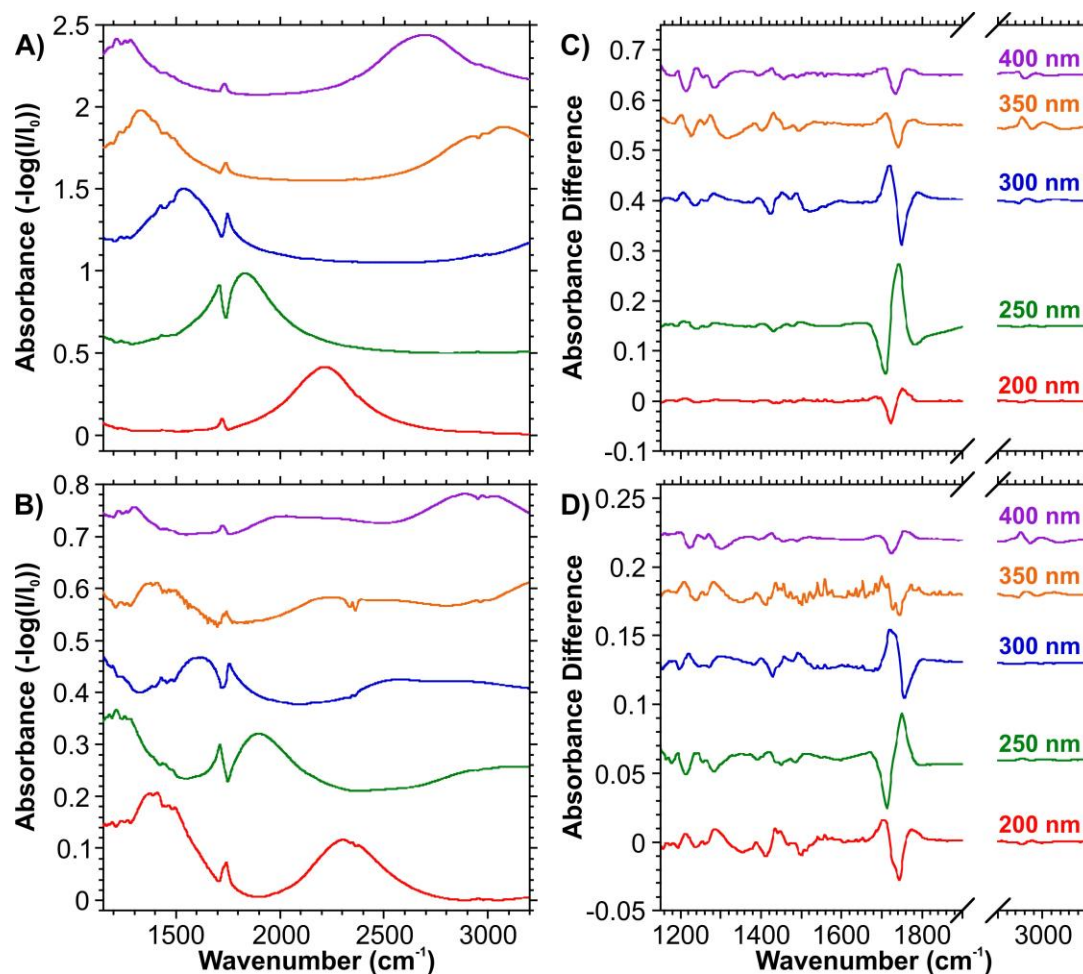


Figure 5.11 Absorbance measurements on PMMA coated dendritic fractals for A) five-branched second-order and B) three-branched fifth order generation dendritic fractals. Resulting absorbance difference spectra of C) five-branched second-order and D) three-branched fifth-order generation dendritic fractals.

Depending on the size of the nanorods within the fractal, it is possible to have LSPRs that are in resonance with the molecular vibrations of PMMA. The most noticeable anti-resonance occurs between 1720 and 1750 cm⁻¹ and corresponds to the C=O stretch. A maximum intensity was observed for the 250 nm side lengths (Figure 5.11C). With a side length of 300 nm, it is still possible to enhance the C=O vibrational mode, while also enhancing other modes at 1390, 1438, 1452, and 1487 cm⁻¹. Further increasing of the side length enables the lower energy vibrational modes found between 1150-1153, 1194-1200, 1238-1246, and 1267-1275 cm⁻¹ to be enhanced. Assignments for the vibrational modes

can be found in Supplementary Information Table S1. In addition, the higher energy resonance associated with the outer branches can also be used to enhance the asymmetric C–H stretching modes. This is best observed with the absorbance difference spectrum for the 350 nm side lengths where resonances at 2954 and 2995 cm^{-1} .

Table 5.1 SEIRA vibrational mode assignment for PMMA

Peak Range (cm^{-1})	Peak Assignment	References
1148 - 1153	C–O–C stretching	26, 43, 64, 68
1192 - 1205	CH ₂ twisting	33, 68
1238 - 1252	C–O–C stretching / C–O stretching	26, 43, 64, 68
1269 - 1282	C–O stretching	33, 68
1383 - 1390	–O–CH ₃ deformation / –CH ₃ bending	33, 68
1429 - 1437	–CH ₂ scissoring / CH ₃ stretching / CH ₃ deformation	33, 68
1444 - 1450	–CH ₂ scissoring / CH ₃ stretching / CH ₃ deformation	33, 68
1481 - 1485	–CH ₂ scissoring / CH ₃ stretching / CH ₃ deformation	33, 68
1720 - 1750	C=O stretching	26, 33-34, 36, 43, 64, 68
2947 - 2954	C–H asymmetric stretching	33-34, 36, 68
2989 - 2995	C–H asymmetric stretching	34, 36

The three-branched fifth-order generation dendritic fractals also exhibit SEIRA compatibility (Figure 5.11D). Since this fractal exhibits more resonances in the

fingerprint region, it is possible to enhance more of the PMMA vibrational modes using the smaller sized structures (200-300 nm). However, enhancing the vibrational modes associated with the asymmetric C–H stretches requires still required the use of the larger sized structures.

5.3.5 Surface-Enhanced Infrared Absorption of a Monolayer

SEIRA measurements were performed on samples functionalized with 4-nitrothiophenol (4-NTP). 4-NTP was selected as a model analyte due to the strong absorption of the NO₂ symmetric stretching mode at 1340 cm⁻¹ (Figure 5.12A) that matches one of the dominant plasmon resonance seen throughout our various dendritic structures.³⁵ In order to more easily identify the absorption of the analyte near 1340 cm⁻¹, a polynomial fit was applied to the SEIRA spectra. The resulting fit corresponding to absorption of the structure was then subtracted from the SEIRA spectrum. This was applied to multiple patterns under resonance conditions (i.e. the plasmon resonance is tuned with the molecular vibration) as shown in Figure 5.12B. The patterns used in the acquisition of the SEIRA spectra all had resonances between 1230 and 1410 cm⁻¹. The previous work of Vogt *et al.* demonstrated that a slight red-shift of the vibrational frequency of the analyte relative to the frequency of the plasmon resonance yields the greatest SEIRA enhancement.⁶⁹ The results of Figure 5.12B shows that the strongest signal for the ν_s(NO₂) occurs when the ratio of ω_{vib}/ω_{res} = 0.96, consistent with the previously mentioned study.⁶⁹ This leads us to conclude that the prepared dendritic fractals are compatible with SEIRA based measurements at the monolayer level. To maximize the enhancement for SEIRA, additional design considerations should be considered, notably the presence of an LSPR that is slightly blue-shifted relative to the frequency of vibration for an analyte. Once this has been obtained, further modifications can yield additional enhancement. For example, configuring the structure such that it is on a pedestal has been shown to provide an additional order of magnitude of enhancement.²⁷ Future studies involving SEIRA on the dendritic fractals should focus on these types of modifications.

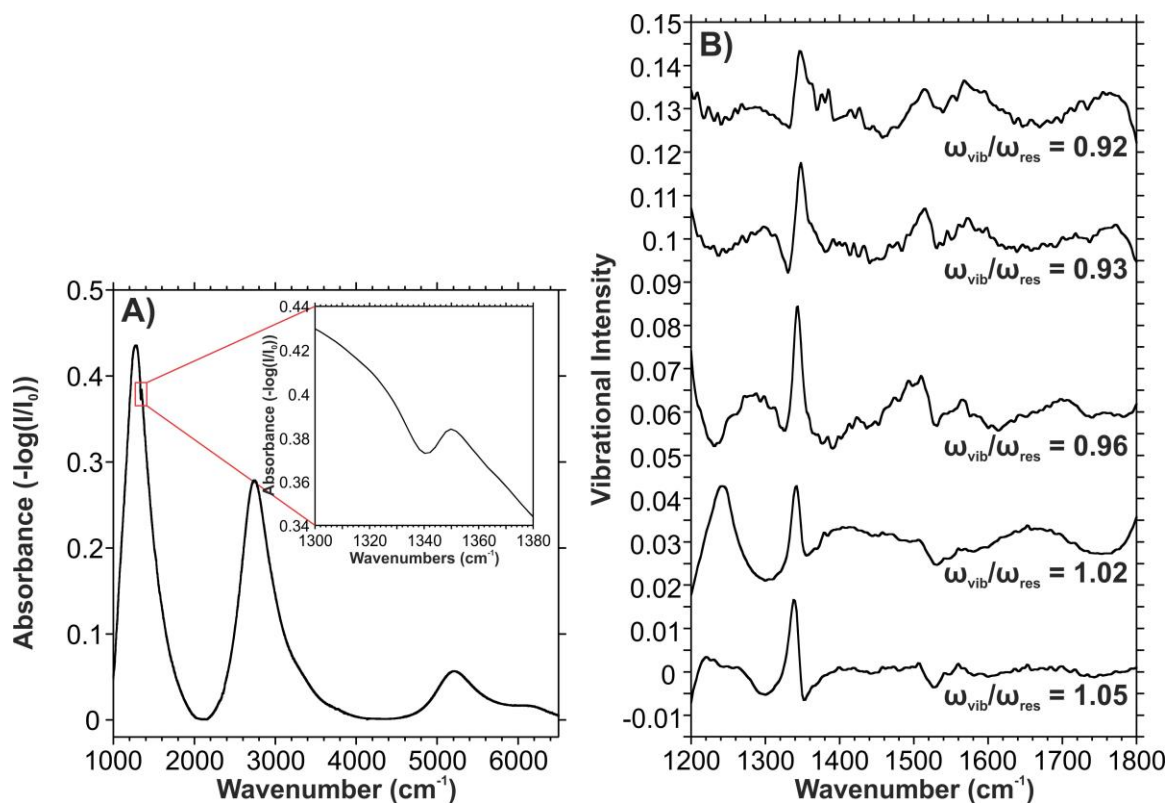


Figure 5.12 SEIRA measurements of 4-NTP functionalized dendritic fractals. A) Truncated 8 branched second-order generation dendritic fractal (same as Figure 6D). The inset in the figure highlights the symmetric stretch of NO_2 . **B)** SEIRA spectra of 4-NTP on different dendritic fractals with a polynomial fit having been removed. The spectra are offset for clarity and the ratios of $\omega_{\text{vib}}/\omega_{\text{res}}$ are included.

5.4 Conclusion

We have demonstrated the design, fabrication, characterization, and application of dendritic fractals for SEIRA. The dendritic structures can generate multiple LSPRs that span the near- and mid-infrared spectral regions. In the first-order generation of the dendritic fractal, there is a single resonance. With each subsequent generation, a new absorption is introduced at lower wavenumbers. These new absorptions correspond to the additional generations, with the lowest energy absorption being the global LSPR of the structure and are tentatively explained using the hybridization model. By tuning the size of the individual nanorods that comprise the dendritic fractal, it is possible to tune spectral position of the absorptions with a high degree of control. Increasing the number

of internal branches results in a blue-shift of the higher energy absorptions, and decreases the polarization dependence of the structure. However, as the number of branches in the first-order generation increases, less space exists for the greater number of branches needed in the higher-order generations. Thus, it becomes necessary to truncate the fractal to maintain the rod like structure of the outer branches. These changes do not significantly alter the global LSPR, and instead allow for tuning of the higher energy absorption. We have demonstrated how the lower energy resonances, such as the global LSPR, can be used to detect a molecule of interest when there is spectral overlap between the resonance of the structure and the vibrational mode of the molecule. Overall, the dendritic fractals provide a simple means of preparing nanostructures that exhibit broad optical properties across the near- and mid-infrared spectral ranges. Further work on the dendritic fractal should emphasize optimizing the enhancement of the electromagnetic signal. This can be achieved by altering the configuration of the plasmonic platform. Additionally, due to the thin width (50 nm) of the individual nanorods that make up the dendritic fractal, the structure may also exhibit optical properties in the visible region. These absorptions could then be used for techniques such as SERS and surface-enhanced fluorescence. Such a study could then validate the dendritic fractal as being another structure capable of multispectral molecular plasmonics.

5.5 References

1. Bhattacharya, R.; Indukuri, C.; Begam, N.; Seeck, O. H.; Basu, J. K., *Adv. Funct. Mater.* **2015**, *25*, 7233-7242.
2. Bailey, M. R.; Martin, R. S.; Schultz, Z. D., *J. Phys. Chem. C* **2016**, *120*, 20624-20633.
3. Henry, A.-I.; Sharma, B.; Cardinal, M. F.; Kurouski, D.; Van Duyne, R. P., *Anal. Chem.* **2016**, *88*, 6638-6647.
4. Tabatabaei, M.; Wallace, G. Q.; Caetano, F. A.; Gillies, E. R.; Ferguson, S. S. G.; Lagugne-Labarthet, F., *Chem. Sci.* **2016**, *7*, 575-582.
5. Wang, W.; Zhang, L.; Li, L.; Tian, Y., *Anal. Chem.* **2016**, *88*, 9518-9523.
6. Deckert-Gaudig, T.; Kurouski, D.; Hedegaard, M. A. B.; Singh, P.; Lednev, I. K.; Deckert, V., *Sci. Reports* **2016**, *6*, 33575.
7. Liao, M.; Jiang, S.; Hu, C.; Zhang, R.; Kuang, Y.; Zhu, J.; Zhang, Y.; Dong, Z., *Nano Lett.* **2016**, *16*, 4040-4046.

8. Choi, H.-K.; Park, W.-H.; Park, C.-G.; Shin, H.-H.; Lee, K. S.; Kim, Z. H., *J. Am. Chem. Soc.* **2016**, *138*, 4673-4684.
9. dos Santos, D. P.; Temperini, M. L. A.; Brolo, A. G., *J. Phys. Chem. C* **2016**, *120*, 20877-20885.
10. Simoncelli, S.; Roller, E.-M.; Urban, P.; Schreiber, R.; Turberfield, A. J.; Liedl, T.; Lohmüller, T., *ACS Nano* **2016**, *10*, 9809-9815.
11. Ross, M. B.; Mirkin, C. A.; Schatz, G. C., *J. Phys. Chem. C* **2016**, *120*, 816-830.
12. Cerjan, B.; Yang, X.; Nordlander, P.; Halas, N. J., *ACS Photonics* **2016**, *3*, 354-360.
13. Li, Y.; Simeral, M. L.; Natelson, D., *J. Phys. Chem. C* **2016**, *120*, 22558-22564.
14. Morhart, T. A.; Quirk, A.; Lardner, M. J.; May, T. E.; Rosendahl, S. M.; Burgess, I. J., *Anal. Chem.* **2016**, *88*, 9351-9354.
15. Le Ru, E. C.; Etchegoin, P. G., *Chem. Phys. Lett.* **2006**, *423*, 63-66.
16. Yampolsky, S.; Fishman, D. A.; Dey, S.; Hulkko, E.; Banik, M.; Potma, E. O.; Apkarian, V. A., *Nat. Photon.* **2014**, *8*, 650-656.
17. Butet, J.; Brevet, P.-F.; Martin, O. J. F., *ACS Nano* **2015**, *9*, 10545-10562.
18. Hou, R.; Shynkar, V.; Lafargue, C.; Kolkowski, R.; Zyss, J.; Lagugne-Labarthe, F., *Phys. Chem. Chem. Phys.* **2016**, *18*, 7956-7965.
19. Lagugné-Labarthe, F.; Shen, Y. R., Nonlinear Optical Microscopy. In *Optical Imaging and Microscopy: Techniques and Advanced Systems*, Török, P.; Kao, F.-J., Eds. Springer Berlin Heidelberg: Berlin, Heidelberg, 2007; pp 237-268.
20. Valev, V. K., *Langmuir* **2012**, *28*, 15454-15471.
21. Kauranen, M.; Zayats, A. V., *Nat. Photon.* **2012**, *6*, 737-748.
22. Rao, G. P. C.; Tharmaraj, V.; Yang, J., *RSC Adv.* **2015**, *5*, 20390-20395.
23. Rao, G. P. C.; Yang, J., *Appl. Spectrosc.* **2015**, *69*, 37-44.
24. Le, F.; Brandl, D. W.; Urzhumov, Y. A.; Wang, H.; Kundu, J.; Halas, N. J.; Aizpurua, J.; Nordlander, P., *ACS Nano* **2008**, *2*, 707-718.
25. Brown, L. V.; Zhao, K.; King, N.; Sobhani, H.; Nordlander, P.; Halas, N. J., *J. Am. Chem. Soc.* **2013**, *135*, 3688-3695.
26. Abb, M.; Wang, Y.; Papasimakis, N.; de Groot, C. H.; Muskens, O. L., *Nano Lett.* **2014**, *14*, 346-352.
27. Huck, C.; Toma, A.; Neubrech, F.; Chirumamilla, M.; Vogt, J.; De Angelis, F.; Pucci, A., *ACS Photonics* **2015**, *2*, 497-505.
28. Limaj, O.; Etezadi, D.; Wittenberg, N. J.; Rodrigo, D.; Yoo, D.; Oh, S.-H.; Altug, H., *Nano Lett.* **2016**, *16*, 1502-1508.
29. Aksu, S.; Yanik, A. A.; Adato, R.; Artar, A.; Huang, M.; Altug, H., *Nano Lett.* **2010**, *10*, 2511-2518.

30. Aksu, S.; Cetin, A. E.; Adato, R.; Altug, H., *Adv. Opt. Mater.* **2013**, *1*, 798-803.
31. Zhang, M.; Bechstein, D. J. B.; Wilson, R. J.; Wang, S. X., *Nano Lett.* **2014**, *14*, 333-338.
32. Bagheri, S.; Weber, K.; Gissibl, T.; Weiss, T.; Neubrech, F.; Giessen, H., *ACS Photonics* **2015**, *2*, 779-786.
33. Braun, A.; Maier, S. A., *ACS Sens.* **2016**, *1*, 1155-1162.
34. Cetin, A. E.; Korkmaz, S.; Durmaz, H.; Aslan, E.; Kaya, S.; Paiella, R.; Turkmen, M., *Adv. Opt. Mater.* **2016**, *4*, 1274-1280.
35. Wallace, G. Q.; Tabatabaei, M.; Zuin, M. S.; Workentin, M. S.; Lagugné-Labarthe, F., *Anal. Bioanal. Chem.* **2016**, *408*, 609-618.
36. Chen, K.; Adato, R.; Altug, H., *ACS Nano* **2012**, *6*, 7998-8006.
37. Hartstein, A.; Kirtley, J. R.; Tsang, J. C., *Phys. Rev. Lett.* **1980**, *45*, 201-204.
38. Aroca, R. F.; Ross, D. J.; Domingo, C., *Appl. Spectrosc.* **2004**, *58*, 324A-338A.
39. Neubrech, F.; Huck, C.; Weber, K.; Pucci, A.; Giessen, H., *Chem. Rev.* **2017**, *117*, 5110-5145.
40. Neuman, T.; Huck, C.; Vogt, J.; Neubrech, F.; Hillenbrand, R.; Aizpurua, J.; Pucci, A., *J. Phys. Chem. C* **2015**, *119*, 26652-26652.
41. De Zuani, S.; Reindl, T.; Rommel, M.; Gompf, B.; Berrier, A.; Dressel, M., *ACS Photonics* **2015**, *2*, 1719-1724.
42. Gottheim, S.; Zhang, H.; Govorov, A. O.; Halas, N. J., *ACS Nano* **2015**, *9*, 3284-3292.
43. Aslan, E.; Aslan, E.; Wang, R.; Hong, M. K.; Erramilli, S.; Turkmen, M.; Saracoglu, O. G.; Dal Negro, L., *ACS Photonics* **2016**, *3*, 2102-2111.
44. Hasan, D.; Ho, C. P.; Lee, C., *ACS Omega* **2016**, *1*, 818-831.
45. Volpe, G.; Volpe, G.; Quidant, R., *Opt. Express* **2011**, *19*, 3612-3618.
46. Hsu, K. H.; Back, J. H.; Fung, K.-H.; Ferreira, P. M.; Shim, M.; Fang, N. X., *J. Raman Spectrosc.* **2010**, *41*, 1124-1130.
47. Guanhai, L.; Xiaoshuang, C.; Bo, N.; Oupeng, L.; Lujun, H.; Yuan, J.; Weida, H.; Wei, L., *Nanotechnol.* **2013**, *24*, 205702.
48. Hegde, R. S.; Khoo, E. H., *Plasmonics* **2016**, *11*, 465-473.
49. Kischkat, J.; Peters, S.; Gruska, B.; Semtsiv, M.; Chashnikova, M.; Klinkmüller, M.; Fedosenko, O.; Machulik, S.; Aleksandrova, A.; Monastyrskyi, G.; Flores, Y.; Ted Masselink, W., *Appl. Opt.* **2012**, *51*, 6789-6798.
50. Lehmann, F.; Richter, G.; Borzenko, T.; Hock, V.; Schmidt, G.; Molenkamp, L. W., *Microelectron. Eng.* **2003**, *65*, 327-333.
51. Palik, E. D., In *Handbook of Optical Constants of Solids*, Academic Press: Burlington, 1997.

52. Shih, W.-C.; Santos, G. M.; Zhao, F.; Zenasni, O.; Arnob, M. M. P., *Nano Lett.* **2016**, *16*, 4641-4647.
53. Kearns, H.; Bedics, M. A.; Shand, N. C.; Faulds, K.; Detty, M. R.; Graham, D., *Analyst* **2016**, *141*, 5062-5065.
54. Prodan, E.; Radloff, C.; Halas, N. J.; Nordlander, P., *Science* **2003**, *302*, 419-422.
55. Larsson, E. M.; Hao, F.; Eurenus, L.; Olsson, E.; Nordlander, P.; Sutherland, D. S., *Small* **2008**, *4*, 1630-1634.
56. Fang, Z.; Thongrattanasiri, S.; Schlather, A.; Liu, Z.; Ma, L.; Wang, Y.; Ajayan, P. M.; Nordlander, P.; Halas, N. J.; Garcia de Abajo, F. J., *ACS Nano* **2013**, *7*, 2388-2395.
57. Vedraïne, S.; Hou, R.; Norton, P. R.; Lagugné-Labarthe, F., *Opt. Express* **2014**, *22*, 13308-13313.
58. Shimada, T.; Nakashima, H.; Kumagai, Y.; Ishigo, Y.; Tsushima, M.; Ikari, A.; Suzuki, Y., *J. Phys. Chem. C* **2016**, *120*, 534-541.
59. D'Andrea, C.; Bochterle, J.; Toma, A.; Huck, C.; Neubrech, F.; Messina, E.; Fazio, B.; Maragò, O. M.; Di Fabrizio, E.; Lamy de La Chapelle, M.; Gucciardi, P. G.; Pucci, A., *ACS Nano* **2013**, *7*, 3522-3531.
60. Aslan, E.; Turkmen, M., *Sens. Actuator A-Phys.* **2017**, *259*, 127-136.
61. Chen, K.; Duy Dao, T.; Nagao, T., *Sci. Rep.* **2017**, *7*, 44069.
62. Hoffmann, J. M.; Yin, X.; Richter, J.; Hartung, A.; Maß, T. W. W.; Taubner, T., *J. Phys. Chem. C* **2013**, *117*, 11311-11316.
63. Wang, T.; Nguyen, V. H.; Buchenauer, A.; Schnakenberg, U.; Taubner, T., *Opt. Express* **2013**, *21*, 9005-9010.
64. Dayal, G.; Chin, X. Y.; Soci, C.; Singh, R., *Adv. Opt. Mater.* **2017**, *5*, 1600559.
65. Merklin, G. T.; He, L.-T.; Griffiths, P. R., *Appl. Spectrosc.* **1999**, *53*, 1448-1453.
66. Verger, F.; Nazabal, V.; Colas, F.; Němec, P.; Cardinaud, C.; Baudet, E.; Chahal, R.; Rinnert, E.; Boukerma, K.; Peron, I.; Deputier, S.; Guilloux-Viry, M.; Guin, J. P.; Lhermite, H.; Moreac, A.; Compère, C.; Bureau, B., *Opt. Mater. Express* **2013**, *3*, 2112-2131.
67. Neubrech, F.; Pucci, A.; Cornelius, T. W.; Karim, S.; Garcia-Etxarri, A.; Aizpurua, J., *Phys. Rev. Lett.* **2008**, *101*, 157403.
68. Juneja, R.; Roy, I., *RSC Adv.* **2014**, *4*, 44472-44479.
69. Vogt, J.; Huck, C.; Neubrech, F.; Toma, A.; Gerbert, D.; Pucci, A., *Phys. Chem. Chem. Phys.* **2015**, *17*, 21169-21175.

Chapter 6

6 Exploiting Anisotropy of Plasmonic Nanostructures with Polarization-Modulation Infrared Linear Dichroism Microscopy (μ PM-IRLD)

(A version of this work has been published in the journal *Advanced Optical Materials*: Wallace, G.Q.; Read, S.T.; McRae, D.M.; Rosendahl, S.M.; Lagugné-Labarhet, F. *Adv. Opt. Mater.*, **2018**, 6, 1701336)

Metallic nanostructures that exhibit plasmon resonances in the mid-infrared range are of particular interest for a variety of optical processes where the infrared excitation and/or emission could be enhanced. This plasmon-mediated enhancement can potentially be used towards highly sensitive detection of an analyte(s) by techniques such as surface-enhanced infrared absorption (SEIRA). To maximize the SEIRA enhancement, it is necessary to prepare highly tuned plasmonic resonances over a defined spectral range that can span over several microns. Noteworthy, nanostructures with anisotropic shapes exhibit multiple resonances that can be exploited by controlling the polarization of the input light. This study demonstrates the role of polarization-modulation infrared linear dichroism coupled to microscopy measurements (μ PM-IRLD) as a powerful means to explore the optical properties of anisotropic nanostructures. Quantitative μ PM-IRLD measurements were conducted on a series of dendritic fractals as model structures to explore the role of structural anisotropy on the resulting surface-enhanced infrared absorption and sensing application. Once functionalized with an analyte, the μ PM-IRLD SEIRA results highlight that it is possible to selectively enhance further vibrational modes of analytes making use of the structural anisotropy of the metallic nanostructure.

6.1 Introduction

Polarized light can be readily used to probe the orientation, and anisotropy of molecular systems, including thin films,¹⁻² proteins,³⁻⁴ and self-assembled monolayers.⁵⁻⁷ When combined with microscopy, polarized light measurements can yield critical information about the orientation of crystallographic axes in microstructures or enable the ability to map the distribution of anisotropic domains.⁸⁻⁹ Raman,¹⁰⁻¹² infrared,¹³⁻¹⁴ and sum-

frequency generation are examples of vibrational spectroscopies that yield molecular anisotropy information using a set of polarized measurements.¹⁵⁻¹⁷ Noteworthy, polarized spectroscopic measurements can be of interest to probe metamaterials, such as plasmonic nanostructures, that exhibit an anisotropic response under polarized light.¹⁸⁻²³

This anisotropic response can manifest itself in different ways. First, the spectral position of localized surface plasmon resonances (LSPRs) can be tuned to different spectral domains. Metallic nanorod arrays are a classical example of this where an LSPR can exist in the mid-IR for a polarization parallel to the long axis of the nanorod, and for a polarization perpendicular to the long axis, the LSPR lies in the visible region.²⁴ Second, the spatial distribution of nanoscale electromagnetic enhancement, known as hot-spots, can be tailored by changing the polarization of the input light.²⁵ These two plasmonic properties can be simultaneously exploited by correctly tailoring the opto-geometric properties of the nanostructure.²⁶

Of the spectral domains of interest for vibrational spectroscopy, the mid-IR remains a significant challenge as it spans a domain of 2.5 to 20 μm ($500\text{-}4000\text{ cm}^{-1}$). Achieving a single broad resonance that covers that entire range is incredibly difficult, thus alternative approaches are required to perform plasmon-enhanced measurements. By exploiting the anisotropic response of nanostructures and metasurfaces, it is possible to overcome the need for a single broad resonance by instead generating a series of polarization dependent resonances.²⁷⁻³¹ An advantage of this approach is that a given resonance or set of resonances can be individually tuned to a specific frequency,³²⁻³³ or frequencies,³⁴ and therefore individually excited with a given polarization. Structures that support multiple polarization dependent resonances can be applied to a variety of applications. These include: polarized plasmon-mediated surface chemistry where a surface is functionalized with different analytes using different polarizations,³⁵ or polarized optical filters with distinct polarization responses.³⁶⁻³⁷ An interesting, yet under explored aspect of anisotropic nanostructures is the differential absorbance, ΔA , that is associated with the dichroic (linear or circular) properties of the structure. By exploiting the improved sensitivity offered by a plasmon-enhanced ΔA measurement, the local molecular anisotropy of an adsorbed analyte can be probed.³⁸⁻⁴⁰ Furthermore, it may be possible to

induce local anisotropy to the analyte through the interaction between the adsorbed analyte and a locally polarized plasmon. Such a sensitive interaction could be used to favor molecular adsorption of chiral molecules using plasmonic structures with differential responses to left and right circularly polarized light.

In this study, we first explore the linear dichroic properties of plasmonic nanostructures using polarization modulation (PM) spectroscopy in the mid-IR spectral range. These measurements were performed on fractal gold nanostructures fabricated using electron-beam lithography and probed under microscopy conditions using a synchrotron mid-IR beam line (Canadian Light Source). In PM infrared spectroscopy, a photoelastic modulator (PEM) modulates the light between two linear orthogonal polarizations at high frequency. The collected differential signal is proportional to the differential absorption, ΔA , that can also be exploited to enhance the sensitivity of the plasmon-mediated spectroscopic measurement due to the spectral and spatial anisotropy of the plasmon resonances. Specifically, micro polarization-modulation infrared linear dichroism (μ PM-IRLD) measurements were conducted to probe adsorbed analytes on a series of dendritic fractal structures. The dendritic fractals were chosen as our model structure because they support multiple LSPRs together with a large density of hot-spots that are anisotropically distributed. Finite difference time domain (FDTD) calculations were performed to relate the spatial anisotropy of the structure to the dichroic infrared spectra. Since the tuning of the spectral position of the resonances is critical to the development of new plasmonic structures in the infrared range, we explore how altering the dimensions of the structure (size), configuration (number of inner branches), and number of resonances (generation of the fractal), changes the resulting differential set of calibrated spectra. Last, the platforms were functionalized with an analyte, so that a self-assembled monolayer was formed on the surface, and μ PM-IRLD surface-enhanced infrared absorption (SEIRA) measurements could be performed. This study demonstrates an important development towards the understanding of polarization dependence of molecular systems by working with structures that exhibit polarization dependence.

6.2 Experimental

6.2.1 Materials

CaF₂ substrates (13 mm diameter × 2 mm) were purchased from Spectral Systems LLC (NY, USA). Poly(methyl methacrylate) A2 950 resist and isopropanol were purchased from MicroChem Corp. (MA, USA). AquaSave was obtained from Mitsubishi Rayon America Inc. (NY, USA). Acetone (CHROMASOLV), and 4-nitrothiophenol (4-NTP) were procured from Sigma-Aldrich (MO, USA).

6.2.2 Electron-Beam Lithography

CaF₂ windows were first cleaned by UV-Ozone exposure for 30 min to ensure adhesion of the thin film of resist. Details of the process for EBL are described in detail in Appendix C. Prior to imaging the structures by SEM, the sample was coated with 5 nm of osmium. The sample used for imaging was one of the samples used to acquire the μ PM-IRLD spectra.

6.2.3 Static Polarization Infrared Measurements

Fourier transform infrared (FT-IR) spectroscopy measurements were performed at the Mid-IR beamline synchrotron facility located at the Canadian Light Source (Beamline 01B-01). Information regarding the set-up at the beamline end station is provided in 2.5.2 and Figure 2.13. The apertures size chosen (1.5) allowed for the beam diameter to be slightly smaller than the $50 \times 50 \mu\text{m}^2$ patch. Measurements were collected from 8000-800 cm^{-1} with a spectral resolution of 4 cm^{-1} . Each spectrum is the average of 512 spectra.

6.2.4 Polarization-Modulated Infrared Linear Dichroism Microscopy Measurements

The same beamline, spectrometer, and microscope were used for the polarization-modulation (PM) measurements, with the following alterations. The general configuration of the PM set-up is similar to the one described by Schmidt *et al.*⁴¹ and is shown in Figure 2.13. In the new set-up, a photoelastic modulator (PEM, Hinds Instruments Inc., OR, USA) was placed after the polarizer, and was positioned at a 45°

angle relative to the polarizer. This portion of the set-up is contained within a purged polycarbonate box to minimize the presence of atmospheric water vapor. The PEM optical head is linked to the controller (Hinds Instruments PEM-100 Controller). The signal obtained from the MCT is then sent to a synchronous sampling demodulator (SSD 100, GWC Technologies, WI, USA). The difference and sum interferograms are obtained from this demodulator through two separate channels and undergo Fourier transformation. The ratio of the difference and sum is then calculated prior to calibration. To perform the calibration measurements, a polarizer is placed after the sample and oriented along the parallel (C_{\parallel}) and perpendicular (C_{\perp}) with respect to the first polarizer placed before the PEM. The two acquired polarized calibration files are then used in (6.1) to provide a quantitative ΔA value.

6.2.5 Surface-Enhanced Infrared Absorption

For the μ PM-IRLD SEIRA measurements, the samples were functionalized for 6 hours in a freshly prepared 10^{-3} M solution of 4-NTP prepared in ethanol. The functionalized sample was dipped in ethanol to remove any unbound 4-NTP and was dried under air. PM-SEIRA spectra were then collected using the parameters previously mentioned.

6.2.6 Electromagnetic Field Modelling

Finite-difference time-domain (FDTD) modelling (Lumerical) was used to simulate the absorption and electromagnetic fields of the dendritic fractals. The lengths of the individual nanorods are those described in the text, with widths of 50 nm, heights of 20 nm for gold, and 3 nm of titanium placed beneath the gold. Palik dielectric values for gold and titanium were used for the FDTD calculations.⁴² The structures were placed on a substrate with a constant refractive index of 1.42 representing the CaF₂ window. Periodic boundary conditions on the x - and y -axes conditions were no smaller than 700 nm and were representative of the periodicity of the fabricated structures. Last, a perfectly matched layer (PML) was used in the z -axis. Mesh sizes of 7.5 nm were used in the x - and y -axes and 3 nm in the z -axis.

6.3 Results and Discussion

6.3.1 Polarization Dependence of Dendritic Fractals

Inspired by the Cayley Tree fractal,⁴³ we have previously explored a more general version of radial fractals, classified as dendritic fractals.⁴⁴ For such structures, with each additional generation, a new lower energy (lower wavenumber) resonance is introduced. The spectral position of the resonance can then be tuned by altering the size, shape, and configuration of the fractal.⁴⁴ Since studies involving SEIRA emphasize the detection of small molecules, polymers, proteins, and lipids, the spectral regions between 1000 – 2000, and 2800 – 3200 cm^{-1} are of the greatest interest. Therefore, the design of the dendritic fractals was chosen such that resonance(s) would be in, or near those regions.

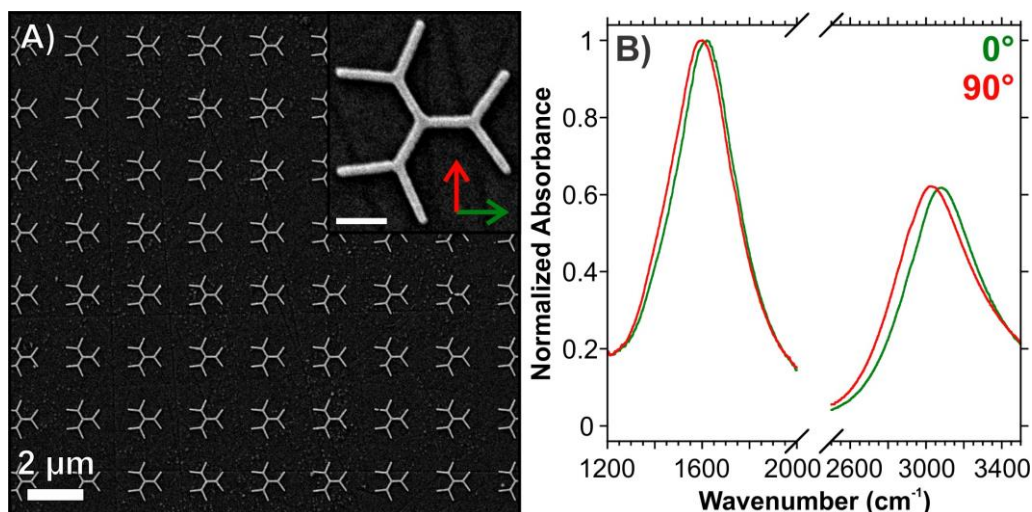


Figure 6.1 A) Scanning electron micrograph of three-branched second-order generation dendritic fractals prepared by electron-beam lithography. B) Experimental absorbance spectra obtained using orthogonal polarizations on the same sample as A). The scale bar on the inset SEM image is 350 nm. The arrows in the inset correspond to the polarization directions reported in A).

For this study, the focus was placed on the second-order generation structure. To highlight the polarization dependence of the structure, a three-branched dendritic fractal was chosen (Figure 6.1A). The side length of the nanorods was written as 350 nm because based on our previous study, such dimensions would provide resonances near the

relevant spectral regions of 1000-2000 and 2800-3200 cm^{-1} . When probed, the structurally tailored fractal exhibited two resonances between 1200 and 3500 cm^{-1} (Figure 6.1B). Additionally, the spectral positions of the resonances measured with orthogonal polarizations exhibit a slight polarization dependence as shown by the spectral shifts observed between the spectra obtained at 0 and 90 degrees.

6.3.2 Polarization-Modulated Measurements of Dendritic Structures

Polarization modulation (PM) infrared spectroscopy is a technique of choice to probe a variety of surfaces and interfaces in reflection and transmission modes, revealing the molecular orientation at the monolayer level.⁴⁵⁻⁵⁰ Linear dichroism can be measured with high accuracy over a large spectral range using polarization modulation spectroscopy that yields the differential absorption measurement $\Delta A = A_{0^\circ} - A_{90^\circ}$, where A_{0° and A_{90° are the absorbances along the two orthogonal polarizations. The value of ΔA can then be exploited to determine the orientation of vibrational modes through the measurement of their anisotropy.

Most infrared PM measurements have been conducted macroscopically, where the infrared beam that emerges from the infrared interferometer is focused with a long focal lens onto the sample surface. By coupling the PM measurements with a microscope and a synchrotron source, it is possible to obtain measurements of the linear dichroism with a typical spatial resolution slightly better than 10 μm .⁴¹ Such μPM -IRLD measurements have been applied to a very limited number of systems to determine hydrogen bonding and orientation in wood polymer fibres,⁵¹ and the anisotropy of crystalline or semicrystalline domains.⁵²⁻⁵³ To the best of our knowledge, no previous studies have coupled this approach with plasmonic nanostructures.

For arrays of nanostructures prepared by electron-beam lithography, the dimensions of the individual arrays are typically limited to between $50 \times 50 \mu\text{m}^2$ and $100 \times 100 \mu\text{m}^2$ ($50 \times 50 \mu\text{m}^2$ for this study) and are further arranged into grids. Thus, to probe the anisotropic response of an individual structure, a field of view of $50 \times 50 \mu\text{m}^2$ is necessary and must involve the coupling of PM-IRLD with an IR-compatible microscope. Performing classical absorbance measurements with the PEM provides the average absorbance, A_{ave}

$= (A_{0^\circ} + A_{90^\circ})/2$, of the two orthogonal polarizations. Figure 6.2A shows that there is no significant difference between the results of the PEM and the average static polarization measurements with both showing absorption maxima near 1600 and 3000 cm^{-1} .

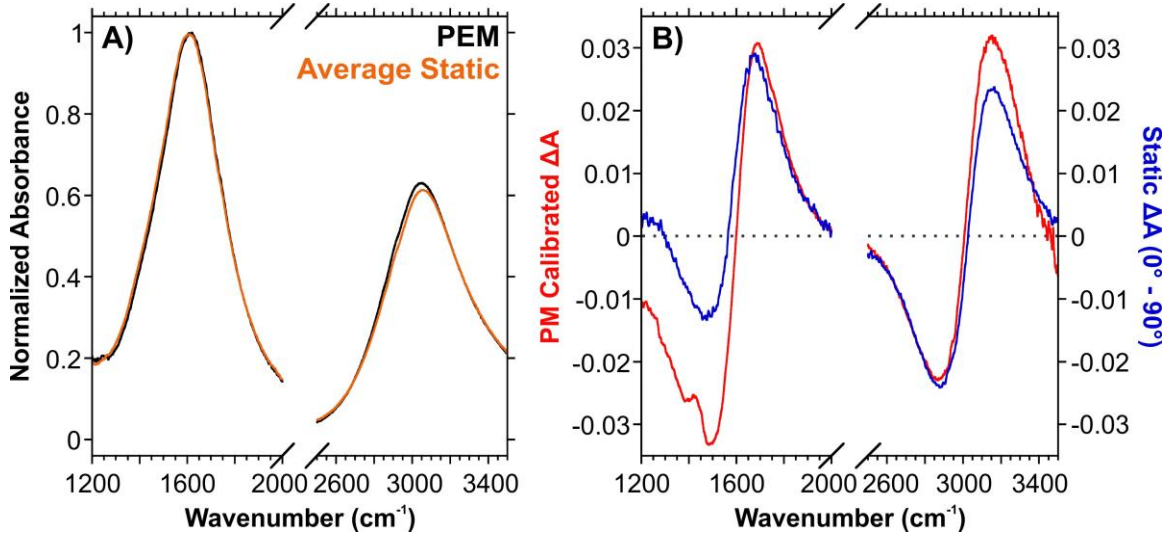


Figure 6.2 A) Comparison of the absorbance spectrum taken with the PEM (from the sum interferogram) and the average absorbance spectrum of the static polarization measurements (0° and 90°) from Figure 1. B) Comparison of the dichroic spectra obtained using the $\mu\text{PM-IRLD}$ (with a modulation centered at $\lambda = 1500 \text{ cm}^{-1}$) and the sequential measurement of A_{0° and A_{90° . The $\mu\text{PM-IRLD}$ spectrum is shown after calibration.

Quantitative ΔA spectra were obtained by calibrating the raw PM results and comparing it to the difference of the polarized absorbances. To calibrate the spectra, a linear polarizer was introduced with orientations that were parallel (C_{\parallel}) and perpendicular (C_{\perp}) to the polarizer positioned before the PEM. The spectra of I_{diff}/I_{sum} for C_{\parallel} and C_{\perp} is shown in Figure 6.3A. The calibrated difference spectrum can be obtained using equation (6.1):⁵⁴

$$\Delta A = \log \left(\frac{C_{\perp} \left(\frac{G}{G'} C_{\parallel} - S \right)}{C_{\parallel} \left(\frac{G}{G'} C_{\perp} + S \right)} \right) \quad (6.1)$$

where G is the gain during the experimental measurements (10), and G' is the gain used during the calibration (2). Figure 6.2B shows the comparison between the calibrated

spectrum and the result of $\Delta A = A_{0^\circ} - A_{90^\circ}$ obtained using the spectra of Figure 6.1B. Each resonance is split into two portions. The lower energy portion exhibits a negative ΔA value, and the higher energy a positive ΔA . Absolute values of ΔA are typically less than 4×10^{-2} . This response confirms that the three-branched second-order dendritic fractals exhibit an anisotropic character split into negative and positive contributions for both resonances. Although both spectra have similar intensities, the calibrated PM results have less noise than the spectrum obtained simply by subtracting the absorbances from the static polarization spectra. The response of going from negative to positive dichroism for $\Delta A = A_{0^\circ} - A_{90^\circ}$ was also established using finite-difference time-domain (FDTD) calculations (Figure 6.3B).

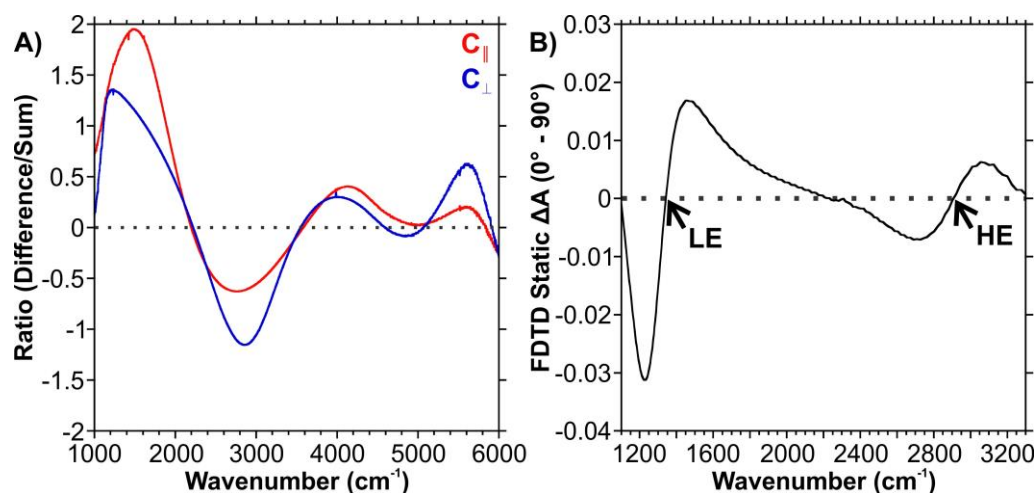


Figure 6.3 A) Raw PM absorption ratio spectra needed to perform the calibration. These were obtained by introducing a polarizer that was positioned parallel ($C_{||}$) or perpendicular (C_{\perp}) with respect to the polarizer direction positioned in front of the PEM. B) Calculated dichroic spectrum from FDTD calculations. The points indicated by LE and HE correspond to the low energy and high resonance positions used to generate the EM field maps.

At the higher energy (HE) overlap, the enhancement of the EM field occurs only in the outermost structures (Figure 6.4A, B), whereas the lower energy (LE) overlap incorporated the structures from both the first and second-order generations (Figure 6.4C,

D). This distribution has been previously related to the hybridization of the LSPRs associated with the incorporation of more structures with increasing generations.⁴³⁻⁴⁴

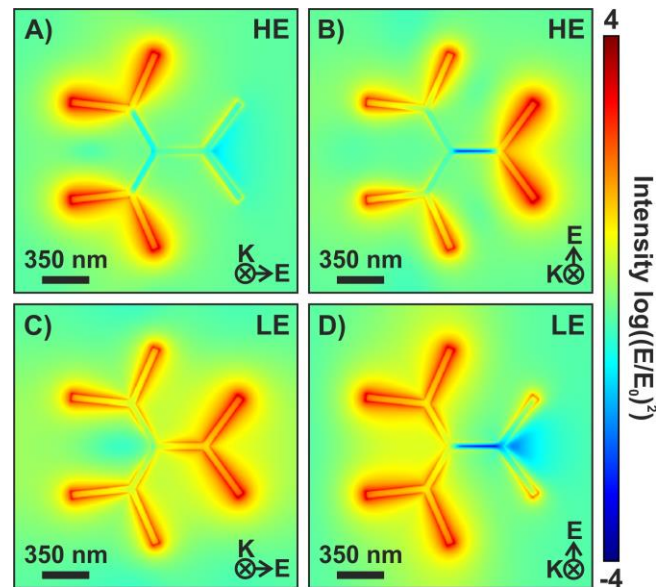


Figure 6.4 A-D) FDTD calculations of the electric field $(|E/E_0|)^2$: log scale representation at the high energy (HE) and low energy (LE) wavelengths where the absorbance spectra overlap at orthogonal polarizations for a second-order generation dendritic fractal composed of gold nanorods with side lengths of 350 nm.

6.3.3 Polarization-Modulation and Optical Tuning

As mentioned earlier, the optical properties of the dendritic fractals can be tuned by a variety of methods. The spectral positions of the resonances can be tuned by altering the size, and the number of inner branches. Coupling this tuning with expanding to higher-order generations allows for the incorporation of additional resonances. To explore how the PM measurements are influenced by each of these structural changes, additional dendritic fractals were studied.

6.3.4 Increasing the Side Lengths of the Nanorods

Altering the dimensions of the fractal nanostructures is a practical way to tune the spectral position of their resonances, as was shown in previous studies where a 1 nm increase in the side length yields a red spectral shift of 6 to 7 nm.⁴³⁻⁴⁴ To demonstrate that

this size dependence continues with increasing side length, a narrow range of sizes (350-400 nm) were prepared such that the two LSPRs of the three-branched second-order generation were still located within the spectral range of interest. Additionally, structures with side lengths over 700 nm were also prepared with the aim of tuning the LSPR of the structures from the outermost branches within the lower energy region of interest.

The absorbance spectra of the structures with the smaller side lengths are shown in Figure 6.5A, and the longer side lengths are shown in Figure 6.5B. By increasing the side lengths, the dipolar mode attributed to the outermost branches appears in the fingerprint region of the mid-IR. Additionally, weaker absorptions were observed at higher energy, and are attributed to higher order modes (quadrupolar). The calibrated μ PM-IRLD spectra (Figure 6.5C, D) exhibit the characteristic modes associated with PM measurements of the three-branched second-order generation dendritic fractals. It is interesting to note that as the resonances shift to lower wavenumbers (lower energy), the relative ratio of the calibrated absorbance before and after $\Delta A = 0$ changes. This is attributed to the setting of the PEM controller to a fixed frequency of 1500 cm^{-1} . This frequency was selected as it lies at the center of the fingerprint region of the mid-IR. As expected, it was observed that both the resonances and the corresponding dichroic responses can be tuned based on the side length of the nanostructure. This is an important feature, particularly for SEIRA measurements, since it was demonstrated that maximum enhancement depends on the ratio of $\omega_{\text{vib}}/\omega_{\text{res}}$ where ω_{vib} is the frequency of the vibrational mode of the molecular species deposited onto the plasmonic surface and ω_{res} is the frequency of the LSPR. Specifically, it was shown that the ideal measurement is obtained when the ratio of $\omega_{\text{vib}}/\omega_{\text{res}} = 0.95$.⁵⁵

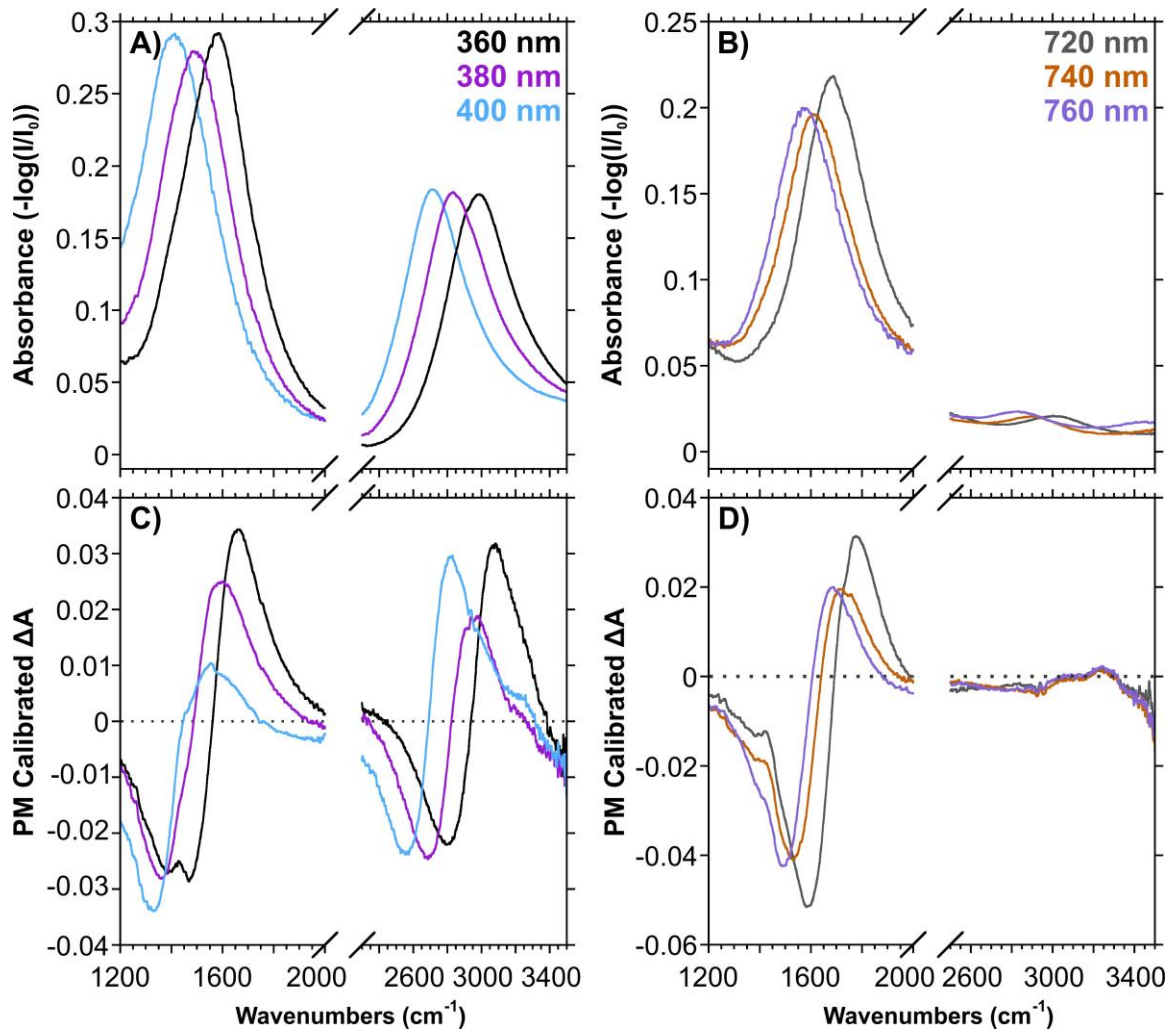


Figure 6.5 Changes to the absorbance (A and B), and the calibrated PM absorption spectra (C and D) because of altering the side length of the gold nanorods in the dendritic fractal.

6.3.5 Increasing the Number of Inner Branches

A second means of tuning the LSPRs of the dendritic fractal is by increasing the number of inner branches (n), and in turn, the number of branches in higher-order generations ($n - 1$). Representative SEM images of the second-order dendritic fractals for varying the number of inner branches are shown as insets in Figure 6.6A-C. An advantage of increasing the number of branches is that it may allow for a greater density of hot-spots over the surface of the structure. For μ PM-IRLD measurements, it is also likely that

compared with the three-branched structures, increasing the number of branches is also likely to have varying effects on the polarization dependence.

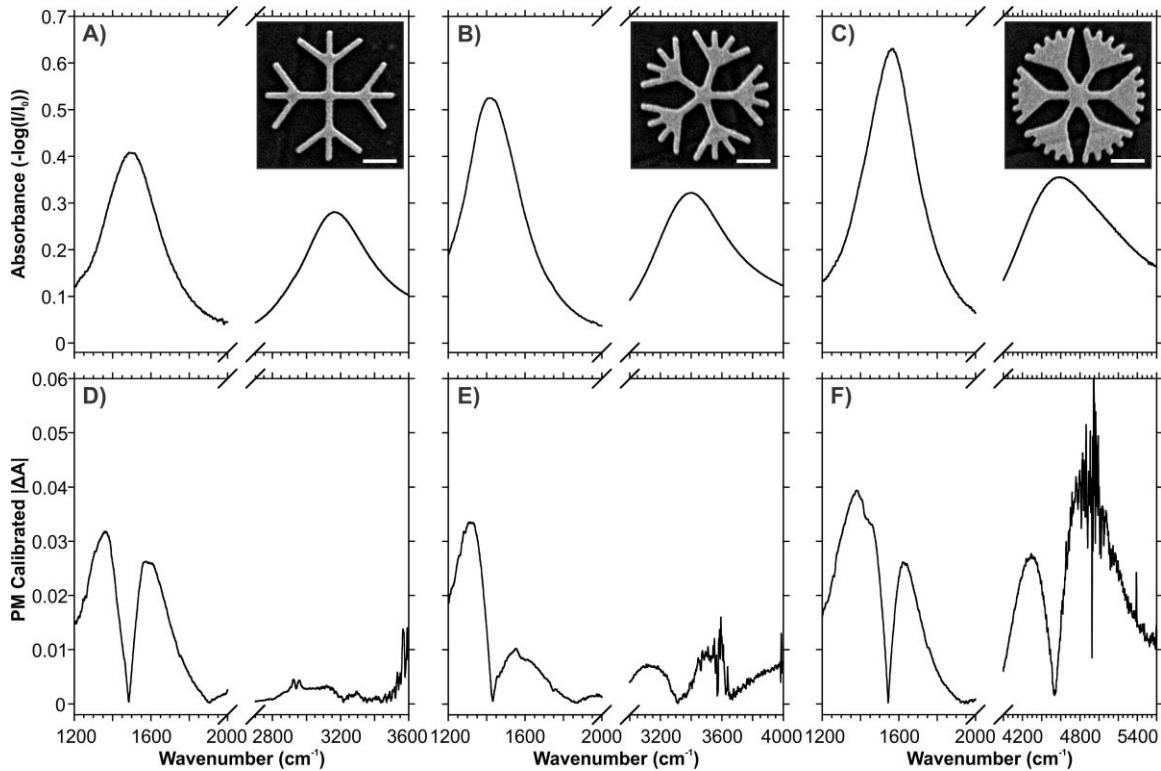


Figure 6.6 Influence of increasing the number of inner branches on the A-C) absorbance, and D-F) calibrated PM absorption spectra. Shown as insets in A-C) are SEM images corresponding to A) four-, B) five-, and C) six-branched second-order generation dendritic fractals. The scale bar of the inset images is 350 nm.

The absorbance spectra shown in Figure 6.6A-C all contain two LSPRs consistent with second-order generation dendritic fractals. As the number of inner branches increases, a noticeable blue-shift of the higher-energy resonance corresponding to the outermost structures is observed. Such observations have previously been reported for 3-dimensional multi-branched nanostructures.⁵⁶ As can be observed in the inset SEM images, increasing the number branches results in the branches becoming closer together. In the case of the six-branched structures, the branches are sufficiently close together that when prepared during the EBL process, a large portion of the branches are connected. This results in a small portion of the outerbranches being separated, resulting in a "duck

foot"-like appearance. This decrease in exposed length may be the reason for the blue-shift of the higher-energy resonance, especially the larger shift going from five to six branches compared to going from four to five. Altering the geometry of the nanorods, specifically the width, may help to minimize the duck foot structure.

The PM calibrated spectra also exhibit unique characteristics with increasing number of inner branches (Figure 6.6D-F). By definition, a structure that exhibits C_4 symmetry (four-branched dendritic fractals), should not exhibit any anisotropy. However, the μ PM-IRLD measurements in Figure 6.6D shows a dichroic response for the LE resonance. The five- and six-branched structures (Figure 6.6E and F) exhibiting C_5 and C_6 symmetries exhibit a polarization dependence for both resonances, as shown by the dichroic responses. It is important to note that both spectra also exhibit spectral noise, that we believe is characteristic of modulating the PEM at 1500 cm^{-1} , as opposed to closer to the HE resonances at 3200 and 4600 cm^{-1} . This presence of spectral noise is evidenced by examining the calibrated μ PM-IRLD spectrum obtained on CaF_2 (Figure 6.7).

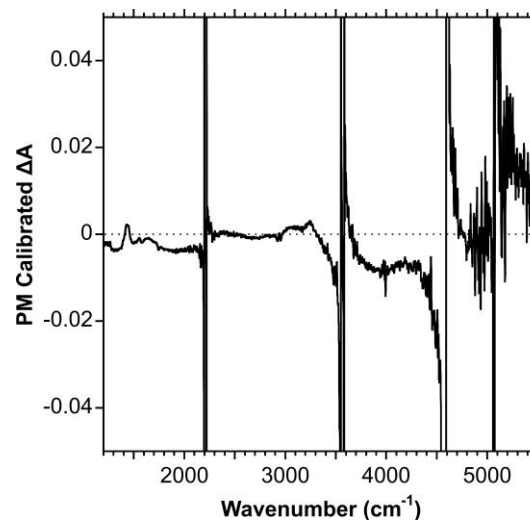


Figure 6.7 Calibrated PM spectrum obtained on CaF_2 .

To better understand the observed dichroism for the four-branched structures, FDTD calculations were performed to determine the spatial distribution of the enhancement (Figure 6.8A, B). Consistent with the calculations for the three-branched fractal (Figure 6.4), the HE resonance is localized to the outer branches (Figure 6.8A), while the LE

resonance incorporates the inner and outer branches (Figure 6.8B), yielding the global response of the structure.

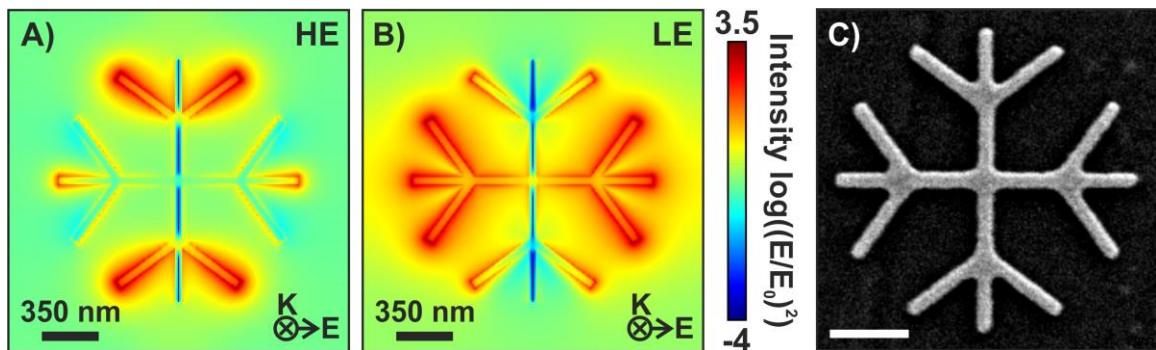


Figure 6.8 FDTD calculations of the electric field $(|E/E_0|)^2$: log scale representation at the A) high energy (HE) and B) low energy (LE) resonance wavelengths for a four-branched second-order generation dendritic fractal composed of gold nanorods with side lengths of 360 nm. C) SEM image of the four-branched second-order dendritic fractal with side lengths of 360 nm. The scale bar in the SEM image is 350 nm.

There are two primary sources that can introduce nanoscale defects resulting in the introduction of a dichroic response. The first is the presence of polishing defects in the surface of the CaF_2 window (scratches), as best observed in Figure 6.1A. After fabrication, the fractals often overlap with the substrate defects, yielding nanoscale changes in the structure. The second, and more likely cause for a dichroic response is the presence of any differences in the dimensions of the nanorods along the x and y -axes. Based on the SEM image shown in Figure 6.8C, although written to be identical, the constituent nanorods do exhibit differences. For example, the outermost structures, especially the angled branches, appear to have nanoscale differences in the lengths and widths. At the HE resonance, the dominant contribution is from the angled branches of the second-order generation. As the differences appear to exhibit some symmetry, it is likely that the dichroic response would be minimal. At the HE resonance, the inner branches play a role in the EM enhancement, along with a greater contribution from the central rods of the second-order generation. Since this resonance incorporates a greater portion of the structure, any anisotropy associated with the fabrication of the structure

would result in a dichroic response of this resonance. In the case of the structure shown in Figure 6C, the total length along the y-axis (90° polarization) is approximately 7 nm longer than the total length along the x-axis (0° polarization). Although this difference may seem minimal, it is important to recognize that the μ PM-IRLD measurements are performed on a $50 \times 50 \mu\text{m}^2$ array, containing 576 fractals in the case of this pattern. As such, a cumulative effect of the structural anisotropy will occur.

Overall, the results of the four-branched structure not only demonstrate the sensitivity of the μ PM-IRLD measurements, but also the sensitivity of the relationship between the interaction of light with plasmonic nanostructures.

6.3.6 Third-Order Generation Dendritic Fractals

As higher-order generations are fabricated, additional resonances are introduced. However, as the number of inner branches increases, it becomes more difficult to fabricate higher-order generations because the nanorods of the outermost generation overlap significantly. Once fabricated, a "duck foot"-like structure is observed. This effect can be minimized by truncating (removing branches) from the outer generation,⁴⁴ and/or increasing the length of the nanorods so that a greater portion of the structures are isolated from their surrounding nanorods. With a particular interest in working with the intrinsic fractal, we have decided to not explore truncated fractals in this study. Furthermore, although increasing the length may work, the resulting red-shift of the resonances would likely lead to the loss structure's global LSPR due to substrate interference above 1000 cm^{-1} . Therefore, we found that the only structure that met our requirements was a three-branched, third-order generation dendritic fractal where the sidelengths were rather small (200 – 250 nm).

Included as an inset of Figure 6.9A is an SEM image of a three-branched third-order dendritic fractal with a side length 220 nm. As expected for this order-generation, three LSPRs were observed (Figure 6.9A), with two in the mid-IR (1600 and 2500 cm^{-1}) and one in the near-IR (5000 cm^{-1}). We focus here only on the anisotropy of the mid-IR resonances (Figure 6.9B). The anisotropy of the lower energy resonances is especially important as the electromagnetic field enhancement results from the whole or most of the

structure as opposed to the highest energy resonance that is only derived from the outermost branches. Specifically, the lowest energy resonance can be described as the global resonance of the structure, while the second lowest resonance incorporates the structures introduced in the second- and third-order generations. Once functionalized with an analyte, given equivalent enhancement, the greater the number of hot-spots present on the surface, the stronger the vibrational signal of the target molecule.

Consistent with the obtained results for the various three-branched second-order generation structures, the mid-infrared μ PM-IRLD spectra indicate that the resonances are anisotropic. As the structure maintains its C3 symmetry, this result can be explained due to the difference in total length of the structure along the 0 and 90 degree directions. Additionally, much like with what was observed in Figure 6.6, Figure 6.9B shows spectral noise introduced by modulating the PEM at 1500 cm^{-1} . However, as this noise lay outside of the spectral regions of interest, it was not necessary to choose a different modulation frequency.

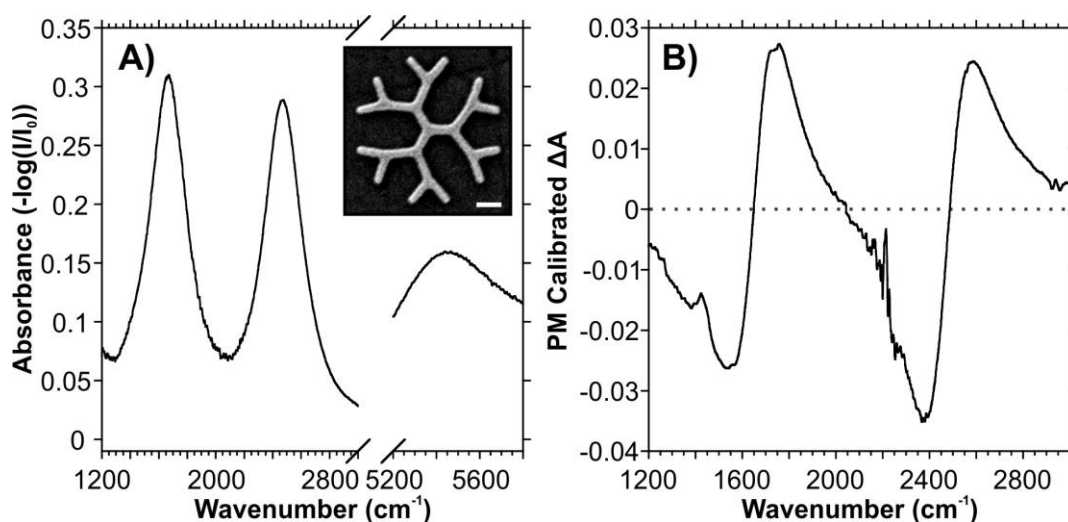


Figure 6.9 A) Absorbance and B) calibrated PM measurements for a three-branched third-order dendritic fractal. Included as an inset of A) in an SEM image of the structure with a scale bar of 200 nm.

6.3.7 Polarization-Modulated Surface-Enhanced Infrared Absorption

By tuning the position of the LSPRs of a structure(s), it is possible to enhance the vibrational fingerprint of a target located near the surface of the metal nanostructure. As previously mentioned, a ratio of 0.95 between the frequency of a vibrational mode and the resonance frequency maximizes the enhancement.⁵⁵ Owing to the incorporation of the PEM in these measurements, we will use the description of μ PM-IRLD SEIRA for these results.

For the μ PM-IRLD SEIRA measurements, the dendritic fractals were functionalized with a monolayer of 4-nitrothiophenol (4-NTP). 4-NTP is an ideal analyte for SEIRA measurements in the mid-IR as the vibrational fingerprint only contains a few peaks in the fingerprint region that can be readily assigned. In both the absorbance and PM calibrated spectra (Figure 6.10A, B), dips are observed for the vibrational modes of 4-NTP. By subtracting the baseline from the spectra, the vibrational intensities associated with 4-NTP can be obtained (Figure 6.10C, D). The peaks near 1340 and 1515 cm^{-1} can be assigned to the symmetric and asymmetric NO_2 modes, and those near 1570 and 1590 cm^{-1} correspond to the ring modes.⁵⁷⁻⁵⁸ Furthermore, the mode at 1340 cm^{-1} has an asymmetric shape, characteristic of a Fano resonance. This type of resonance occurs when the frequency of the plasmon resonance associated with the structure matches the vibrational frequency of the analyte. As the sizes of the structures were specifically tuned to be near 1340 cm^{-1} , this is the vibrational mode that would experience the greatest enhancement, and therefore exhibit the greatest Fano line shape. Importantly, the μ PM-IRLD SEIRA spectrum (Figure 6.10D) exhibits a similar spectrum to that of the traditional SEIRA spectrum (Figure 6.10C), with the 4-NTP peaks appearing in similar positions. Although the intensity of the peaks is quite weak, it is important to recognize that these measurements were performed with only a monolayer (or less) of the 4-NTP present on the gold surface.

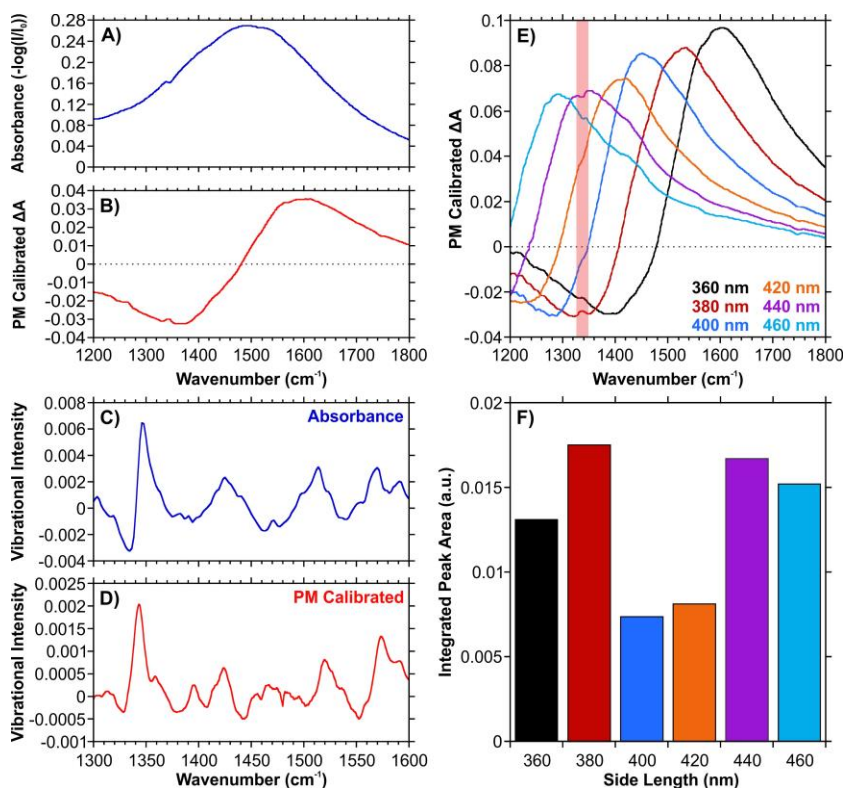


Figure 6.10 A) Absorbance and B) PM calibrated measurements of a 4-NTP functionalized sample (three-branched second-order generation). Vibrational intensity spectra obtained from C) the absorbance spectrum, and D) the PM calibrated spectrum. E) PM calibrated spectra for a series of three-branched second-order dendritic fractals functionalized with 4-NTP, and F) the corresponding integrated peak area from $1328 - 1346 \text{ cm}^{-1}$, corresponding to the symmetric NO_2 stretch as indicated by the shaded region of E).

As was previously demonstrated, it is possible to tune the position of the dip in the μPM -IRLD spectra by varying the size. To explore how the position of the change in dichroism influences this μPM -IRLD SEIRA measurements, a series of second-order generation three-branched dendritic fractals were prepared, with side lengths varying from 360 to 460 nm (Figure 6.10E). Although a value of 0.95 for the ratio of $\omega_{\text{vib}}/\omega_{\text{dip}}$ (equivalent to $\omega_{\text{vib}}/\omega_{\text{res}}$) was obtained for 380 nm, and did yield the strongest response (Figure 6.10F), a new distribution for intensity was observed. As the frequency of $\Delta A = 0$ approached the vibrational frequency position of the symmetric NO_2 mode, the integrated peak area decreased (Figure 6.10E), and then proceeded to increase once past the vibrational mode.

This observation is unique compared to the previously mentioned study where the enhancement with respect to $\omega_{\text{vib}}/\omega_{\text{res}}$ was observed to follow a Lorentzian fit.⁵⁵ Here, we attribute this difference to the fundamental differences between SEIRA and $\mu\text{PM-IRLD}$ SEIRA measurements. In $\mu\text{PM-IRLD}$ measurements, a ΔA between two orthogonal polarizations is reported, and has been mentioned, $\Delta A = 0$ occurs at the average absorbance of both polarizations, whereas only a single polarization is typically used in SEIRA experiments. The FDTD calculations of Figure 6.4 showed that no one polarization offered significantly greater electromagnetic enhancement or spatial distribution at the frequency of overlap. Therefore, once functionalized with an analyte, we would expect that both polarizations would exhibit similar Fano resonances, thus when the difference is taken, little to no signal would be observed. Additionally, unlike the SEIRA results where a single maxima is observed, the $\mu\text{PM-IRLD}$ SEIRA measurements show two local maxima. One of the maxima is observed as a negative dichroism ($A_{0^\circ} < A_{90^\circ}$) and the other as positive dichroism ($A_{0^\circ} > A_{90^\circ}$). Both of these maxima can be used to strongly enhance the vibrational signal (Figure 6.10E and F), thus leading to measurements that offer enhanced sensitivity. These maxima occur at the positions where the two absorbance spectra exhibit the greatest differences. It is important to note that these do not correspond to the individual absorbance maxima for each polarization. Therefore, when performing $\mu\text{PM-IRLD}$ SEIRA measurements it is important to tune the positions of these maxima so that they are in relevant positions, while also positioning $\Delta A = 0$ in a spectral domain void of vibrational modes of interest. As this is difficult to achieve in the fingerprint region, we propose that the fabrication of a series of structures (as was performed in this study) is ideal.

6.4 Conclusions

We have demonstrated that polarization-modulated measurements can be readily coupled with plasmonic nanostructures for probing the optical properties of the structure in the mid-IR. The LSPRs of dendritic fractals do exhibit orthogonal polarization dependence in the mid-IR and are therefore an ideal set of structures for PM measurements. Since the difference between the orthogonally polarized absorbances is small, calibrated PM-IRLD measurements yielded the absolute dichroic response over a large spectral range showing

negative and positive dichroic responses centered around the maximum resonance. By increasing the side lengths of the constituent nanorods or their symmetrical arrangement, it is possible to accurately tune the spectral position of the resonances and respective linear dichroism to spectroscopically relevant regions in the mid-IR. With sufficient tuning of the structure, such that the LSPR spectral position is near the vibrational frequency of an analyte, and that the maximum dichroism occurs in a spectral region void of vibrational modes, it is possible to detect an analyte of interest by SEIRA.

Furthermore, the incorporation of analytes that exhibit linear dichroism to the measurements could potentially enable surface-enhanced vibrational linear dichroism studies in the mid-IR. Such studies could then be used to probe surface-sensitive reactions at low concentrations. Lastly, due to the radial nature of the dendritic fractals, surface-enhanced vibrational circular dichroism may also be possible by tailoring the chiroptical properties of the fractal structures.²²

6.5 References

1. Snell, K. E.; Hou, R.; Ishow, E.; Lagugné-Labarhet, F., Enhanced Rates of Photoinduced Molecular Orientation in a Series of Molecular Glassy Thin Films. *Langmuir* **2015**, *31*, 7296-7305.
2. Laventure, A.; Bourotte, J.; Vapaavuori, J.; Karperien, L.; Sabat, R. G.; Lebel, O.; Pellerin, C., Photoactive/Passive Molecular Glass Blends: An Efficient Strategy to Optimize Azomaterials for Surface Relief Grating Inscription. *ACS Appl. Mater. Interfaces* **2017**, *9*, 798-808.
3. Zhang, G.; Li, J.; Cui, P.; Wang, T.; Jiang, J.; Prezhdo, O. V., *J. Phys. Chem. Lett.* **2017**, *8*, 1031-1037.
4. Bulheller, B. M.; Rodger, A.; Hicks, M. R.; Dafforn, T. R.; Serpell, L. C.; Marshall, K. E.; Bromley, E. H. C.; King, P. J. S.; Channon, K. J.; Woolfson, D. N.; Hirst, J. D., *J. Am. Chem. Soc.* **2009**, *131*, 13305-13314.
5. Guardingo, M.; Bellido, E.; Miralles-Llumà, R.; Faraudo, J.; Sedó, J.; Tatay, S.; Verdaguier, A.; Busqué, F.; Ruiz-Molina, D., *Small* **2014**, *10*, 1594-1602.
6. Sang, L.; Mudalige, A.; Sigdel, A. K.; Giordano, A. J.; Marder, S. R.; Berry, J. J.; Pemberton, J. E., *Langmuir* **2015**, *31*, 5603-5613.
7. Lobo Maza, F.; Méndez De Leo, L.; Rubert, A. A.; Carro, P.; Salvarezza, R. C.; Vericat, C., *J. Phys. Chem. C* **2016**, *120*, 14597-14607.
8. Lee, H.; Kim, J. H.; Dhakal, K. P.; Lee, J. W.; Jung, J. S.; Joo, J.; Kim, J., *Appl. Phys. Lett.* **2012**, *101*, 113103.

9. Al-Atar, U.; Bokov, A. A.; Marshall, D.; Teichman, J. M. H.; Gates, B. D.; Ye, Z.-G.; Branda, N. R., *Chem. Mater.* **2010**, *22*, 1318-1329.
10. Wen, W.; Zhu, Y.; Liu, X.; Hsu, H.-P.; Fei, Z.; Chen, Y.; Wang, X.; Zhang, M.; Lin, K.-H.; Huang, F.-S.; Wang, Y.-P.; Huang, Y.-S.; Ho, C.-H.; Tan, P.-H.; Jin, C.; Xie, L., *Small* **2017**, *13*, 1603788.
11. Zhang, S.; Mao, N.; Zhang, N.; Wu, J.; Tong, L.; Zhang, J., *ACS Nano* **2017**, *11*, 10366-10372.
12. Lin, J.; Liang, L.; Ling, X.; Zhang, S.; Mao, N.; Zhang, N.; Sumpter, B. G.; Meunier, V.; Tong, L.; Zhang, J., *J. Am. Chem. Soc.* **2015**, *137*, 15511-15517.
13. Ivanovski, V.; Mayerhöfer, T. G.; Kriltz, A.; Popp, J., *Spectrochim. Acta Mol. Biomol. Spectrosc.* **2017**, *173*, 608-617.
14. Kharintsev, S. S.; Shukhina, K. L.; Fishman, A. I.; Saikin, S. K., *J. Mater. Chem. C* **2017**, *5*, 6828-6833.
15. Hong, Y.; Zhou, H.; Qian, W.; Zuo, B.; Wang, X., *J. Phys. Chem. C* **2017**, *121*, 19816-19827.
16. Nihonyanagi, S.; Yamaguchi, S.; Tahara, T., *Chem. Rev.* **2017**, *117*, 10665-10693.
17. Schaefer, J.; Gonella, G.; Bonn, M.; Backus, E. H. G., *Phys. Chem. Chem. Phys.* **2017**, *19*, 16875-16880.
18. Gansel, J. K.; Thiel, M.; Rill, M. S.; Decker, M.; Bade, K.; Saile, V.; von Freymann, G.; Linden, S.; Wegener, M., *Science* **2009**, *325*, 1513-1515.
19. Hu, J.; Zhao, X.; Li, R.; Zhu, A.; Chen, L.; Lin, Y.; Cao, B.; Zhu, X.; Wang, C., *Opt. Express* **2016**, *24*, 11023-11032.
20. Kong, X.-T.; Zhao, R.; Wang, Z.; Govorov, A. O., *Nano Lett.* **2017**, *17*, 5099-5105.
21. Hentschel, M.; Schäferling, M.; Duan, X.; Giessen, H.; Liu, N., *Sci. Adv.* **2017**, *3*.
22. Luo, Y.; Chi, C.; Jiang, M.; Li, R.; Zu, S.; Li, Y.; Fang, Z., *Adv. Opt. Mater.* **2017**, *5*, 1700040.
23. Wang, X.; Tang, Z., *Small* **2017**, *13*, 1601115.
24. D'Andrea, C.; Bochterle, J.; Toma, A.; Huck, C.; Neubrech, F.; Messina, E.; Fazio, B.; Maragò, O. M.; Di Fabrizio, E.; Lamy de La Chapelle, M.; Gucciardi, P. G.; Pucci, A., *ACS Nano* **2013**, *7*, 3522-3531.
25. Thomas, R.; Swathi, R. S., *J. Phys. Chem. C* **2016**, *120*, 18733-18740.
26. Wallace, G. Q.; Tabatabaei, M.; Hou, R.; Coady, M. J.; Norton, P. R.; Simpson, T. S.; Rosendahl, S. M.; Merlen, A.; Lagugné-Labarthe, F., *ACS Photonics* **2016**, *3*, 1723-1732.
27. Chen, X.; Wang, C.; Yao, Y.; Wang, C., *ACS Nano* **2017**, *11*, 8034-8046.
28. Aouani, H.; Šípová, H.; Rahmani, M.; Navarro-Cia, M.; Hegnerová, K.; Homola, J.; Hong, M.; Maier, S. A., *ACS Nano* **2013**, *7*, 669-675.

29. Cerjan, B.; Yang, X.; Nordlander, P.; Halas, N. J., *ACS Photonics* **2016**, *3*, 354-360.
30. Cetin, A. E.; Turkmen, M.; Aksu, S.; Etezadi, D.; Altug, H., *Appl. Phys. B* **2015**, *118*, 29-38.
31. Aslan, E.; Aslan, E.; Turkmen, M.; Saracoglu, O. G., *Sens. Actuator A Phys.* **2017**, *267*, 60-69.
32. Limaj, O.; Etezadi, D.; Wittenberg, N. J.; Rodrigo, D.; Yoo, D.; Oh, S.-H.; Altug, H., *Nano Lett.* **2016**, *16*, 1502-1508.
33. Etezadi, D.; Warner Iv, J. B.; Ruggeri, F. S.; Dietler, G.; Lashuel, H. A.; Altug, H., *Light Sci. Appl.* **2017**, *6*, e17029.
34. Chen, K.; Adato, R.; Altug, H., *ACS Nano* **2012**, *6*, 7998-8006.
35. Tijunelyte, I.; Kherbouche, I.; Gam-Derouich, S.; Nguyen, M.; Lidgi-Guigui, N.; de la Chapelle, M. L.; Lamouri, A.; Levi, G.; Aubard, J.; Chevillot-Biraud, A.; Mangeney, C.; Felidj, N., *Nanoscale Horiz.* **2017**.
36. Song, Y.; Tran, V. T.; Lee, J., *ACS Appl. Mater. Interfaces* **2017**, *9*, 24433-24439.
37. Grant, J.; McCrindle, I. J. H.; Cumming, D. R. S., *Opt. Express* **2016**, *24*, 3451-3463.
38. Nesterov, M. L.; Yin, X.; Schäferling, M.; Giessen, H.; Weiss, T., *ACS Photonics* **2016**, *3*, 578-583.
39. Besteiro, L. V.; Zhang, H.; Plain, J.; Markovich, G.; Wang, Z.; Govorov, A. O., *Adv. Opt. Mater.* **2017**, *5*, 1700069.
40. Zhang, W.; Wu, T.; Wang, R.; Zhang, X., *J. Phys. Chem. C* **2017**, *121*, 666-675.
41. Schmidt, M.; Schade, U.; Grunze, M., *Infrared Phys. Technol.* **2006**, *49*, 69-73.
42. Palik, E. D., In *Handbook of Optical Constants of Solids*, Academic Press: Burlington, **1997**.
43. Gottheim, S.; Zhang, H.; Govorov, A. O.; Halas, N. J., *ACS Nano* **2015**, *9*, 3284-3292.
44. Wallace, G. Q.; Foy, H. C.; Rosendahl, S. M.; Lagugné-Labarthe, F., *J. Phys. Chem. C* **2017**, *121*, 9497-9507.
45. Green, M. J.; Barner, B. J.; Corn, R. M., *Rev. Sci. Instrum.* **1991**, *62*, 1426-1430.
46. Barner, B. J.; Green, M. J.; Saez, E. I.; Corn, R. M., *Anal. Chem.* **1991**, *63*, 55-60.
47. Buffeteau, T.; Desbat, B.; Turlet, J. M., *Appl. Spectrosc.* **1991**, *45*, 380-389.
48. Blaudez, D.; Turlet, J.-M.; Dufourcq, J.; Bard, D.; Buffeteau, T.; Desbat, B., *J. Chem. Soc., Faraday Trans.* **1996**, *92*, 525-530.
49. Buffeteau, T.; Pézolet, M., *Appl. Spectrosc.* **1996**, *50*, 948-955.
50. Cornut, I.; Desbat, B.; Turlet, J. M.; Dufourcq, J., *Biophys. J.* **1996**, *70*, 305-312.

51. Schmidt, M.; Gierlinger, N.; Schade, U.; Rogge, T.; Grunze, M., *Biopolym.* **2006**, *83*, 546-555.
52. Schmidt, M.; Lee, J. S.; Schade, U., *Infrared Phys. Technol.* **2010**, *53*, 157-161.
53. Santoro, G.; Schmidt, M.; Schade, U.; Marco, C.; Ellis, G., *J. Phys. Conf. Ser.* **2012**, *359*, 012005.
54. Pézolet, M.; Pellerin, C.; Prud'homme, R. E.; Buffeteau, T., *Vib. Spectrosc.* **1998**, *18*, 103-110.
55. Vogt, J.; Huck, C.; Neubrech, F.; Toma, A.; Gerbert, D.; Pucci, A., *Phys. Chem. Chem. Phys.* **2015**, *17*, 21169-21175.
56. Chirumamilla, M.; Chirumamilla, A.; Roberts, A. S.; Zaccaria, R. P.; De Angelis, F.; Kjær Kristensen, P.; Krahe, R.; Bozhevolnyi, S. I.; Pedersen, K.; Toma, A., *Adv. Opt. Mater.* **2017**, *5*, 1600836.
57. Zhang, Z.; Imae, T., *J. Colloid Interface Sci.* **2001**, *233*, 99-106.
58. Merklin, G. T.; He, L.-T.; Griffiths, P. R., *Appl. Spectrosc.* **1999**, *53*, 1448-1453.

Chapter 7

7 Plasmonic Properties of Lithographically Prepared Dendrimers and their Applicability to SERS-Based Sensing

(A version of this work is in preparation: Wallace, G.Q.; McRae, D.M.; McConnell, E.M.; Therien, D.A.B.; DeRosa, M.C.; Lagugné-Labarthe, F.)

Plasmon-mediated spectroscopies, such as surface-enhanced Raman spectroscopy (SERS), rely on a large local enhancement of the electromagnetic field at the surface of a conductive structure. These structures are often prepared by rational design so that they exhibit optical properties tailored to specific spectral domains. Of note are fractal structures due to their multiplicity of plasmon modes enabled by the presence of multiple generations in the structure. Furthermore, these structures can support a large density of electromagnetic enhancement area. Dendrimer-like structures are known to exhibit these optical properties in the near- to mid-infrared. In this study, a series of dendritic fractals are prepared by electron-beam lithography, and their plasmonic properties in the visible to near-infrared are explored. By increasing the number of inner branches in the dendrimer, a balance between the number of resonances and the density of electromagnetic enhancement is achieved. This is validated first using SERS measurements of 4-nitrothiophenol functionalized structures. The applicability of the dendrimers is then further demonstrated using SERS-based detection of the neurotransmitter dopamine. With the mid-infrared compatibility already highlighted in Chapter 5, this Chapter helps to further establish the multispectral compatibility of fractal structures that can be tuned over the visible and mid-infrared range opening a new window to perform sensing measurements.

7.1 Introduction

The ability to design and fabricate conductive nanostructures and metasurfaces has become an area of intense focus in recent years. This interest derives from the ability of these structures to support localized surface plasmon resonances (LSPRs). Upon illumination, the LSPR permits the structure to greatly enhance local electromagnetic

(EM) fields in nanoscale regions known as hot-spots. By altering the structural properties, notably metal composition, size and geometry,¹ it is possible to tune this enhancement to general spectral domains,² or specific wavelengths. Once tuned, the structures can be used for biomedical,³ catalytic,⁴ photovoltaics,⁵ and molecular sensing applications.⁶⁻⁷

Molecular sensing can be performed using either label-free or in-direct methods. One method of sensing relies on detecting changes to a fluorescence signal upon an analyte interacting with the fluorophore-containing molecule or structure.⁸⁻⁹ When coupling this with plasmonic nanostructures, this technique is known as plasmon- or surface-enhanced fluorescence.¹⁰ Alternative methods rely on detecting the vibrational fingerprint of the analyte, and/or changes in the spectroscopic signature because of molecule-molecule interactions. The molecule specific binding of a target analyte to an aptamer is such an interaction.¹¹⁻¹² When mid-infrared (IR) light is used in combination with the plasmonic structure, the resulting technique is known as surface-enhanced infrared absorption (SEIRA).¹³ Likewise, surface-enhanced Raman spectroscopy (SERS) relies on the use of visible or near-IR light. Although both techniques have shown ultrasensitive detection capabilities at sub-monolayer and single-molecule levels,¹⁴⁻¹⁶ SERS is by far the more commonly studied technique. This is attributed to the fact that the wavelengths associated with Raman shifts are small ($1000 - 1800 \text{ cm}^{-1}$ corresponds to 676-714 nm for 633 nm excitation). As such, the resonances do not need to be as broad in the visible region. It is important to note that the SERS enhancement contains both EM, and chemical components. As the EM enhancement is not analyte-dependent, ensuring that the plasmonic properties of the structure provide sufficient surface enhancement for general sensing applications is thus necessary.

Structures that exhibit fractal or fractal-like properties have found in use for a variety of applications, including molecular sensing. In the case of SERS-based detection, fractal structures can be used for ultrasensitive single molecule measurements.¹⁷ For measurements involving SERS, one of the most commonly prepared fractal structures are those that exhibit a dendrimer-like appearance. Such structures are predominantly prepared electrochemically,¹⁸⁻²⁶ though other approaches do exist.²⁷⁻²⁹ Much like other multi-branched nanostructures,³⁰ notably stars,^{15, 31} flowers,³² and urchins,³³ the dendritic

structures can support a large density of hot-spots. This is an important design aspect as it leads to an increase in the probability that a molecule will be present, enabling a greater likelihood of detection.

With advancements in nanofabrication processes, such as focused ion beam and electron-beam lithography (EBL), it has become possible to reproducibly fabricate fractal nanostructures and metasurfaces with controlled geometries. Examples of EBL prepared fractals include: Koch,³⁴ Cesaro,³⁵ Hilbert,³⁶ Sierpiński,³⁷⁻³⁸ and other iterative-based structures.³⁹⁻⁴¹ These types of structures are of interest as they can exhibit a combination of multiple resonances and sufficient hot-spot densities.

In this work, the plasmonic properties of EBL prepared gold dendrimers in the visible to near-IR region is explored. Emphasis is placed on two critical design features: (i) the order of the fractal generation, and (ii) the number of inner branches. In the near- to mid-IR, the order of the fractal is known to influence the number of resonances as well as their spectral positions,⁴²⁻⁴⁴ while the number of inner branches can provide an increase in the number of hot-spots over the surface of the fractal.⁴³⁻⁴⁴ We then combine these design characteristics with changes in side length, so as to provide further opportunities for tuning the resonances. Visible to near-IR absorption measurements are used to characterize the spectral position of the resonances, and finite-difference time-domain (FDTD) calculations provide information regarding the spatial distribution of electromagnetic enhancement near the hot-spot. Finally, the applicability of the fabricated dendrimer-based structures is tested against SERS-based sensing. A model molecule (4-nitrothiophenol, 4-NTP) is first used to determine the compatibility of the various dendritic fractal geometries. To further illustrate the sensing capabilities of the dendrimers, plasmon-mediated detection of dopamine is shown. Changes in dopamine concentrations in cerebrospinal fluid have been observed in those with neurological diseases including Huntington's,⁴⁵ and Parkinson's.⁴⁶ Since SERS has emerged as a possible tool for detecting dopamine,^{8, 47-50} we explore how direct and aptamer-derived SERS-based detection methods can be performed using the dendritic fractals.

7.2 Experimental

7.2.1 Materials

Glass microscope cover slips ($22 \times 22 \times 0.15$ mm) were purchased from Fisher Scientific (ON, CAN). Poly(methyl methacrylate) A2 950 resist and isopropanol were purchased from MicroChem Corp. (MA, USA). AquaSave was obtained from Mitsubishi Rayon America Inc. (NY, USA). Acetone (CHROMASOLV), 4-nitrothiophenol (4-NTP), dopamine hydrochloride, and 6-mercaptohexanol (MCH) were procured from Sigma-Aldrich (MO, USA).

7.2.2 Electron-Beam Lithography

CaF₂ windows were first cleaned by reactive O₂ plasma for 10 minutes to ensure adhesion of the thin film of resist. Details of the process for EBL are described at length in Appendix C. Prior to imaging the structures by SEM, the sample was coated with 5 nm of osmium.

7.2.3 Visible to Near-Infrared (400-1000 nm) Absorption

The set-up for obtaining the visible to near-infrared absorption spectra is very similar to the one described in 2.4.1 and shown in Figure 2.10. A Nikon Diaphot inverted optical microscope, and a USB 4000-VIS-NIR-ES spectrometer (Ocean Optics, FL, USA) were used for these experiments. An acquisition time of 7 milliseconds per spectrum was used, and each spectrum shown is the result of 2000 accumulated spectra.

7.2.4 Electromagnetic Field Calculations

Finite-difference time-domain (FDTD) modelling (Lumerical) was performed to simulate the absorption and electromagnetic fields of the dendritic fractals. The lengths of the individual nanorods were set to 175 nm, with widths of 55 nm unless otherwise stated, heights of 20 nm for gold, and 3 nm of titanium placed beneath the gold as an adhesion layer. CRC and Palik dielectric values for gold and titanium were used for the FDTD calculations respectively.⁵¹⁻⁵² The structures were placed on a glass substrate, with the refractive index determined using the material explorer. A total-field scattered field source was used. Perfectly matched layer (PML) boundary conditions were used in the x -,

y-, and z-axes. Mesh sizes of 3 nm were used along the x and y-axes, and 2 nm along the z-axis.

7.2.5 Surface-Enhanced Raman Measurements with 4-NTP

Samples were immersed in a 10^{-3} M solution of 4-nitrothiophenol (4-NTP), prepared in ethanol for 24 hours. Raman measurements were collected with a LabRAM HR spectrometer equipped with a liquid nitrogen cooled CCD. A helium neon laser ($\lambda = 632.8$ nm, power of ~ 500 μ W at the sample) was used as an excitation source, and a $100\times$ (N.A. = 0.9) objective was used to collect the back scattered light. An acquisition time of 10 seconds per spectrum was used for the measurements.

7.2.6 Raman and Surface-Enhanced Raman Measurements with Dopamine

A 10 mM solution of dopamine hydrochloride was prepared in Milli-Q water. 30 μ L solution was then drop casted onto the cover slip containing the dendritic fractals. The Raman and SERS measurements using the dopamine solution were performed using the same excitation source as the powder dopamine, however, a $40\times$ (N.A. = 0.6) objective was used. An acquisition time of 10 seconds per acquisition window was used.

7.2.7 Surface-Enhanced Raman Measurements with Aptamer

A 1 mM solution of 6-mercaptohexanol (MCH) was prepared in ethanol. 30 μ L of the MCH solution was drop casted onto the dendritic fractals. The fractals were subsequently functionalized with 30 μ L of a 1 μ M solution of DNA dopamine aptamer (5'-GTC-TCT-GTG-TGC-GCC-AGA-GAC-ACT-GGG-GCA-GAT-ATG-GGC-CAG-CAC-AGA-ATG-AGG-CCC-3') or non-binding aptamer (5'-GTC-TCT-GTG-CCA-AAC-AGA-GAC-ACT-GGG-GCA-GAT-ATG-GGC-CCG-CAC-AGA-ATC-CGG-CCC-3') that had been prepared on a Mermade 6 oligonucleotide synthesizer (Bioautomation).⁵³ The 5' end had been chemically modified to contain a 6-carbon chain with a thiol group, so the aptamer could bind to the gold surface. 20 second acquisition times with 5 accumulations were used for the SERS measurements involving the aptamer.

7.3 Results and Discussion

7.3.1 Optical Properties of Dendritic Fractals in the Visible to Near-Infrared Region

Dendritic fractals, such as the Cayley Tree,⁴² are an iterative structure starting with n number of branches in the first-order generation. In each subsequent generation, the number of rods added to each branch is $n - 1$. Figure 7.1A-C include SEM images of first-order generation dendritic fractals, with the corresponding absorbance measurements in Figure 7.1D. Here, all spectra shown exhibit an LSPR with a maximum between 560 and 570 nm. In the work of Gottheim *et al.*, the first-order generation Cayley Tree fractals were fabricated with side lengths ranging from 100 to 180 nm, with the observed dipolar resonances of the structures ranging from 1035 to 1515 nm.⁴² The absorbance spectra of Figure 7.1D correspond to those obtained for structures with side lengths of 175 nm. Even though the other dimensions (width and metal thickness) are also not the same between this study and the previously mentioned one, it is unlikely that these differences would yield a shift large enough to characterize the 560-570 nm resonance as the global dipolar resonance. This is further supported by the observation that this peak does not undergo any significant red-shifts as the side length is increased (Figure 7.1E). Increasing the length does however introduce newer resonances, as is seen in the spectrum obtained with a side length of 250 nm. These weaker modes are attributed to the higher-order modes (quadrupolar, hexapolar, etc.) of the nanorod that is along the polarization axis.⁵⁴ Absorbance spectra were calculated by finite-difference time-domain (FDTD) methods for four-branched first-order generation fractals with varying widths (Figure 7.2). These calculated spectra show a clear red-shift of the resonance as the width increases. By examining the spatial distribution of the EM field as determined by the FDTD calculations at the resonance wavelength of the first-order generation fractals (Figure 7.3), the enhancement is associated with the width of the structure. Furthermore, the distribution is known as the transverse dipolar resonance, and is well known to be found in the visible region for gold nanorods.⁵⁵⁻⁵⁷ The characteristic anisotropy of the plasmonic resonances of metallic nanorods, with a transverse dipolar resonance in the visible region and a longitudinal resonance in the near- to mid-IR,⁵⁸ also appears to be the case for the first-order generation dendritic fractals.

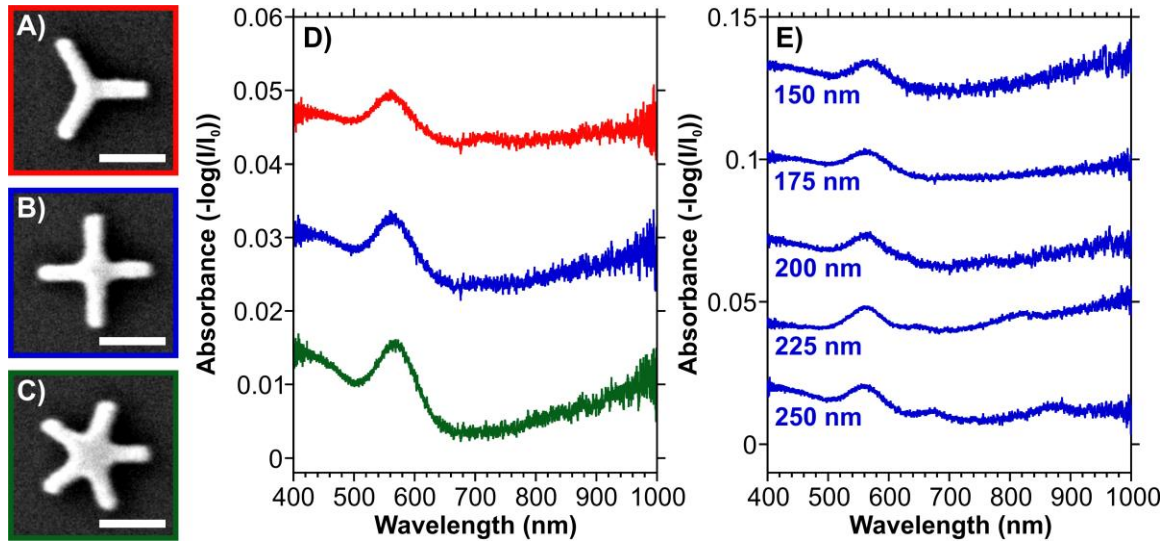


Figure 7.1 SEM images of first-order dendritic fractals with A) three, B) four, and C) five inner branches. The scale bar in the SEM images is 200 nm. D) Absorbance spectra of the first-order dendritic fractals with side lengths of 175 nm. E) Absorbance spectra of four-branched first-order dendritic fractals with side lengths from 150 to 250 nm.

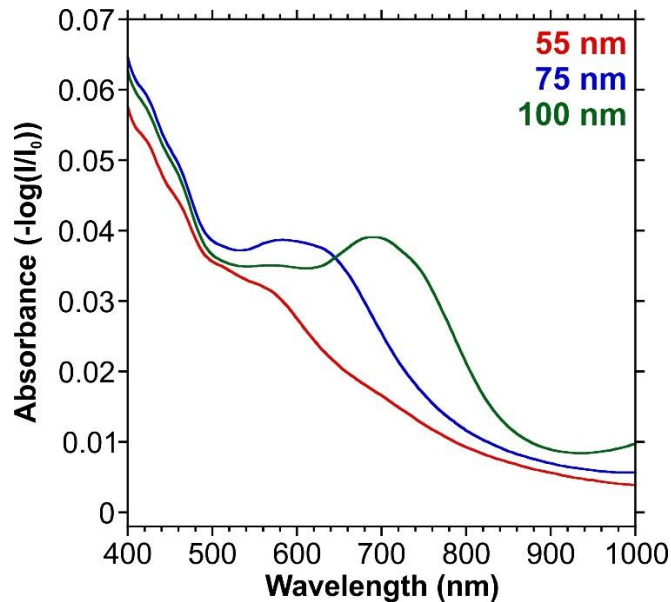


Figure 7.2 Absorbance spectra from finite-difference time-domain (FDTD) calculations of four-branched first-order dendritic fractals with side lengths from 175 nm and varying widths.

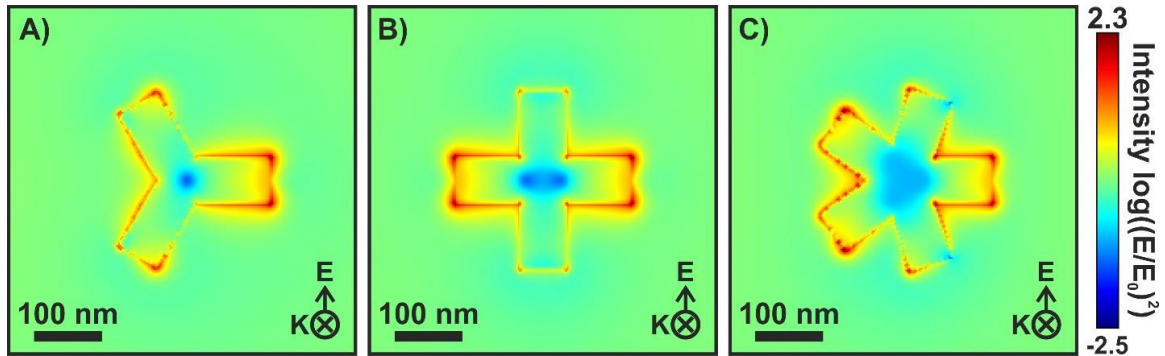


Figure 7.3 FDTD calculations of the electric field $(|E/E_0|)^2$: log scale representation at the observed resonance for first-order generation dendritic fractals with A) three, B) four, and C) five inner branches.

Expanding to a second-order generation (Figure 7.4) introduces interesting optical properties. From the first- to second-order generation, the three-branched structures exhibit similar optical properties, including a resonance near 565 nm (labelled i Figure 7.4D). The same is true for the four- and five-branched fractals. This further supports the assignment of this resonance being the transverse dipolar mode. More importantly, additional resonances (ii through iv) are observed, and are quite strong for the fractals with four and five inner branches. An interesting feature of the resonances labelled ii, iii, and iv, is that as the number of inner branches increases, a significant blue-shift is observed. This same effect is observed in the near- to mid-IR for the dendritic fractals,⁴³⁻⁴⁴ and the near-IR for multi-branched planar structures.³⁰

The presence of multiple resonances in the near- to mid-IR for dendritic fractals has been previously explained using hybridization models.⁴²⁻⁴³ This model is an electromagnetic analog of molecular orbital theory and is used to explain the interaction between the elementary plasmons of nanostructures.⁵⁹ In the context of the dendritic fractals, this involves the interaction between the plasmons of the inner branches with the plasmons of the outer branches or generations. Given that the global and hybridized dipolar resonances associated with the dendritic fractals are known to appear in the near- to mid-IR, the observed resonances in Figure 7.4D correspond to the global multipolar and hybridized multipolar modes. Once again, FDTD calculations were performed to determine the spatial distribution of EM enhancement. As the four-branched second-

order generation dendritic fractal has well four well defined modes, this was the one selected (Figure 2).

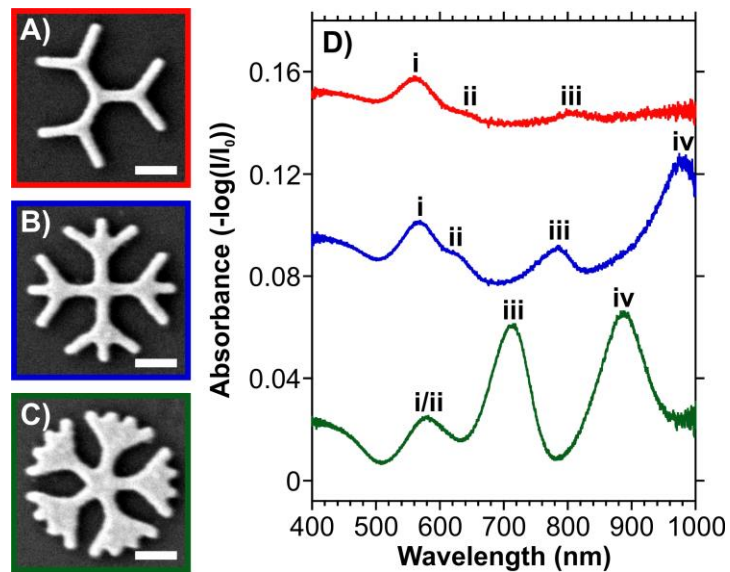


Figure 7.4 SEM images of second-order dendritic fractals with A) three, B) four, and C) five inner branches. The scale bar in the SEM images is 200 nm. D) Absorbance spectra of the second-order dendritic fractals with side lengths of 175 nm.

The highest energy resonances (labelled i and ii) once again correspond to the transverse dipolar modes associated with the widths of the nanorods within the dendritic fractal. At the second resonance (ii), the greatest amount of EM enhancement is localized to the tips of the angled outermost nanorods. At the third resonance (Figure 7.4C, (iii)) a greater contribution from the innermost portions of the outer nanorods is observed. Interestingly, the EM field enhancement at the outer branches appears to exhibit minimal polarization dependence. For the same resonance, the small enhancement along the sides of the inner nanorods does favour the structures along the polarization axis (y-axis). The most striking EM field map occurs for the lowest energy resonance (Figure 7.4D, (iv)). Here, the structures along the polarization axis, especially the inner structures, exhibit the greatest enhancement. The overall profile along the y-axis bears a resemblance with a quadrupolar mode of a traditional nanorod.⁶⁰ We therefore describe this resonance as being the global quadrupolar mode of the fractal.

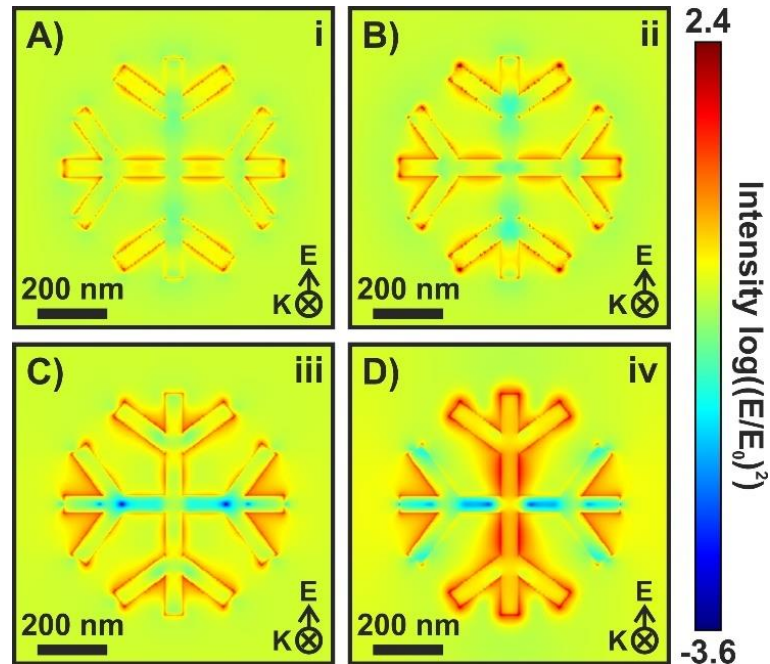


Figure 7.5 FDTD calculations of the electric field $(|E/E_0|)^2$: log scale representation at the resonances of a four-branched second-order dendritic fractal with side lengths of 175 nm. The numbers correspond to those indicated in Figure 7.4D.

Further increasing to the order of the generation was only possible for the fractals with three of four inner branches (Figure 7.6A, B). In the outermost generation of the four-branched configuration, many of the nanorods were near each other, yielding significant overlap. As such, there was concern that the structures would not resolve once fabricated, and instead result in a “duck foot”-like structure.⁴³⁻⁴⁴ To this end, some of the outermost nanorods were removed, yielding a truncated configuration (Figure 7.6C). Removing the structures yields only a slight red-shift of the resonances found above 600 nm, without introducing any new resonances in the visible to near-IR (Figure 7.6D). FDTD calculations were further performed on the four-branched third-order generation fractal (Figure 7.7) to determine if the spatial distribution of EM enhancement varied from that of the second-order generation. With a total of 52 nanorods, the various resonances provide EM across the entire fractal, encompassing portions of both the inner and outer nanorods. This is not the case in the mid-IR, where instead each resonance can be viewed as the culmination of each generation beginning with the outermost branches at the highest energy and the global resonance at the lowest energy.

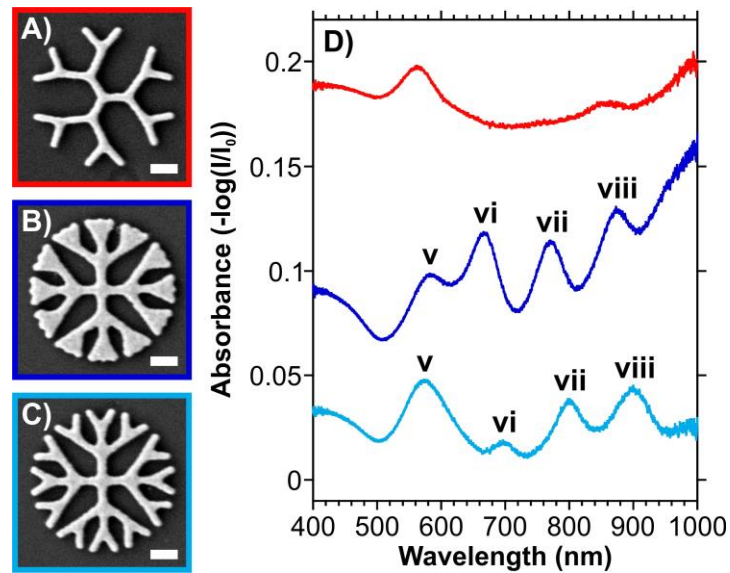


Figure 7.6 SEM images of third-order dendritic fractals with A) three, B) four inner branches. C) SEM images of a truncated version of B). The scale bar in the SEM images is 200 nm. D) Absorbance spectra of the third-order dendritic fractals with side lengths of 175 nm.

It is important to also recognize that if the number of inner branches is increased, it becomes necessary to truncate the fractal at lower-order generations. Figure 7.8 shows the fractal progression for fractals with six inner branches. Consistent with the results for fractals with four and five inner branches, the absorbance spectrum for the first-order generation (Figure 7.8D) contains only a single resonance in the visible to near-IR, whereas the truncated second-order generations show up to four resonances in the same spectral domain (400-1000 nm). Once again, by altering how the fractal is truncated, the resonances can be moderately tuned. Specifically, except for the transverse dipolar mode, all the remaining resonances red-shift as the number of outer branches decreases during truncation. This is the same effect that was observed in Figure 7.6D for the truncated four-branched second-order generation fractal.

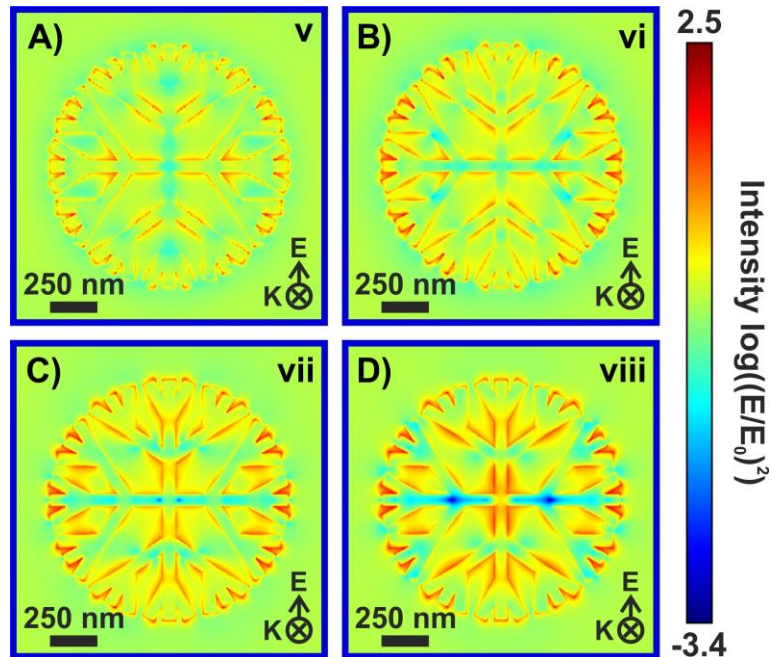


Figure 7.7 FDTD calculations of the electric field $(|E/E_0|)^2$: log scale representation at the resonances of a four-branched third-order dendritic fractal with side lengths of 175 nm. The numbers correspond to the indicated resonances in Figure 7.6.

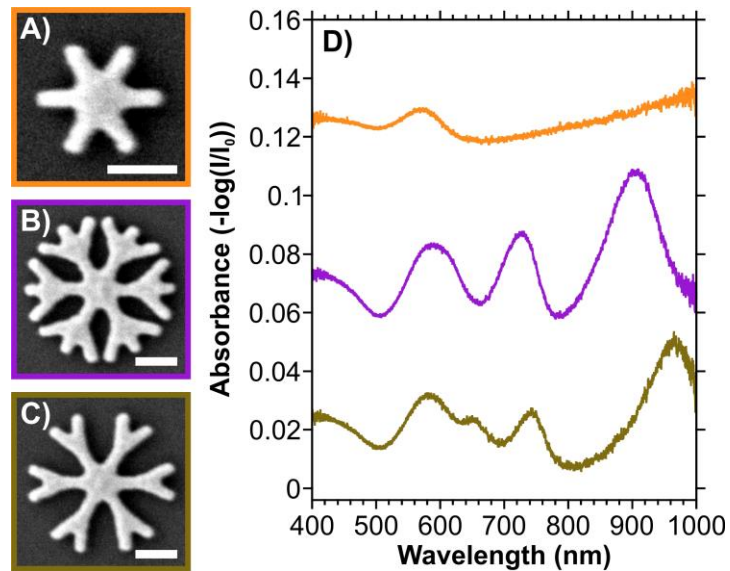


Figure 7.8 SEM images of 6-branched A) first-order, B and C) truncated second-order generation fractals. The scale bar in the SEM images is 200 nm. D) Absorbance spectra of the second-order dendritic fractals with side lengths of 175 nm.

7.3.2 Further Tuning the Spectral Positions of the Localized Surface Plasmon Resonances

As opposed to altering the configuration of the fractal, tuning of the plasmon resonances can also be achieved by altering the dimensions of the nanorods that make up the fractal. Here, the effect of altering either the length or the widths of the nanorods is highlighted.

Increasing the side length of the nanorods within the fractal yields various red-shifts of the resonances, with the exception being the transverse dipolar mode. A necessary aspect of fabricating plasmonic nanostructures is the ability to readily tune the spectral position of the resonances. As can be observed in Figure 7.9A, and Figure 7.10, the increasing the side lengths yields linear changes to the spectral position of the resonances. The amount of red-shift per 1 nm increase in side length of the individual nanorods varies from 1 to 3 nm. It is necessary to note that in these fractals, the side length from generation to generation is constant. Altering the side lengths in each individual generation can lead to further spectral tuning.

Alternatively, the spectral position of the resonances can also be tuned by changing the width of the nanorods within the dendritic fractal. Consistent with the results previously discussed in Figure 7.2, altering the width will change the spectral position of the transverse dipolar mode. However, as Figure 7.9B also shows, the red-shift of the transverse dipolar mode is coupled with a blue-shift of the other modes present. This origin of this blue-shift is attributed to the opposite effect of truncating the structures. Here, as the width of the nanorods increases, a greater overlap between the outer rods occurs. This results in less of the outer surface of the nanorods being exposed to the surrounding media (i.e. air). By coupling the changes in length and width, a high degree of tuning can be achieved. When coupled with altering the number of inner branches and the order of the fractal, it is possible to achieve large numbers of resonances in the visible to near-IR with varying spatial distributions of EM enhancement.

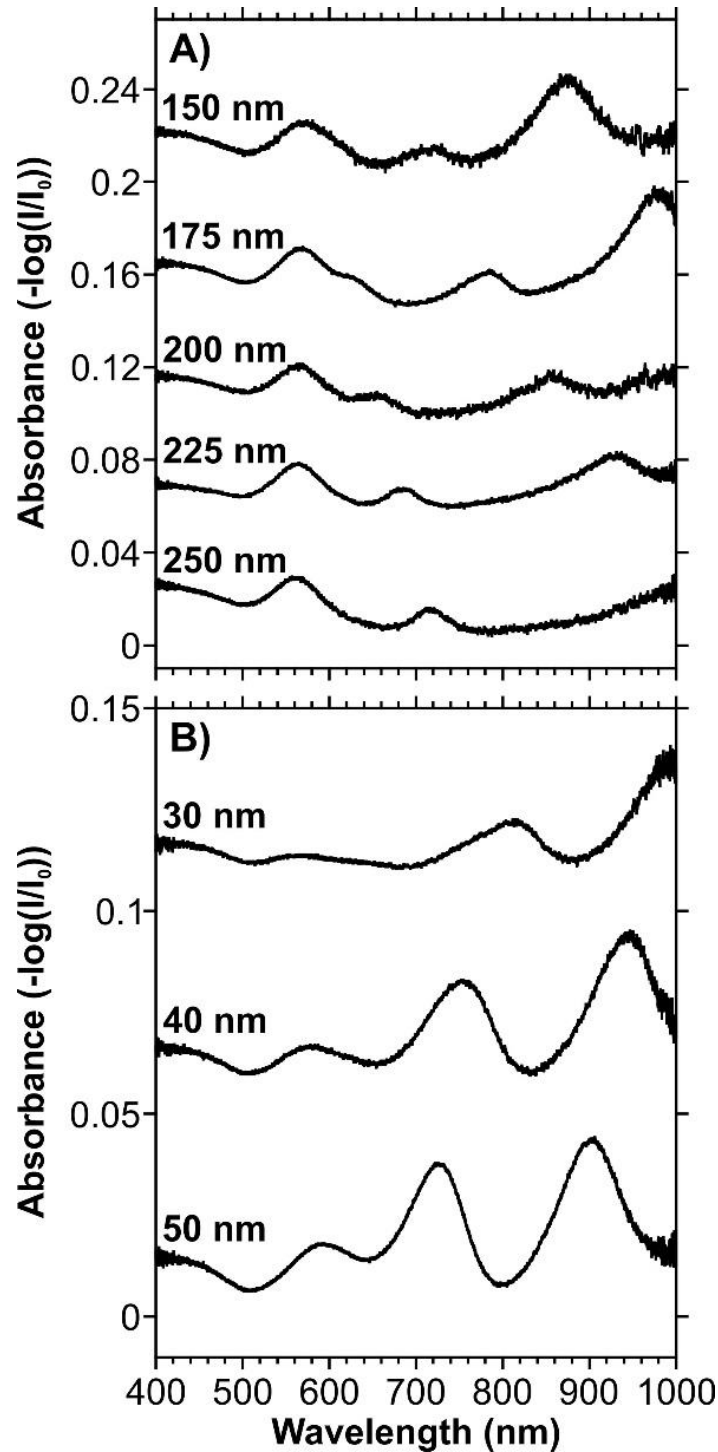


Figure 7.9 A) Absorbance spectra of four-branched second-order generation dendritic fractals with side lengths ranging from 150 to 250 nm. B) Absorbance spectra of five-branched second-order generation dendritic fractals with written widths ranging from 30 to 50 nm.

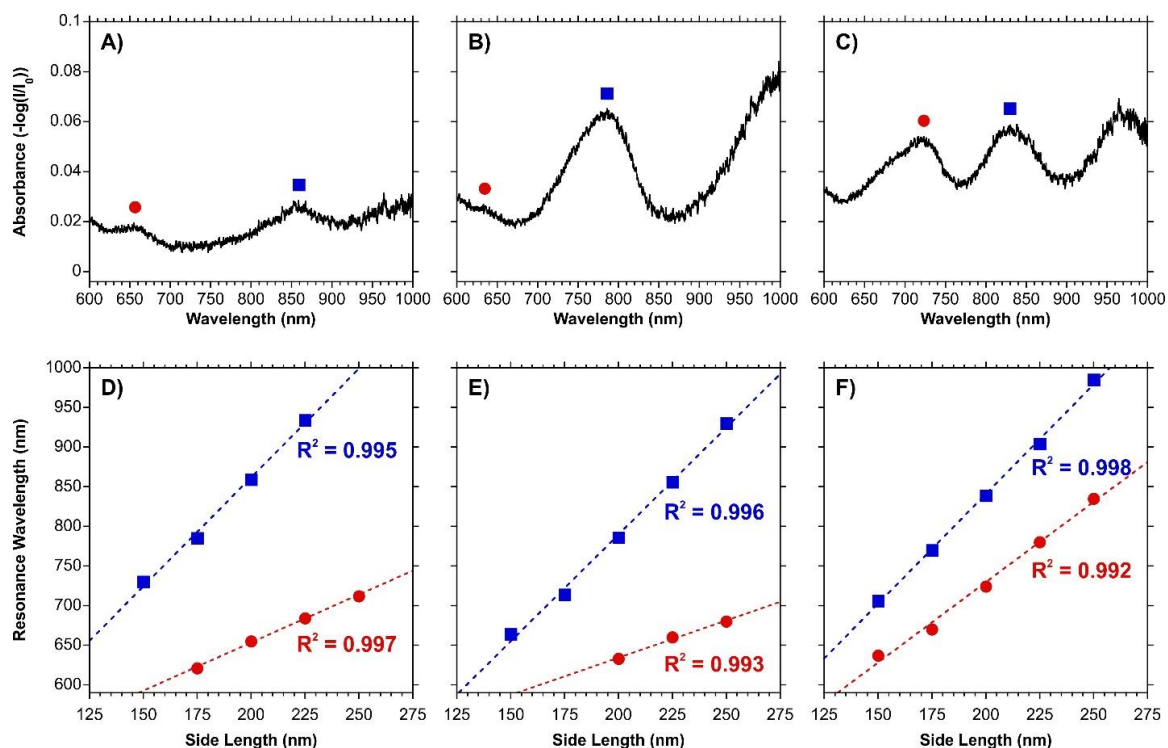


Figure 7.10 Absorbance spectra of **A)** four-branched second-order generation, **B)** five-branched second-order generation, and **C)** four-branched third-order generation dendritic fractals with rod side lengths of 200 nm. **D-F)** Changes in the spectral position of the indicated resonances as the side length of the nanorods is altered.

7.3.3 SERS Compatibility of the Dendritic Fractals

As the various dendritic fractals fabricated exhibit resonances in the visible region, it was decided to probe their compatibility with SERS. Here, we focus on an excitation wavelength of 633 nm as it does not correspond to the transverse dipolar mode, but instead to a higher-order mode originating from the fractal itself. This highlights an advantage of the dendritic fractals over classic nanorods. It is also important to note that other excitation wavelengths, such as 785 nm, would also meet the same requirement.

Furthermore, the presence of multiple resonances can lead to enhancing a greater portion of the Raman spectrum associated with the analyte of interest. As was discussed in Chapter 2, the SERS enhancement is dependent not only on the excitation wavelength,

but also the wavelength associated with the Raman scattered light. For an excitation wavelength of 633 nm, the Raman scattered light at 1000 cm^{-1} is at a Raman wavelength of 676 nm. With 785 nm excitation, the same Raman shift is at 852 nm. As the LSPR exhibits broadness, the vibrational modes in the fingerprint region can be readily enhanced as the shifts in wavelength for the scattered light is quite small. However, in the case of a structure that exhibits only a single resonance, enhancing the vibrational modes associated with larger Raman shifts, such as the C-H modes near 3000 cm^{-1} , remains a challenge as the Raman wavelengths are 781 and 1027 nm for 633 and 785 nm excitations respectively. Overcoming this limitation requires that the structure exhibit multiple resonances, and ideally a similar distribution of EM field enhancement at those resonances. Both conditions are achieved for the dendritic fractals.

For the SERS validation experiments, the fractals were functionalized with 4-nitrothiophenol (4-NTP). The SERS spectrum of 4-NTP is characterized by a strong vibrational mode near 1335 cm^{-1} corresponding to the symmetric NO_2 stretch, as well as bands at 1080 and 1572 cm^{-1} assigned to the S-C stretching mode and C=C stretching mode of the benzenyl ring respectively.⁶¹ Figure 7.11A shows the SERS response obtained on the various first-order generation fractals. The relatively weak intensity is consistent with the lack of a distinct resonance at the excitation wavelength (633 nm) or at the wavelengths corresponding to the shown Raman shifts (667 – 714 nm). However, it is still possible to observe the vibrational mode of the NO_2 group. The increase in intensity observed by increasing the number of inner branches follows the concept that multibranched structures can support a greater density of hot-spots. Other configurations, especially those with a combination of resonances that are close to the excitation wavelength and a high hot-spot density, yield considerably stronger SERS responses (Figure 7.11B). In these spectra, all the key peaks of 4-NTP are well defined and consistently observed. It was therefore decided to focus on the second- and third-order generation fractals with inner branches ranging from four to six. Furthermore, as increasing side lengths results in shifting the resonances, only the fractals prepared with nanorods of 150 and 175 nm side lengths were further explored.

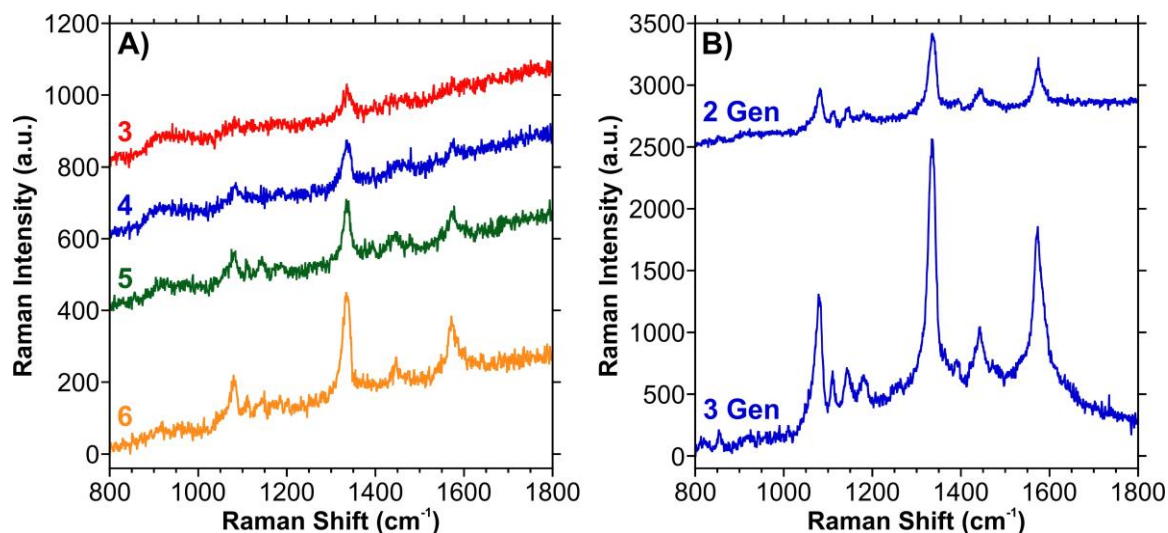


Figure 7.11 SERS response of 4-NTP functionalized dendritic fractals. A) First-order generation fractals where the number above the spectrum indicates the number of inner branches. B) Four-branched dendritic fractals in the indicated order generation.

7.3.4 Direct SERS-Based Detection of Dopamine

Catecholamines neurotransmitters, such as dopamine, have been studied by SERS since the late 1980's.⁶² Unlike 4-NTP, these molecules do not form a covalent bond with the surface of a metal nanostructure. As the importance of neurotransmitters, especially dopamine, with respect to neurological disorders becomes better understood, developing new means of detection becomes important. In this regard, SERS-based detection based on the vibrational fingerprint is an emerging approach since it could be combined with real-time and in-vivo measurements of dopamine release. Here, we focus on the introductory use of the dendritic fractals for on-chip sensing. Future incorporation of microfluidic channels could yield a more complete device for in-vitro SERS-based sensing.

The Raman spectrum obtained of a 10 mM dopamine solution (Figure 7.12), exhibits broad Raman bands with weak intensities. The spectrum is similar to that of a previously reported Raman spectrum of aqueous dopamine (DA) under basic conditions.⁶³ When SERS measurements are performed on a four-branched third-order generation dendritic

fractal (Figure 7.12), a clear difference is observed. It is important to note that under our experimental conditions, only a single fractal is irradiated when performing the SERS measurements. The observed SERS spectrum is consistent with many previously published SERS spectra of dopamine.^{47-50, 64-66} For our spectra, the distinct peaks are at 1270, 1331, 1484, and 1583 cm^{-1} . The dominant peak at 1484 cm^{-1} corresponds to the C=C stretching mode of the phenyl group.⁴⁷ The enhancement occurs because the phenol moieties of the dopamine interact with the gold surface. Furthermore, as was well demonstrated by Bailey *et al.*, this interaction can be applied to other neurotransmitters and catechols.⁴⁸ When several neurotransmitters are present, analyzing the SERS spectra by multiplexing methods, such as barcoding, can be used to rapidly differentiate between the neurotransmitters.⁴⁹

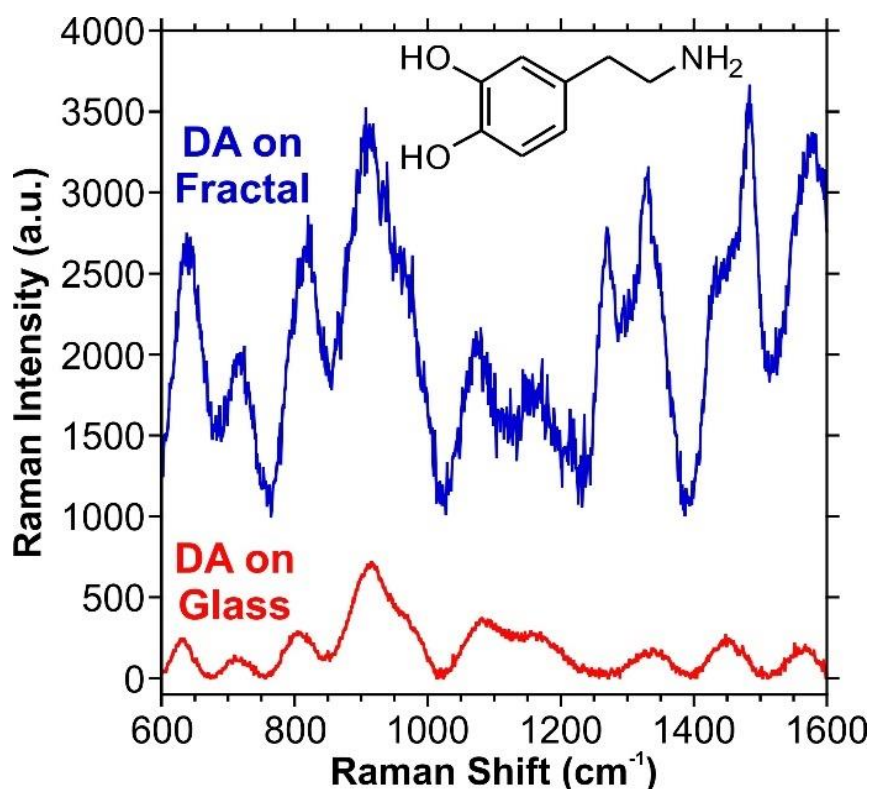


Figure 7.12 Raman spectrum obtained of a 10 mM solution of dopamine (DA) on glass. SERS spectrum obtained of the dopamine solution using a four-branched third-order dendritic fractal. Included as an inset is the chemical structure of dopamine. A polynomial baseline correction has been applied to the spectra.

7.3.5 Indirect SERS-Based Detection of Dopamine

To indirectly detect dopamine by SERS, a dopamine binding aptamer was introduced. Aptamers have emerged as an attractive means of detecting analytes due to their specificity towards specific analytes. Aptamers have been used in SERS studies for the detection of ochratoxin A,¹¹⁻¹² adenosine triphosphate,⁶⁷ cocaine,⁶⁸ and pesticides.⁶⁹ As the concentration of the aptamer solutions are often quite low (1 μM), it is necessary to prevent non-specific binding to the metal surface. In this regard, small alkane thiol molecules, referred to as backfill molecules, are added to functionalize any remaining bare surface. This prevents the target analyte from reaching the surface. 6-mercaptohexanol (MCH) is often employed as a backfill molecule in aptamer studies.⁶⁹ For our functionalization process, we first introduced the MCH onto the surface as a short functionalization, with the aim of forming an incomplete self-assembled monolayer on the surface.

The SERS spectra obtained of the mercaptohexanol and aptamer functionalized dendritic fractals is shown in the blue spectra of Figure 7.13. Here, the peaks in the spectra show a large degree of similarity. Previous results with MCH have shown that in a mixture of MCH and an aptamer, the contribution from the MCH in the resulting SERS spectrum is minimal.⁷⁰ The SERS spectra of single and double stranded DNA are quite complex,^{12, 71-73} exhibiting contributions from not only the DNA bases, but from the deoxyribose and phosphate backbone as well. As the emphasis of this study is on the detection of dopamine as opposed to the study of DNA, no vibrational mode analysis is performed.

After performing the SERS measurements on the MCH and aptamer functionalized surface, a solution of dopamine was introduced. After immersion in the dopamine solution for 10 minutes, SERS spectra were recorded using the functionalized four-branched third-order generation dendrimers. The green spectra of Figure 7.13 exhibit the key peaks from before the introduction of dopamine, along with two new peaks indicated by * and **. These new peaks at 1271 and 1487 cm^{-1} match spectral position of the vibrational modes observed in Figure 7.12 for just the SERS response of dopamine (1270 and 1484 cm^{-1}). With the functionalization procedure used, the aim was to completely cover the surface a combination of MCH and the aptamer. If some of the surface was not

functionalized, there exists a possibility that non-specific binding of the dopamine to the gold surface could occur. As no covalent bond is formed between the gold surface and dopamine, a rinsing step was introduced to try and remove any dopamine that was interacting with the metal surface.

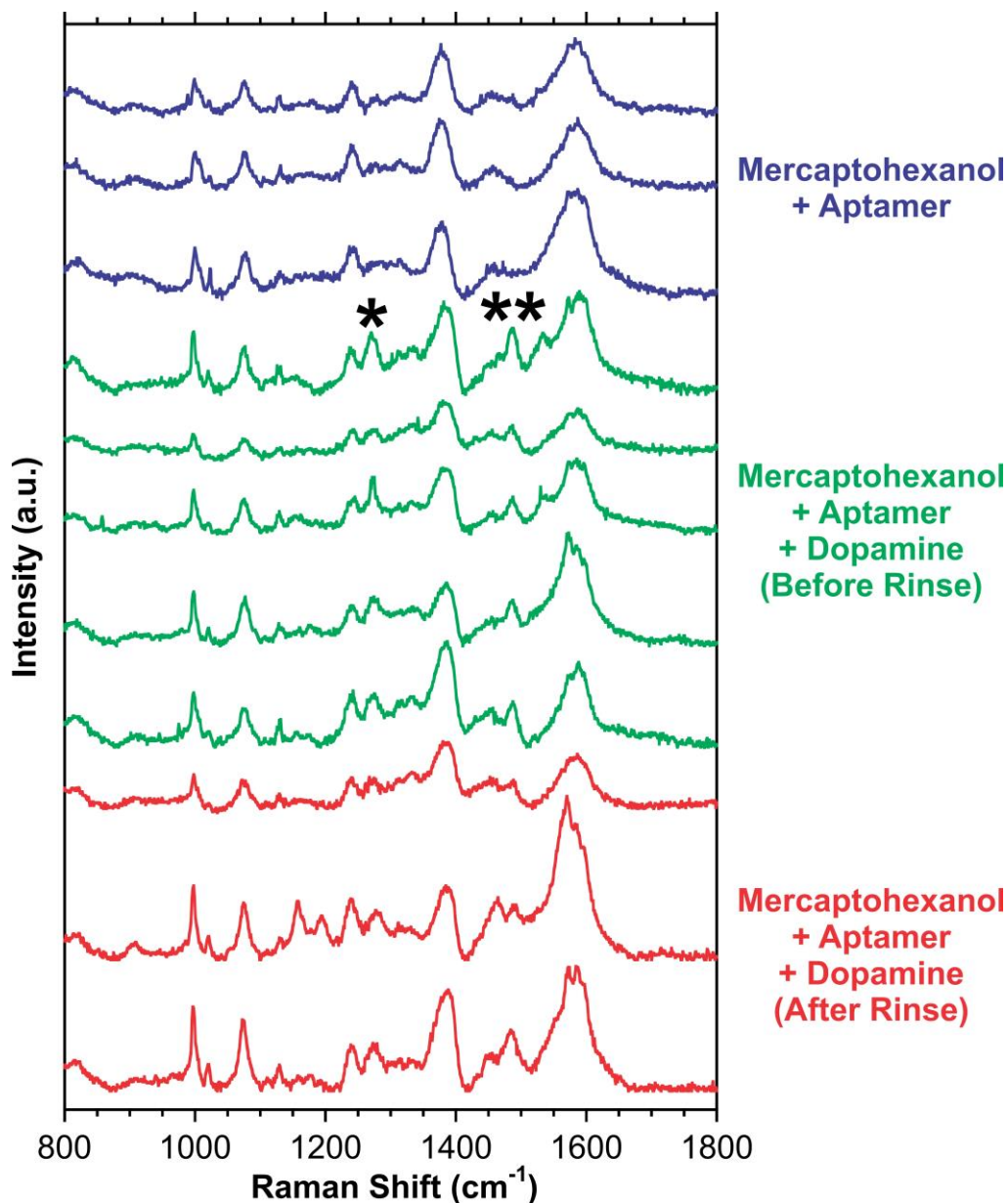


Figure 7.13 SERS spectra obtained on the dendritic fractals under various conditions involving the dopamine binding aptamer and dopamine. The peaks indicated by * and ** correspond to peaks that appear once dopamine is introduced. A polynomial baseline correction has been applied to the spectra.

The red spectra of Figure 7.13 still show the two new peaks. This leads us to believe that these peaks are that of dopamine that is interacting with the aptamer. To further explore this approach to the SERS-based detection of dopamine, additional analysis of the required results is required. Specifically, principle component analysis may provide greater detail regarding the changes in the SERS spectra,^{12, 74} beyond just the introduction of new peaks. It has previously been shown that for SERS-based aptasensing, changes in the spectra can be related to the interaction of the analyte with the aptamer.¹¹ Detailing these types of responses can provide greater detail in the applicability of the dendrimers for indirect SERS detection, specifically emphasizing the detection of dopamine. Additionally, introducing other catecholamines or neurotransmitters,⁴⁸ such as epinephrine, can be used to demonstrate the sensitivity of the aptamer,⁵³ and further validate the employed protocol of detection.

7.4 Conclusion

Since fractal structures support multiple resonances, they are ideal structures for enhancing the vibrational fingerprint of analytes located near their surfaces. We have thoroughly demonstrated how to tune not only the number of resonances, but also the spectral position of the resonances in the visible to near-IR spectral domain. Fractals with a greater number of inner branches and at higher generations can support the greatest number of resonances. Correlative FDTD calculations provide insight into the distribution of EM enhancement at these various resonances. The observed multipolar modes can be assigned to the quadrupolar modes of the outer branches, and the entire fractal, and higher and lower energies respectively. The spectral positions of these resonances can be adjusted by altering length and widths of the nanorods that form the fractal. Once sufficiently tuned, the fractals can then be used to enhance the Raman vibrational fingerprint of analytes located at or near the surface of the structure. By emphasizing the structures that offer the greatest density of hot-spots, it is possible to maximize the observed SERS signal. Finally, the applicability of the dendrimers to SERS-based sensing was demonstrated using dopamine as a target analyte and two different sensing approaches. For direct detection, the dendrimers were immersed in a solution of dopamine, while indirect detection relied on the use of a dopamine binding

aptamer. Regardless of the approach used, the dendritic fractals can be used to detect the dopamine by SERS. Further work on the development of the sensing capabilities of the dendrimers should focus on maximizing the EM enhancement to yield a stronger SERS response, and exploring the design considerations necessary for correlative SERS and SEIRA measurements.

7.5 References

1. Albrecht, G.; Ubl, M.; Kaiser, S.; Giessen, H.; Hentschel, M., *ACS Photonics* **2018**, *5*, 1058-1067.
2. Wallace, G. Q.; Tabatabaei, M.; Hou, R.; Coady, M. J.; Norton, P. R.; Simpson, T. S.; Rosendahl, S. M.; Merlen, A.; Lagugné-Labarthe, F., *ACS Photonics* **2016**, *3*, 1723-1732.
3. Cialla-May, D.; Zheng, X. S.; Weber, K.; Popp, J., *Chem. Soc. Rev.* **2017**, *46*, 3945-3961.
4. Ren, X.; Cao, E.; Lin, W.; Song, Y.; Liang, W.; Wang, J., *RSC Adv.* **2017**, *7*, 31189-31203.
5. Enrichi, F.; Quandt, A.; Righini, G. C., *Renew. Sust. Energ. Rev.* **2018**, *82*, 2433-2439.
6. Feliu, N.; Hassan, M.; Garcia Rico, E.; Cui, D.; Parak, W.; Alvarez-Puebla, R., *Langmuir* **2017**, *33*, 9711-9730.
7. Sun, F.; Galvan, D. D.; Jain, P.; Yu, Q., *Chem. Commun.* **2017**, *53*, 4550-4561.
8. Gao, F.; Liu, L.; Cui, G.; Xu, L.; Wu, X.; Kuang, H.; Xu, C., *Nanoscale* **2017**, *9*, 223-229.
9. Kannegulla, A.; Liu, Y.; Wu, B.; Cheng, L.-J., *J. Phys. Chem. C* **2018**, *122*, 770-776.
10. Li, J.-F.; Li, C.-Y.; Aroca, R. F., *Chem. Soc. Rev.* **2017**, *46*, 3962-3979.
11. Galarreta, B. C.; Tabatabaei, M.; Guieu, V.; Peyrin, E.; Lagugné-Labarthe, F., *Anal. Bioanal. Chem.* **2013**, *405*, 1613-1621.
12. Gillibert, R.; Triba, M. N.; Lamy de la Chapelle, M., *Analyst* **2018**, *143*, 339-345.
13. Neubrech, F.; Huck, C.; Weber, K.; Pucci, A.; Giessen, H., *Chem. Rev.* **2017**, *117*, 5110-5145.
14. de Albuquerque, C. D. L.; Sobral-Filho, R. G.; Poppi, R. J.; Brolo, A. G., *Anal. Chem.* **2018**, *90*, 1248-1254.
15. Tanwar, S.; Haldar, K. K.; Sen, T., *J. Am. Chem. Soc.* **2017**, *139*, 17639-17648.
16. Dong, L.; Yang, X.; Zhang, C.; Cerjan, B.; Zhou, L.; Tseng, M. L.; Zhang, Y.; Alabastri, A.; Nordlander, P.; Halas, N. J., *Nano Lett.* **2017**, *17*, 5768-5774.

17. Wang, Z.; Pan, S.; Krauss, T. D.; Du, H.; Rothberg, L. J., *Proc. Natl. Acad. Sci. U.S.A.* **2003**, *100*, 8638-8643.
18. Ye, W.; Shen, C.; Tian, J.; Wang, C.; Hui, C.; Gao, H., *Solid State Sci.* **2009**, *11*, 1088-1093.
19. Liu, R.; Li, S.; Yu, X.; Zhang, G.; Ma, Y.; Yao, J.; Keita, B.; Nadjro, L., *Cryst. Growth Des.* **2011**, *11*, 3424-3431.
20. Li, D.; Liu, J.; Wang, H.; Barrow, C. J.; Yang, W., *Chem. Commun.* **2016**, *52*, 10968-10971.
21. Dies, H.; Raveendran, J.; Escobedo, C.; Docoslis, A., *Nanoscale* **2017**, *9*, 7847-7857.
22. Hu, L.; Liu, Y. J.; Han, Y.; Chen, P.; Zhang, C.; Li, C.; Lu, Z.; Luo, D.; Jiang, S., *J. Mater. Chem. C* **2017**, *5*, 3908-3915.
23. Cho, F.-H.; Kuo, S.-C.; Lai, Y.-H., *RSC Adv.* **2017**, *7*, 10259-10265.
24. Wang, P.; Pang, S.; Pearson, B.; Chujo, Y.; McLandsborough, L.; Fan, M.; He, L., *Anal. Bioanal. Chem.* **2017**, *409*, 2229-2238.
25. Xu, D.; Dong, J.; Zhang, S.; Chen, J., *Sens. Actuator A-Phys.* **2018**, *271*, 18-23.
26. Dies, H.; Raveendran, J.; Escobedo, C.; Docoslis, A., *Sens. Actuator B-Chem.* **2018**, *257*, 382-388.
27. Wang, J.; Zhang, X.-B.; Wang, Z.-L.; Wang, L.-M.; Xing, W.; Liu, X., *Nanoscale* **2012**, *4*, 1549-1552.
28. Ye, S. J.; Kim, D. Y.; Kim, D. W.; Park, O. O.; Kang, Y., *J. Mater. Chem. A* **2016**, *4*, 578-586.
29. Feng, J.-J.; Liu, L.; Huang, H.; Wang, A.-J., *Sens. Actuator B-Chem.* **2017**, *238*, 91-97.
30. Chirumamilla, M.; Chirumamilla, A.; Roberts, A. S.; Zaccaria, R. P.; De Angelis, F.; Kjær Kristensen, P.; Krahne, R.; Bozhevolnyi, S. I.; Pedersen, K.; Toma, A., *Adv. Opt. Mater.* **2017**, *5*, 1600836.
31. Zhu, J.; Liu, M.-J.; Li, J.-J.; Li, X.; Zhao, J.-W., *Spectrochim. Acta A* **2018**, *189*, 586-593.
32. Kariuki, V. M.; Hoffmeier, J. C.; Yazgan, I.; Sadik, O. A., *Nanoscale* **2017**, *9*, 8330-8340.
33. Issaad, D.; Moustou, H.; Medjahed, A.; Lalaoui, L.; Spadavecchia, J.; Bouafia, M.; de la Chapelle, M. L.; Djaker, N., *J. Phys. Chem. C* **2017**, *121*, 18254-18262.
34. Bellido, E. P.; Bernasconi, G. D.; Rossouw, D.; Butet, J.; Martin, O. J. F.; Botton, G. A., *ACS Nano* **2017**, *11*, 11240-11249.
35. Aslan, E.; Aslan, E.; Wang, R.; Hong, M. K.; Erramilli, S.; Turkmen, M.; Saracoglu, O. G.; Dal Negro, L., *ACS Photonics* **2016**, *3*, 2102-2111.
36. Grigorenko, I., *Appl. Phys. Lett.* **2013**, *103*, 043123.

37. Volpe, G.; Volpe, G.; Quidant, R., *Opt. Express* **2011**, *19*, 3612-3618.
38. Sederberg, S.; Elezzabi, A. Y., *Opt. Express* **2011**, *19*, 10456-10461.
39. Coluccio, M. L.; Gentile, F.; Das, G.; Nicastrì, A.; Perri, A. M.; Candeloro, P.; Perozziello, G.; Proietti Zaccaria, R.; Gongora, J. S. T.; Alrasheed, S.; Fratolocci, A.; Limongi, T.; Cuda, G.; Di Fabrizio, E., *Sci. Adv.* **2015**, *1*.
40. Fang, J.; Wang, D.; DeVault, C. T.; Chung, T.-F.; Chen, Y. P.; Boltasseva, A.; ShalaeV, V. M.; Kildishev, A. V., *Nano Lett.* **2017**, *17*, 57-62.
41. Kenney, M.; Grant, J.; Shah, Y. D.; Escorcìa-Carranza, I.; Humphreys, M.; Cumming, D. R. S., *ACS Photonics* **2017**, *4*, 2604-2612.
42. Gottheim, S.; Zhang, H.; Govorov, A. O.; Halas, N. J., *ACS Nano* **2015**, *9*, 3284-3292.
43. Wallace, G. Q.; Foy, H. C.; Rosendahl, S. M.; Lagugnè-Labarthe, F., *J. Phys. Chem. C* **2017**, *121*, 9497-9507.
44. Wallace, G. Q.; Read, S. T.; McRae, D. M.; Rosendahl, S. M.; Lagugnè-Labarthe, F., *Adv. Opt. Mater.* **2018**, *6*, 1701336.
45. Cepeda, C.; Murphy, K. P. S.; Parent, M.; Levine, M. S., *Prog. Brain Res.* **2014**, *211*, 235-254.
46. Buddhala, C.; Loftin, S. K.; Kuley, B. M.; Cairns, N. J.; Campbell, M. C.; Perlmutter, J. S.; Kotzbauer, P. T., *Ann. Clin. Trans. Neurol.* **2015**, *2*, 949-959.
47. Wang, P.; Xia, M.; Liang, O.; Sun, K.; Cipriano, A. F.; Schroeder, T.; Liu, H.; Xie, Y.-H., *Anal. Chem.* **2015**, *87*, 10255-10261.
48. Bailey, M. R.; Martin, R. S.; Schultz, Z. D., *J. Phys. Chem. C* **2016**, *120*, 20624-20633.
49. Lussier, F.; Brule, T.; Bourque, M.-J.; Ducrot, C.; Trudeau, L.-E.; Masson, J.-F., *Faraday Discuss.* **2017**, *205*, 387-407.
50. Liu, Y.; Xu, C.; Lu, J.; Zhu, Z.; Zhu, Q.; Manohari, A. G.; Shi, Z., *Appl. Surf. Sci.* **2018**, *427*, 830-836.
51. Lide, D. R.; Haynes, W. M., *CRC Handbook of Chemistry and Physics : A Ready-Reference Book of Chemical and Physical Data*; CRC Press: Boca Raton, 2009.
52. Palik, E. D., Preface. In *Handbook of Optical Constants of Solids*, Academic Press: Burlington, 1997.
53. Walsh, R.; Ho, U.; Wang, X. L.; DeRosa, M. C., *Can. J. Chem.* **2015**, *93*, 572-577.
54. Laurent, G.; Félidj, N.; Aubard, J.; Lévi, G.; Krenn, J. R.; Hohenau, A.; Schider, G.; Leitner, A.; Aussenegg, F. R., *J. Chem. Phys.* **2005**, *122*, 011102.
55. Nguyen, M.; Kherbouche, I.; Gam-Derouich, S.; Ragheb, I.; Lau-Truong, S.; Lamouri, A.; Levi, G.; Aubard, J.; Decorse, P.; Felidj, N.; Mangeney, C., *Chem. Commun.* **2017**, *53*, 11364-11367.

56. Karker, N. A.; Carpenter, M. A., *Sens. Actuator B-Chem.* **2017**, *252*, 385-390.
57. Osberg, K. D.; Harris, N.; Ozel, T.; Ku, J. C.; Schatz, G. C.; Mirkin, C. A., *Nano Lett.* **2014**, *14*, 6949-6954.
58. D'Andrea, C.; Bochterle, J.; Toma, A.; Huck, C.; Neubrech, F.; Messina, E.; Fazio, B.; Maragò, O. M.; Di Fabrizio, E.; Lamy de La Chapelle, M.; Gucciardi, P. G.; Pucci, A., *ACS Nano* **2013**, *7*, 3522-3531.
59. Prodan, E.; Radloff, C.; Halas, N. J.; Nordlander, P., *Science* **2003**, *302*, 419-422.
60. Guiton, B. S.; Iberi, V.; Li, S.; Leonard, D. N.; Parish, C. M.; Kotula, P. G.; Varela, M.; Schatz, G. C.; Pennycook, S. J.; Camden, J. P., *Nano Lett.* **2011**, *11*, 3482-3488.
61. Dong, B.; Fang, Y.; Xia, L.; Xu, H.; Sun, M., *J. Raman Spectrosc.* **2011**, *42*, 1205-1206.
62. Lee, N. S.; Hsieh, Y. Z.; Paisley, R. F.; Morris, M. D., *Anal. Chem.* **1988**, *60*, 442-446.
63. Pande, S.; Jana, S.; Sinha, A. K.; Sarkar, S.; Basu, M.; Pradhan, M.; Pal, A.; Chowdhury, J.; Pal, T., *J. Phys. Chem. C* **2009**, *113*, 6989-7002.
64. Bu, Y.; Lee, S. W., *Microchim. Acta* **2015**, *182*, 1313-1321.
65. Chen, R.; Zhang, L.; Li, X.; Ong, L.; Soe, Y. G.; Sinsua, N.; Gras, S. L.; Tabor, R. F.; Wang, X.; Shen, W., *ACS Sens.* **2017**, *2*, 1060-1067.
66. Palanisamy, S.; Yan, L.; Zhang, X.; He, T., *Anal. Methods* **2015**, *7*, 3438-3447.
67. Shi, H.; Chen, N.; Su, Y.; Wang, H.; He, Y., *Anal. Chem.* **2017**, *89*, 10279-10285.
68. Oroval, M.; Coronado-Puchau, M.; Langer, J.; Sanz-Ortiz, M. N.; Ribes, Á.; Aznar, E.; Coll, C.; Marcos, M. D.; Sancenón, F.; Liz-Marzán, L. M.; Martínez-Mañez, R., *Chem. Eur. J.* **2016**, *22*, 13488-13495.
69. Pang, S.; Labuza, T. P.; He, L., *Analyst* **2014**, *139*, 1895-1901.
70. Yang, J.; Palla, M.; Bosco, F. G.; Rindzevicius, T.; Alstrøm, T. S.; Schmidt, M. S.; Boisen, A.; Ju, J.; Lin, Q., *ACS Nano* **2013**, *7*, 5350-5359.
71. Barhoumi, A.; Zhang, D.; Tam, F.; Halas, N. J., *J. Am. Chem. Soc.* **2008**, *130*, 5523-5529.
72. Mackanic, D. G.; Mabbott, S.; Faulds, K.; Graham, D., *J. Phys. Chem. C* **2016**, *120*, 20677-20683.
73. Wu, Y.; Xiao, F.; Wu, Z.; Yu, R., *Anal. Chem.* **2017**, *89*, 2852-2858.
74. Campos, A. R.; Gao, Z.; Blaber, M. G.; Huang, R.; Schatz, G. C.; Van Duyne, R. P.; Haynes, C. L., *J. Phys. Chem. C* **2016**, *120*, 20961-20969.

Chapter 8

8 Conclusions and Outlook

In this thesis, we have developed and investigated a series of nanostructures and platforms that display multiple plasmon resonances over a large spectral domain, thus offering multispectral compatibility from the visible to the mid-IR. This enabled us to perform experiments involving a variety of plasmon-mediated techniques, with an emphasis on surface-enhanced Raman spectroscopy (SERS) and surface-enhanced infrared absorption (SEIRA). These two techniques are of particular interest due to their applications involving molecular and biomolecular detection.¹⁻⁶

After a general introduction of the very dynamic field of molecular plasmonics, and of its application to plasmon-mediated chemistry and small molecule detection, the second chapter focusses on the design considerations of plasmonic nanostructures along with the distinct fabrication methodologies. This chapter also explores the various plasmon-mediated techniques used in this thesis: SERS, SEIRA, and surface-enhanced fluorescence (SEF).

One of the critical aspects of plasmonic nanostructures remains the engineering of nanoscale regions of electromagnetic enhancement known as hot-spots. Chapter 3 describes the fabrication of arrangements of anisotropic nanostructures that generate a higher density of hot-spots. In this chapter, a series of structures composed of nanorods and nanoprisms were devised with varying features within the probed regions. For the nanorods, singlet and doublet arrangements were used. In the case of the nanoprisms, dimer through hexamer configurations were used. By performing finite difference time domain, the spatial distribution the electromagnetic enhancement over the surface of the structures was determined. To increase the number of hot-spots along with increasing the number of resonances, nanoprisms were superimposed onto each other to generate nanoarrowheads. The nanorods, nanoprisms, and nanoarrowheads were evaluated for SERS using a monolayer of 4-nitrothiophenol as a probe analyte. This chapter also introduces fractal plasmonics by generating a hexagonal Sierpiński gasket fractal using

the hexamer configuration of nanoprisms. The result of the fractal is that resonances are introduced closer to the mid-IR.

To prepare platforms that exhibit a broad multispectral compatibility, Chapter 4 develops a plasmonic platform composed of superimposed arrays of nanoprisms. Driven by the concept that dimensions of the structures are a critical parameter to determining the spectral position of resonances, arrays of small nanoprisms are overlaid with arrays of larger nanoprisms. The smaller structures exhibit resonances in the visible to near-IR, while the larger nanoprisms have resonances that span the near- to mid-IR. Much like the nanoarrowheads, when the small and large nanoprisms overlap, the resonance for the large nanoprisms shifts to longer wavelengths. As well, an increase in the density of hot-spots also occurs. The resulting platforms exhibit compatibility for SEF, SERS, and SEIRA. By performing both SERS and SEIRA measurements over the same platform, it is possible to perform correlative spectroscopic measurements.

As nanostructures and metasurfaces derived from fractals can exhibit multiple resonances, Chapters 5 through 7 explore dendritic fractals for different applications involving different spectral domains. Chapter 5 studies the spectral properties of dendritic fractals in the near- to mid-IR. The various relationships associated with the structural properties of the fractals and the connections between the resulting resonances is explored using a hybridization model. As the number of generations in the fractal increases through an iterative process, so does the number of resonances that can be linked to previous generations. By tailoring the size and the number of inner branches, it is possible to tune the spectral position of the resonances in the near- to mid-IR spectral range, opening the possibility to perform SEIRA measurements. Additionally, an important property of the dendritic fractals is that they exhibit a polarization dependence due to their anisotropic geometry. Chapter 6 focusses on the use of polarization-modulation infrared linear dichroism microscopy (μ PM-IRLD) applied to the study of the dendritic fractals. This is the first time that PM-ITLD is combined with microscopy measurements and applied to plasmonic nanostructures. This was possible due to the use of a synchrotron light source (Canadian Light Source) that provides sufficient brightness to enable an excellent signal-to-noise ratio for the dichroic measurements over the mid-IR

range. Interestingly, the anisotropy appears to be null at the exact average resonant frequencies of the plasmon modes and with negative and positive linear dichroism at lower and higher energies with respect to the exact plasmon resonance. As the spectral position of the dichroic response changes, so does the sensitivity towards detecting an analyte at the surface by SEIRA, and the matching between the resonance frequencies of both the plasmon and the considered vibrational modes must be carefully selected. Beyond exhibiting resonances in the near- to mid-IR, the dendritic fractals can also exhibit resonances in the visible to near-IR. Chapter 7 explores tuning the number and spatial position of the resonances in the visible region. The dendrimers are then functionalized with small molecules, and a dopamine binding aptamer, and are probed by SERS. As the properties of the dendritic fractal can be tuned for the visible and mid-IR regions, with sufficient tailoring of the structural properties, it should be possible to perform correlative spectroscopic measurements.

There are several natural extensions to the various work presented in this thesis. In the context of this thesis, fractal structures should be emphasized, especially those that exhibit varying dimensions. Geometries derived from H-like designs have been especially useful for SEIRA applications as the structures exhibit polarization dependence.⁷ The H-tree fractal incorporates this design feature,⁸ where the length of each rod is $\sqrt{2}$ the length of the previous perpendicular rod. By creating multiple generations, a series of polarization dependent resonances can be prepared with resonances that can presumably be tuned over a large spectral domain depending on the involved dimensions. An interesting alternative design is shown in Figure 8.1A. Instead of solid lines, shorter dashed lines can be used instead. This would not only provide additional structures to increase the absorbance, but also provide hot-spots between the adjacent nanorods. Furthermore, with such a diverse range in sizes over the fractal, resonances across the visible through mid-IR can be sought after.

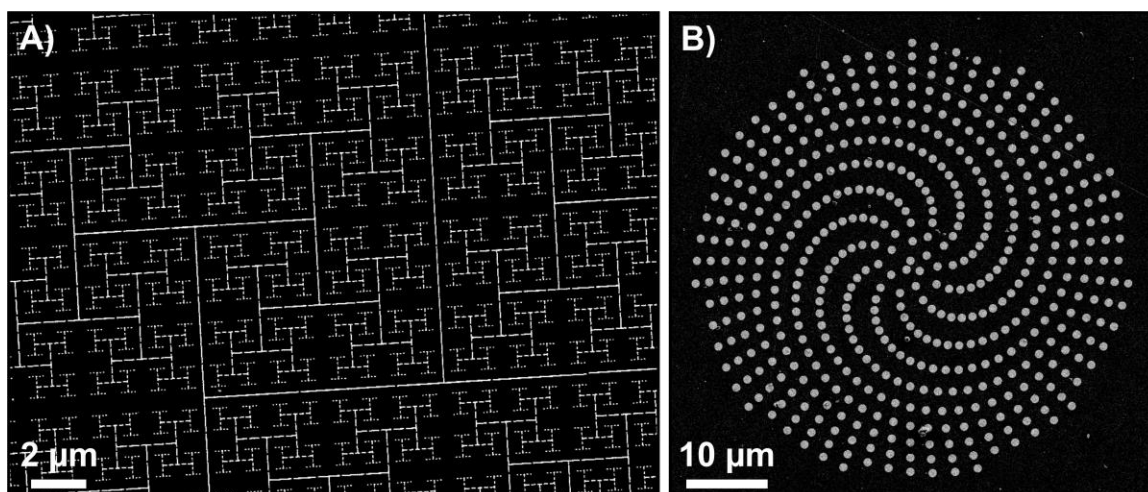


Figure 8.1 SEM images of other structures that have been prepared by EBL for different applications in plasmonics. A) Dashed H-tree fractal, and B) chiral spiral metasurface composed of 1 μm diameter gold nanodisks.

Throughout this thesis, light that is linearly polarized is used to perform the various spectroscopic measurements. An emerging approach is to instead use circularly polarized light. This sub-field is known as chiral optics or chiral plasmonics.⁹ Here, the fabricated individual nanostructures can be chiral or achiral, and can be further arranged into chiral or achiral configurations. An example of a metasurface composed of achiral nanodisks arranged into a chiral geometry (Fermat's spiral) is shown in Figure 8.1B. Currently, the dominant approach is to use the plasmonic nanostructures to enhance the circular dichroism spectrum of an analyte that is near or is adsorbed onto the surface of the structure. With respect to vibrational spectroscopy, the use of circularly polarized light in the visible region this is known as Raman optical activity, and vibrational circular dichroism in the mid-IR. By combining plasmonics with these spectroscopies,¹⁰ it is possible to enhance the vibrational fingerprint, as is done in more traditional SERS and SEIRA experiments. To date, coupling surface-enhancement and Raman optical activity has been examined by only a few groups,¹¹⁻¹⁴ but no results have yet been collected to demonstrate enhanced vibrational circular dichroism. The difficulty of such studies derives from the low level of circular dichroism and coupling between linear and circular dichroism. Generally, the contribution of linear dichroic effects is greater than those from the circular dichroism effects. For either approach, many of the structures prepared in this

thesis given a few structural changes, most notably the dendrimers, may be applicable for studies involving chiral plasmonics.

The structures explored in this thesis have the potential to be investigated for other optical processes. Currently, the applicability of the dendritic fractals for nonlinear optical processes, specifically second-harmonic generation,¹⁵⁻¹⁶ is being explored in our group.¹⁷ Other spectroscopic methods involving pico- and femtosecond excitation sources that can benefit from the structures that have resonances in the visible and near-IR. These processes can include surface-enhanced femtosecond stimulated Raman spectroscopy,¹⁸ surface-enhanced coherent anti-Stokes Raman spectroscopy (SE-CARS),¹⁹ and time-resolved SE-CARS.²⁰

Critical to this thesis, FDTD calculations were performed to determine the spatial distribution of electromagnetic enhancement over the surface of the nanostructures, and to determine the polarization of the plasmon modes. Recent advancements have been made to use experimental methods to determine the spatial distribution of enhancement and confirm the results predicted by FDTD modelling. In some cases, performing chemistry at the nanoscale at the nanoscale is an ideal method.²¹⁻²³ Currently, the applicability of the dendrimers for nanoscale grafting is being explored using diazonium salts as the probe analytes. This work is presently being conducted through an international collaboration with the Universities of Paris Diderot and Paris Descartes (group of N. Félidj and C. Mangeney). Upon irradiation, a diaryl film forms at the hot-spots of the dendrimers. AFM and SEM measurements can then be used to visualize the spatial distribution of enhancement. Multiple analytes can potentially be spatially positioned on the structure by properly selecting the actinic wavelength and/or the polarization of the excitation light. Such differential functionalization paves the way to the development of sensors with multianalyte detection. Alternatively, tip-enhanced Raman spectroscopy (TERS) can also be used to observe the hot-spots.²⁴⁻²⁵ By functionalizing either the metal tip or the surface of the nanostructure, when the TERS tip is located within the hot-spot of the structure, additional enhancement can be observed. TERS mapping would then reveal the position of hot-spots, albeit with long acquisition times that are typically associated to TERS-mapping. By coupling this approach with the

plasmon-mediated grafting, it would be possible to experimentally validate where each analyte is grafted onto the surface based on their unique vibrational fingerprints. The challenge for both of those approaches is that the resonance(s) of the structures must match the available excitation wavelengths, or the resonance wavelength of the TERS tip. Electron energy loss spectroscopy (EELS) does not have this limitation, and has therefore been used extensively throughout the literature to map the distribution of hot-spots of plasmonic nanostructures.²⁶ Recently, a study involving EELS and a fractal nanostructure has been published.²⁷ This study highlights the power of this technique with respect to multiresonant structures as well as the interest for fractal structures and is thus relevant to the structures described in this thesis.

Arguably the most relevant application of the work described throughout this thesis is on-chip sensing.²⁸⁻²⁹ To best achieve this, the designed structures should be incorporated into micro- and/or nanofluidic channels and devices.³⁰ Although EBL can be used to determine the idealized geometries of the nanostructures, for end-goal use, alternative fabrication methodologies that offer higher-throughput fabrication are required. For example, a recent work combined nanoimprint lithography, reactive-ion etching, and atomic layer deposition to reliably prepare plasmonic nanostructures with sub-nanometer resolution over an area of 1.4×1.4 inches.³¹ These types of fabricated platforms represent the next generation of on-chip sensors that can be incorporated into a variety of applications, ranging from materials research to life sciences.

Over the last decade, the field of plasmonics, and the subsequent sub-fields such as molecular plasmonics, have rapidly grown. With advancements in nanofabrication, it is now becoming possible to prepare nanostructures with tailored optical properties. One limitation is the creation of arrays of 2D structures. Very little work has been done with multilayered structures or three-dimensional structures. The plasmonic and optical properties can then be exploited for a variety of applications, with a dominant one being molecular sensing using plasmon-mediated surface-enhanced techniques. Currently, the focus is on SERS. However, it is important to recognize the capabilities of other techniques, such as SEIRA, and to further develop approaches that can couple techniques together. Doing so will provide not only critical fundamental advancements in the field,

but also provide advancements in the various applications that can benefit from plasmonics.

8.1 References

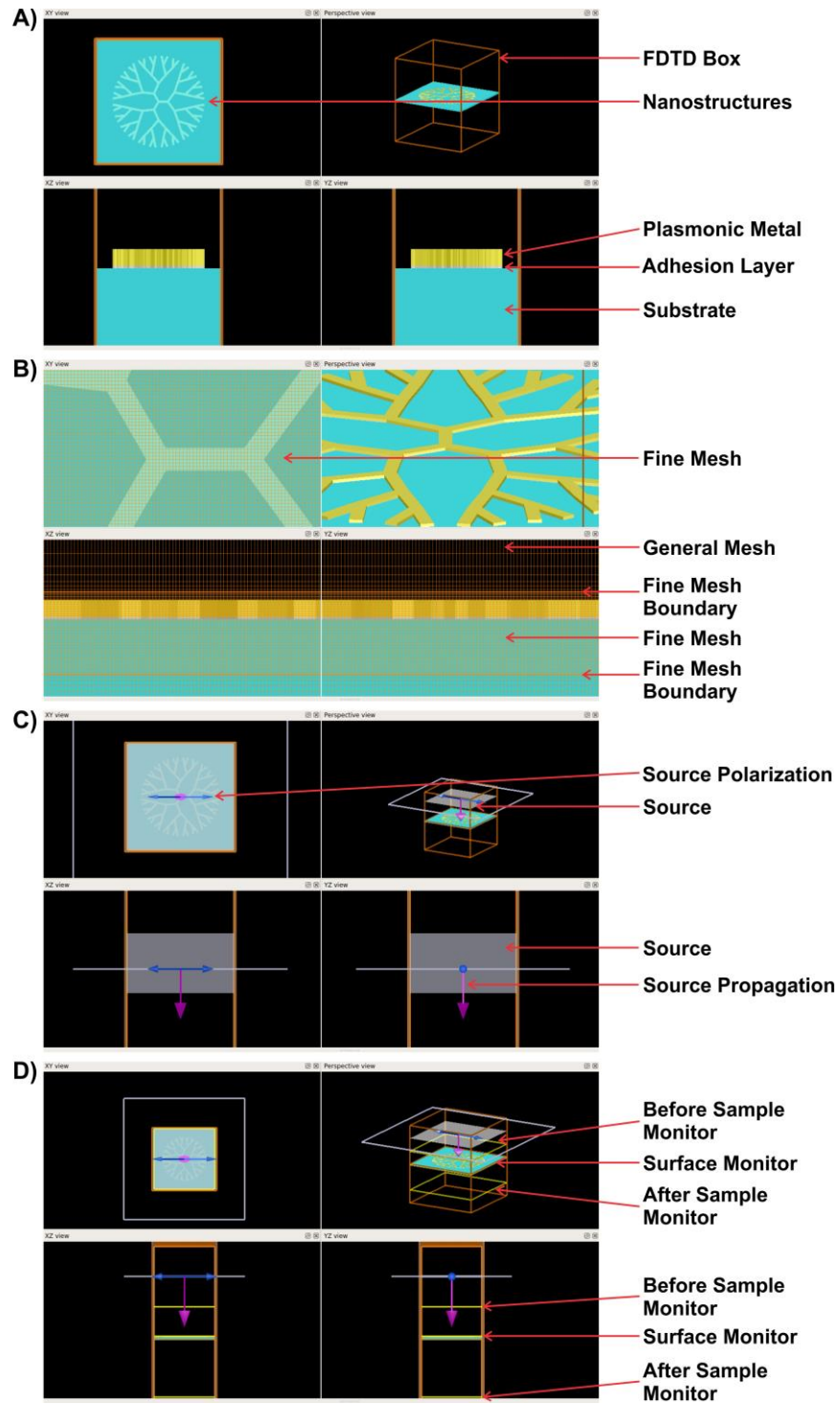
1. Bailey, M. R.; Martin, R. S.; Schultz, Z. D., *J. Phys. Chem. C* **2016**, *120*, 20624-20633.
2. Kearns, H.; Goodacre, R.; Jamieson, L. E.; Graham, D.; Faulds, K., *Anal. Chem.* **2017**, *89*, 12666-12673.
3. Lussier, F.; Brulé, T.; Vishwakarma, M.; Das, T.; Spatz, J. P.; Masson, J.-F., *Nano Lett.* **2016**, *16*, 3866-3871.
4. Feliu, N.; Hassan, M.; Garcia Rico, E.; Cui, D.; Parak, W.; Alvarez-Puebla, R., *Langmuir* **2017**, *33*, 9711-9730.
5. Quirk, A.; Lardner, M. J.; Tun, Z.; Burgess, I. J., *Langmuir* **2016**, *32*, 2225-2235.
6. Limaj, O.; Etezadi, D.; Wittenberg, N. J.; Rodrigo, D.; Yoo, D.; Oh, S.-H.; Altug, H., *Nano Lett.* **2016**, *16*, 1502-1508.
7. Cetin, A. E.; Turkmen, M.; Aksu, S.; Etezadi, D.; Altug, H., *Appl. Phys. B* **2015**, *118*, 29-38.
8. Guanhai, L.; Xiaoshuang, C.; Bo, N.; Oupeng, L.; Lujun, H.; Yuan, J.; Weida, H.; Wei, L., *Nanotechnology* **2013**, *24*, 205702.
9. Wang, X.; Tang, Z., *Small* **2017**, *13*, 1601115.
10. Abdali, S.; Blanch, E. W., *Chem. Soc. Rev.* **2008**, *37*, 980-992.
11. Ostovar pour, S.; Rocks, L.; Faulds, K.; Graham, D.; Parchaňský, V.; Bouř, P.; Blanch, E. W., *Nat. Chem.* **2015**, *7*, 591.
12. Wu, T.; Zhang, X.; Wang, R.; Zhang, X., *J. Phys. Chem. C* **2016**, *120*, 14795-14804.
13. Ren, X.; Lin, W.; Fang, Y.; Ma, F.; Wang, J., *RSC Adv.* **2017**, *7*, 34376-34381.
14. Hu, L.; Xi, F.; Qv, L.; Fang, Y., *ACS Omega* **2018**, *3*, 1170-1177.
15. Rahmani, M.; Shorokhov, A. S.; Hopkins, B.; Miroshnichenko, A. E.; Shcherbakov, M. R.; Camacho-Morales, R.; Fedyanin, A. A.; Neshev, D. N.; Kivshar, Y. S., *ACS Photonics* **2017**, *4*, 454-461.
16. Hazra, B.; Das, K.; Chandra, M., *Phys. Chem. Chem. Phys.* **2017**, *19*, 18394-18399.
17. Hou, R.; Shynkar, V.; Lafargue, C.; Kolkowski, R.; Zyss, J.; Lagugne-Labarthe, F., *Phys. Chem. Chem. Phys.* **2016**, *18*, 7956-7965.
18. Negru, B.; McAnally, M. O.; Mayhew, H. E.; Ueltschi, T. W.; Peng, L.; Sprague-Klein, E. A.; Schatz, G. C.; Van Duyne, R. P., *J. Phys. Chem. C* **2017**, *121*, 27004-27008.

19. He, J.; Fan, C.; Ding, P.; Zhu, S.; Liang, E., *Sci. Rep.* **2016**, *6*, 20777.
20. Yampolsky, S.; Fishman, D. A.; Dey, S.; Hulkko, E.; Banik, M.; Potma, E. O.; Apkarian, V. A., *Nat. Photon.* **2014**, *8*, 650.
21. Hobbs, R. G.; Putnam, W. P.; Fallahi, A.; Yang, Y.; Kärtner, F. X.; Berggren, K. K., *Nano Lett.* **2017**, *17*, 6069-6076.
22. Nguyen, M.; Kherbouche, I.; Gam-Derouich, S.; Ragheb, I.; Lau-Truong, S.; Lamouri, A.; Levi, G.; Aubard, J.; Decorse, P.; Felidj, N.; Mangeney, C., *Chem. Commun.* **2017**, *53*, 11364-11367.
23. Tijunelyte, I.; Kherbouche, I.; Gam-Derouich, S.; Nguyen, M.; Lidgi-Guigui, N.; de la Chapelle, M. L.; Lamouri, A.; Levi, G.; Aubard, J.; Chevillot-Biraud, A.; Mangeney, C.; Felidj, N., *Nanoscale Horiz.* **2018**, *3*, 53-57.
24. Awada, C.; Plathier, J.; Dab, C.; Charra, F.; Douillard, L.; Ruediger, A., *Phys. Chem. Chem. Phys.* **2016**, *18*, 9405-9411.
25. Dab, C.; Awada, C.; Merlen, A.; Ruediger, A., *Phys. Chem. Chem. Phys.* **2017**, *19*, 31063-31071.
26. Wu, Y.; Li, G.; Camden, J. P., *Chem. Rev.* **2018**, *118*, 2994-3031.
27. Bellido, E. P.; Bernasconi, G. D.; Rossouw, D.; Butet, J.; Martin, O. J. F.; Botton, G. A., *ACS Nano* **2017**, *11*, 11240-11249.
28. Bibikova, O.; Haas, J.; Lopez-Lorente, A. I.; Popov, A.; Kinnunen, M.; Meglinski, I.; Mizaikoff, B., *Analyst* **2017**, *142*, 951-958.
29. Liu, C.; Wang, Z.; Li, E.; Liang, Z.; Chakravarty, S.; Xu, X.; Wang, A. X.; Chen, R. T.; Fan, D., *ACS Sens.* **2017**, *2*, 346-353.
30. Jahn, I. J.; Zukovskaja, O.; Zheng, X. S.; Weber, K.; Bocklitz, T. W.; Cialla-May, D.; Popp, J., *Analyst* **2017**, *142*, 1022-1047.
31. Song, B.; Yao, Y.; Groenewald, R. E.; Wang, Y.; Liu, H.; Wang, Y.; Li, Y.; Liu, F.; Cronin, S. B.; Schwartzberg, A. M.; Cabrini, S.; Haas, S.; Wu, W., *ACS Nano* **2017**, *11*, 5836-5843.

Appendix A – Details for FDTD Calculations

The FDTD box (indicated in A) defines the region where the calculations will be performed. The boundary conditions (typically periodic or perfectly matched layers (PML)) reflect the parameters used. For example, if the structure occurs periodically over the surface, then periodic conditions will typically be used. The geometry chosen for the nanostructures can be based either on the ideal dimensions (those that were designed in DesignCAD for EBL) or the actual dimensions (determined by SEM images). The metal thicknesses used correspond to the amounts deposited onto the surface. Determining the ideal dimensions for the substrate thickness is often the result of multiple calculations to see what parameters give results closest to the experimental measurements. Within the FDTD box, a grid mesh (labelled as general mesh) is built. To obtain high resolution EM field maps, a region with a finer mesh must be defined. Depending on the memory capabilities of the computer used, these mesh units typically have dimensions smaller than 10 nm. It is important that this region of fine mesh incorporates some medium above the structure(s), the structure(s) and a portion of the substrate.

The source used to irradiate the sample is placed above the structures (C). There are a variety of sources that can be chosen, with plane waves typically being used in this thesis. Once again, selecting the correct type of source and the ideal height above the sample is often the result of repeated calculations. Within the source parameters, the polarization and propagation directions along with the wavelength range can be chosen. The polarization can be selected to match the experimental conditions, with a propagation (described as injection) direction towards the sample. The wavelength range can be wide, corresponding to absorption measurements, or a single wavelength for EM field map calculations. Monitors are placed at the surface of the structures to calculate the EM field, to determine the spatial distribution of EM enhancement. The monitors placed above and below the sample are used in calculating the theoretical absorption or extinction spectra.



General design for FDTD calculations with the highlighted geometries and positions for A) nanostructures, B) mesh, C) source, and D) monitors.

Appendix B – Fabrication Details for Nanosphere Lithography

To prepare substrates compatible with nanosphere lithography, microscope cover slips and silicon wafers are sonicated in acetone for 5 minutes followed by cleaning in Nochromix solution in concentrated sulphuric acid for 15 minutes. After being thoroughly rinsed in Milli-Q ultrapure water (18.2 M Ω ·cm), the samples are sonicated in a 1:1:5 solution of ammonium hydroxide:hydrogen peroxide:ultrapure water for 1 hour. The cleaned substrates are then rinsed, and stored in Milli-Q water. In the developed protocol for Chapter 4, the complete NSL process (as demonstrated in Figure 2.5) is performed twice. In the first round of NSL, a suspension of 1 μ m diameter polystyrene spheres are diluted in anhydrous ethanol to a ratio of 1:25. An o-ring with an internal diameter of 8 mm is placed onto the center of the substrate, and 30 μ L of the dilute polystyrene solution is drop-casted into the middle of the o-ring. Once dried, the o-ring is removed, and 3 nm of titanium followed by 30 nm of gold are deposited by electron-beam evaporation at a rate no greater than 0.5 $\text{\AA}/\text{s}$. The substrates are then sonicated in anhydrous ethanol to remove the polystyrene particles. In the second round of nanosphere lithography, a suspension of 6 μ m polystyrene spheres are diluted in an anhydrous ethanol to a ratio of 1:1. An o-ring with the same diameter is aligned on the gold coated substrate, and 30 μ L of the dilute 6 μ m polystyrene solution is drop-casted into the middle of the o-ring. Once the solution is dried, a further 3 nm of titanium and 30 nm of gold are deposited over the surface. The 6 μ m polystyrene spheres are then removed by sonication in anhydrous ethanol. Although this approach does not provide as large surface coverage compared to other methods (spin-coating and air-water interface), this approach does provide macroscopic regions (mm^2) that can be readily observed by visual inspection.

Appendix C – Fabrication Details for Electron-Beam Lithography

Prior to performing the electron-beam lithography (EBL), the desired patterns, and subsequent $50 \times 50 \mu\text{m}^2$ arrays were designed in DesignCAD. Next, run files were prepared using a nano-pattern generating software to control the sequence and position of the arrays once proceeding with the EBL process. Silicon, glass cover slips, and CaF_2 windows were used as substrates throughout this thesis. To prepare the substrates for EBL, the substrates were cleaned by exposure to either oxygen plasma (Chapter 3, 4, 5, and 7) or ultraviolet light and ozone (Chapter 6) for between 10 and 30 minutes. Once cleaned, a 50-100 nm thin layer of poly(methyl methacrylate) (PMMA) was spin-coated onto the surface, first at 500 rpm for 5 seconds to spread the resist over the surface, followed by 3000 rpm for 60 seconds to thin the thickness of the resist layer. For non-conductive substrates (glass cover slips, and CaF_2), a thin layer of a conductive polymer (AquaSave) was applied to the PMMA surface. The AquaSave was gently spread over the surface prior to spinning at 1000 rpm for 45 seconds. All of the EBL was performed in a Leo Zeiss 1530 SEM using a 30 kV acceleration voltage, a $10 \mu\text{m}$ aperture, and at an $800\times$ magnification. Following exposure to the e-beam, glass and CaF_2 substrates were immersed in water to remove the AquaSave. All EBL samples were developed in a 1:3 solution of methyl isobutyl ketone and isopropanol for 2 minutes to dissolve the e-beam exposed PMMA, and then dried under air. E-beam evaporation was then used to deposit a 3 nm adhesion layer of titanium followed by 20 nm of gold at a rate no greater than 0.5 \AA/s . The lift-off of the remaining PMMA was performed in acetone, followed by immersion in isopropanol, and drying under nitrogen.

Appendix D – Copyrights



RightsLink®

Home

Account Info

Help



ACS Publications
Most Trusted. Most Cited. Most Read.

Title: Superimposed Arrays of Nanoprisms for Multispectral Molecular Plasmonics

Author: Gregory Q. Wallace, Mohammadali Tabatabaei, Renjie Hou, et al

Publication: ACS Photonics

Publisher: American Chemical Society

Date: Sep 1, 2016

Copyright © 2016, American Chemical Society

Logged in as:
Gregory Wallace

LOGOUT

PERMISSION/LICENSE IS GRANTED FOR YOUR ORDER AT NO CHARGE

This type of permission/license, instead of the standard Terms & Conditions, is sent to you because no fee is being charged for your order. Please note the following:

- Permission is granted for your request in both print and electronic formats, and translations.
- If figures and/or tables were requested, they may be adapted or used in part.
- Please print this page for your records and send a copy of it to your publisher/graduate school.
- Appropriate credit for the requested material should be given as follows: "Reprinted (adapted) with permission from (COMPLETE REFERENCE CITATION). Copyright (YEAR) American Chemical Society." Insert appropriate information in place of the capitalized words.
- One-time permission is granted only for the use specified in your request. No additional uses are granted (such as derivative works or other editions). For any other uses, please submit a new request.

BACK

CLOSE WINDOW

Copyright © 2018 Copyright Clearance Center, Inc. All Rights Reserved. [Privacy statement](#), [Terms and Conditions](#).
Comments? We would like to hear from you. E-mail us at customercare@copyright.com



RightsLink®

Home

Account Info

Help



ACS Publications
Most Trusted. Most Cited. Most Read.

Title: Dendritic Plasmonics for Mid-Infrared Spectroscopy
Author: Gregory Q. Wallace, Hayden C. Foy, Scott M. Rosendahl, et al
Publication: The Journal of Physical Chemistry C
Publisher: American Chemical Society
Date: May 1, 2017
Copyright © 2017, American Chemical Society

Logged in as:
Gregory Wallace

LOGOUT

PERMISSION/LICENSE IS GRANTED FOR YOUR ORDER AT NO CHARGE

This type of permission/license, instead of the standard Terms & Conditions, is sent to you because no fee is being charged for your order. Please note the following:

- Permission is granted for your request in both print and electronic formats, and translations.
- If figures and/or tables were requested, they may be adapted or used in part.
- Please print this page for your records and send a copy of it to your publisher/graduate school.
- Appropriate credit for the requested material should be given as follows: "Reprinted (adapted) with permission from (COMPLETE REFERENCE CITATION). Copyright (YEAR) American Chemical Society." Insert appropriate information in place of the capitalized words.
- One-time permission is granted only for the use specified in your request. No additional uses are granted (such as derivative works or other editions). For any other uses, please submit a new request.

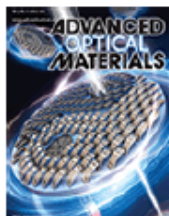
BACK

CLOSE WINDOW

Copyright © 2018 Copyright Clearance Center, Inc. All Rights Reserved. [Privacy statement](#), [Terms and Conditions](#).
Comments? We would like to hear from you. E-mail us at customercare@copyright.com



RightsLink®

[Home](#)
[Account Info](#)
[Help](#)


Title: Exploiting Anisotropy of Plasmonic Nanostructures with Polarization Modulation Infrared Linear Dichroism Microscopy (μ PM-IRLD)

Author: Gregory Q. Wallace, Stuart T. Read, Danielle M. McRae, Scott M. Rosendahl, François Lagugné-Labarthet

Publication: Advanced Optical Materials

Publisher: John Wiley and Sons

Date: Jan 29, 2018

© 2018 WILEY-VCH Verlag GmbH & Co. KGaA, Weinheim

Logged in as:
Gregory Wallace
Account #:
3001243513

[LOGOUT](#)

Order Completed

Thank you for your order.

This Agreement between Mr. Gregory Wallace ("You") and John Wiley and Sons ("John Wiley and Sons") consists of your license details and the terms and conditions provided by John Wiley and Sons and Copyright Clearance Center.

Your confirmation email will contain your order number for future reference.

[printable details](#)

License Number	4278800865216
License date	Jan 30, 2018
Licensed Content Publisher	John Wiley and Sons
Licensed Content Publication	Advanced Optical Materials
Licensed Content Title	Exploiting Anisotropy of Plasmonic Nanostructures with Polarization Modulation Infrared Linear Dichroism Microscopy (μ PM-IRLD)
Licensed Content Author	Gregory Q. Wallace, Stuart T. Read, Danielle M. McRae, Scott M. Rosendahl, François Lagugné-Labarthet
Licensed Content Date	Jan 29, 2018
Licensed Content Pages	1
Type of use	Dissertation/Thesis
Requestor type	Author of this Wiley article
Format	Print and electronic
Portion	Full article
Will you be translating?	No
Title of your thesis / dissertation	Multiresonant Anisotropic Nanostructures for Plasmon-Mediated Spectroscopies
Expected completion date	Mar 2018
Expected size (number of pages)	165
Requestor Location	Mr. Gregory Wallace
Publisher Tax ID	EU826007151
Total	0.00 CAD



RightsLink®

Home

Account Info

Help



ACS Publications
Most Trusted. Most Cited. Most Read.

Title: Mapping Photoemission and Hot-Electron Emission from Plasmonic Nanoantennas

Logged in as:
Gregory Wallace

LOGOUT

Author: Richard G. Hobbs, William P. Putnam, Arya Fallahi, et al

Publication: Nano Letters

Publisher: American Chemical Society

Date: Oct 1, 2017

Copyright © 2017, American Chemical Society

PERMISSION/LICENSE IS GRANTED FOR YOUR ORDER AT NO CHARGE

This type of permission/license, instead of the standard Terms & Conditions, is sent to you because no fee is being charged for your order. Please note the following:

- Permission is granted for your request in both print and electronic formats, and translations.
- If figures and/or tables were requested, they may be adapted or used in part.
- Please print this page for your records and send a copy of it to your publisher/graduate school.
- Appropriate credit for the requested material should be given as follows: "Reprinted (adapted) with permission from (COMPLETE REFERENCE CITATION). Copyright (YEAR) American Chemical Society." Insert appropriate information in place of the capitalized words.
- One-time permission is granted only for the use specified in your request. No additional uses are granted (such as derivative works or other editions). For any other uses, please submit a new request.

If credit is given to another source for the material you requested, permission must be obtained from that source.

BACK

CLOSE WINDOW

Copyright © 2018 Copyright Clearance Center, Inc. All Rights Reserved. [Privacy statement](#), [Terms and Conditions](#).
Comments? We would like to hear from you. E-mail us at customer-care@copyright.com

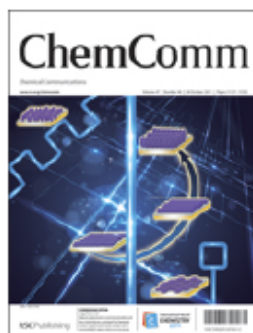


RightsLink®

Home

Account
Info

Help



Title: Regioselective surface functionalization of lithographically designed gold nanorods by plasmon-mediated reduction of aryl diazonium salts

Author: Mai Nguyen, Issam Kherbouche, Sarra Gam-Derouich, Iman Ragheb, Stéphanie Lau-Truong, Aazdine Lamouri, Georges Lévi, Jean Aubard, Philippe Decorse, Nordin Félidj, Claire Mangeney

Logged in as:
Gregory Wallace
Account #:
3001243513

LOGOUT

Publication: Chemical Communications (Cambridge)

Publisher: Royal Society of Chemistry

Date: Sep 26, 2017

Copyright © 2017, Royal Society of Chemistry

Order Completed

Thank you for your order.

This Agreement between Mr. Gregory Wallace ("You") and Royal Society of Chemistry ("Royal Society of Chemistry") consists of your license details and the terms and conditions provided by Royal Society of Chemistry and Copyright Clearance Center.

Your confirmation email will contain your order number for future reference.

[printable details](#)

License Number	4278800494466
License date	Jan 30, 2018
Licensed Content Publisher	Royal Society of Chemistry
Licensed Content Publication	Chemical Communications (Cambridge)
Licensed Content Title	Regioselective surface functionalization of lithographically designed gold nanorods by plasmon-mediated reduction of aryl diazonium salts
Licensed Content Author	Mai Nguyen, Issam Kherbouche, Sarra Gam-Derouich, Iman Ragheb, Stéphanie Lau-Truong, Aazdine Lamouri, Georges Lévi, Jean Aubard, Philippe Decorse, Nordin Félidj, Claire Mangeney
Licensed Content Date	Sep 26, 2017
Licensed Content Volume	53
Licensed Content Issue	82
Type of Use	Thesis/Dissertation
Requestor type	academic/educational
Portion	figures/tables/images
Number of figures/tables/images	1
Distribution quantity	25
Format	print and electronic
Will you be translating?	no
Order reference number	
Title of the thesis/dissertation	Multiresonant Anisotropic Nanostructures for Plasmon-Mediated Spectroscopies
Expected completion date	Mar 2018
Estimated size	165

Requestor Location Mr. Gregory Wallace

Billing Type
Billing address

Total Attn: Mr. Gregory Wallace
0.00 CAD

[ORDER MORE](#) [CLOSE WINDOW](#)

Copyright © 2018 [Copyright Clearance Center, Inc.](#) All Rights Reserved. [Privacy statement](#), [Terms and Conditions](#).
Comments? We would like to hear from you. E-mail us at customercare@copyright.com



RightsLink®

Home

Account Info

Help



ACS Publications
Most Trusted. Most Cited. Most Read.

Title: Wet Etching-Assisted Colloidal Lithography: A General Strategy toward Nanodisk and Nanohole Arrays on Arbitrary Substrates

Logged in as:
Gregory Wallace

LOGOUT

Author: Jingjing Wang, Guotao Duan, Yue Li, et al

Publication: Applied Materials

Publisher: American Chemical Society

Date: Jun 1, 2014

Copyright © 2014, American Chemical Society

PERMISSION/LICENSE IS GRANTED FOR YOUR ORDER AT NO CHARGE

This type of permission/license, instead of the standard Terms & Conditions, is sent to you because no fee is being charged for your order. Please note the following:

- Permission is granted for your request in both print and electronic formats, and translations.
- If figures and/or tables were requested, they may be adapted or used in part.
- Please print this page for your records and send a copy of it to your publisher/graduate school.
- Appropriate credit for the requested material should be given as follows: "Reprinted (adapted) with permission from (COMPLETE REFERENCE CITATION). Copyright (YEAR) American Chemical Society." Insert appropriate information in place of the capitalized words.
- One-time permission is granted only for the use specified in your request. No additional uses are granted (such as derivative works or other editions). For any other uses, please submit a new request.

If credit is given to another source for the material you requested, permission must be obtained from that source.

BACK

CLOSE WINDOW

Copyright © 2018 Copyright Clearance Center, Inc. All Rights Reserved. [Privacy statement](#), [Terms and Conditions](#). Comments? We would like to hear from you. E-mail us at customer@copyright.com



RightsLink®

Home

Account Info

Help



ACS Publications
Most Trusted. Most Cited. Most Read.

Title: Moiré Nanosphere Lithography

Author: Kai Chen, Bharath Bangalore Rajeeva, Zilong Wu, et al

Publication: ACS Nano

Publisher: American Chemical Society

Date: Jun 1, 2015

Copyright © 2015, American Chemical Society

Logged in as:

Gregory Wallace

Account #:

3001243513

LOGOUT

PERMISSION/LICENSE IS GRANTED FOR YOUR ORDER AT NO CHARGE

This type of permission/license, instead of the standard Terms & Conditions, is sent to you because no fee is being charged for your order. Please note the following:

- Permission is granted for your request in both print and electronic formats, and translations.
- If figures and/or tables were requested, they may be adapted or used in part.
- Please print this page for your records and send a copy of it to your publisher/graduate school.
- Appropriate credit for the requested material should be given as follows: "Reprinted (adapted) with permission from (COMPLETE REFERENCE CITATION). Copyright (YEAR) American Chemical Society." Insert appropriate information in place of the capitalized words.
- One-time permission is granted only for the use specified in your request. No additional uses are granted (such as derivative works or other editions). For any other uses, please submit a new request.

If credit is given to another source for the material you requested, permission must be obtained from that source.

BACK

CLOSE WINDOW

Copyright © 2018 [Copyright Clearance Center, Inc.](#) All Rights Reserved. [Privacy statement](#). [Terms and Conditions](#). Comments? We would like to hear from you. E-mail us at customer@copyright.com



RightsLink®

Home

Account Info

Help



ACS Publications
Most Trusted. Most Cited. Most Read.

Title: Mid-Infrared Localized Plasmons through Structural Control of Gold and Silver Nanocrescents

Author: Cindy T. Cooper, Miguel Rodriguez, Steve Blair, et al

Publication: The Journal of Physical Chemistry C

Publisher: American Chemical Society

Date: May 1, 2015

Copyright © 2015, American Chemical Society

Logged in as:
Gregory Wallace
Account #:
3001243513

LOGOUT

PERMISSION/LICENSE IS GRANTED FOR YOUR ORDER AT NO CHARGE

This type of permission/license, instead of the standard Terms & Conditions, is sent to you because no fee is being charged for your order. Please note the following:

- Permission is granted for your request in both print and electronic formats, and translations.
- If figures and/or tables were requested, they may be adapted or used in part.
- Please print this page for your records and send a copy of it to your publisher/graduate school.
- Appropriate credit for the requested material should be given as follows: "Reprinted (adapted) with permission from (COMPLETE REFERENCE CITATION). Copyright (YEAR) American Chemical Society." Insert appropriate information in place of the capitalized words.
- One-time permission is granted only for the use specified in your request. No additional uses are granted (such as derivative works or other editions). For any other uses, please submit a new request.

If credit is given to another source for the material you requested, permission must be obtained from that source.

BACK

CLOSE WINDOW

Copyright © 2018 Copyright Clearance Center, Inc. All Rights Reserved. [Privacy statement](#), [Terms and Conditions](#).
Comments? We would like to hear from you. E-mail us at customer-care@copyright.com

Curriculum Vitae

Name:	Gregory Q. Wallace
Post-secondary Education and Degrees:	<p>The University of Western Ontario London, Ontario, Canada 2009-2013 B.Sc.</p> <p>The University of Western Ontario London, Ontario, Canada 2013-2018 Ph.D.</p>
Honours and Awards:	<p>CSC Travel Award 2017</p> <p>Elsevier Spectrochimica Acta A Student Oral Presentation Award at the 9th International Conference on Advanced Vibrational Spectroscopy 2017</p> <p>2nd Place in Poster Competition (Physical / Computational / Theoretical) at the 100th Canadian Chemistry Conference and Exhibition 2017</p> <p>3rd Place in Western University's Sixth Annual 3 Minute Thesis Competition 2017</p> <p>Doctoral Excellence Research Award 2016-2018</p> <p>NSERC Postgraduate Scholarship Doctoral (PGSD) 2016-2018</p> <p>Ontario Graduate Scholarship (Declined) 2016-2017</p>
Related Work Experience	<p>Teaching Assistant The University of Western Ontario 2013-2018</p>

Publications:

13. Kolhatkar, G.; Merlen, A.; Dab, C.; **Wallace, G.Q.**; Lagugné-Labarthet, F.; Ruediger, A. A method to enhance the near-field contribution in apertureless scanning near-field optical microscopy images. *Submitted to Beilstein J. Nanotechnol.*
12. **Wallace, G.Q.**; Read, S.T.; McRae, D.M.; Rosendahl, S.M.; Lagugné-Labarthet, F. Exploiting anisotropy of plasmonic nanostructures with polarization-modulation infrared linear dichroism microscopy (μ PM-IRLD) *Adv. Opt. Mater.*, 2018, 6, 1701336.
11. Coady, M.J.; Wood, M.; **Wallace, G.Q.**; Nielsen, K.; Lagugné-Labarthet, F.; Kietzig, A-M., Ragona, P.J. Icephobic behavior of UV-cured polymer networks incorporated into slippery lubricant-infused porous surfaces: Improving SLIPS durability. *ACS Appl. Mater. Interfaces*, 2018, 10, 2890-2896.
10. **Wallace, G.Q.**; Foy, H.C.; Rosendahl, S.M.; Lagugné-Labarthet, F. Dendritic plasmonics for mid-infrared spectroscopy. *J. Phys. Chem. C*, 2017, 121, 9497-9507.
9. Garreau, A.; Tabatabaei, M.; Hou, R.; **Wallace, G.Q.**; Norton, P.R.; Lagugné-Labarthet, F. Probing the plasmonic properties of heterometallic nanoprisms with near-field fluorescence microscopy. *J. Phys. Chem. C*, 2016, 120, 20267-20276.
8. **Wallace, G.Q.**; Tabatabaei, M.; Hou, R.; Coady, M.J.; Norton, P.R.; Rosendahl, S.M.; Merlen, A.; Lagugné-Labarthet, F. Superimposed arrays of nanoprisms for multispectral molecular plasmonics. *ACS Photonics*, 2016, 3, 1723-1732.
7. Marinovich, R.; Soenjaya, Y.; **Wallace, G.Q.**; Zuskov, A.; Dunkman, A.; Foster, B.; Ao, M.; Lam, V.; Rizkalla, A.; Beier, F.; Somerman, M.J.; Holdsworth, D.; Soslowsky, L.; Lagugné-Labarthet, F.; Goldberg, H.A. The role of bone sialoprotein in the tendon-bone insertion. *Matrix Biol.*, 2016, 52-54, 325-338.
6. **Wallace, G.Q.**; Tabatabaei, M.; Zuin, M.S.; Workentin, M.S.; Lagugné-Labarthet, F. A nanoaggregate-on-mirror platform for molecular and biomolecular detection by surface-enhanced Raman spectroscopy. *Anal. Bioanal. Chem.*, 2016, 408, 609-618.
5. Tabatabaei, M.; **Wallace, G.Q.**; Caetano, F.A.; Gillies, E.R.; Ferguson, S.S.G.; Lagugné-Labarthet, F. Controlled positioning of analytes and cells on a plasmonic platform for glycan sensing using surface enhanced Raman spectroscopy. *Chem. Sci.*, 2016, 7, 575-582.
4. **Wallace, G.Q.**; Zuin, M.S.; Tabatabaei, M.; Gobbo, P.; Lagugné-Labarthet, F.; Workentin, M.S. Gold nanosponges: (AuNS): A versatile structure for surface-enhanced Raman spectroscopic detection of molecules and biomolecules. *Analyst*, 2015, 140, 7278-7282.
3. Cheng, X.R.; **Wallace, G.Q.**; Lagugné-Labarthet, F.; Kerman, K. Au nanostructures surfaces for electrochemical and localized surface plasmon resonance-based monitoring of α -synuclein-small molecule interactions. *ACS Appl. Mater. Interfaces*, 2015, 7, 4081-4088.
2. **Wallace, G.Q.**; Pashaei, F.; Hou, R.; Tabatabaei, M.; Lagugné-Labarthet, F. Plasmonic nanostructures for enhanced Raman spectroscopy: SERS and TERS of thiolated monolayers. *Proc. SPIE 9126, Nanophotonics V*, 2014, 912610.

1. **Wallace, G.Q.**; Tabatabaei, M.; Lagurné-Labarthe, F. Towards attomolar detection using a surface-enhanced Raman spectroscopy platform fabricated by nanosphere lithography. *Can J. Chem.*, 2014, 92, 1-8.

Presentations as presenting author:

Oral

6. **Wallace, G.Q.**; Lagurné-Labarthe, F. (2017) Dendritic structures for fractal plasmonics in the near- and mid-infrared. 9th International Conference on Advanced Vibrational Spectroscopy (ICAVS), Victoria, British Columbia, Canada.
5. **Wallace, G.Q.**; Tabatabaei, M.; Pashae, F.; Caetano, F.A.; Ferguson, S.S.G.; Lagurné-Labarthe, F. (2016) Probing extra- and intracellular biomolecules by tip-enhanced Raman spectroscopy. 99th Canadian Chemistry Conference and Exhibition, Halifax, Nova Scotia, Canada.
4. **Wallace, G.Q.**; Tabatabaei, M.; Hou, R.; Coady, M.J.; Merlen, A.; Lagurné-Labarthe, F. (2016) Plasmonic platforms for multispectral surface-enhanced spectroscopies. 99th Canadian Chemistry Conference and Exhibition, Halifax, Nova Scotia, Canada.
3. **Wallace, G.Q.**; Zuin, M.S.; Tabatabaei, M.; Gobbo, P.; Workentin, M.S.; Lagurné-Labarthe, F. (2015) Molecular and biomolecular detection by surface-enhanced Raman spectroscopy using a nanoaggregate-on-mirror plasmonic sensor. 98th Canadian Chemistry Conference and Exhibition, Ottawa, Ontario, Canada.
2. **Wallace, G.Q.**; Zuin, M.S.; Tabatabaei, M.; Gobbo, P.; Caetano, F.A.; Ferguson, S.S.G.; Workentin, M.S.; Lagurné-Labarthe, F. (2015) Boronic acid functionalized plasmonic nanosensors for glycol-sensing applications. Centre for Advanced Materials and Biomaterials Research (CAMBR) Day, London, Ontario, Canada.
1. **Wallace, G.Q.**; Tabatabaei, M.; Lagurné-Labarthe, F. (2013) Determining the limit of detection of a platform fabricated by nanosphere lithography for surface-enhanced Raman spectroscopy. 41st Southern Ontario Undergraduate Student Chemistry Conference (SOUSCC), Hamilton, Ontario, Canada.

Poster

11. **Wallace, G.Q.**; McConnell, E.M.; Foy, H.C.; Rosendahl, S.M.; DeRosa, M.C.; Lagurné-Labarthe, F. (2017) Dendritic fractals as plasmonic platforms for multispectral molecular sensing. 100th Canadian Chemistry Conference and Exhibition, Toronto, Ontario, Canada.
10. **Wallace, G.Q.**; Foy, H.C.; Lagurné-Labarthe, F. (2017) Optical properties of arrays of plasmonic nanoarrowheads: an alternative to nanoprisms. 100th Canadian Chemistry Conference and Exhibition, Toronto, Ontario, Canada.

9. **Wallace, G.Q.;** Tabatabaei, M.; Hou, R.; Coady, M.J.; Foy, H.C.; Norton, P.R.; Simpson, T.S.; Rosendahl, S.M.; Merlen, A.; Lagugné-Labarhet, F. (2017) Superimposing nanostructures: a means of fabricating multi-resonant plasmonic platforms. The Fallona Family Interdisciplinary Science Showcase, London, Ontario, Canada.
8. **Wallace, G.Q.;** Tabatabaei, M.; Hou, R.; Coady, M.J.; Foy, H.C.; Norton, P.R.; Simpson, T.S.; Rosendahl, S.M.; Merlen, A.; Lagugné-Labarhet, F. (2016) Superimposing nanostructures: a means of fabricating multi-resonant plasmonic platforms. 7th Annual Nano Ontario Conference, Guelph, Ontario, Canada.
7. **Wallace, G.Q.;** Tabatabaei, M.; Hou, R.; Coady, M.J.; Norton, P.R.; Simpson, T.S.; Rosendahl, S.M.; Merlen, A.; Lagugné-Labarhet, F. (2016) Development of plasmonic platforms for multispectral surface-enhanced spectroscopies. SciX 2016, Minneapolis, Minnesota, United States of America.
6. **Wallace, G.Q.;** Marinovich, R.M.; Soenjaya, Y.; Goldberg, H.A.; Lagugné-Labarhet, F. (2015) Studying the effects of knocking out bone sialoprotein in mice by Raman spectroscopy. 98th Canadian Chemistry Conference and Exhibition, Ottawa, Ontario, Canada.
5. **Wallace, G.Q.;** Lagugné-Labarhet, F. (2015) The role of Raman spectroscopy in musculoskeletal research. Bone & Joint Research Retreat, London, Ontario, Canada.
4. **Wallace, G.Q.;** Zuin, M.S.; Tabatabaei, M.; Gobbo, P.; Workentin, M.S.; Lagugné-Labarhet, F. (2014) Functionalized Au films combined with Au nanoaggregates for glucose detection by surface-enhanced Raman spectroscopy. The Fallona Family Interdisciplinary Science Showcase, London, Ontario, Canada.
3. **Wallace, G.Q.;** Zuin, M.S.; Tabatabaei, M.; Gobbo, P.; Workentin, M.S.; Lagugné-Labarhet, F. (2014) Functionalized Au films combined with Au nanoaggregates for glucose detection by surface-enhanced Raman spectroscopy. 5th Annual Nano Ontario Conference, Windsor, Ontario, Canada.
2. **Wallace, G.Q.;** Bouchet, M.; Hou, R.; Tabatabaei, M.; Lagugné-Labarhet, F. (2013) Adapting an ultrasensitive SERS substrate fabricated by nanosphere lithography for infrared spectroscopies. Centre for Advanced Materials and Biomaterials Research (CAMBR) Day, London, Ontario, Canada.
1. **Wallace, G.Q.;** Tabatabaei, M.; Lagugné-Labarhet, F. (2013) Determining the limit of detection of a SERS platform fabricated by nanosphere lithography. 96th Canadian Chemistry Conference and Exhibition, Québec City, Québec, Canada.